Seasonal breaching of coastal barriers

Seasonal breaching of coastal barriers

Proefschrift

ter verkrijging van de graad van doctor
aan de Technische Universiteit Delft
op gezag van de Rector Magnificus Prof. dr. ir. J.T. Fokkema,
voorzitter van het College voor Promoties,
in het openbaar te verdedigen
op dinsdag 19 juni 2007 om 12:30 uur

door

Thieu Quang Tuan
Master of Science in Hydraulic Engineering,
UNESCO-IHE Delft
geboren te Thanh Hoa, Vietnam

Dit proefschrift is goedgekeurd door de promotor:

Prof. dr. ir. M.J.F. Stive

Toegevoegd promotor:

Dr. ir. P.J. Visser

Samenstelling promotiecommissie:

Rector Magnificus	Voorzitter
Prof. dr. ir. M.J.F. Stive	Technische Universiteit Delft, promotor
Dr. ir. P.J. Visser	Technische Universiteit Delft, toegevoegd promotor
Prof. dr. D. X. Hoc	Water Resources University, Vietnam
Prof. dr. H. Hanson	Lund University, Sweden
Prof. dr. ir. H.J. de Vriend	Technische Universiteit Delft
Prof. dr. ir. L.C. van Rijn	Utrecht University
Em. Prof. ir. K. d' Agremond	Technische Universiteit Delft
Prof. ir. H. Ligteringen	Technische Universiteit Delft, reservelid

Ir. H.J. Verhagen heeft als begeleider in belangrijke mate aan de totstandkoming van het proefschrift bijgedragen.

The research was carried out with the financial support from the Royal Dutch Embassy in Hanoi through a co-operational project in Coastal Engineering between Delft University and Hanoi Water Resources University.

Front cover image: the time-dependent response of a barrier during a storm surge, results of a laboratory test carried out in the present research.

ISBN: 978-90-9021954-7

Printed by Sieca Repro, the Netherlands

SUMMARY

Seasonal breaching of coastal barriers

Breaching is a complex morphodynamic process occurring as water overflows the crest of a narrow landmass. A breach in a coastal barrier (a barrier spit, a barrier island, or lagoon barrier) is initiated as the water level on either side of the barrier exceeds a certain threshold level. From the bay side, the rise in water level can be a result of heavy rainfall in the bay watershed or river catchment. From the seaward side the water level can be elevated by surges during storm. Prior to overflow, storm surges at sea can appreciably narrow (dune erosion) and lower (wave overwash) the barrier and thus initiate breaching even when the water level is well below the initial barrier crest level. During a tropical cyclone event, both phenomena may occur, i.e. first the attack by waves and surge on the seaward side and then by flooding on the bay side. Natural or unintended breaching can be catastrophic, causing loss of human lives and damage to infrastructures, buildings and natural habitats. Quantitative understanding of coastal barrier breaching is therefore of great importance to vulnerability assessment of protection works as well as to spatial planning against flooding hazards.

Initiated by the above issues, the main objective of the present research is to develop a reliable process-based numerical model of coastal barrier breaching, which is capable of simulating both the breach initiation during storm surges and the barrier breaching due to overflow. The model is limited to homogeneous coastal sand barriers or similar types only, such as sand-dikes and sand dunes. The newly-developed model is referred to as a site model, i.e. the simulation domain is restricted to a representative cross-section of a barrier and the question where in plan a breach will occur is not answered by the model.

The overall barrier response during storm surges can be distinguished in two parts associated with two major across-shore transport processes, i.e. beach and dune erosion on the seaward side and wave overwash on the landward side. The latter process is a focal topic in the present research. Despite numerous historical incidents, state-of-the-art modelling of wave overwash on coastal barriers is still far from advanced and predictive tools are seriously lacking. This is, in part, because data on overwash are scarce and mainly qualitative. Pre- and post-storm profiles are available in some cases but not the hydraulic conditions associated with those events. Hence, they cannot be used for quantitative investigation of the transport processes and corresponding morphological changes of barriers during overwash events.

Two successive laboratory experiments were carried out to increase physical insight into wave overwash and to generate data for the development of a new numerical model of barrier response during storm surges. The first, a fixed-bed model experiment, aims to investigate wave overtopping closer to its nature, i.e. to better describe the intermittent character. The reason behind this is that wave overtopping should be treated as an event-based process that may not be simplified, as is done conventionally, as a time independent process characterised by an average discharge. This experiment has resulted in newly formulated overtopping parameters, namely the wave-averaged overtopping time, the relative total overtopping time, the overtopping asymmetry, and the average instantaneous discharge. Also, a new approach for defining the equivalent slope of low-crested sandy profiles has been proposed in the overtopping parameterizations that takes effects of the wave period into account.

Modelling of the morphological development of overwash channels and of the breach growth due to overflow in coastal barriers has many features in common. Hence, a common process-based approach has been developed for modelling the growth of these erosional channels. The flow modelling is based on the shallow water equations, which are solved using a robust upwind numerical scheme to resolve numerical difficulties such as stemming from discontinuities in the flow (intermittent overtopping or hydraulic jump in the breach) and from abrupt and arbitrary variations of the channel bed (especially in the case of breaching). Regarding channel morphology, channel growth is a result of an erosion process induced by overflow. By the nature of the process, bed changes are much more dynamic in the streamwise direction than those in the transverse direction. Also, the channel length is relatively short, so the streamwise variation of the channel width is negligible compared to the streamwise variation of the channel bed. As a result, the bed profile along the channel (the vertical growth) must be known in detail while an instantaneous uniform width quantity is usually sufficient to represent the overall channel lateral growth. Therefore, a set of equations for growth of erosional channels has been developed, in which the channel bed changes in lateral and vertical directions are related. A representative (volumetric) channel width has been defined and used in quantifying the channel lateral growth while variations of the channel width in the stream-wise direction are possible. The system of equations is closed through an additional relation between the channel vertical and lateral growth rate. This relation, the cross-sectional growth index, based on the relative capacity of transporting sediment along the bottom and the sides of channel, is found to depend largely on the instantaneous channel geometry and the exponent in the sediment transport formula. The index has been calibrated with existing laboratory data of breach growth in sand-dikes of Caan (1996, see also Visser, 1998) and experimental data of overwash channel development of the present research (the second, mobile-bed experiment).

The second experiment aims to increase understanding of morphological processes involved in the barrier response during storm surges and to generate data for calibration of the model. Mobile (sand) model barriers of various widths and heights were put under attack of random waves. Detailed 3D topographic changes of the barrier were measured, building a complete dataset of the time-dependent barrier response. Comparison of the computational results with the measurement of the barrier response in both lateral and vertical directions gives fairly good agreement. The newly-

formulated overwash parameters have proven to better represent the overwash nature and are suitable for overwash modelling.

In the present research, breaching of coastal barriers is regarded as a gradual erosion process induced by water overflow through a pilot channel in the barrier crest. Once breaching occurs, effects of waves on the breach development are neglected. The breach flow modelling is primarily based on the unsteady open channel flow equations and modelling of the breach growth follows the approach mentioned earlier. However, it is found that a hydraulic jump in the breach plays a role in the breach morphological development, especially regarding scour formation and development. The hydraulic jump should therefore be considered as part of the flow through the breach and its turbulence effects on the breach sediment transport must be taken into account. To this end, a jump-related turbulence source term has been derived and added to the horizontal momentum balance equation to capture the jump profile reliably. The jump modelling has been calibrated with various existing jump data of Gharangik and Chaudhry (1991) and Hermann and Hager (1998). For simulating the scour formation and development, a locally-refined module of flow and bed changes is associated to the turbulent hydraulic jump and activated wherever it appears.

In general, the present barrier breach model is capable of simulating the breach erosion process in sand barriers under arbitrary hydraulic conditions on both sides of the breach. The time-dependent breach growth in both vertical and lateral directions, including the scour formation and development, is successfully modelled without defining any evolutional stages (as done by Visser, 1998). The model has been calibrated with the laboratory data of Caan (1996) and verified against the data of the Zwin'94 field breach experiment (Visser, 1998). On the whole, agreement of the measured breach growth with that predicted by the model is fairly good considering uncertainties in the breach data. The computational results give less resemblance in terms of the scour depth for the last stages (Visser, 1998) after the complete washing-out of the sand plug in the breach, when the scour continues to develop (at much slower rate) whilst the jump has considerably weakened or even vanished. This suggests that another scouring mechanism rather than the jump-induced scour should be incorporated in the modelling of the vertical breach growth for this last period of the breaching process.

The developed model of coastal barrier breaching was applied to reconstruct and assess the situation of a historical breach incident of Hue lagoon in the central coast of Vietnam induced by cyclone EVE in 1999. It has also been done to investigate the model capability of simulating such a prototype breach event. In spite of uncertainty in the available data, the simulations of the breach initiation by the barrier response during the storm surge and the time-dependent breach growth of the barrier due to flood overflow were successful. Satisfactory agreement with reported data has been achieved. From these results, implications for the lagoon safety management and precaution on the breaching threat to the lagoon barrier in general have been derived.

In conclusion, the present study has resulted in an increased insight into the breaching processes of coastal sand barriers under attack by tropical cyclones. A process-based numerical model for coastal barrier breaching has been developed, in which the breach initiation during storm surges and the breach erosion process due to overflow

are the two process components. The new overtopping formulations are one step forward in the description of the wave overtopping nature, necessary for the morphological modelling of wave overwash. The new process-based approach has proven to be efficient and reliable. The jump-induced scouring mechanism has been developed to simulate the scour formation and development in the breach. It is shown to improve the model prediction of breach growth significantly.

Principal recommendations for future research include the necessity of acquisition of more quantitative, preferably time-dependent, data of breach growth and barrier response during storm surges both in large-scale laboratory and field conditions. More specific laboratory studies should be carried out to investigate intra-flow sediment transport processes in wave overwash and under turbulent hydraulic jumps.

SAMENVATTING

Seizoensgerelateerde doorbraak van duinregels

Bresgroei is een gecompliceerd morfodynamisch proces dat optreedt wanneer water over de kruin van een relatief smal grondlichaam stroomt. Een bres in een duinregel (een landtong, een eiland langs de kust of een zandrug langs een lagune) ontstaat als de waterstand aan één van de zijden van de duinregel een kritieke waarde overschrijdt. Landwaarts kan de stijging van de waterstand het gevolg zijn van hevige regenval in de lagune en het stroomgebied van de in de lagune uitstromende rivier. Op zee kan de waterstand stijgen door een stormvloed. Voorafgaand aan het overstromen van de duinregel kan deze door erosie aan de zeezijde (door golfaanval) en aan de landzijde (door overslaande golven) al aanzienlijk versmald en verlaagd zijn. Op deze manier kan een initiële bres ontstaan, zelfs wanneer de waterstand aanzienlijk lager is dan de oorspronkelijke kruinhoogte van de duinregel. Tijdens een tropische cycloon kunnen beide gebeurtenissen plaatsvinden, d.w.z. bresinitiatie vanuit zee en vervolgens overstromen van de duinregel vanuit de lagune. Deze natuurlijke en ongewilde bresvorming kan rampzalige gevolgen hebben, met verlies aan mensenlevens en schade aan infrastructuur, gebouwen en natuurgebieden tot gevolg. Het kwantitatief begrijpen van het doorbreken van duinregels is van groot belang voor gevoeligheidsanalyses van zowel beschermingswerken als ruimtelijke plannen ter beperking van overstromingsrisico's.

Bovenstaande overwegingen hebben geleid tot het onderhavige onderzoek, waarvan het hoofddoel is om een betrouwbaar, op fysische processen gebaseerd, numeriek model voor het bressen van duinregels te ontwikkelen dat in staat is om zowel de bresinitiatie vanuit zee als de bresgroei door overstromen van de duinregel te simuleren. Het toepassingsgebied van het model is beperkt tot duinregels van zand of vergelijkbare zandlichamen als zanddijken en duinen. Het ontwikkelde model is een 2D model, wat inhoudt dat het zich beperkt tot een representatief dwarsprofiel van de duinregel; het model is dus niet in staat te bepalen waar een bres zal ontstaan.

De reactie van een duinregel op stormvloeden kan uit twee met het dwarstransport gerelateerde processen bestaan, namelijk 1) erosie van het strand en de zeewaartse kant van de duinregel en 2) erosie door golfoverslag van de landwaartse zijde van de duinregel. Het laatste proces is een belangrijk aandachtspunt in het onderhavige onderzoek. Ondanks het feit dat in het verleden talloze duinregels zijn doorgebroken, zijn de bestaande modellen van de erosie van de landwaartse zijde van duinregels door golfoverslag nog allesbehalve geavanceerd. Modellen waarmee betrouwbare

voorspellingen kunnen worden gedaan, worden dan ook node gemist. De gebrekkigheid van de bestaande modellen wordt deels veroorzaakt doordat er nauwelijks meetgegevens zijn van de erosie door golfoverslag en doordat de waarnemingen die er zijn, vooral kwalitatief van aard zijn. In sommige gevallen zijn dwarsprofielen van duinregels van voor en na de storm bekend, maar ontbreken de hydraulische randvoorwaarden van de stormvloed. Deze meetgegevens kunnen dus niet worden gebruikt voor het kwantitatief onderzoeken van de transportprocessen en de resulterende morfologische ontwikkelingen van duinregels als gevolg van golfoverslag.

Twee laboratoriumexperimenten zijn uitgevoerd om het inzicht te vergroten in het proces van erosie door golfoverslag en om meetgegevens te verkrijgen voor de ontwikkeling van een nieuw numeriek model voor het gedrag van duinregels tijdens stormvloeden. Het eerste experiment betreft een proef met een vaste bodem, bedoeld om het intermitterende karakter van de golfoverslag nauwkeurig te onderzoeken. De achtergrond hiervan is dat golfoverslag beschouwd moet worden als een tijdsafhankelijk proces en niet, zoals vaak wordt gedaan, vereenvoudigd mag worden als een per tijdseenheid gemiddelde hoeveelheid overslaand water. Deze proef heeft geleid tot een aantal nieuwe overslagparameters, namelijk de over een golf gemiddelde overslagtijd, de relatieve totale overslagtijd, de overslagasymmetrie, en de gemiddelde momentane afvoer. Ten behoeve voor de parametrisering van de golfoverslag, wordt ook een nieuwe benadering voorgesteld voor de definitie van de equivalente helling van zandige profielen met een relatief lage kruinhoogte, waarin rekening wordt gehouden met de effecten van de golfperiode.

De modellering van de morfologische ontwikkeling van initiële stroomgaten en van de bresgroei in duinregels door overstromen omvat een groot aantal verschijnselen. Daarom is hiervoor een algemene, op fysische processen gebaseerde, benadering ontwikkelt. De mathematische beschrijving van de stroming is gebaseerd op de ondiepwatervergelijkingen, die worden opgelost met een robuust 'upwind' numeriek schema. Dit laatste om te voorkomen dat er zich problemen voordoen met discontinuïteiten in de stroming (door intermitterende golfoverslag of door een watersprong in de bres) en door abrupte en willekeurige variaties in de bodem van het stroomgat (vooral bij bresgroei). Wat de morfologie van het stroomgat betreft, is de groei van het stroomgat het resultaat van een erosieproces door het overstromende water. Inherent aan de fysica van dit proces zijn bodemveranderingen aanzienlijk dynamischer in de stroomrichting dan in de richting loodrecht op de stroming. Ook is de lengte van het stroomgat relatief kort, dus de variatie van de breedte van het stroomgat in de stroomrichting is verwaarloosbaar t.o.v. de variatie van de ligging van de bodem van het stroomgat in de stroomrichting. Als gevolg hiervan moet het langsprofiel van de bodem (de verticale groei) nauwkeurig bekend zijn terwijl een momentane uniforme stroomgatbreedte meestal voldoende is voor een representatieve bepaling van de groei van de bresbreedte. Daarom is een stelsel vergelijkingen voor de groei van stroomgaten ontwikkeld waarin de veranderingen van de bodemligging in de bres in de breedterichting en in de verticale richting aan elkaar zijn gekoppeld. Een representatief (volumetrische) stroomgatbreedte wordt gedefinieerd en gebruikt voor de bepaling van de breedtegroei terwijl variaties van de bresbreedte in de richting van de stroming mogelijk zijn. Het stelsel van vergelijkingen wordt gecompleteerd door

een additionele relatie tussen de verticale en zijdelingse groei van het stroomgat. Deze relatie, de zogenoemde groei-index van de dwarsdoorsnede, is gebaseerd op de verhouding van de zandtransportcapaciteit langs de bodem met die op de hellingen van het stroomgat. Er is gevonden dat deze relatie vooral afhankelijk is van de momentane geometrie van het stroomgat en van de exponent in de sedimenttransportformule. De index is gekalibreerd met de gegevens van het laboratoriumonderzoek naar bresgroei in zanddijken van Caan (1996, zie ook Visser, 1998) en de meetgegevens van een experiment van het onderhavige onderzoek naar de ontwikkeling van een stroomgat door golfoverslag (het tweede experiment, uitgevoerd met een zandbed).

Het tweede experiment heeft als doel om beter begrip te krijgen van de morfologische processen die optreden bij de vorming van initiële bressen tijdens stormvloeden en om een dataset te verkrijgen voor de kalibratie van het model. Schaalmodellen van duinregels van zand met verschillende breedtes en hoogtes werden onderworpen aan golfaanval met onregelmatige golven. Er werden gedetailleerde 3D topografische veranderingen van de duinregel gemeten, waarmee een complete dataset van de tijdsafhankelijke ontwikkeling van de duinregel is verkregen. De vergelijking van de rekenresultaten met de meetresultaten laat een behoorlijk goede overeenkomst zien, zowel van de zijdelingse als verticale ontwikkeling van het stroomgat in de duinregel. Het blijkt dat de nieuwe parameters voor de erosie door golfoverslag hiervoor een betere beschrijving geven en dat deze geschikt zijn voor het modelleren van dit proces.

In dit onderzoek wordt het bressen van duinregels beschouwd als een geleidelijk erosieproces, teweeggebracht door water dat door een initiële bres in de kruin van de duinregel stroomt. Zodra eenmaal het proces van bresgroei optreedt, worden effecten van golven op de ontwikkeling van de bres verwaarloosd. De beschrijving van de stroming door de bres is vooral gebaseerd op de niet-stationaire vergelijkingen voor de stroming in waterlopen en de modellering van de bresgroei is gedaan met de, hierboven beschreven, gebruikelijke aanpak. De watersprong in de bres blijkt echter een belangrijke rol te spelen in de ontwikkeling van de bres, en dan vooral bij de ontwikkeling van de ontgrondingskuil. De watersprong moet daarom beschouwd worden als onderdeel van de stroming door de bres en de effecten van de turbulentie op het sedimenttransport door de bres moeten worden meegenomen. Daartoe is een aan de watersprong gerelateerde bronterm van turbulentie afgeleid en toegevoegd aan de balansvergelijking van horizontale impuls om de vorm van de watersprong nauwkeurig te benaderen. Het watersprongmodel is gekalibreerd met de meetgegevens van Gharangik en Chaudhry (1991) en Hermann en Hager (1998). Voor het simuleren van de ontwikkeling van de ontgrondingskuil, is een lokaal verfijnde module voor de stroming en de bodemveranderingen gekoppeld met de turbulentie in de watersprong en deze wordt geactiveerd waar dat nodig is.

In het algemeen is het ontwikkelde model voor bresgroei in duinregels in staat om het proces te beschrijven voor willekeurige hydraulische condities aan beide zijden van de duinregel. De tijdsafhankelijke groei van de bres in zowel verticale als zijdelingse richting, inclusief de ontwikkeling van de ontgrondingskuil, is met succes gemodelleerd zonder daarvoor stadia op te leggen (als gedaan door Visser, 1998). Het model is gekalibreerd met de meetgegevens van het laboratoriumexperiment van Caan (1996)

en geverifieerd met de meetgegevens van het Zwin'94 veldexperiment (Visser, 1998). Over het algemeen is de overeenkomst van de modelvoorspellingen met de gemeten bresgroei tamelijk goed, gezien ook de onzekerheden in de meetgegevens. De diepte van de ontgrondingskuil in de laatste stadia (Visser, 1998) van het bresgroeiproces wordt minder goed voorspeld. In deze laatste stadia, wanneer de duinregel in de bres volledig is verdwenen, groeit de ontgrondingskuil verder (maar langzamer) terwijl de watersprong aanzienlijk lager is geworden of zelfs is verdwenen. Dit doet vermoeden dat een ander ontgrondingsmechanisme dan dat van de watersprong zou moeten worden opgenomen in de beschrijving van de verticale bresgroei voor de laatste stadia van het bresgroeiproces.

Het ontwikkelde model is toegepast op het bressen van een duinregel van de Hue Lagune aan de kust in Centraal Vietnam, veroorzaakt door de cycloon EVE in 1999. Dit is ook gedaan om te onderzoeken in hoeverre het model een dergelijke gebeurtenis kan simuleren. Ondanks de onzekerheid in de beschikbare meetgegevens, zijn de bresinitiatie door de stormvloed en de tijdsafhankelijke bresgroei door overstroming van de duinregel door de hoge waterstand met behoorlijke overeenstemming gesimuleerd. Met deze resultaten zijn, voor het lokale bestuur van belang zijnde, maatregelen voor de veiligheid van de lagune en het waarschuwen voor het doorbreken van de duinregel geformuleerd.

Geconcludeerd wordt dat de onderhavige studie heeft geresulteerd in een toegenomen inzicht in het bresgroeiproces van duinregels veroorzaakt door tropische cyclonen. Een op fysische processen gebaseerd numeriek model voor de doorbraak van duinregels is ontwikkeld, waarin de bresinitiatie door stormvloeden en de groei van de bres door overstromen van de duinregel de twee van belang zijnde processen zijn. De nieuwe formuleringen voor golfoverslag betekenen een vooruitgang voor de beschrijving van dit proces, noodzakelijk voor de morfologische modellering van erosie door golfoverslag. De nieuwe methode is efficiënt en betrouwbaar gebleken. Een aan een watersprong gerelateerd mechanisme van de groei van de ontgrondingskuil is ontwikkeld om de groei van de ontgrondingskuil en de bres te simuleren. Het blijkt dat met dit mechanisme de bresgroei aanzienlijk beter wordt voorspeld.

De belangrijkste aanbevelingen voor toekomstig onderzoek behelzen de noodzakelijke verkrijging van meer kwantitatieve, bij voorkeur tijdsafhankelijke meetgegevens van bresinitiatie en bresgroei in duinregels onder invloed van stormvloeden, zowel grootschalige experimenten in het laboratorium als veldproeven. Verder zouden specifieke laboratoriumstudies moeten worden gedaan om het sedimenttransport door overslaand water en in turbulente watersprongen te onderzoeken.

CONTENTS

Chapter 1

INTRODUCTION

1.1 COASTAL BARRIER BREACHING

Breaching is a complex morphodynamic process that is initiated as water overflows a depressed portion in a narrow landmass such as a barrier spit, a barrier island or a dike. Given sufficient time the flow will create a new outlet. A breach can be triggered intentionally or naturally. Intended breaching, induced by digging a pilot channel, is used to alleviate flooding or to improve water quality of a bay (lagoon, estuary, river) environment. Unintended breaching can be catastrophic, causing loss of human lives and damage to infrastructure and to natural habitats. Natural breaching is initiated as the water level on either side of a barrier exceeds a certain threshold level, which, in the case of coastal breaching, is not necessarily above the crest level of a barrier. From the bay side, the rise in water level can be a result of heavy rainfall in the bay watershed or river catchment. From the seaward side the water level can be elevated by a surge during a storm.

The crest level and width of barriers are two main factors that prescribe the barrier breaching potential. Excluding geotechnical-related causes such as seepage and liquefaction, there are two major hydrodynamic driving forces typically involved in coastal breaching. First, breaching is a gradual erosion process, in which the water head difference over the barrier is the principal driving force. Second, however, wave attack, causing seaward erosion and wave overwash, during a storm surge on a low-crested barrier can lower and narrow the barrier cross-section appreciably and thus initiate breaching even when the water level is well below the initial barrier crest level. In such a case, breaching can happen at a much lower surge elevation and wave overwash and wave-induced offshore transport are acting as initial driving forces. Breaching potential is also enhanced by negative effects of protection works such as blockage or reduction of sediment supply to the leeside of a jetty that leads to severe scour of the seaward barrier section.

Breaching is a classical and worldwide phenomenon. Numerous breaches occur naturally every year at many coasts around the world. Coastal breaching hazards are difficult to anticipate. Measures should be taken to prevent or alleviate negative effects of unintended breaching. Also, knowledge is required to take advantage of positive ef-

fects of artificial breaching. Despite recent efforts in the development of breach modelling, our knowledge is still far from advanced and reliable. Better understanding of coastal breaching processes is crucial to good coastal engineering practice.

1.2 COASTAL BREACHING DUE TO TROPICAL CYCLONES: THE VIETNAMESE EXPERIENCE

1.2.1 Tropical cyclones in the Northwest Pacific Ocean and the South China Sea

The Northwest Pacific Ocean and the South China Sea are the two main basins of tropical cyclones in the world severe weather system. About 1500 tropical cyclones were formed over the Northwest Pacific Ocean alone in the period between 1951 and 2004. Annually, on average, 28 tropical cyclones originate from the northwest Pacific Ocean and 10 cyclones track over the South China Sea. This high activity of tropical cyclones poses a constant threat to the local population. The near-coast regions are most affected by cyclones, suffering from high waves, surges, and especially heavy rainfall in vast inland areas. As a result, tropical cyclones always bring about a flooding hazard, which, depending on topographical conditions, can be either from the sea (surge) or from the bay (river-induced flooding). Flooding on the bay side and waves and surges on the sea side are the dual hydrological impact of a tropical cyclone on the coast. The coast is therefore subject to the heaviest impact of tropical cyclones. Wave and surge attacks on the coast are always occurring before the flooding from the bay side. However, depending on local conditions and storm duration, at a certain moment, these two forces can concurrently attack the coast. In the worst case the attack of these forces can cause breakthroughs at weak sections in the sea defence works (e.g. in dikes, dunes and barriers), usually leading to catastrophic consequences.

1.2.2 Tropical cyclone-induced coastal breaching in Vietnam

Vietnam is situated in the eastern part of the Indochinese peninsular, which is well within the main regions visited by tropical cyclones. On the east side, its coast stretches over three thousand kilometres along the South China Sea (also known as the East Sea in Vietnam). The inland territory is bounded to the west with the coast-parallel mountain ranges that create a steep terrain to the East Sea (see Fig. 1).

Vietnam has a tropical monsoon climate with high annual precipitation. Rainfall is seasonal and closely related to activities of tropical cyclones and monsoons. Of all cyclones formed over the northwest Pacific Ocean and the South China Sea, a considerable number will eventually make landfall at or affect the coast of Vietnam. Statistics over 38 years (from 1954 to 1991, see Table 1.1) of storms impacting on Vietnam indicate that the average occurrence frequency is about 5 cyclones per year. Most cyclones make landfall over the central and northern coastal region. Generally, the cyclone season lasts about six months per year from June to November, which is also

the rainy season in the northern and central parts of Vietnam. This implies that tropical cyclones prominently contribute to the average annual precipitation. Typically, precipitation increases because rainfall is much more torrential and widespread when a tropical cyclone encounters one of the local typical climatologic features such as a northern cold front, a southwest monsoon, or an inter-tropical convergence zone. Meteorological data show that about 60 ~ 80 % of the total annual rainfall in the northern and central regions is related to tropical cyclones. Table 1.2 classifies the total rainfall measured in a single cyclone event by its magnitude and probability of occurrence. It follows that heavy precipitation between 300 ~ 400 mm occurs in nearly one half of the total tropical cyclone events.

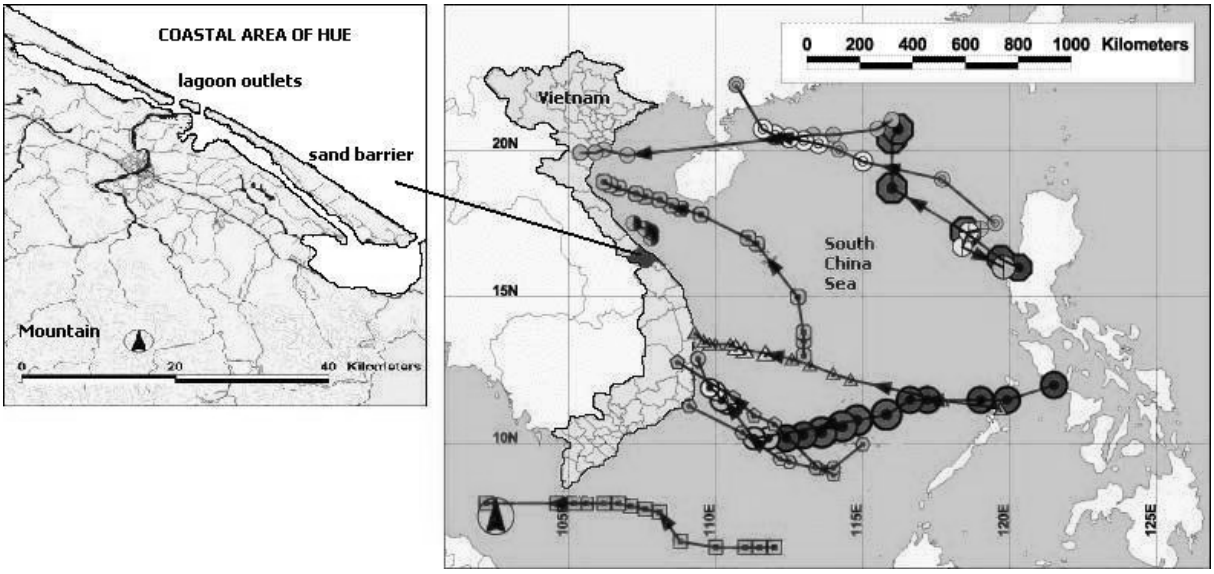

Figure 1.1 Activity of tropical cyclones in 1998 over the coast of Vietnam, Hue province (left inset): a typical vulnerable area in the central coast.

During cyclone EVE that made landfall at the central region in November 1999, the total rainfall measured in Hue was 2288 mm, which is the heaviest rainfall in 40 years. Statistical data also show that tropical cyclones are annually responsible for over 30 % of the total flooding events in the northern region and for about 80 ~ 90 % in the central region. Because of the steep catchment area to the East Sea (responsible for a quick rise in flood level at the coast) and high activity of tropical cyclones, river flooding is an annual threat to almost any river delta in Vietnam during the tropical cyclone season.

Besides river flooding, the coast is also under attack of high waves and surges from the sea side during tropical cyclones. This attack is straightforward and usually takes place a couple of days before the river floods reach the coast.

Table 1.3 summarizes the major losses of property and human life by the recent, most severe cyclones in the northern and central coast of Vietnam, also indicating the cause of breaching (see also Le and Bui, 2000 and UNDP-Vietnam, 2002). It is observed that both surge (and wave) and river-induced flooding are responsible for

coastal breaching. Incidents that are related to surge (and wave) attacks hold for a large number. In the case of coastal lagoon barriers and estuarine dikes, breaching is mostly triggered by river flooding with enforcing effects of high surge and wave.

Table 1.1 Spatial and monthly distributions of tropical cyclones in Vietnam (1954-1991) (After Villegas, 2004)

Locations	**Jan**	**Feb**	**Mar**	**Apr**	**May**	**Jun**	**Jul**	**Aug**	**Sep**	**Oct**	**Nov**	**Dec**	**Total**
Northern	0	0	0	0	0	15	24	28	22	7	1	0	97
Central	0	0	0	1	2	0	0	14	23	35	6	0	81
Southern	0	0	3	1	1	7	0	0	3	6	20	6	47
Total	0	0	3	2	3	22	24	42	48	48	27	6	225

Table 1.2 Classes of the total rainfall in a single cyclone event and probability of occurrence (After Le and Bui, 2000)

Rainfall (mm)	**150 – 200**	**200 – 300**	**300 – 400**	**400 – 500**	**> 500**
Occurrence (%)	12	25	45	15	5

In conclusion, the geographical conditions of Vietnam make the coast very vulnerable to cyclone-induced coastal flooding hazards, especially along the narrow low-lying coastal strip in the central coast region. Coastal breaching is catastrophic and cyclone induced coastal breaching is an annual threat to the population living along the coast of Vietnam.

1.3 STUDY OBJECTIVE

Breach modelling capability is of great importance for the management of flooding hazards as well as for the design of flood-defence works. Breaching is a highly complex process involving many uncertain variables. Despite recent efforts in describing the breaching process our understanding of coastal breaching is still far from complete. Existing breach models are largely empirical. The complexity of processes involved as well as scarceness and incompleteness of breaching data both on field and laboratory scales have been obstructive to the development of reliable breach models. Development of more reliable, hydrodynamic-based breach models is thus required. Also, for disaster management implications, it is critical to be able to assess the potential of coastal barrier breaching as a result of wave actions during storm surges. This phenomenon is known as the breach initiation phase; the mechanisms behind this are not well understood in coastal breaching.

The above observations have led to the main objective of the present study, viz. to develop a more reliable process-based model of coastal barrier breaching. The model should be able to predict:

Table 1.3 Major events of cyclone-induced coastal breaching (1981-2005)

Cyclones and dates landed	Affected locations (province)	Breaching	Cause		Loss of properties and lives
			Max. surge (m)	Peak river flood (m)	
KELLY 5/6/1981	Nghe An Central coast	2.0 km of seadikes	2.9	–	- 535 houses collapsed - 1,000 ha crops - 120 boats sunk - 35 dead.
NANCY 18/10/1982	Nghe An Central coast	40 broken sections: removal of 660,000 m^3 of seadike body materials	3.2	–	- 68,950 houses - 30,000 ha crops - 500 boats sunk - 70 dead.
CECIL 15/10/1985	Hue (Hue lagoon), Binh Dinh Central coast	removal of 1,500,000 m^3 of lagoon barrier and levee body materials	×	×	- 70,000 houses - 1,770 boats sunk - 900 dead
CARY 22/8/1987	Nghe An Central coast	removal of 310,000 m^3 of seadike body materials	2.7	–	- 8,100 houses - 1,600 ha crops - 20,000 evacuated - 10 dead.
DAN 13/10/1989	Ha Tinh Central coast	most provincial seadikes and some estuarine dikes	3.5 ~ 4.0	×	- 9,850 houses collapsed and damaged - 34,000 ha crops - hundreds of thou sands evacuated.
FRANKIE Typhoon 24/7/1996	Northern coast from Thanh Hoa to Quang Ninh	2 km of seadikes and 5km of levees	×	9.97 on Red river, 4.52 on Thai Binh river	- 39,750 houses - 161,500 ha crops - 67 dead and missing
EVE 19/10/1999 followed by two-week torrential rain and flooding 1–6/11/1999	Central coast from Quang Binh to Binh Dinh	Hue lagoon barrier broken at six locations, largest 750 m at Hoa Duan, Hue.	2.5	5.94 historical record on Huong river - Hue lagoon	- 255,300 houses - 6,500 ha crops - 15,000 households evacuated - 600 dead.
DAMREY 27/9/2005	Central to northern coast from Quang Ninh to Da Nang	3 km of seadikes broken, Hue lagoon barrier overtopped by high surge	4.5	–	- 10,000 houses - 60,000 ha crops - 54 km seadikes damaged - 337,000 evacuated.

Note: (×) applicable but without specific data (–) inapplicable

- Breach initiation by the barrier response during storm surges: the initiating or enforcing effects of waves and surge (dune and beach erosion and wave overwash) on coastal breaching. This part is called the "barrier response" sub-model, in which wave overwash is an important component.

- Time-dependent breach growth in both lateral and vertical directions. This part is called the "barrier breach" sub-model.

1.4 STUDY APPROACH

Seaward erosion and severe overwash at coastal barriers during storms can narrow and lower the barrier profile considerably and thus increase barrier breaching potential from either the offshore or inshore side significantly. In the present study, breach initiation (or barrier breaching potential) is limited to the response caused by seaward, offshore impacting processes only. The barrier response to wave attack is modelled following a "wave-averaged" concept, in which wave-induced cross-shore transport and overwash are interrelated.

Fixed-bed laboratory experiments were carried out to increase insights into wave overwash on barriers. New overtopping parameters are formulated to better describe the strength and discontinuous character, essential to overwash modelling. The overwash flow on the barrier is modelled according to the shallow water equations, which are solved using an upwind numerical scheme. For modelling the development of the overwash channel induced by the flow (and also the breach channel later on), a set of general equations of channel growth is derived, in which the channel bed changes in lateral and vertical directions are related. The system of equations is closed using a morphologic relation between the channel vertical and lateral development. This growth relation, based on the relative capacity of transporting sediment along the bottom and the sides of channel, is found to depend largely on the instantaneous breach geometry and sediment transport characters. Mobile bed (sand) model experiments of barrier under attack of random waves were performed for the purpose of model calibration on the barrier response.

In the present study, breaching is regarded as a gradual erosion process induced by overflow. The breach flow modelling is primarily based on the unsteady open channel flow equations. Also, it is found that a hydraulic jump in the breach channel plays a role in the breach morphological development, especially in the formation and development of scour in the first stages of the breaching process. The jump is therefore considered as a sort of breach flow condition while its turbulence is taken into account in the breach sediment transport. In order to deal with a discontinuous, mixed-regime flow as well as an abrupt bed level variation during breaching, a robust upwind numerical approach needs to be adopted to resolve the flow equations. Once breaching occurs, effects of waves on the breach flow condition and thus on the breach development (breach sediment transport) are neglected. The channel width increase is also predicted using the generic morphological approach mentioned earlier for erosional channels. The barrier breach model is calibrated and verified using laboratory and field data from previous studies.

The present study is limited to the coastal breaching processes of homogeneous coastal sand barriers and of similar types only, such as sand-dikes and sand dunes. The newly-developed model is referred to as a site model, i.e. the simulation domain

is restricted to a representative cross-section of a barrier and the question where in plan a breach is to occur is not answered by the model.

Figure 1.2 represents the computational layout of the coastal barrier breaching model, in which the initiation of breaching by the barrier response during storm surges is also incorporated.

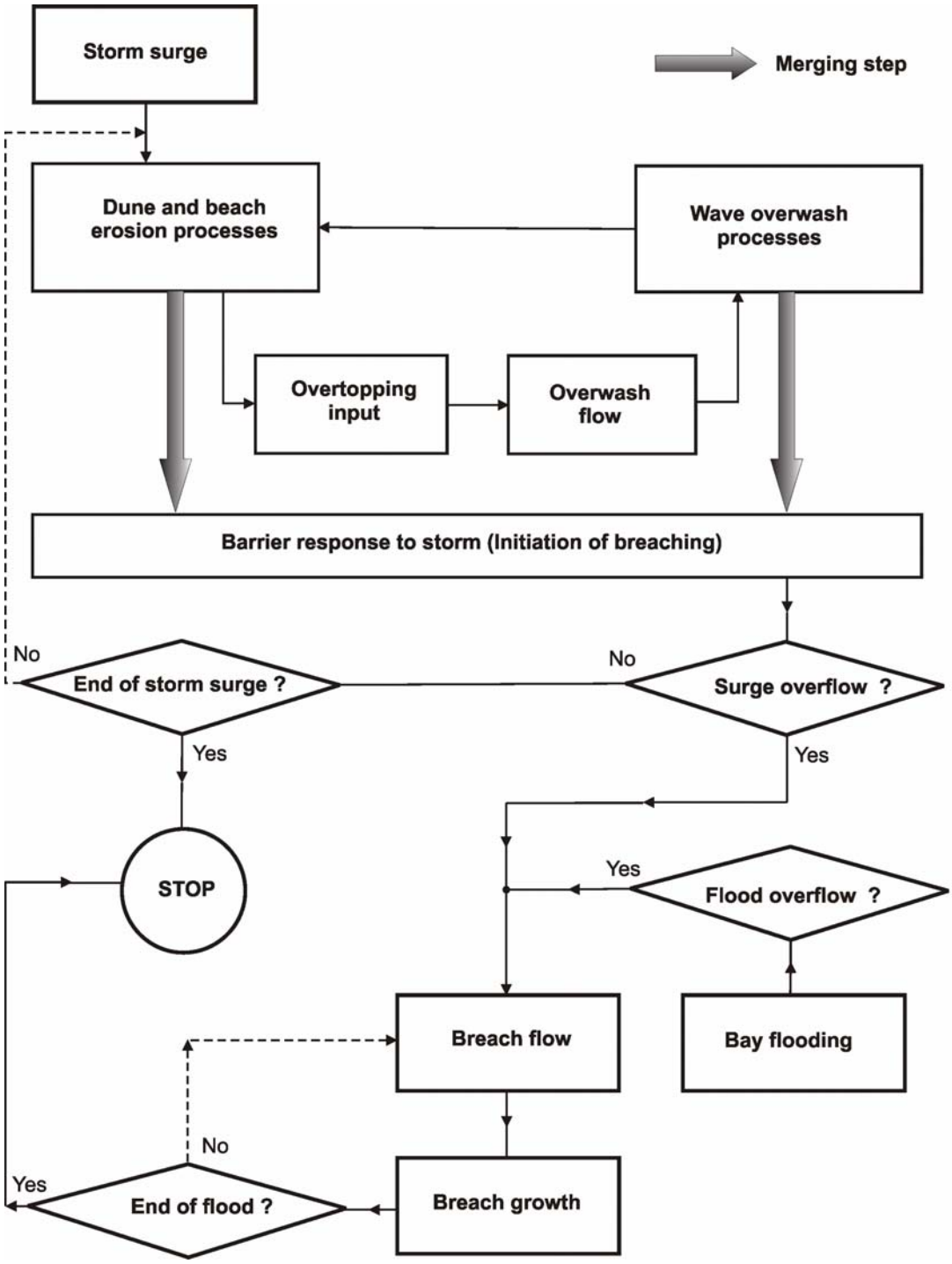

Figure 1.2 Computational layout of the new coastal barrier breaching model

1.5 THESIS OUTLINE

A literature review on barrier breaching processes is carried out in Chapter 2. This includes breach initiating processes, i.e. beach and dune erosion and wave overwash during storm surges, and the breach erosion process due to overflow. Implications for the development of a new model are then proposed.

Chapter 3 deals with a fixed-bed model experiment of wave overwash on low-crested beach barriers. Several new overtopping parameters are derived and formulated based on the experimental results.

In Chapter 4, a new process-based approach for modelling growth of an erosional channel induced by overflow, used later on for modelling both the breach growth and development of overwash channel, is presented. A set of equations describing channel growth is derived in connection with several new morphological factors such as the channel characteristic width and the cross-sectional growth index.

In Chapter 5, a mobile (sand) laboratory experiment of wave overwash and the development of a numerical model for barrier response during storm surges are described. The model utilizes the findings of Chapter 3 and Chapter 4. The experimental results are then used for calibration of the model.

Chapter 6 focuses on modelling the breach erosion process in coastal sand barriers due to overflow. A hydraulic jump is considered as part of the breach flow conditions and its turbulence effects on the breach sediment transport must be taken into account. The breach growth is then modelled according to the common approach presented in Chapter 4. The formation and development of scour in the breach channel in connection with the hydraulic jump are simulated.

In Chapter 7, the newly developed breach model is applied to study the breaching vulnerability of the coastal lagoon of Hue (Vietnam) due to tropical cyclones.

Finally, conclusions and recommendations from the present study are drawn in Chapter 8.

Chapter 2

COASTAL BARRIER BREACHING PROCESSES

2.1 INTRODUCTION

In this chapter a literature review on the modelling of processes related to the breaching of coastal sand barriers is carried out. As a result, requirements for the development of a new model are derived.

As hinted at in Chapter 1, the considered processes are classified into two main groups according to their relevance for breaching due to tropical cyclones:

- Response of low-crested barriers to wave attack during storm surges (initiation of breaching): this consists of two major wave-induced across-shore transport processes, viz. dune and beach erosion and wave overwash on barriers.
- Barrier breach development: the breach erosion process induced by water overflowing the crest of barriers due to either a high sea surge level or a high bay level.

The review of the first group of processes is given in Section 2.2 with more emphasis on wave overwash modelling as it is a research focus. The state of the art of modelling of dune and beach erosion is considered sufficiently reliable for our present purpose and is thus not further addressed in the present work. However, because of its connection with wave overwash, a brief review is also given in Subsection 2.2.1 in search for a suitable modelling approach. In Section 2.3, a variety of breach modelling techniques is discussed first followed by a review of most relevant breach models. Implications for the new coastal breaching model are also drawn. The chapter ends with a summary and conclusions in Section 2.4.

2.2 RESPONSE OF SAND BARRIERS TO WAVE ATTACK DURING STORM SURGES

2.2.1 Dune and beach erosion during storm surges

Models of dune and beach erosion during storm surges are referred to as short-term

cross-shore transport models with typical time scales of hours to a few days. The model spatial domain is from the surfzone up to the dune face. There have been lots of efforts in understanding the physical processes and in developing models of this kind. As a result, numerous models have been developed with various levels of complexity and reliability. In the present work it is not aimed to advance this modelling issue. Instead, a quick survey on relevant models is carried out in order to select a reliable but appropriate approach in conjunction with a new overwash process description to arrive at a new model of barrier response to wave attack.

Models of dune and beach erosion can be classified by the level of detail of description of physical processes involved. These are empirical erosion profile, semi-physically-based, and physically-based models.

Empirical erosion profile models

Empirical erosion profile models are generally based on the concept of an equilibrium beach profile (EBP). These are widely used as practical tools for quick estimates of the beach erosion amount under a sufficiently long time (infinitely in some cases) period of constant sea state.

It started with the well-known "Bruun-rule" (Bruun, 1954), which proposes a power law for the equilibrium beach profile.

$$h = Ax^{2/3} \tag{2.1}$$

in which h is the water depth at an offshore distance x. A is a dimensional empirical constant or a shaping factor based on properties of the bed material (see e.g. Dean, 1977).

The Bruun hypothesis was further supported and developed by other researchers such as Dean (1977, 1987, and 1991), who related the shaping factor to a measure of wave energy dissipation in the surfzone and/or to the sediment properties.

Based on the results from small and large scale model tests and prototype observations, Vellinga (1986) formulated the dune erosion profile under Dutch conditions, viz. the average Dutch cross-shore profile and the standard conditions of a North Sea storm surge, which is incorporated in the DUROS model. In this model, an arbitrary initial profile is reshaped to an erosion profile after the storm surge, which reads:

$$(\frac{7.6}{H_{os}})y = 0.47\left((\frac{7.6}{H_{os}})^{1.28}(\frac{w_s}{0.0268})^{0.56}x + 18\right)^{0.5} - 2.00 \tag{2.2}$$

where x and y are the profile co-ordinates defined as seaward distance from the dune foot and the water depth below the maximum surge level, respectively. H_{os} and w_s are the deep water significant wave height and the sediment fall speed respectively.

The amount of dune erosion is simply determined by comparing this post-storm profile with the pre-storm profile.

In conclusion, models based on an empirical erosion profile do not describe any of the physical processes of wave-induced erosion. Also, the concept of an equilibrium profile (long-lasting constant conditions) is not applicable when short-term variations of the beach profile develop during storms with durations of hours. Any time-dependent infor-

mation such as of the sediment transport and thus of the beach profile evolution is just unavailable. As a result, models of this kind are not able to predict the development of the dune and beach erosion of a non-standard beach profile under effects of an arbitrary storm event.

Semi-physically-based models

Semi-physically-based models contain a limited level of description of physical processes involved. The time-dependent profile evolution is computed. However, most of the models still rely on the concepts of equilibrium profile and equilibrium energy dissipation. Larson and Kraus (1990) based on vast data of large scale experiments developed the numerical SBEACH model, which focuses mainly on the development of the main morphological features of the profile e.g. bars and berms. Linear wave theory is used to determine the cross-shore wave parameters distribution, in which the concept of stable wave energy is introduced to calculate the wave energy dissipation. Four different zones of sediment transport are defined according to the division of the profile in near-shore wave dynamics and the sediment characteristics under various flow conditions. The net local sediment transport rate is then calculated in a semi-empirical way for each zone as a function of the local and the equilibrium wave energy dissipation. Bed level changes are obtained from the mass conservation equation. SBEACH has been verified against both large wave tank and field data.

In a quite similar approach (Larson et al., 1990; Kriebel, 1990), it is assumed that the cross-shore sediment transport rate is a function of the difference between the actual and the equilibrium values of energy dissipation. The amount of energy dissipation is evaluated using shallow wave theory and spilling breaker waves. In addition an ad hoc geometrical treatment is introduced to interpret the profile in the swash zone. The model was verified against the existing large scale laboratory data of Vellinga (1986) and several collected site data.

Similar to empirical erosion profile models, semi-empirically-based models are restricted to specific conditions for which they have been developed. Changes in hydraulic conditions and sediment characteristics may lead to large variations of empirical constants used in these models, which are not able to be determined properly under new circumstances.

Physically-based models

Physically-based models are also referred to as process-based models as they are based on the understanding of physical processes involved and oriented to the description of these phenomena without assumptions modifying their physics. Nowadays, process-based models of dune and beach erosion are usually preferred because of their broad applicability with less calibration efforts.

The principal cross-shore phenomena, i.e. the max flux above the wave trough, the undertow, boundary layer streaming, and wave asymmetry are identified in most physically-based models of cross-shore transport. However, the description and incorporation of these processes in the modelling varies between models. The instantaneous transport rate for every bed location along the computational domain is required to update the new bed level. For this, most models distinguish two modes of transport, viz. suspended

load above the bed and bed load.

Of the total transport load, the suspended load carried by the undertow (offshore mean flow) is the major contributor. The basic equation for the net local suspended sediment transport rate through a vertical plane with a unit width reads:

$$S_s(x) \approx \int_{z=z_b(x)}^{\overline{\eta}} \overline{u}(z)\,\overline{c}(z)dz \tag{2.3}$$

in which

$S_s(x)$ the net suspended transport rate in x direction
x, z the horizontal and vertical co-ordinates respectively
$\overline{\eta}$ the local mean surface elevation at distance x
$z_b(x)$ the local bottom elevation at distance x or a specified level
$\overline{u}(z)$ the local time-averaged cross-shore velocity profile (over a number of wave cycles)
$\overline{c}(z)$ the local time-averaged concentration profile (over a number of wave cycles)

Equation 2.3 holds the basic formulation for a vast number of cross-shore transport models. To resolve it the velocity and concentration profiles are usually specified in several layers over the water column. The balance of the wave-induced mass flux between these layers is the principle for elaborating the mean current profile. The concentration profile is based on the convection-diffusion equation with a specified reference concentration near the bed.

Although it is considered a small contribution, in some models the bed load transport is also incorporated and computed as a function of the local instantaneous bed shear stress or the local near-bed orbital velocity.

In the following several typical models of this type are briefly reviewed. For more exhaustive reviews reference is made to Steetzel (1993) and Schoonees and Theron (1995).

DUROSTA (Steetzel, 1993)

Steetzel (1993) developed the DUROSTA model, a time-dependent cross-shore transport model. The model is specifically aimed to predict dune and beach erosion during storm surges.

The time-averaged velocity profile as well as the suspended transport rate is formulated for two different zones above and below the mean wave trough level. The mass flux balance combines with a constant vertical gradient of the shear stress to obtain the mean flow profile of the lower zone. Steetzel argued that during storm conditions the suspended transport is predominant and bed load transport is thus neglected. The concentration profile is derived directly from the Rouse equation, assuming a linear distribution of the mixing coefficient above the bed. The reference concentration is related to the mode of wave breaking and the dissipated amount of turbulent kinetic energy. The sediment concentration of the upper zone is assumed to be constant and given by the value at the mean water level.

The model parameters such as the concentration, velocity, transport rate, etc. were calibrated using numerous data from large and small scale experiments. The model was also tested with 43 model tests and 3 prototype data. The model predictions for the erosion amount were rather good. Some other model extensions provide additional capabilities to

predict the profile changes in non-standard cases such as dune revetment and effects of long-shore transport.

Srinivas and Dean (1996)

Following the idea of Dally and Dean (1984), Srinivas and Dean (1996) divide the vertical fluid domain into two layers, viz. the upper layer where the mean current (undertow) is considered and the lower layer where both mean current and first-order oscillation are accounted for. The interface between these two layers is determined by the falling distance of uniform sediment within a full wave cycle. Linear wave theory is used to predict the first order orbital velocity and the second-order mean velocity of the return flow. The model considers two patterns of the mass flux distribution corresponding to two distinct cases with and without water level overtopping. Thereby, the mass flux balance outside and inside the surfzone in each case is determined to derive the mean flow profile. The suspended transport rate is computed in both layers according to Eq. 2.3. The concentration profile is exponential with extra consideration of turbulent kinetic energy in the surfzone. The energy dissipation in the bottom boundary layer and the horizontal wave asymmetry are the two contributing mechanisms in the bed load transport. The model was tested against laboratory experimental data. It was shown to simulate fairly correct trends of erosion, deposition, and wash-over in case of water level overtopping.

UNIBEST-TC

UNIBEST-TC (TC: Time-dependent Cross-shore) is a process-based model, which has been developed by Delft Hydraulics over nearly two decades (originally based on Stive and Wind, 1986 and Roelvink and Stive, 1989 and recently updated by Bosboom, 2000). The model includes the principles of the major cross-shore processes such as wave asymmetry, streaming, undertow, mass flux, gravity, wave-current interaction, etc. The model identifies the water column in three layers, following the approach by De Vriend and Stive (1987).

- The trough-to-crest layer: the mass flux is transported through this layer. The layer also imposes a forcing boundary (compensating effective shear stress from wave decay and wind stress) on the middle layer;
- The middle layer: from the mean water level down to the bottom (wave) boundary layer;
- The bottom wave boundary layer.

The cross-shore current profile is derived from the equations of horizontal momentum balance in combination with an eddy-viscosity model (zero turbulence model). A parabolic distribution of the eddy viscosity is assumed so that the velocity can be derived analytically. The eddy viscosity is expressed as the product of a shaping function and the depth-averaged eddy viscosity. The depth-averaged eddy viscosity combines effects of turbulence from various sources such as wave breaking, slope-driven and wind-driven currents, and increased turbulence in the wave boundary layer.

The mass flux and the compensating shear stress at the mean trough level are modelled according to De Vriend and Stive (1987) added with the surface roller effect given by Nairn (1990). The concentration profile is determined numerically by integrating the standard convection-diffusion equation from a near bed reference level to the mean water surface. The reference concentration is according to Van Rijn (1984b). The suspended

transport rate is then computed using Eq. 2.3 from the bed load layer to the mean surface level. The generalized formula of Ribberink (1998) is used for determining the bed load transport rate, which requires the instantaneous effective bed shear stress. To calculate this stress, the time-series of the near-bed velocity signal due to non-linear short waves and long waves related to wave groups are generated according to the approach described in Roelvink and Stive (1989).

The UNIBEST-TC model has been calibrated and tested with a large number of laboratory and field experimental data on the cross-shore profile changes in both short (during storms) and mid term (seasonal variations) scales.

In conclusion, the physically-based approach is the state-of-the-art in numerical modelling of cross-shore transport. Since models of this kind are aiming at the prediction of the seaward profile evolution of relatively high beaches and dunes, the landward transport beyond the runup limit or the dune crest is not considered. In other words, the process of overwash in the case of heavy wave overtopping has not been described and modelled.

Discussion

Both the empirical erosion profile and the semi-physically-based approach are not able to model dune and beach erosion under arbitrary storm conditions with non-standard beach characteristics. Instead, the physically-based approach is undoubtedly the most capable for this purpose.

Regarding the study objective of modelling the barrier response to wave attack, the incorporation of overwash can only be done given detailed input from the seaward boundary, i.e. sea conditions and sediment transport at a prescribed transitional boundary. This implies that the physically-based approach is the most appropriate choice.

2.2.2 Wave overwash on low-crested beach barriers

The term “overwash” used in the literature varies widely. In the context of the present study wave overwash (or simply “overwash” for the sake of clarity) refers to the processes induced by any swash surge that passes over the crest of a beach barrier. This means overwash is supposed to occur rather under conditions of storm surges. In this sense overwash involves processes of wave overtopping and overflow, which induce sediment transport in the landward direction. Also, a distinction should be made between breaching and overwash during a storm surge event. As soon as the surge level exceeds the barrier crest then the associated process is addressed as breaching (with or without waves), no longer as overwash. This is the reason for not addressing literature, in which “overwash” is a result of surge overflow.

Overwash is a worldwide phenomenon, which can occur when a low barrier is exposed to attack by storm surges. Qualitative observation of the overwash processes and overwash-related coastal hazards has long been discussed in the coastal engineering literature (see e.g. Leatherman, 1981). Surprisingly, the state-of-the-art modelling of wave overwash is still far from advanced and predictive tools are seriously lacking. To the author’s knowledge, so far only a few study attempts have been made as described in the following.

It was first initiated with a series of small scale dune experiments carried out by Hancock and Kobayashi (1994) to examine the profile evolution and the landward sediment transport caused by minor to serious wave overwash. In these experiments, both the overtopping rate and the over-washed sediment content were measured.

The study was then followed by a closer look at overwash by Kobayashi et al. (1996), in which the sediment transport rate at the dune crest (the overwash rate) was calculated as the product of the overtopping rate and the sediment concentration:

$$q_{s,ovw} = C_s q_{ovt} \tag{2.4}$$

where $q_{s,ovw}$ and q_{ovt} are the sediment overwash rate and the average overtopping rate respectively. C_s is the sediment concentration.

The empirical formulation of Van der Meer and Janssen (1995) was recalibrated with the data of the earlier dune experiments to determine the average overtopping rate.

$$q_{ovt} = \frac{g}{2\pi} H_s T_p \sqrt{m} q_b \tag{2.13}$$

where q_b is the dimensionless overtopping parameter

$$q_b = 0.06 \exp\left(-\frac{5.2}{\gamma_h \xi_p} \frac{R_c}{H_s}\right) \tag{2.14}$$

ξ_p is the surf similarity parameter or Irribarren number (Battjes, 1974) based on the peak wave period T_p and the significant wave height H_s at the seaward boundary. m is a uniform equivalent slope averaged over the horizontal distance from the dune crest to the position where water depth equals H_s. γ_h is the overtopping reduction coefficient due to shallow water effects. R_c is the crest freeboard relative to the still water level.

As a result, with a median sand diameter of 0.38mm of the model dunes, the overwash concentration was found to vary in the range of 0.02~0.06 kg/m^3. The experimental data also indicate that the accuracy of empirical overtopping estimates is relatively sensitive to the calculated magnitude of the equivalent slope.

For wider applications, Tega and Kobayashi (1996) attempted to formulate the overwash concentration as a function of the overtopping parameters and the sediment properties. This was done by testing several sediment transport approaches in combination with the overtopping output from the RBREAK2 model (Kobayashi and Poff, 1994). This model was claimed to predict the overtopping rate on sloping revetments within ± 40% accuracy. However, the formulation for the overwash concentration was unsatisfactory since large scattering was present in the data set. Their final recommendation was that an overwash concentration of 0.04 kg/m^3 is a reasonable estimate, except for very fine or coarse sands.

Eventually, Tega and Kobayashi (1999) combined all the above findings in a dune erosion model. A constant sand concentration of 0.038 kg/m^3 was used for the computation of overwash. The seaward (below SWL) sediment transport rate follows a simple empirical relation proposed by Kobayashi (1987). However, the agreement between the measured and predicted dune profiles was rather poor probably due to the simplistic description of the across-shore transport processes on both the seaside and the dune crest.

In another recent attempt, Larson et al. (2005) modified the SBEACH model to improve its reliability in predicting dune and breach erosion with occurrence of wave overwash. The sediment transport in the swash zone is computed according to the approach by Larson et al. (2004) in which ballistics theory is used to determine the front speed of the up-rushing bore and the swash submerging time. The transport rate at the dune crest (overwash transport) is assumed to be proportional to the average overtopping volume, which is supported by the previous overwash study of Hancock and Kobayashi (1994) and Kobayashi et al. (1996).

$$q_D = K_s 2\sqrt{\frac{2g}{R}}(R - z_D)^2 \tag{2.15}$$

where q_D is the overwash rate (at the dune crest), K_s is an empirical transport coefficient, R is the fictitious runup height neglecting overwash, z_D is the dune crest elevation above the mean water level.

To model the back-dune profile evolution due to overwash, an empirical spatial distribution of the sediment transport rate is assumed as follows.

$$q_f = \frac{q_D}{1 + \mu s / B_D} \tag{2.16}$$

in which q_f is the transport rate at a point on the back dune with a horizontal distance s from the dune crest, μ is a spreading coefficient, B_D is the width of the overwash flow in the throat (crest).

The new incorporation of overwash in the model was validated with two storm field erosion data from Ocean City (November 1990 to January 1991) and Assateague Island (January to February 1998).

Discussion

More physical insight into wave overtopping on beach barriers is required in order to model overwash more accurately. Clearly, the use of the conventional average overtopping discharge is inadequate since it is unable to represent the intermittent character and the associated strength of the flow.

Also, for the sake of modelling of the barrier response as a whole, it is advantageous to make intelligent use of the many empirical formulations for wave overtopping discharge at dikes and breakwaters from literature. To do this a single-valued equivalent slope for a natural beach, implying a composite slope, needs to be derived instead of the slope conventionally defined for hard sloping structures.

2.2.3 Summary and conclusions

Dune and beach erosion and wave overwash are the two major processes forming the response of low-crested beach barriers during storm surges. These two processes are physically-linked, so the physically-based approach is the most natural for modelling the time-dependent barrier response under an arbitrary storm event with non-standard beach sediment characteristics.

For hydrodynamic modelling of overwash, a more elaborate description of wave overtopping instead of the conventional average discharge is necessary. New parameters should be proposed to closely describe the overtopping nature, i.e. its intermittence and associated strength.

Regarding the modelling of the seaward profile change, the cross-shore transport approach of the UNIBEST-TC model is adopted. The model is considered the most physically-contained and well-calibrated.

2.3 COASTAL BREACHING MODELS

2.3.1 Categories of breach models

In the past decades breaching has increasingly become a critical issue in engineering practice to be further investigated. Physical insight into the processes involved is still limited while quantitative prediction is urgently needed. As a result, numerous breach models have been developed imposing assumptions and simplifications. Each model has its own specific constraints of application without general validity.

Regarding the structure types, distinction is made between models for dams (see Singh, 1996), coastal dikes (Visser, 1998), fuse-plug spillways (Tinney and Hsu, 1961), and natural sand barriers along the coast (Gordon, 1991; Odd et al., 1995). Breach models are also restricted in applicability due to the beach material such as homogenous non-cohesive (sand), homogenous cohesive (e.g. clay or sand clay). On mathematical grounds one can further classify breach models into empirical, analytical (e.g. Kraus, 2003), parametric (e.g. Visser, 1998), and numerical (e.g. Ponce and Tsivoglou, 1981) categories.

At this moment all breach models are for overflow conditions i.e. breaching is a gradual erosion process induced by water overflowing through a channel. Therefore, most breach models are based on two process components, namely the breach hydrodynamics and the breach morphology. However, amongst models, there is a variety in the level of description of physical processes in these two components.

On the level of breach hydrodynamics one can classify breach models into semi-hydrodynamic and full hydrodynamic. In the first category, to which a large number of models belong, empirical flow formulations such as the broad-crested weir formula are used for describing the breach flow in several flow regimes. Some examples of models of this kind are the BREACH model of Fread (1984), the BEED model of Singh and Scarlatos (see Singh, 1996), the model of Moijb (1990), and the BRES model (Visser, 1998). In the latter group (Peviani, 1999; Busnelli, 2001) the breach flow is resolved in a full hydrodynamic way usually using the system of 1-D shallow water or St. Venant equations.

The second and probably the most intricate part of a breach model is the breach morphology, through which the breach enlargement in both vertical and lateral directions is displayed. The breach morphology concerns the following aspects:

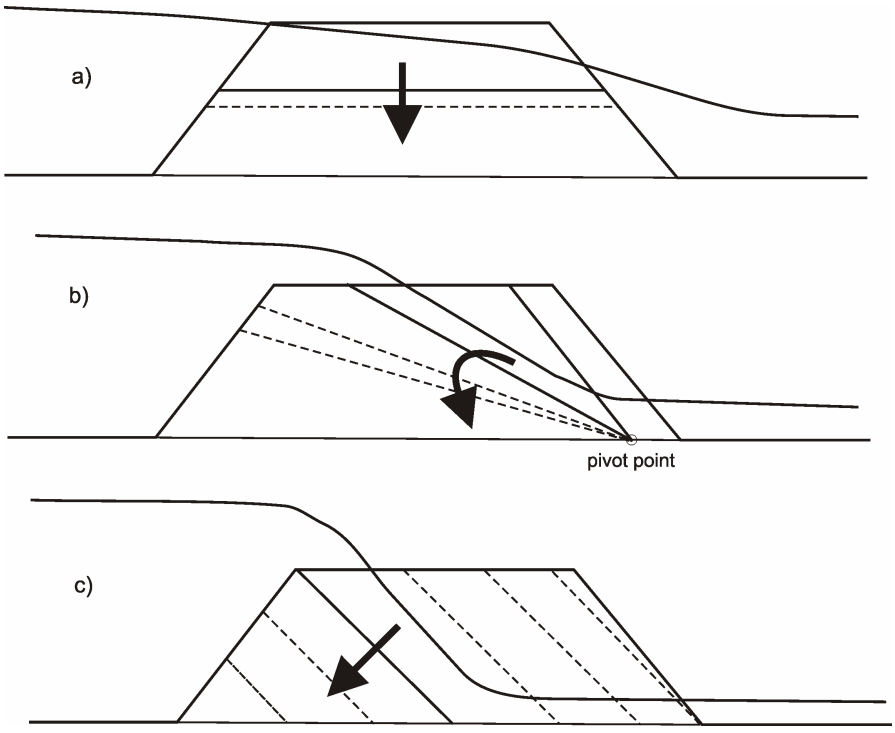

Figure 2.1 Typical schematized vertical breach growth
a) parallel horizontal growth (e.g. DEICH_P model, Broich, 1998)
b) rotating around a pivot point growth (NPCBREACH model, Coleman et al., 2002)
c) parallel inclined growth (e.g. DAMBRK model Singh, 1996; BRES model Visser, 1998)

- Breach shape (cross-section of the breach channel);
- Breach evolution (the lateral and vertical breach development);
- Side slope instability (avalanching mechanism);
- Sediment transport.

Depending on the level of physical content of a considered model, each of the first three issues of the breach morphology can be either determined automatically or must be imposed. We discuss each of the above aspects of the breach morphology in the following.

In 1-D or 2DV breach models the shape of the breach cross-section must be prescribed in order to resolve the flow and subsequently the breach development. However, the breach shape varies between models and can also be varied in time or in stage within a model. A trapezoidal section, with the sides slope determined by the breach soil properties, is very common (see Singh, 1996; Visser, 1998). In some models cross-sections of rectangular, parabolic or even triangular shapes are also used (Moijb, 1990; Broich, 1998; Coleman et al., 2002).

Regarding breach evolution assumptions about the morphological regimes or stages of the vertical breach growth and the breach deepening-widening relation need to be imposed.

In a full hydrodynamic model assumptions about the vertical breach growth are not needed since the bed profile along the breach is computed from the equation of mass

conservation with the known sediment transport rates along the breach. Whereas, in a semi-hydrodynamic model the flow parameters and so the erosion rates are only known at a few prescribed locations such as at the breach sill (e.g. using a broad-crested weir formula), conceptual schematizations of the breach longitudinal profile evolution are therefore indispensable in order to update the breach morphology.

The breach lateral enlargement is usually computed in relation to the erosion rate of the breach bottom. This morphological relation is either empirical or just based on geometrical arguments (see Visser, 1998 for an example of the geometrically-based relation). Figs.2.1 and 2.2 show some typical conceptual schematizations of breach development in vertical and lateral directions, respectively.

Models with imposed assumptions about the breach evolution are also known as parametric models. Typical examples are the BRES model (Visser, 1998) and the NPC BREACH model (Coleman et al., 2002).

Side slope instability (shear slide) has been observed in most breach experiments, especially when the breach material is non-cohesive. This mode of soil failure feeds lateral blocks of sediment intermittently into the breach flow and is known as the discrete erosion process coexisting with the continuous erosion process induced by the flow. Depending on the soil properties and the interaction with the flow the mass-instability can have a certain influence on the breach development. Most of the existing dam-break models contain a module to handle this issue, in which a potential slide plane is defined and the mass instability is checked through a safety factor (BREACH model, BEED model, see Singh, 1996).

The transport of the breach material is believed to occur in both bed and suspended modes, although, under certain breach conditions, one may dominate the other. To compute the erosion rate a sediment transport formulation is needed, which is also a critical part of the breach morphology in any breach model. Most sediment transport formulae have been developed for laboratory flow conditions, which are far calmer than the extreme breach flow conditions, i.e. very high velocities (up to 5m/s, see Visser, 1998) while very steep slopes (sometimes larger than the angle of sediment internal friction) occur.
The applicability of sediment transport approaches to breach modelling has been examined by several researchers (see e.g. Visser, 1998). Discrepancies were found amongst formulations due to their different validity ranges. Visser (1998) resolved this issue by adopting different transport approaches to different stages of the breaching process based on their validity ranges.

In general, the mechanism of the transport processes under breaching conditions is not well understood. As a result, none of the available models is able to describe the breach transport processes properly. Some commonly-used and probably most applicable approaches for transport of non-cohesive materials associated with coastal breaching are Engelund and Hansen (1967) (total load), Bailard (1981) (total load), Van Rijn (1984a, b) (bed load and suspended load), Bagnold-Visser (1989) (bed load and suspended load, see Visser, 1998), Ribberink (1998) (general bed load formula).

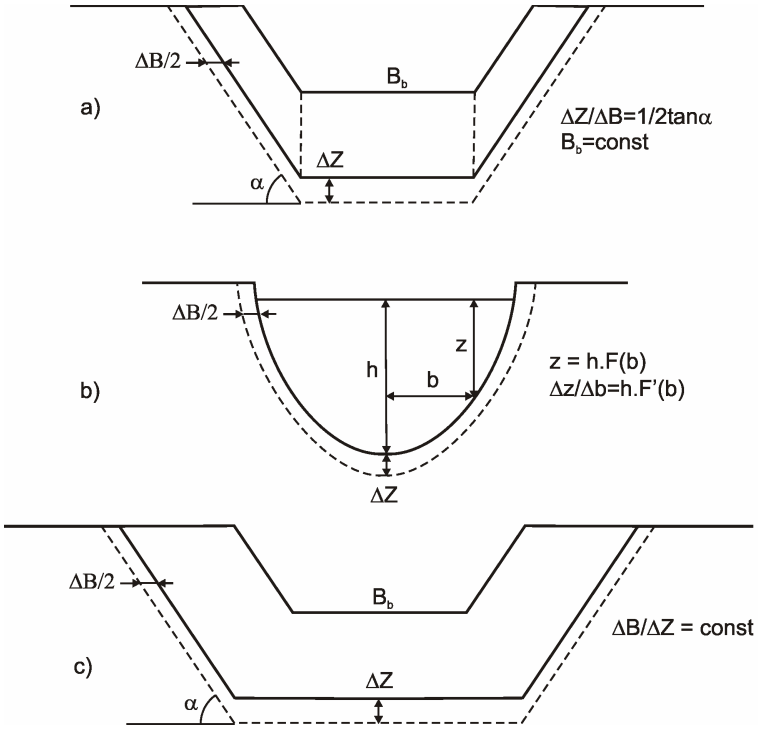

Figure 2.2 Typical schematized lateral breach growth
a) and b) geometrically-based relation (e.g. Visser, 1998; Coleman et al., 2003)
c) empirically-based relation (e.g. Visser, 1998)

2.3.2 Modelling of coastal breaching

Amongst various breach models, only few are explicitly aimed for coastal breaching, especially for coastal sand barriers. However, all breach models of non-cohesive bodies such as sand-dams, sand-dikes, and coastal sand barriers have some common features in the breaching process. In principle, they are all applicable to modelling breaches under overflow conditions. In the following, the most recent and relevant models of breaching of homogenous non-cohesive bodies are briefly reviewed. This includes breaching of sand-dikes (Visser, 1998; Busnelli, 2001), breaching of sand-barriers (Gordon, 1991 and Odd, 1995; Kraus, 2003), and breaching of non-cohesive dams (Coleman et al., 2002; Rozov, 2003). Descriptions of the major characteristics of these models are given in Table 2.1.

Coastal sand-dikes breaching (Visser, 1998; Busnelli, 2001)

Visser (1998) proposes five successive stages of breach growth in sand-dikes, which is an extension of the earlier work by Fujita and Tamura (1987) on breaching of alluvial dikes. In the first three stages, the supercritical breach flow digs its way through the dike. Erosion of the inner slope occurs retrogressively with a constant inclined angle and consequently narrows and lowers the dike crest down to its base at the polder level (see also Fig.2). During this period, it is assumed that deepening causes the breach to be widened, keeping a constant breach width at the bottom. Therefore, the breach width is geometrically related to the depth of the breach.

Table 2.1 Typical breach erosion models of non-cohesive bodies

Model	Breach type	Hydrodynamics/ Morphodynamics	Breach morphology			
			Breach shape	Lateral growth	Vertical growth	Side collapse
BRES (Visser, 1998)	coastal sand-dikes	semi-hydrodynamic, parametric, 2D breach growth	trapezoidal	geometrically-based, linear	schematized, five-stage evolution	implicit
Busnelli (2001)		full hydrodynamic 1DH morphologic	rectangular	constant width	numerically computed	-
TELEMAC2D Odd (1995)	coastal sand barriers	full hydrodynamic, 2DH breach growth	automatic	numerically computed	numerically computed	not considered
Kraus (2001)		analytical 2D breach growth	rectangular	exponential decay towards equilibrium	exponential decay towards equilibrium	implicit
Baso and Shin (1999)		full hydrodynamic 1DH morphologic	unit width	-	numerically computed	-
NPCBREACH Coleman et al. (2002)	non-cohesive dams	empirical, analytical 3D breach growth	U-shaped, hourglass-shape channel	empirical time-dependent	schematized, rotating	-
Rozov (2003)		empirical, analytical 1D breach growth	idealized rectangular	empirical	not considered	implicit

Note: (–) inapplicable

In the fourth stage, the critical flow stage, the breach continues to grow mainly laterally while the vertical growth depends on the erodibility of the base material and the foreland level. At this point, three types of breach base are distinguished. In a Type A breach (with solid or clay foundation), the breach is prevented from further vertical erosion. In a Type B (high foreland) or Type C (low foreland, no obstruction) breach, the breach width increases linearly with the reduction rate of the breach sill level. This linear relation is found by simplifying the equation of mass conservation. The breach flow becomes subcritical in the fifth stage as the water head difference over the dike is gradually neutralized. The relation for the lateral growth as used in the fourth stage still holds valid for this stage. Stages IV and V of the breaching process are considered critical for the final breach dimensions since most of the discharge as well as breach erosion takes place in this period. The BRES model of Visser (1998) was calibrated through a field experiment (the Zwin'94 experiment, see Visser, 1998) and then validated against a small scale laboratory test (Caan, 1996; also reported in Visser, 1998). Good agreement between the measurement and the model prediction for the increase of the breach width was found. The five-stage breach erosion process and associated transport regimes proposed by Visser (1998) bear general applicability. However, the vertical breach growth observed in the laboratory tests does not comply much with these stages. This is because a scour hole

develops in the breach channel, which appears to take out a large part of the dike even in the first stage. The scour, a noticeable morphological feature of the breach growth, is still an unsolved phenomenon. Also, in the model, the pilot channel (initial breach width and depth) does not play a role in the breaching process even in the first stages, while it appears opposite in the field.

Busnelli (2001) attempted to numerically simulate the first two stages of the breach erosion process defined by Visser (1998), using a 1D morphological model. The simulation followed the physical setup of the sand-dike breach experiment conducted at the laboratory of Delft University of Technology (see Caan, 1996). The width of the rectangular pilot channel was kept unchanged during this period. Although the simulations were not undertaken for comparisons, the study has shown that numerical models are capable of simulating the breach erosion process in a full hydro-dynamic way without defining stages. Busnelli (2001) also concluded that hydraulic jumps tend to disappear on mobile beds, so 1-D morphological models are capable of simulating breach growth in sand-dikes. Therefore, to be more efficient in the computation of sand-dikes breaches, a 1D hydrodynamic model can be used in stead of a 3D or 2DH model, provided that a vertical-to-lateral growth relation must be adopted. However, for the development of local scour in the breach channel more refined modelling or 3D model study is needed.

Sand-barriers breaching (Gordon, 1991 and Odd, 1995; Basco and Shin, 1999; Kraus, 2003)

Gordon (1991) describes qualitatively the breaching process of coastal lagoon barriers due to overflowing induced by heavy rainfall runoff. This lagoon breakout process is observed to consist of three distinct stages. In the first stage, a preferred scour channel (initial channel) is formed and cuts backwards across the barrier. The flow is subcritical in the breach section and supercritical on the down slope. The second stage commences when a crescent-shaped weir forms in the main sand plug followed by a series of steps in the channel. The breach width increases rapidly as the breach flow is highly turbulent and supercritical. Once the main sand plug has been washed out completely, the final stage begins with a slower rate of breach deepening and widening.

Later on, Odd (1995) confirmed these three stages described in Gordon (1991) in a numerical study on the Wamberal lagoon (Australia) breakout using the TELEMAC 2D model. However, the model's quantitative prediction was calibrated by scaling up the transport approach of Van Rijn (1984b) by a factor 4 to achieve agreement with the observation.

A one-dimensional hydrodynamic model was developed to study the profile change across a barrier island during storms events by Basco and Shin (1999). Four modelling stages of the barrier breaching process identified in the model are: (1) storm surge, wave attack and the dune/beach physics; (2) overwash and overland island flow; (3) storm tidal flooding from ocean to bay; and (4) storm ebbing from bay to ocean. Stage 1 is modelled using the SBEACH model (Larson and Kraus, 1990). The breach flow (due to flooding from bay or ocean overflowing the barrier crest) during the last three stages is modelled using the system of shallow water equations with the Lax-Wendroff explicit scheme for Stage 2 and the Preissmann implicit scheme for Stages 3 and 4. The model focuses only on the barrier profile change without considering the breach lateral enlargement. The

model was not verified against any measured data.

Kraus (2003) derived an analytical model for breaching of coastal sand barriers, in which an idealized rectangular breach evolves gradually towards the equilibrium situation. The analytical solutions indicate an exponentially decaying behaviour in the development of the breach dimensions. The model assumes that breach growth in sand barriers is governed by seven variables: initial dimensions of the breach (depth and width), equilibrium dimensions of the breach (depth and width), width of the barrier, and maximum or initial net sediment transport rates at the bottom and sides of the breach. The model describes qualitatively the general tendency of breach growth as observed in nature and in laboratories. However, its quantitative descriptions rely heavily on empirical estimates, which are hard to quantify in advance such as the maximum transport rates and the equilibrium breach dimensions.

Non-cohesive dams breaching (Coleman et al., 2002; Rozov, 2003)

Most models of sand dam breaching have been derived empirically based on observations from small-scale physical tests. Coleman et al. (2002) derived an empirical model for breaching of homogenous sand dams under a constant upstream reservoir level, in which 3D breach growth is described. Regarding the vertical development, it is assumed that the invert slope of the breach is initially parallel to itself and then rotating around a pivot point located on the breach bottom. The invert angle of the rotating slope decreases down to a terminal value, which is about 1.5%. Since the laboratory dams were founded directly on the solid flume bottom local scour was not observed and thus not described in the model. The breach has a composite U-shaped cross-section that is parabolic below water and near-vertical above water. In plan, the breach channel has an hourglass shape that is based on the concept of a minimum energy loss channel. A time-dependent empirical relation is derived for the increase of the breach width at the crest section. The model is purely empirical and therefore only valid within the tested laboratory conditions.

Also based on small-scale physical tests, Rozov (2003) developed a simple analytical model that describes breach growth of non-cohesive dams mainly in lateral direction, i.e. the breach widening. Initially, an idealized rectangular breach channel is assumed to cut through the dam and the breach bottom lies directly on the dam base. This rectangular shape of the breach section is kept invariable for the whole breaching process. The breach widening is directly related to the sediment discharge along the breach, which turns to be dependent on the reservoir depth and an empirical erosion coefficient.

2.3.3 Implications for a new coastal barrier breach model

Due to arbitrary variations of the water levels on both sides of the barrier, the breach flow can be mixed-regime, viz. supercritical, subcritical, and transitional with discontinuities (hydraulic jumps). Of course, the time-dependent evolution of breach growth is governed by these flow conditions. It is without doubt that the parametric and empirical approaches are not capable of describing these complex processes in a generic way.

In terms of flow modelling, a new model of coastal barrier breaching should be hydrodynamic and be able to reliably capture and describe hydraulic jumps as part of the breach

flow conditions.

The time-dependent vertical breach growth is then computed directly by the model without any assumptions about morphological stages as well as flow regimes. Also, the scour development in the breach channel should be modelled considering the turbulence effects of the hydraulic jump, especially in the early period of the process and in case the downstream water level is low. In return, the numerical scheme must be sufficiently robust to handle such strong variations of the breach bottom.

A one dimensional morphological model would be sufficient to simulate the breach development, providing that the growth relation between the breach widening and the breach deepening can be established for the case of an arbitrarily varying breach bottom.

2.4 Conclusions

In this chapter a literature review is carried out on processes involved with the breaching process of coastal sand barrier under the effects of tropical cyclones. The following conclusions are drawn as implications for the development of a new numerical model of coastal barrier breaching addressed in the next four chapters:

The response of low-crested sand barriers during storm surges is largely responsible for the breach initiation of coastal sand barriers. The processes of the barrier response include beach and dune erosion, and wave overwash (wave overtopping and overflow) respectively. The use of the conventional average overtopping discharge as the hydraulic input for the morphological modelling of wave overwash on barriers is found inadequate. More physical insight into wave overtopping is therefore needed to better describe its intermittent character and associated strength so as to model wave overwash properly. This can be done by a laboratory investigation of wave overtopping on fixed-bed model barriers. For modelling of the overall barrier response, new development of wave overwash needs to be coupled with a time-dependent process-based model of dune and beach erosion. Also, laboratory (mobile-bed) overwash experiments are needed to increase understanding of the processes of barrier response during storm surges and to generate data for calibration of the developed model.

Growth of an erosional channel induced by overflow, viz. the overwash morphological development or the breach growth in a sand barrier, needs to be modelled according to a hydrodynamic approach, in which both the lateral and vertical channel growth are simulated. Three-dimensional morphodynamic modelling of this erosion process requires lots of efforts and is computationally expensive. Therefore, it is desirable to develop a new process-based approach for a more efficient computation of the channel growth. To improve the model prediction of the vertical breach growth, the scour development in the breach channel also needs to be accounted for in connection with the turbulence effects of the hydraulic jump.

Chapter 3

WAVE OVERWASH: FIXED-BED EXPERIMENTS AND PARAMETERIZATION*

3.1 BACKGROUND

Numerical modelling of wave overwash relies heavily on the prediction of overtopping parameters as the requisite hydraulic input at the entrance crest boundary (see problem schematization in Fig. 3.1).

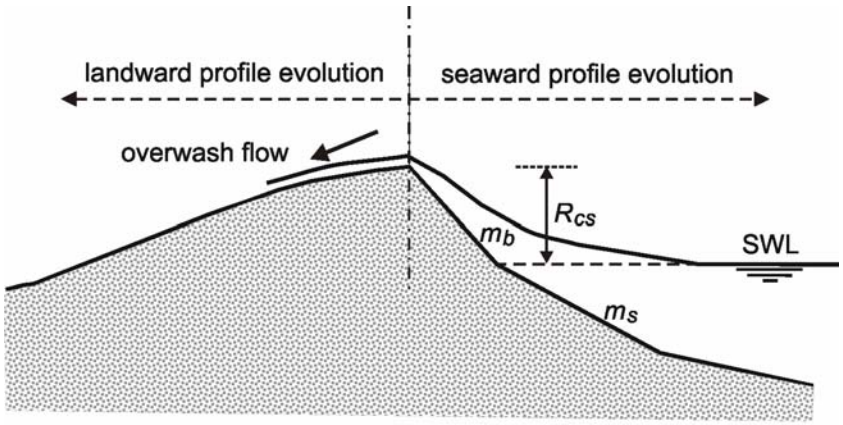

Figure 3.1 Wave overtopping as the hydraulic input for overwash modelling

As a starting point we adopt overtopping discharge formulations from breakwater literature. Most of these formulations have been developed for laboratory conditions where uniform slopes were used. On natural beaches, the profile is more very complex and thus an appropriate equivalent slope for use in those predictive formulae is not straightforward. Different slope definitions can lead to substantial differences in overtopping estimates.

Kobayashi *et al.* (1996) carried out tests on overwash of dunes and compare overtop-

* Content of this chapter was published as: Tuan, T.Q. *et al.*, 2006a. Wave overwash at low-crested beach barriers, *Coastal Engineering Journal*, World Scientific and JSCE, 48, 4, pp. 371-393.

ping rates with the existing formulations of Van der Meer *et al.* (1995), which were originally developed for hard slope coastal structures. An equivalent uniform slope also according to Van der Meer *et al.* (1995) was used. These formulae were found to predict only the order of magnitude of the measured overtopping rates. The study reveals that the accuracy of overtopping estimates is relatively sensitive to the magnitude of the calculated equivalent slope. The adaptation of the uniform equivalent slope concept from a hard slope to a sandy beach is therefore an issue to be further considered.

Prediction of runup on sandy beaches encounters a similar problem. Mayer and Kriebel (1994) combined the Hunt runup formula and Saville's hypothetical slope concept to provide first-order estimates of wave runup over composite slope beaches. Improvements over the existing formulae were found and attributed to proper adjustment of the beach slope. However, the finding is rather an ad hoc modification of wave runup formulae than a direct improvement on the equivalent slope for sandy beaches.

Tuan (2003) investigated from literature the characteristics of dune profile development during storms. It was noted that short-term evolution of sandy profiles can be well distinguished into two parts i.e. above (dry beach) and below (submerged beach) the still water line. Based on this notion, the author proposed a general form of the equivalent slope that can be used in the calculation of wave overtopping discharge, using existing empirical formulations.

Based on the findings of Kobayashi *et al.* (1996), Tega and Kobayashi (1999) performed a numerical study on dune evolution due to wave overwash. The model failed to reproduce the measured dune profiles satisfactorily. This was, in part, due to the use of the conventional average overtopping discharge, which is too simplistic in this case. It was recommended to seek for a better description of wave overtopping.

In general, discharge due to wave overtopping is intermittent and concentrates in a duration less than one wave period. The average discharge is therefore unsuitable to characterize the discontinuous character of overtopping. Instead, e.g. for purposes of morphological modelling, wave overtopping should be treated as an event-based process, and this process should be characterized by a new set of descriptive parameters.

In pursuit of the above issues, an experimental investigation of wave overtopping at composite slope barriers on shallow foreshores was carried out, which is described in detail in this chapter. Section 3.2 describes the physical setup and the test programme for the experiment. Low-crested conditions associated with moderate to severe overtopping were selected for the tests. In Section 3.3, the data processing procedure and analysis is briefly explained. Descriptions of key overtopping parameters are also given. In Section 3.4, the experimental data are used to formulate the event-based wave overtopping discharge under the assumption of form similarity between individual events. Also, the new slope definition for sandy beaches, as proposed in the previous work of Tuan (2003), is extended and calibrated. The results of this experimental study are discussed in Section 3.5. Summary and conclusions of this chapter are finally given in Section 3.5.

3.2 EXPERIMENTAL SET-UP

A scale model was constructed in the 40m long wave flume at the laboratory of Delft University of Technology. The wave maker, which is equipped with Active Reflection Compensation, is capable of generating regular and irregular waves up to 25cm.

The experimental setup consisted of impermeable model barriers on a 1/35 sloping foreshore with two different crest freeboards and slope compositions (see Fig.3.2). The barrier slopes were made smooth securing a roughness reduction to achieve a proper scaling for wave overtopping. The initial water level in the flume was always related to the transition point of the barrier slope at the depth of 0.70 m. Overtopping volume is collected using a basin behind the barrier.

Five wave height meters (WHM) were placed at various locations along the flume. WHM1-3 and WHM4 were used for the decomposition of the incident and reflected waves at the seaward most boundary and at the toe of the barrier.

Wave by wave overtopping is of crucial interest, WHM5 was therefore installed on the barrier crest. Since a minimum water depth of 5cm is always required, WHM5 is accommodated with a well of 10cm deep. In order to sense the presence of water even with minor disturbances, this gauge was set to a range of high sensitivity.

Random waves with standard JONSWAP-shaped spectra were employed in the experiment. Test parameters were chosen in such a way that the wave heights H_{mo} at the toe of the barrier are larger than the crest freeboards R_{cs} (or the ratio R_{cs}/H_{mo} ≤1), which corresponds to the condition of moderate to heavy wave overtopping. This resulted in a test program consisting of 35 tests with parameters as specified in Table 3.1.

3.3 ANALYSIS OF EXPERIMENTAL RESULTS

Since there was no means of disturbance-free supply of water back into the flume, the mean water level was slowly falling during the measurement. This means in fact that the crest freeboard was slowly increasing, depending on the severity of overtopping. To account for this effect, an averaged crest freeboard is determined for each test as follows:

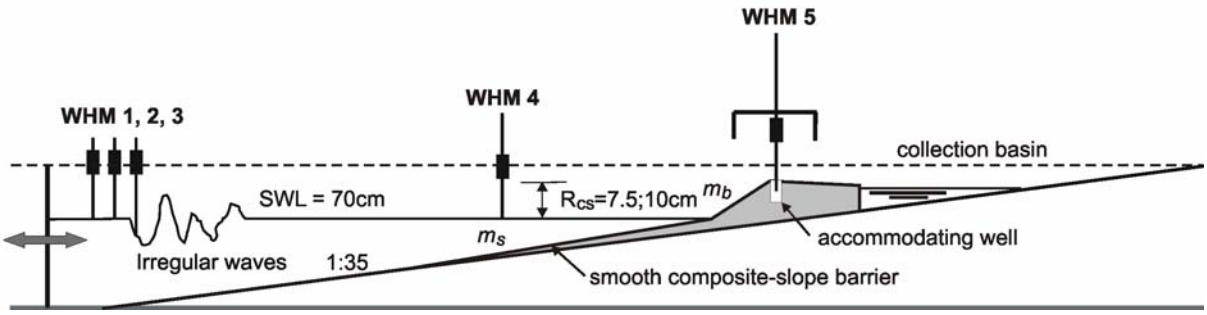

Figure 3.2 Experimental set-up showing the barrier on a shallow foreshore

Table 3.1 Experimental conditions.

Test	T	$H_{m0,i}$	T_P	S_{op}	$T_{m-1.0,\,toe}$	$H_{m0,toe}$	$\frac{R_{cs}}{H_{mo,toe}}$	$\xi_{m,toe}$	$\frac{H_{mo,i}}{d_{toe}}$
	(min.)	(m)	(sec.)	(-)	(sec.)	(m)	(-)	(-)	(-)
Crest freeboard R_{cs} = 7.5 cm m_s = 0.064 m_b = 0.138									
1	30	0.123	1.50	0.035	1.36	0.098	0.82	0.35 ~ 0.75 (0.45)	1.30
2	30	0.139	1.50	0.040	1.40	0.101	0.80	0.35 ~ 0.76 (0.45)	1.15
3	36	0.106	1.70	0.024	1.41	0.097	0.83	0.36 ~ 0.78 (0.47)	1.51
4	36	0.125	1.70	0.028	1.44	0.102	0.80	0.36 ~ 0.78 (0.46)	1.28
5	36	0.142	1.70	0.031	1.49	0.104	0.80	0.37 ~ 0.80 (0.47)	1.13
6	40	0.107	2.00	0.017	1.51	0.100	0.82	0.38 ~ 0.82 (0.49)	1.50
7	40	0.126	2.00	0.020	1.57	0.104	0.81	0.39 ~ 0.84 (0.50)	1.27
8	40	0.144	2.00	0.023	1.67	0.106	0.82	0.41 ~ 0.88 (0.52)	1.11
9	40	0.163	2.00	0.026	1.77	0.107	0.82	0.43 ~ 0.93 (0.55)	0.98
10	42	0.107	2.30	0.013	1.62	0.101	0.84	0.41 ~ 0.88 (0.52)	1.50
11	42	0.127	2.30	0.015	1.71	0.106	0.82	0.42 ~ 0.91 (0.54)	1.26
12	42	0.146	2.30	0.018	1.84	0.107	0.84	0.45 ~ 0.97 (0.57)	1.10
13	42	0.165	2.30	0.020	1.96	0.109	0.83	0.47 ~ 1.02 (0.60)	0.97
14	45	0.108	2.50	0.011	1.68	0.102	0.84	0.42 ~ 0.91 (0.54)	1.48
15	48	0.127	2.50	0.013	1.80	0.106	0.84	0.44 ~ 0.95 (0.56)	1.26
16	45	0.147	2.50	0.015	1.94	0.108	0.84	0.47 ~1.02 (0.60)	1.09
17	50	0.108	2.70	0.009	1.75	0.102	0.86	0.44 ~ 0.94 (0.56)	1.48
18	50	0.127	2.70	0.011	1.89	0.106	0.86	0.46 ~ 1.00 (0.59)	1.26
Crest freeboard R_{cs} = 10 cm m_s = 0.064 m_b = 0.125									
1	30	0.142	1.50	0.040	1.39	0.104	0.97	0.34 ~ 0.67 (0.45)	1.13
2	30	0.158	1.50	0.045	1.44	0.106	0.96	0.35 ~ 0.69 (0.46)	1.01
3	35	0.127	1.70	0.028	1.43	0.104	0.97	0.35 ~ 0.69 (0.46)	1.26
4	35	0.145	1.70	0.032	1.48	0.107	0.95	0.36 ~ 0.71 (0.47)	1.10
5	35	0.163	1.70	0.036	1.54	0.108	0.95	0.37 ~ 0.73 (0.49)	0.98
6	40	0.118	2.00	0.019	1.54	0.105	0.97	0.38 ~ 0.74 (0.50)	1.36
7	40	0.146	2.00	0.023	1.65	0.109	0.96	0.40 ~ 0.78 (0.52)	1.10
8	40	0.164	2.00	0.026	1.74	0.109	0.97	0.42 ~ 0.82 (0.55)	0.98
9	40	0.128	2.30	0.016	1.69	0.108	0.96	0.41 ~ 0.80 (0.54)	1.25
10	40	0.148	2.30	0.018	1.79	0.111	0.96	0.43 ~ 0.84 (0.56)	1.08
11	40	0.168	2.30	0.020	1.89	0.112	0.96	0.45 ~ 0.88 (0.59)	0.95
12	45	0.110	2.50	0.011	1.66	0.101	1.00	0.42 ~ 0.82 (0.55)	1.45
13	46	0.129	2.50	0.013	1.77	0.106	0.99	0.43 ~ 0.85 (0.57)	1.24
14	45	0.158	2.50	0.016	1.96	0.110	0.99	0.47 ~ 0.92 (0.62)	1.01
15	45	0.140	2.50	0.014	1.83	0.110	0.97	0.44 ~ 0.86 (0.58)	1.14
16	50	0.139	2.70	0.012	1.92	0.112	0.97	0.46 ~ 0.90 (0.60)	1.15
17	50	0.160	2.70	0.014	2.07	0.113	0.98	0.49 ~ 0.96 (0.64)	1.00

Note: Variations of the surf similarity parameter $\xi_{m,toe}$ are associated with the tuning range η = 0~1. Values in brackets are based on the conventional approach by Van der Meer (1998).

$$R_{cs} = R_{cs0} + \frac{1}{2}\Delta R_{cs}. \tag{3.1}$$

in which R_{cs0} is the initial (before test) crest freeboard (10 or 7.5 cm), ΔR_{cs} is the total level fall (at the end of a test) relative to the initial level. On the whole, the maximum fall of the water level was about 2cm, implying 1cm of additional increase of freeboard for the heaviest overtopping (see Eq. 3.1).

In principle, the falling process of the mean water level during a test will influence the waves. Control tests (without overtopping) with a difference in the mean flume level of 1cm showed minor variations in the measured wave heights ($< 1\%$ at the wave-board section and $<5\%$ at the toe section). Furthermore, the level fall effects are actually taken into consideration in the current analysis, explicitly via the use of the test-averaged water level (Eq. 3.1) and implicitly in the measured wave heights themselves. Within the above range of the flume drawdown, its effects on the overtopping parameterization are therefore negligibly small.

The measured data of all 35 tests are given in Appendix A.

3.3.1 Wave reflection

As mentioned earlier, three gauges located at the horizontal portion of the flume before the slope were used to decompose incident and reflected waves. In general, reflected waves were rather small in all tests, owing to the ARC of the wave generator and the mildness of the foreshore slope. The overall reflection coefficient C_r, defined in Eq. 3.2 below, varied between 1 ~ 5 %.

$$C_r = \sqrt{\frac{m_{0,r}}{m_{0,i}}}. \tag{3.2}$$

where $m_{0,i}$ and $m_{0,r}$ are the zeroth spectral moments of incident and reflected waves, respectively.

3.3.2 Signal of wave overtopping

In Fig. 3.3, the disturbance of overtopping waves displayed in volts on the vertical axis is clearly discriminated by discontinuous asymmetric triangles. However, there exists noise between these peaks, which was in fact caused by water level fluctuation within the accommodation well. In order to eliminate this noise and obtain the information needed on each individual overtopping wave, an algorithm of "local threshold" was applied. Any arbitrary reading, which has a signal value larger than its local threshold, is recognized as a registration of an overtopping event. This threshold is determined locally between each pair of overtopping triangles as follows:

$$A_{thres} = \overline{A} + a_{fluct}. \tag{3.3}$$

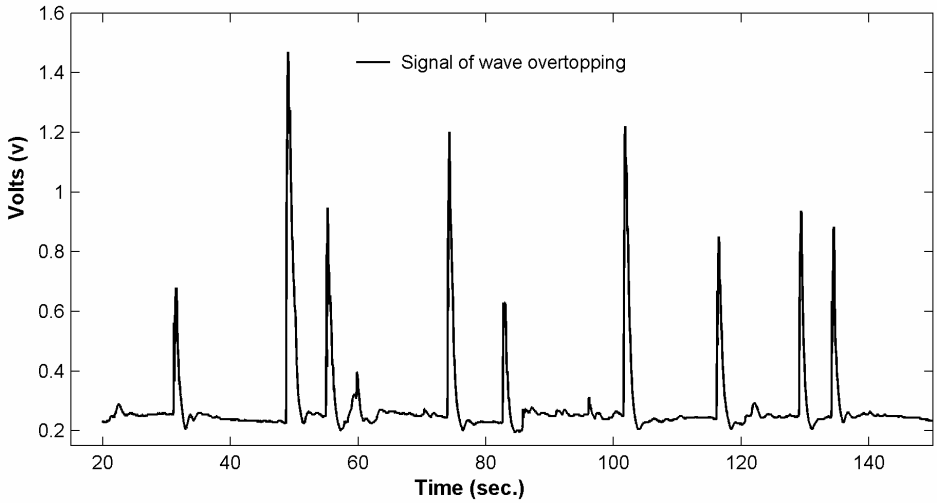

Figure 3.3 A sample of wave overtopping signal

where A_{thres} is a local threshold, $\overline{A}$ is the averaged signal value between two considered peaks, a_{fluct} is the fluctuation margin.

The value of a_{fluct} in Eq. 3.3 was determined by testing the gauge (WHM5) with fluctuating water within the well. This method was also verified against visual observations on the number of overtopping waves in several calibration tests.

The layer thickness of the overtopping flow is very small (of the order of a centimetre). Moreover, the effect of wave rise against the gauge on the overtopping signals is somewhat erratic.

Therefore, although the signal output from this gauge matched well with our visual observations, we concluded that the quantitative values of the layer thickness are unreliable, but that the duration and the instant of maximum discharge of the overwash event are reliable.

3.3.3 Description of key overtopping parameters

As mentioned earlier, it is desired to improve the description of wave overtopping that can be used for various modelling purposes. In the current study, the ultimate goal is to formulate the instantaneous (time-varying) discharge of the overwash event in terms of the barrier geometry and incident hydraulic conditions. The following parameters that were directly or indirectly measured during the experiment are thus proposed in the elaboration.

Average overtopping discharge q ($m^3/s/m$)

This discharge quantity is widely used in coastal engineering designs. It is averaged over the entire test (or storm) duration T.

$$q = \frac{V_{ovt}}{T}. \tag{3.4}$$

where V_{ovt} is the total overtopping volume.

Number of overtopping waves N_{ovt}

This number is counted using the algorithm of local threshold mentioned earlier.

Total overtopping time T_{ovt} (sec.)

T_{ovt} is determined as the summation of overtopping time of all individual waves that pass the barrier crest.

$$T_{ovt} = \sum_{1}^{N_{ovt}} t_{ovt,w}. \tag{3.5}$$

where $t_{ovt,w}$ is the overtopping time of an individual overtopped wave.

Relative total overtopping time F_{cd}

Wave overtopping is discontinuous and condensed to time durations less than one wave period. The relative total overtopping time is therefore defined according to:

$$F_{cd} = \frac{T_{ovt}}{T} = \frac{\sum_{1}^{N_{ovt}} t_{ovt,w}}{T}. \tag{3.6}$$

This parameter represents the discontinuous character of overtopping, viz. the smaller F_{cd} the more discontinuous overtopping and vice versa. By definition, F_{cd} is smaller than unity ($F_{cd} < 1$).

Wave-averaged overtopping time t_{ovt} (sec.)

This quantity is the average overtopping time per wave according to:

$$t_{ovt} = \frac{T_{ovt}}{N_w} = F_{cd} T_m. \tag{3.7}$$

where T_m is a characteristic wave period. N_w is the characteristic number of waves determined according to T_m, $N_w = T/T_m$.

Overtopping Asymmetry

Overtopping peaks as seen in Fig. 3.3 are appreciably similar in shape. This form similarity can be characterized by an overall asymmetric factor which is defined as the ratio of the total rising time to the total overtopping time of all overtopped waves (see also Fig. 3.4).

$$\delta = \frac{\sum_{1}^{N_{ovt}} t_{rise,w}}{T_{ovt}} = \frac{\sum_{1}^{N_{ovt}} t_{rise,w}}{\sum_{1}^{N_{ovt}} t_{ovt,w}} = \frac{t_{rise}}{t_{ovt}} < 1. \tag{3.8}$$

where δ is the asymmetric factor; t_{rise} is the total rising time of overtopping waves; the subscript $(.)_w$ denotes an individual wave value.

Average instantaneous discharge and average maximum discharge

The triangular shapes in the overtopping signal as shown in Fig. 3.3 suggest the existence of a dominating peak discharge in each overtopping wave. We argue that the data are not accurate enough to characterize individual overtopping events. As a first-order approximation we suggest to adopt an average instantaneous discharge schematization based on an asymmetric triangular shape (see Fig. 3.4), constrained by the total overtopping volume. Inaccuracies in the triangular shape assumption will not affect the results in a relative sense and only marginally in absolute sense.

Hence, the average maximum discharge can be derived based on the property of mass conservation:

Mass conservation: $\frac{1}{2} q_{cd\max} t_{ovt} N_{waves} = qT = V_{ovt}$.

Substituting $T_{ovt} = t_{ovt} N_{waves}$ in the above equation yields: $\frac{1}{2} q_{cd\max} T_{ovt} = qT$.

Finally we have:

$$q_{cd\max} = 2\frac{q}{F_{cd}}. \tag{3.9}$$

The triangular discharge histogram (Fig. 3.4) or the average instantaneous discharge can be expressed as functions of time as follows:

$$\frac{q_{cd}(t)}{q_{cd\max}} = \frac{1}{\delta}\frac{t}{t_{ovt}} \qquad \text{with } 0 \le t \le \delta t_{ovt}. \tag{3.10}$$

$$\frac{q_{cd}(t)}{q_{cd\max}} = \frac{1}{1-\delta}\left(1 - \frac{t}{t_{ovt}}\right) \qquad \text{with } \delta t_{ovt} < t \le t_{ovt}. \tag{3.11}$$

$$q_{cd}(t) = 0 \qquad \text{with } t_{ovt} < t \le T_m. \tag{3.12}$$

where $q_{cd}(t)$ and q_{cdmax} are the average instantaneous discharge and its maximum, respectively.

The average instantaneous discharge is one step forward in characterizing the intense, discontinuous temporal variation of wave overtopping. In the current research context, it is used to specify the event-averaged wave-cycle input discharges at the upstream boundary in the numerical modelling of wave overwash. In a broader sense, this event-based description of the discharge is conceptually adaptable to other

coastal research issues such as on structural stability and erosion induced by overtopping flow where the use of the conventional average discharge might be inadequate. An example of such application is the use of the maximum average instantaneous overtopping discharge in a study on the stability of the inner slope of breakwaters (see Verhagen *et al.*, 2005).

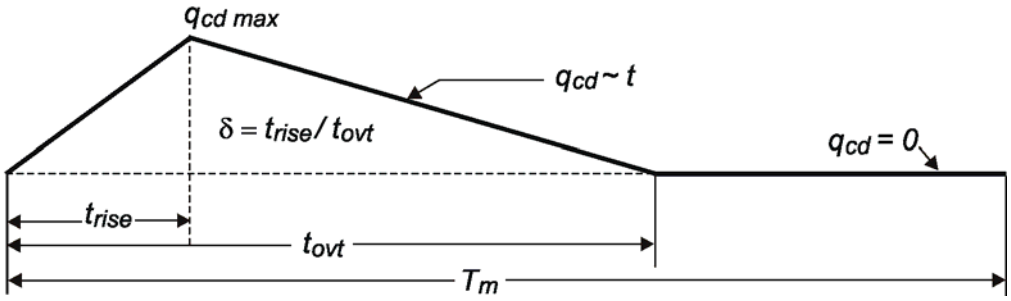

Figure 3.4 Average instantaneous overtopping discharge histogram

3.4 PARAMETERIZATION OF WAVE OVERTOPPING

In this section we first discuss the derivation of the new slope definition used in the formulations of the key overtopping parameters. Next, the formulations of three primary parameters, i.e. the average overtopping discharge, the average overtopping time and the overtopping asymmetry are given. A sensitivity analysis of the data scattering for relevant parameters is then followed to evaluate the effectiveness of the new slope definition.

3.4.1 New definition of the equivalent slope and the composite-slope parameter

In an earlier study, Tuan (2003) derived a general simple equation defining the equivalent slope for sandy beaches, in which the upper and lower slopes together with the relative crest freeboard are variables. It was later found that that definition is too general and needs to be specified further to explicitly include the effect of the wave period. Also, to facilitate the verification of the new approach, an additional parameter (a factor for composite slopes as shown in the following) is introduced. Following this direction, various modifications were tested to come up with a solution which is physically meaningful and mathematically correct. Eventually, a new form of the equivalent slope is given in the following:

$$m = m_s + \eta \frac{4 m_b R_{cs}}{\xi_m H_{mo}} (m_b - m_s) \;\; with \quad \frac{R_{cs}}{H_{mo}} \leq 1. \tag{3.13}$$

where m is the equivalent slope used in the overtopping calculation, m_s and m_b are the respective submerged (below water) and beach (dry) slopes, H_{mo} is the zeroth moment wave height at the toe, ξ_m is the surf similarity parameter based on H_{mo} and the spectral period T_m, η is the composite-slope parameter.

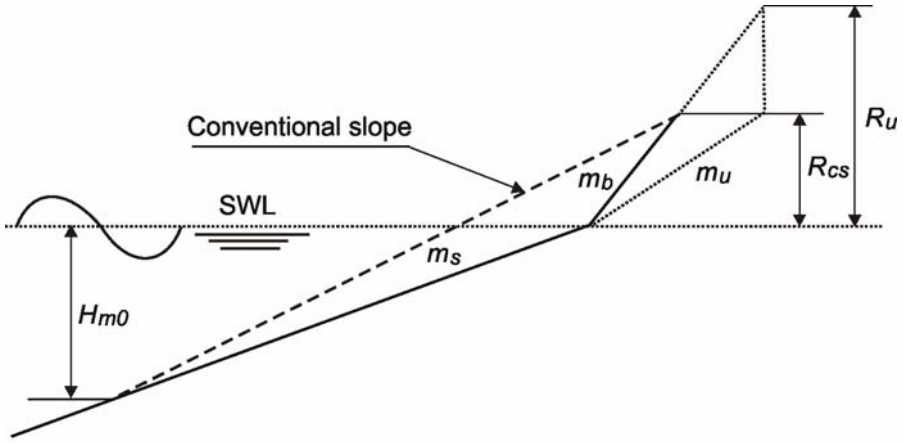

Figure 3.5 New approach for defining the equivalent slope for overwash beaches

The newly defined slope incorporates the effect of wave height and of the wave period. Its performance is discussed later in the analysis of the overtopping data, in which the parameter η is tuned to minimize scattering.

The physical interpretation for this approach can be discerned from Fig. 3.5 and the following Eq. 3.14. Due to the crest shortage, run-up is cut off as waves reach the upper edge of the slope. Therefore, according to the definition of Van der Meer (see Van der Meer *et al.*, 1995; Van der Meer, 1998), hereinafter designated as the conventional approach, seen as the dashed line in Fig. 3.5, this cut-off makes no difference in sloping amongst waves with the same height but various wave periods as long as they overtop the slope. In the new approach, instead, longer waves "sense" gentler slopes as they run over.

Equation 3.13 can be rewritten as follows:

$$m = m_s + \eta' \frac{R_{cs}}{R_u / m_b}(m_b - m_s) = m_s + \eta'(m_b - m_s)m_u = m_s + \eta'' m_u. \tag{3.14}$$

where R_u is the fictitious run-up height, $R_u \sim \xi_m H_{mo}$.

m_u is the upper slope sensed by waves, $m_u = \dfrac{R_{cs}}{R_u / m_b}$ (see Fig. 3.5).

In order to investigate the range of validity for the composite-slope parameter η, a maximum possible value for the equivalent slope in Eq. 3.13 is considered, viz. when it equals the beach slope m_b:

$$m = m_s + \eta \frac{4 m_b R_{cs}}{\xi_m H_{mo}}(m_b - m_s) \le m_b.$$

$$\text{or } \eta \frac{4 m_b R_{cs}}{\xi_m H_{mo}} \le 1.0. \tag{3.15}$$

Substituting $\xi_m = \dfrac{m}{\sqrt{s_m}}$ into Eq. 3.15 yields:

$$\eta_{\max} = 1/4 \times 1/(\frac{R_{cs}}{H_{mo}})_{\max} \times 1/(\frac{m_b}{m})_{\max} \times 1/\sqrt{(s_m)_{\max}}. \quad (3.16)$$

where s_m is the fictitious wave steepness $s_m = \frac{2\pi}{g}\frac{H_{m0}}{T_m^2}$.

In Eq. 3.16, the ratio $(\frac{m_b}{m}) \to \max$ if $m = m_s$, but this only occurs when $m_b = m_s$. Thus, $(\frac{m_b}{m})_{max} = 1$. In addition, taking $(\frac{R_{cs}}{H_{mo}})_{\max} = 1$ and $(s_m)_{max} = 0.06$ gives $\eta_{max} \approx 1.0$.

Theoretically, the composite-slope parameter η lies in the range between 0 and 1 $(0 \le \eta \le 1)$. On typical natural beach barriers, i.e. slopes with a gentle foreshore and without a dune scarp, the contribution from the submerged part seems exaggerated in a physical sense. Therefore, the most likely value of the parameter for the considered cases is between 0 and 0.50.

In the following section, it is shown that the above theoretical range can be further narrowed via a minimization of the scattering of the key overtopping parameters.

Since ξ_m is also a function of the equivalent slope, Eq. 3.13 is a quadratic equation with respect to this variable. Solving this equation gives an explicit expression of this slope according to:

$$m = \frac{1}{2}m_s + \frac{1}{2}\sqrt{m_s^2 + 16\eta m_b \frac{R_{cs}}{H_{mo}}\sqrt{s_m}\,(m_b - m_s)}. \quad (3.17)$$

For the sake of comparison the equivalent slope according to the conventional definition (Van der Meer, 1998) can also be derived from Fig. 3.5:

$$m = \frac{R_{cs} + 1.0H_{mo}}{1.0H_{mo}/m_s + R_{cs}/m_b}. \quad (3.18)$$

Equation (3.18) presents the principle of the two-point method (see Tuan, 2003), in which a composite slope is represented by a uniform equivalent slope within a pair of boundary points.

It is worth noticing, by definition, that the new equivalent slope defined by Eq. 3.13 or Eq. 3.17 is bounded by the upper beach slope m_b. Also, it is realized that, with waves of the same height but different periods, the conventional definition (Eq. 3.18) always gives a fixed value of the equivalent slope whereas the new definition (Eq. 3.17) produces slopes varied between m_s and m_b, depending on also the wave periods.

3.4.2 The optimal wave period

Different characteristic wave periods such as $T_{m0.1}$, $T_{m0.2}$, $T_{m-1.0}$, and T_P have been widely used in formulations of wave run-up and overtopping. Choices of one of these wave periods are also various, depending upon particular purposes. The definition for those periods based on spectral moments is given in Eq. 3.19.

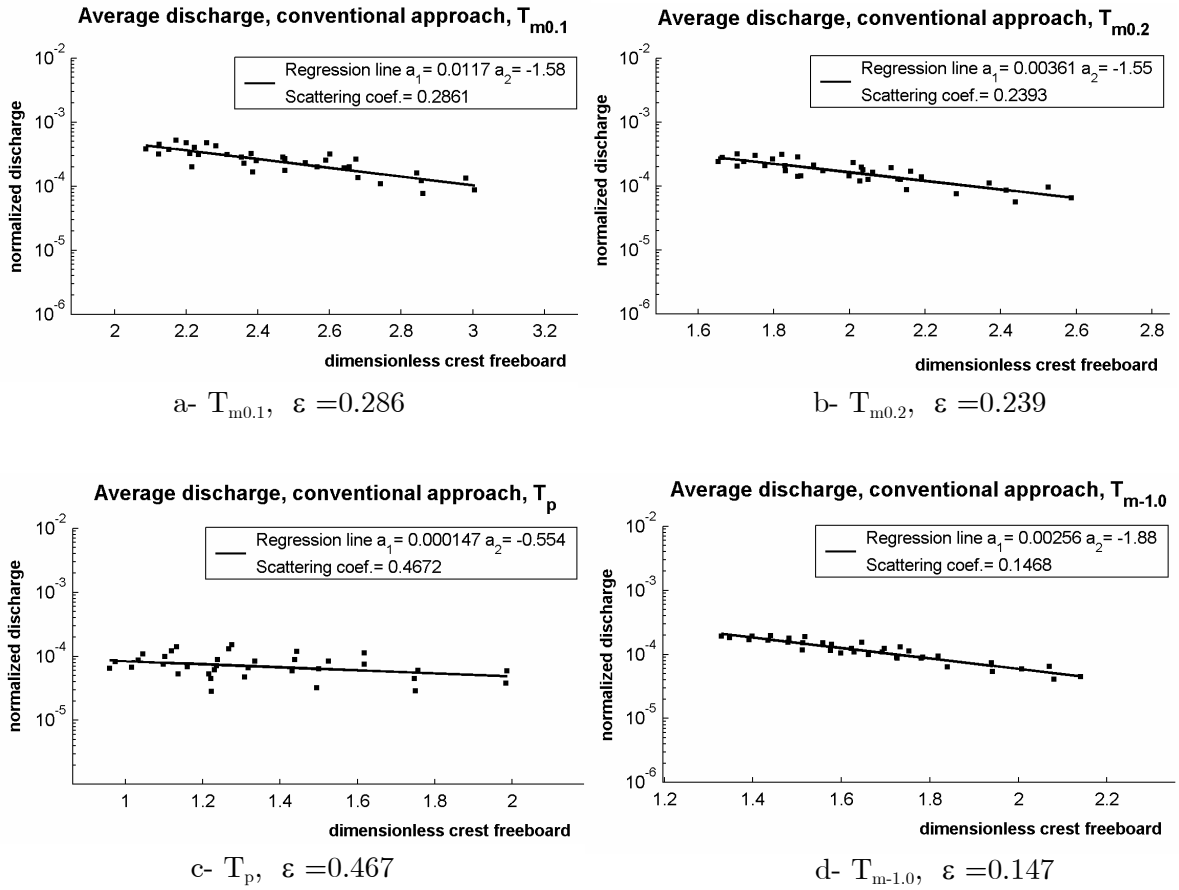

a- $T_{m0.1}$, ε =0.286 b- $T_{m0.2}$, ε =0.239

c- T_p, ε =0.467 d- $T_{m-1.0}$, ε =0.147

Figure 3.6 Normalized average overtopping discharge with different characteristic periods

$$T_{m\alpha.\beta} = \left(\frac{m_\alpha}{m_\beta}\right)^{\frac{1}{\beta-\alpha}} = \left(\frac{\int_0^\infty f^\alpha S(f)df}{\int_0^\infty f^\beta S(f)df}\right)^{\frac{1}{\beta-\alpha}} . \tag{3.19}$$

where m_α and m_β stand for the wave spectral moments, α and β are integers.

A numerical study by Van Gent (2001) suggests to use the spectral period $T_{m-1.0}$ in describing wave run-up and wave overtopping for optimal results in cases of shallow foreshores, where wave spectra are flattened out. This conclusion is experimentally reconfirmed in the present study.

To evaluate the goodness-of-fit of data around a trend line or a prediction curve, a root-mean-square of the relative deviations between the measurement and the computed trend or prediction was used. This is known as the scattering coefficient (Eq. 3.20), of which a smaller value implies a better fit.

$$\varepsilon = \sqrt{\frac{1}{N_p}\sum_{i=1}^{N_p}\left(\frac{Y_{i,computed}}{Y_{i,measured}} - 1\right)^2} . \tag{3.20}$$

where Y is the considered dependent parameter, and N_p is the number of data points.

For the sake of simplicity and without loss of generality, the default slope definition was used to analyze the overtopping data using different characteristic wave periods e.g. $T_{m0.1}$, $T_{m0.2}$, T_P, and $T_{m-1.0}$. Fig. 3.6 clearly shows that $T_{m-1.0}$ gives the least scattering ($\varepsilon = 0.147$), whereas the peak period T_P gives the largest scattering ($\varepsilon = 0.467$).

Hereinafter, this optimal spectral period $T_{m-1.0}$ is consistently used and denoted as T_m in the parameterization of wave overtopping.

3.4.3 Formulations of the overtopping parameters and effectiveness of the new slope definition

The average overtopping discharge, the average overtopping time and the overtopping asymmetry are three primary parameters which we seek to formulate directly from the experimental data as functions of the hydraulic conditions and the barrier geometry. Other parameters such as the relative total overtopping time and the average instantaneous discharge can straightforwardly be deduced from these primary parameters.

In order to explore the effectiveness of the new approach defining the equivalent slope, a sensitivity analysis of the data scattering for relevant parameters is carried out. This is done by tuning η in Eq. 3.13 within its range of validity (between 0 and 1) and inspecting the goodness-of-fit (scattering coefficient ε defined in Eq. 3.20) of the overtopping data. A relationship between the scattering coefficient ε and η (ε~η) is therefore numerically established for each of the considered parameters. For the sake of comparison, the data scattering associated with the slope defined by the conventional definition is also plotted (a constant value for each parameter). By doing so, a favourable range of the composite-slope parameter η is sought that fits the overtopping data the best. The average discharge and the wave-averaged overtopping time are the two reference parameters for this purpose. Tuning is not necessary, as shown later, for the overtopping asymmetry because already good fit is achieved using the conventional slope definition.

Average overtopping discharge

Adopting a slightly modified form as in Van der Meer (1998), the function describing the average overtopping discharge reads:

$$\frac{q}{\sqrt{gH_{mo}^3}}\frac{s_m}{\sqrt{\tan\alpha}} = a_1 \exp\left(a_2 \frac{R_{cs}}{H_{mo}}\frac{\sqrt{s_m}}{\tan\alpha}\right). \tag{3.21}$$

where $\tan\alpha$ = m is the equivalent slope either according to the conventional or the new method. Coefficients a_1 and a_2 are to be determined by means of a least square minimization procedure.

The modification of Eq. 3.21 compared to Van der Meer (1998) concerns the term s_m instead of $\sqrt{s_m}$ on the left hand side. This modification is based on various combination modes to give the best possible degree of regression in the current analysis.

The scattering relation ε~η for the average overtopping discharge is shown as the upper curve in Fig.3.7. The conventional approach gives a fixed value of scattering $\varepsilon = 0.147$ (see also Fig. 3.6d). In compassion with the new approach, it follows that the conventional method introduces larger scattering over a wide range of η between 0 and 0.90. The optimal value of η, corresponding with the least scattering, is 0.19.

Figure 3.8a shows the result for the average discharge data plotted at the point of least scattering.

Wave-averaged overtopping time

Apart from being a function of the dimensionless crest-freeboard and the surf similarity parameter (just like the average discharge), the average overtopping time t_{ovt} is also dependent on the relative total overtopping time F_{cd} as shown in Eq. 3.7. The optimal dimensionless form quantifying t_{ovt} is shown in Eq. 3.22, also based on investigating various modes of parameter combinations to yield the best degree of regression (the least scattering coefficient).

$$\frac{t_{ovt}}{T_m}\sqrt{\frac{s_m}{\tan\alpha}} = F_{cd}\sqrt{\frac{s_m}{\tan\alpha}} = a_1 \exp\left(a_2 \frac{\sqrt{s_m}}{\tan\alpha}\left(\frac{R_{cs}}{H_{mo}}\right)^{3/2}\right). \tag{3.22}$$

The lower curve in Fig. 3.7 shows the relation ε~η for the wave-averaged overtopping time. The scattering resulted from the conventional slope definition is 0.09 (see Fig. 3.8c). In this case, the new approach indicates a better regression over the entire range of the composite-slope parameter. The least scattering is achieved at the optimal value $\eta = 0.35$. The result for the wave-averaged overtopping time at the point of least scattering is shown in Fig. 3.8b.

Overtopping asymmetry

Following the same procedure as for the two previous parameters, the overall asymmetry of overtopping triangles and also the discharge histogram is characterized by the following dimensionless expression:

$$\delta\sqrt{\frac{s_m}{\tan\alpha}} = a_1\left(\frac{\tan\alpha}{\sqrt{s_m}}\frac{R_{cs}}{H_{mo}}\right)^{a_2}. \tag{3.23}$$

Figure 3.8c shows the result for the overtopping asymmetry using the conventional slope definition. It is observed that the data are very well fitted without tuning necessity.

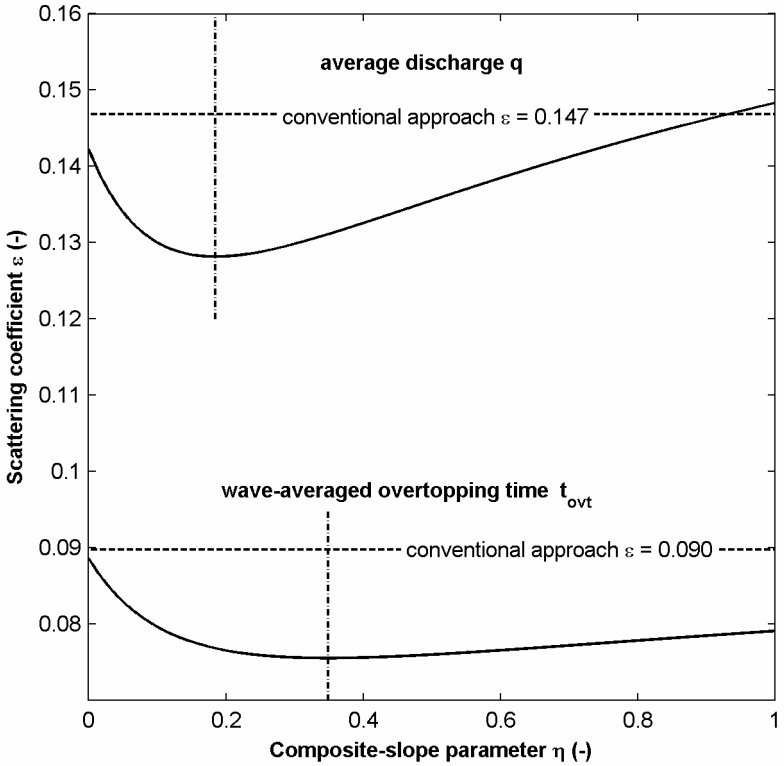

Figure 3.7 Relation $\varepsilon \sim \eta$ for the average discharge (upper) and the wave-averaged overtopping time (lower).

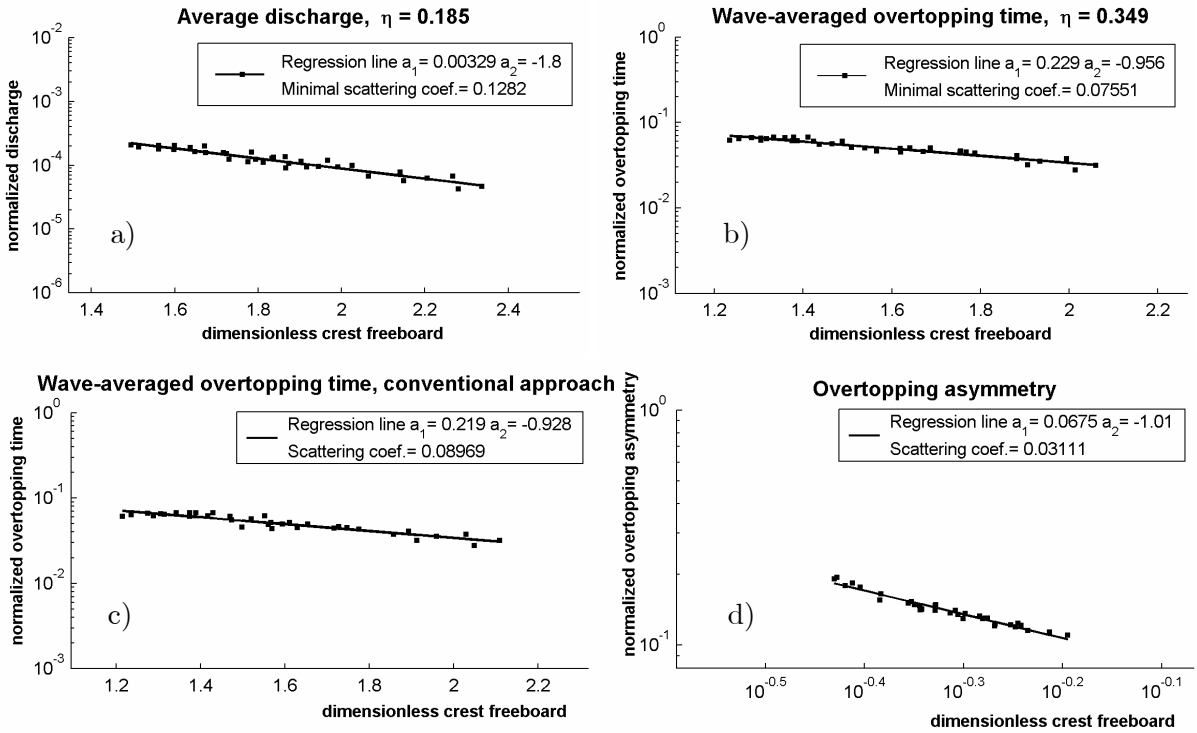

Figure 3.8 Normalized graphs of the primary overtopping parameters. (Data associated with the new slope definition are plotted at the point of least scattering)

Overall effectiveness of the new equivalent slope and the favourable range of η

As mentioned above, the relations ε~η have been established from the experimental data for both the average discharge and the wave-averaged overtopping time as in Fig. 3.7. Overall, the new approach clearly shows its advantage over the conventional one nearly over the entire theoretical range of the composite-slope parameter. Even so, it does not come up with a single best value of the composite-slope parameter since its optimal values for the two reference parameters are not coincident. However, the most concave portions of the both curves in Fig. 3.7 lie between 0.10 and 0.40 on the η-axis, which is also in agreement with the range that is likely to occur in the field mentioned earlier. This would be a compromising range ($\eta = 0.1 \sim 0.4$) if one desires to optimize the tuning with both of the reference parameters.

3.4.4 Numerical optimization of η

We conclude that there exists no single optimal value of the composite-slope parameter, which can simultaneously assure the least scattering of the two reference parameters. However, a favourable range that captures a satisfactory goodness-of-fit can be obtained. We further note that, it is arguable, on mathematical grounds, that a considered quantity (discharge or overtopping time) is in fact a function of geometric conditions (slope steepness and freeboard) and of hydraulic parameters, in which η is an implicit variable. Thereby, the data scattering and the number of data points may affect the optimization of η. With a given measurement error, which is presumed to be the same for all the tests (the same scattering), then the number of data points might be the most influential. It is shown in the following how numerical experiments can be utilized to study this issue. The approach is to generate new datasets to obtain a sufficiently large number of data points over a wide range covering the domain of interest, based on the stochastic properties of the existing experimental data. In this way, new data points of the dimensionless overtopping parameters are randomly generated on the assumption that they obey a normal distribution characterized by mean values and standard deviations (scatterings). To investigate the effect of the data scattering on the optimization of η, different values of the standard deviation coefficients v (standard deviation divided by a mean) are assumed for the analysis including those obtained from the measurement data (0.147 and 0.09 for the average discharge and the wave-averaged overtopping time, respectively, cf. Figs. 3.6d and 3.8c).

The wave data from 35 laboratory tests (Table 3.1) are used to form the basic hydraulic input since they cover a wide range of wave conditions on shallow foreshores. In detail, the mean values of the reference parameters are respectively determined by Eqs. 3.21 and 3.22, using the conventional slope definition and the corresponding regression coefficients from the laboratory experiment (0.0026 and -1.88 for Eq. 3.21, 0.219 and -0.928 for Eq. 3.22, cf. Figs. 3.6d and 3.8c).

The crest freeboard and the slope steepness reflect the two geometric conditions of the barrier. In this numerical experiment, the relative crest freeboard ($R_{cs}/H_{mo,toe}$) is varied over its full range between 0 and 1. A wide range of typical beach slopes from 1/30 to 1/5 is also selected to constitute a number of sets of composite profile.

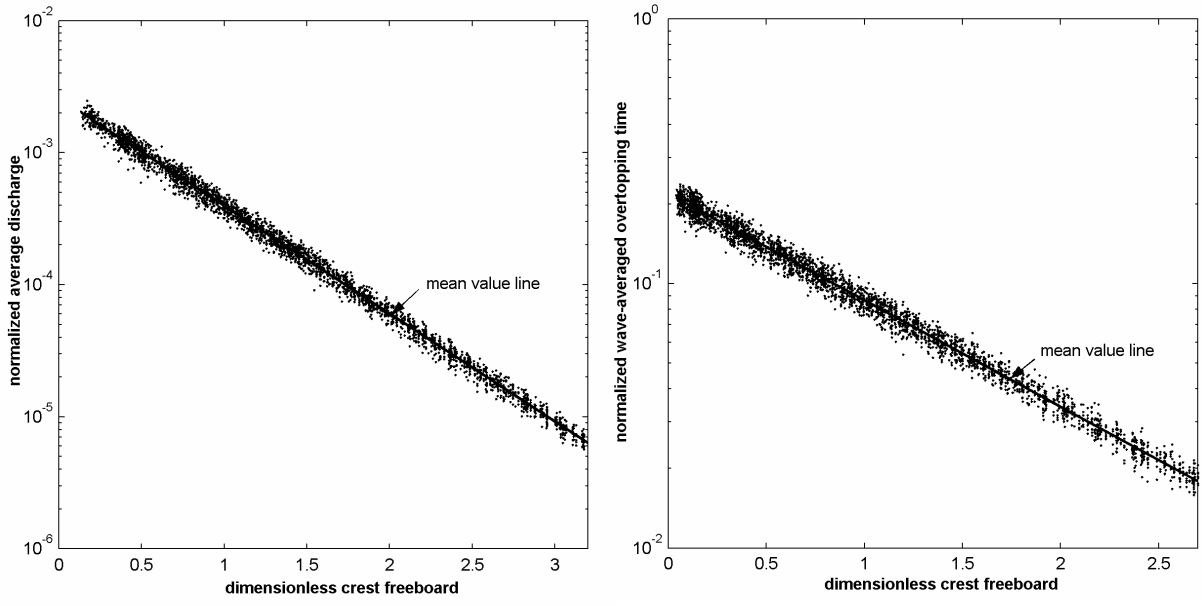

a) Average discharge data b) Wave-averaged overtopping time data

Figure 3.9 Randomly-generated overtopping data (normal distribution) N = 3150 points.

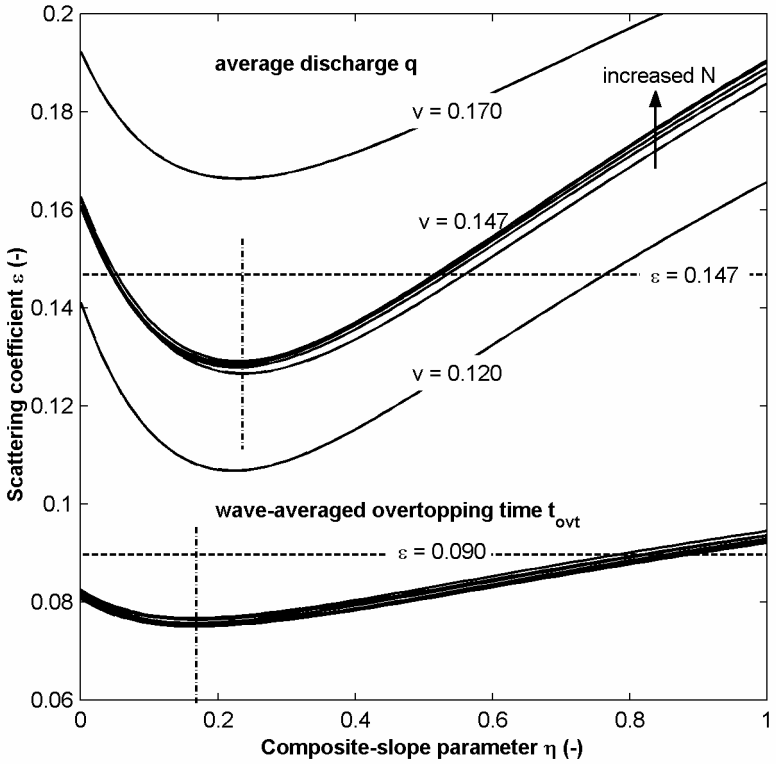

Figure 3.10 Relation ε~η of the randomly-generated overtopping data: effects of scattering and number of data points. Upper graph - the average discharge with different degrees of scattering (standard deviation coefficient $v = 0.12 \sim 0.17$). Lower graph - the wave-averaged overtopping time.

In total, one hydraulic and two geometric conditions form a three-dimension matrix of data points. The size of each matrix dimension can be varied according to the number of data points needed. Figures 3.9a and 3.9b show the result of a generation of 3150 data points (35×18×5) for the average discharge and the wave-averaged overtopping time, respectively. The newly-generated data points are then used for tuning as is done in Subsection 3.4.3. The results from the tuning as shown in Fig. 3.10 indicate that the generation randomness may affect the shape of the (ε~η) curves if the number of data points N is insufficiently large. The curves become stable at $N > 3000$ points. Interestingly, it also follows that the optimization of η is indeed most influenced by the number of data points covering the domain of interest. The position of the peaks of the two curves on the horizontal axis is not sensitive to the change in the data scattering, which is reflected by different values of v. On the whole, the two peaks do not coincide precisely on the η-axis but are quite close. The optimal value of the parameter is now in the range between 0.15 and 0.25 that is appreciably narrower than the one deduced from the laboratory data.

3.4.5 Final formulations

With the above optimal range of η between 0.15 and 0.25, the following Table 3.2 is elaborated for each pairs of regression coefficients in Eq. 3.21 and Eq. 3.22. Equally, these coefficients can be determined as functions of the composite-slope parameter as follows:

Discharge equation (Eq. 3.21):

$$a_1 = 0.0034 - 0.0006\eta \qquad a_2 = -1.64 - \eta \tag{3.24a}$$

Overtopping time equation (Eq. 3.22):

$$a_1 = 0.255 - 0.07\eta \qquad a_2 = -0.788 - 0.45\eta \tag{3.24b}$$

The coefficients in Eq. 3.23 are 0.0675 and approximate -1.0, with the equivalent slope determined using either the conventional approach or the new method since the tuning effect is less sensitive in this case (no significant difference in regression). Eq. 3.23 therefore can be rewritten in the following form:

$$\delta = \frac{0.0675}{\sqrt{\tan\alpha}} \frac{1}{R_{cs} / H_{mo}}. \tag{3.25}$$

Coefficients from Eqs. 3.24a and 3.24b are used to determine the average discharge and the relative total overtopping time according to Eqs. 3.21 and 3.22, respectively. The average instantaneous discharge is then fully determined using Eq. 3.9 to Eq. 3.12.

Table 3.2 Regression coefficients

η	Average discharge (Eq. 3.21)		Overtopping time (Eq. 3.22)	
	a_1	a_2	a_1	a_2
0.10	0.0033	-1.67	0.250	-0.804
0.15	**0.0033**	**-1.75**	**0.245**	**-0.840**
0.20	**0.0033**	**-1.83**	**0.241**	**-0.873**
0.25	**0.0033**	**-1.90**	**0.236**	**-0.903**
0.30	0.0032	-1.96	0.232	-0.930
0.35	0.0032	-2.02	0.229	-0.957
0.40	0.0032	-2.08	0.225	-0.982
0.45	0.0031	-2.13	0.222	-1.010
0.50	0.0031	-2.18	0.219	-1.030

Note: the bold numbers correspond to the most favourable range of the composite-slope parameter ($\eta = 0.15 \sim 0.25$).

3.5 Discussion

In the foregoing sections, key parameters from breakwater overtopping literature were modified to describe the nature of overtopping on beach barriers in conjunction with an improved definition of the equivalent slope. Our aim is to improve the description of wave overtopping discharge for use in numerical modelling of wave overwash. In general, the research results are conceptually adoptable to other practical engineering applications. However, certain aspects involving the use of the findings need to be addressed:

(1) It is technically impossible to generate data from mobile bed (sand) experiments to verify the new slope approach and the formulation of the key overtopping parameters. In the case of a mobile bed, the slope variation and the bed roughness are major factors which may differ overtopping discharge calculation from that of a fixed bed. However, it is shown in the following that possible deviations induced by those two factors can be exempted and the current findings from the fixed-bed experiment are therefore transferable to movable (sand) beds.

First, within a computation time step of one to several wave cycles, the profile evolution of a movable bed is negligibly small and thus the bed may be considered instantaneously fixed. Moreover, the assumption of quasi-steadiness, which is widely accepted for various purposes of numerical modelling, allows the instantaneous overtopping parameters to be related to the instantaneous (through the wave-cycle) slope geometry and incident wave parameters. As a result, effects of the slope variation in the quantification of wave overtopping discharge can be neglected.

Second, as already mentioned in Section 3.2, the model slopes were made smooth to fulfil a proper scaling for wave overtopping. This is because wave runup and overtop-

ping on sloping impermeable structures can be underestimated in model tests due to the inability to scale roughness effects. This is also true for the current situation where the prototype is a mobile (sandy) slope. However, this scale effect, in principle, can be minimized by making model slopes very smooth (see Hughes, 1993, p.215). Also, fixed-bed model tests with smooth slopes are commonly used for studying wave interactions on natural beaches such as wave runup by Battjes (1974), Mayer and Kriebel (1994).

(2) By definition, the new approach for defining the equivalent slope is generally valid for any low-crested (with occurrence of wave overtopping, quantitatively $R_{cs}/H_{mo} \leq 1$) profiles and wave steepness between 0.01 and 0.06. Consequently, the composite-slope parameter theoretically lies between 0 and 1.

It is worth noticing that, given the scope of the present work, the approach was not tested with steep slopes (say larger than 1/6, see also Mayer and Kriebel, 1994) rather than with those of typical many natural beaches. Likewise, the conditions of deep foreshores have not been considered. The validity of this new approach therefore falls under the conditions of sandy beaches with shallow foreshores. Nevertheless, it does not mean that the approach has a limited application. In fact, a large number of natural sea-defence works (dunes and barriers for instance) is found on gently sloping shallow parts of the coast, namely shallow foreshores, where the beach profile exhibits complexity due to high activities of depth-induced wave breaking. On those beaches, the definition of the equivalent slope is a real dilemma and the new approach is a promising solution.

(3) The newly-defined parameters were formulated using the experimental data of wave overtopping at impermeable and smooth slopes. Effects of slope roughness and porosity therefore must be taken into consideration in cases of high permeability and friction such as rock and gravel slopes.

(4) Because the composite-slope parameter is implicitly depending on the overtopping formulations, its value range and the associated regression coefficients (Table 3.2 or Eq. 3.24) actually create an additional flexibility for other calibration purposes. For this reason, in the next step of the current research, it is preferable that the final choice of this parameter within the favourable range will be specified further according to morphological considerations. For the unique purpose of overtopping calculation a value of the composite-slope $\eta = 0.20$ is recommended.

3.6 SUMMARY AND CONCLUSIONS

The use of the conventional average overtopping discharge as the hydraulic input for the morphological modelling of wave overwash on barriers is found inadequate. Instead, discharge due to wave overtopping should be described closer to its nature to account for the intermittent character and the associated strength. Therefore, a laboratory investigation of wave overwash on barriers with focus on this aim was carried out in this chapter. Due to the scope of the present research, the experimental conditions were limited to low-crested barriers with smooth slopes on shallow foreshores.

Our final goal is to describe wave overtopping discharge as an event-based approach i.e. describing its discontinuous and temporal behaviours through the wave cycle. As a result, several new parameters such as the wave-averaged overtopping time, the overtopping asymmetry, the relative total overtopping time, the average maximum discharge and the average instantaneous discharge have been derived and formulated.

An equivalent profile slope is a requisite for use in the empirical determination of wave overtopping discharge. It is found that the ordinary slope definition such as by Van der Meer (1998) is most suitable for hard structures where the crest freeboards are relatively constant and slopes are relatively uniform. On natural sandy beaches, however, the profile is complex with two distinct above and under water parts and can markedly change during wave attack and thus the determination of this slope is somewhat erratic. Hence, there is a need of a new slope definition suitable for sandy profiles, which was also addressed in this chapter. The new definition of the equivalent slope effectively takes into account effects of the wave period, which become significant when large variations in the relative crest freeboard and in slopes are present. The efficiency of the new slope definition is enhanced via the use of the composite-slope parameter η, whose favourable values have been experimentally found in the range between 0.10 and 0.40. This range has been further narrowed to between 0.15 and 0.25 by means of a numerical experiment. Hence, the composite-slope value of $\eta = 0.2$ would be recommended for overtopping estimates. However, for applications where the ultimate goals are not only the overtopping quantities, it is recommended to further calibrate this parameter (within its indicated range) according to additional corresponding criteria (for instance according to overwash morphological judgements). On the whole, it is shown experimentally that the new slope approach has advantage over the ordinary method in describing wave overtopping on smooth, low-crested, and composite-slope barriers.

The overtopping formulations presented in this chapter are valid within the application limit imposed by the scope of the present research, i.e. overwash on low-crested beach barriers on shallow foreshores. These formulations are used in Chapter 5 to quantify the (instantaneous) input flow at the seaward crest boundary for modelling the morphological development of the overwash channel. The appropriateness of these formulations is further investigated (also in Chapter 5) through the model performance of simulating the barrier response during storm surges in comparison with laboratory data from mobile-bed overwash experiments.

Chapter 4

OVERFLOW-INDUCED MORPHOLOGICAL DEVELOPMENT OF AN EROSIONAL CHANNEL*

4.1 INTRODUCTION

The present chapter deals with the morphological modelling of erosional channels, initially induced by overwash and eventually by breach flow. Modelling of this phenomenon has some features in common. In terms of flow characteristics, the overwash and breach flows are both unsteady and display discontinuities such as intermittences (overwash) and hydraulic jumps (breach). In addition, the breach flow can be in the mixed-regime while the overwash flow can be very shallow. Abrupt and arbitrary variations of the channel bed, especially in the case of breaching, further bring about intricacy to the modelling of these flows. All these aspects require a robust numerical method such as an upwind approach in order to capture such complex flow conditions reliably.

Regarding channel morphology, channel growth in both cases is a result of an erosion process induced by 'flash' overflow. By the nature of the process, bed changes are much more dynamic in the streamwise direction than those in the transverse direction. Also, the channel length in the case of breaching and overwash is relatively short, so the streamwise variation of the channel width is negligible compared to the streamwise variation of the channel bed. As a result, the bed profile along the channel (the vertical growth) must be known in detail while an instantaneous uniform width quantity is usually sufficient to represent the overall channel lateral growth. Because of this it is desirable, as indicated in Chapter 2, to be able to generally relate the lateral growth to the vertical growth of the channel. This is feasible for the case of (homogeneous) sand bed channels as indicated for example in Busnelli (2001). With this approach the computation of channel growth in the present considered situation becomes more efficient.

---

* Excerpts from this chapter was submitted for publication as: Tuan, et al., 2007b. Process-based modelling of the overflow-induced growth of erosional channels, *Coastal Engineering*, *Elsevier*.

All the above issues are addressed in this chapter. In Section 4.2 we briefly discuss the general equations for open channel flows and the selected upwind numerical method to resolve these. A general approach for treatment of source terms arising from friction and bed variation is also described. Modelling of the channel morphological development is discussed in Section 4.3, in which a general growth equation for erosional channels is derived in association with the introduction of several new morphological parameters such as the representative channel width and the channel growth index. This chapter ends with conclusions drawn in Section 4.4.

4.2 FLOW MODELLING

4.2.1 Basic flow equations

One-dimensional unsteady flow of water in a channel of slowly varying cross-section is governed by the Saint Venant equations (Cunge *et al.*, 1980). For flows in prismatic channels of arbitrary cross-section, the equations in conservative form read:

$$\frac{\partial U}{\partial t} + \frac{\partial F(x,U)}{\partial x} = S(x,U) \tag{4.1}$$

with conserved vectors *U, F(x,U),* and source term vector *S(x,U)* arising from bed slope and friction are as follows:

$$\begin{aligned} U(x) &= \begin{pmatrix} A \\ Q \end{pmatrix} \\ F(x,U) &= \begin{pmatrix} Q \\ \dfrac{Q^2}{A} + gI_P \end{pmatrix} \\ S(x,U) &= \begin{pmatrix} 0 \\ gA(S_{bx} - S_f) \end{pmatrix} \end{aligned} \tag{4.2}$$

in which A is the wetted cross-sectional area, Q is the discharge, S_{bx} and S_f are bed slope and friction slope, respectively, I_P is a hydrostatic pressure force term acting on the wetted area.

$$\begin{aligned} S_f &= \frac{1}{C^2}\frac{Q^2}{A^2 R} \\ I_P &= \int_0^d (d-z)B(z)dz \\ S_{bx} &= -\frac{dZ_b}{dx} \end{aligned} \tag{4.3}$$

where C is the Chezy coefficient, d is the local water depth, R is the hydraulic radius, Z_b is the local channel bed level, and $B(z)$ is a channel breadth at elevation z above the bottom.

In trapezoidal channels of constant bottom width b and side slopes m, I_P is further specified as:

$$I_P = \frac{1}{2}bd^2 + \frac{1}{3}md^3 \tag{4.4}$$

Discretization of Eq. 4.1 using the Finite Volume Method (FVM) yields:

$$U^{n+1} = U^n - \frac{\Delta t}{\Delta x}(F_{i+1/2} - F_{i-1/2}) + \Delta t S^n \tag{4.5}$$

in which n is a known computed level, Δt and Δx are time and space steps, respectively, $F_{i-1/2}$ and $F_{i+1/2}$ are numerical fluxes at the boundaries of a computed cell.

It is noted that by the nature of the FVM the discretization of Eq. 4.1 into Eq. 4.5 is totally exact without any approximation.

$F_{i-1/2}$ and $F_{i+1/2}$ are determined using the Riemann problem (see also Fig. 4.1):

$$F_{i+1/2} = F_{i+1/2}(U_L, U_R) \text{ with } U = \begin{cases} U_L = U_i^n & x < x_{i+1/2} \\ U_R = U_{i+1}^n & x > x_{i+1/2} \end{cases} \tag{4.6}$$

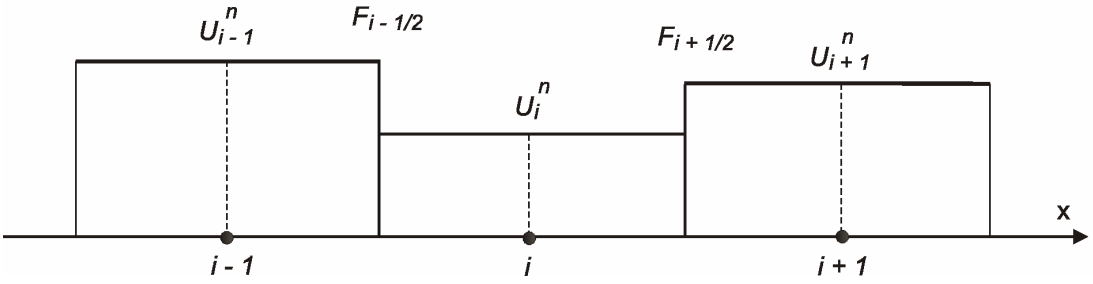

Figure 4.1 Boundary cell numerical fluxes and the Riemann problem

4.2.2 Roe's numerical scheme

To solve Eq. 4.5 with the Riemann problem given by Eq. 4.6 and the source terms as described in Eq. 4.3, a robust numerical scheme must be adopted. Fortunately, recent developments in upwind schemes solved in conjunction with FVM, which were originally introduced in gas dynamics, have provided great means to overcome such difficulties. Numerical schemes of these types are conservative and therefore able to deal with the presence of discontinuities.

An exact solution to Eq. 4.6 is usually impractical and approximate Riemann solvers are therefore favourable. In the present study, the first-order Roe's approximation is adopted to determine the boundary numerical fluxes. The Roe's (Roe, 1981) approximate Riemann solver has been very successful in resolving many problems of

shallow water flows. Basic formulations of this approach are summarized in the following. More details of the elaboration can be found in Toro (1997).

$$F_{i\pm1/2} = \frac{1}{2}(F_i + F_{i\pm1}) - \frac{1}{2}\sum_{k=1}^{2} \alpha^k_{i\pm1/2} \mid \hat{\lambda}^k_{i\pm1/2} \mid \hat{R}^k_{i\pm1/2} \tag{4.7}$$

where:

The Roe's coefficients:

$$\alpha^{1,2}_{i+1/2} = \frac{\Delta Q_{i+1/2} \mp \hat{\lambda}^{1,2}_{i+1/2} \Delta A_{i+1/2}}{2\hat{c}_{i+1/2}} \tag{4.8}$$

with $\Delta(\bullet)_{i+1/2}=(\bullet)_{i+1}-(\bullet)_i$

The eigenvalues of the Roe's matrix:

$$\hat{\lambda}^{1,2}_{i+1/2} = \hat{u}_{i+1/2} \pm \hat{c}_{i+1/2} \tag{4.9}$$

$$\hat{u}_{i+1/2} = \frac{Q_{i+1}/\sqrt{A_{i+1}} + Q_i/\sqrt{A_i}}{\sqrt{A_{i+1}} + \sqrt{A_i}}$$

$$\hat{c}^2_{i+1/2} = \begin{cases} g\dfrac{I_{P\,i+1} - I_{P\,i}}{A_{i+1} - A_i} & \text{if } A_{i+1} \neq A_i \\ \dfrac{g}{2}\left(\dfrac{A_i}{B_i} + \dfrac{A_{i+1}}{B_{i+1}}\right) = g\dfrac{A_i}{B_i} & \text{if } A_{i+1} = A_i;\ \dfrac{I_{P\,i+1} - I_{P\,i}}{A_{i+1} - A_i} < 0 \end{cases} \tag{4.10}$$

The eigenvectors:

$$\hat{R}^{1,2}_{i+1/2} = \begin{pmatrix} 1 \\ \hat{\lambda}^{1,2}_{i+1/2} \end{pmatrix} \tag{4.11}$$

To be consistent with Eq. 4.7, the source terms in Eq. 4.3 have to be discretized also in such a way that the conservation properties of the scheme are well satisfied. In Garcia-Navarro and Vazquez-Cendon (2000) it is shown that this can be best achieved by up-winding also the source terms. Eq. 4.5 now becomes:

$$U^{n+1} = U^n - \frac{\Delta t}{\Delta x}(F_{i+1/2} - F_{i-1/2}) + \frac{\Delta t}{\Delta x}[\frac{1}{2}(\psi_L)_{i-1/2} + \frac{1}{2}(\psi_R)_{i+1/2}] \tag{4.12}$$

$$\psi_L = \hat{\beta}\begin{pmatrix} s_1 - s_2 \\ \hat{\lambda}^1(1+s_1) - \hat{\lambda}^2(1+s_2) \end{pmatrix} \quad \psi_R = \hat{\beta}\begin{pmatrix} s_2 - s_1 \\ \hat{\lambda}^1(1-s_1) - \hat{\lambda}^2(1-s_2) \end{pmatrix} \tag{4.13}$$

with $s_k = sign(\hat{\lambda}^k)$ and $\hat{\beta}$ is a discretized source term coefficient.

$$\hat{\beta} = \frac{g\Delta x}{2\hat{c}}\overline{A}(\overline{S}_{bx} - \overline{S}_f) \tag{4.14}$$

in which $\overline{A}$, $\overline{S}_{bx}$, and $\overline{S}_f$ are the Roe averages at a computed cell.

Because the scheme is explicit, its stability is conditional according to:

$$CFL = \frac{\Delta t \lambda_{\max}}{\Delta x} < 1.0 \tag{4.15}$$

where CFL is the Courant number, $\lambda_{\max}$ is the maximum propagation speed of shock waves.

As argued by Garcia-Navarro and Vazquez-Cendon (2000), the numerical scheme presented so far is robust, satisfying the requirement posed earlier for the flow modelling.

Equation 4.12 is solved in time to model the overwash flow and the breach flow in Chapter 4 and Chapter 6 respectively. For this, the boundary conditions on both sides of the channel need to be specified. In principle, for the present situation, one condition, viz. time series of either the water level or the discharge, one at the upstream boundary and one at the downstream boundary are sufficient. In both cases of breaching and overwash, it is most practical to impose the time-varying water level at those boundaries. In the case of wave overwash (see Chapter 5) the upstream boundary water level is given by the overtopping level as output from the wave modelling. The present research adopts a characteristic variables-based approach of Burguete and Garcia-Navarro (2001) for the numerical treatment at the boundaries.

At a computational time step the channel cross-section is characterized by a representative width, which is specified in Section 4.3. It is noted that, in the case of the breach flow, additional source terms are added to the source term vector $S(x, U)$ in Eq. 4.2 to account for turbulence effects of the hydraulic jump. Consequently, the coefficient $\hat{\beta}$ in Eq. 4.14 is also modified. Source terms by infiltration through the bed are neglected in the case of wave overwash as it is assumed that prior natural processes such as rain, seepage and capillary effects due to a high water level, etc. have caused the barrier to be saturated.

4.3 GROWTH OF AN EROSIONAL CHANNEL

4.3.1 Preceding studies on the breach width increase

Various breach models have used different methods to determine the increase of the breach width, in which a relationship between the lateral erosion and the vertical erosion of the breach is established. This is either a geometrically-based or an empirically-based relation (see Section 2.3).

In breach growth in sand-dikes by Visser (1998) the lateral growth rate in the third and fourth (unobstructed base) stages is increased linearly relative to the vertical growth rate (Eq. 4.16). This relation is in fact based on a simple geometrical argu-

ment of the trapezoidal breach cross-section, assuming that breach deepening widens the breach:

$$\frac{dB_t}{dt} = -\frac{2}{\tan\gamma_1}\frac{dZ_b}{dt} \tag{4.16}$$

where Z_b is the level of the breach bottom that also controls the flow rate through the breach, B_t is the top width, γ_1 is the critical angle of the side slopes.

Kraus (2003) derived an analytical model of coastal barrier breaching, in which the breach evolves exponentially decaying from initial width and depth towards an equilibrium state. An idealized rectangular channel cross-section is presumed:

$$\frac{dB}{dt} = \frac{\alpha}{h}\left(1 - \frac{B}{B_e}\right) \qquad \alpha = \frac{Q_{s,\max}}{L} \tag{4.17}$$

$$\frac{dh}{dt} = \frac{\beta}{B}\left(1 - \frac{h}{h_e}\right) \qquad \beta = \frac{Q_{b,\ \max}}{L} \tag{4.18}$$

where B and h are width and depth of the breach channel, respectively. Notations with subscript $(_e)$ correspond to equilibrium values. $Q_{s,\max}$ and $Q_{b,\max}$ are constant maximum transport rates along the sides and the bottom of the breach, respectively. L is the length of the breach.

In conclusion, the above relations are either too simplistic (only based on a geometric factor, Eq. 4.16) or only qualitative (the equilibrium breach dimensions and the maximum net transport rates along the breach need to be known in advance, Eqs. 4.17 and 4.18) and are unsuitable for use in a process-based hydrodynamic model of breach growth. Moreover, the use of a breach width and a breach depth at a single specific location, e.g. at the middle of the breach, or assuming a constant width and a constant depth along the breach in the computation of breach growth is unrealistic.

In the following sub-sections a new process-based approach to modelling the morphological development of erosional channels is proposed which overcomes the drawbacks of existing semi-empirical models. The approach is efficient and can be easily incorporated in a hydrodynamic-based morphological model.

4.3.2 General equations for channel growth and volumetric channel width

Let us consider a channel (breach or overwash channel) through a homogeneous sand barrier. The channel has an instantaneous length L and an instantaneous trapezoidal cross-section at an arbitrary horizontal distance x as described in Fig. 4.2.

Bed level changes induced by currents are modelled by solving the conventional equation of mass conservation, in which space-and-time-varying sediment transport rates have to be known. When flow is confined in a channel with also erodible banks then changes in bed level and width must both appear in the bottom elevation equation as follows:

$$\frac{\partial Z_b}{\partial t} B_h - \frac{\partial B_h}{\partial t} h + \frac{1}{(1-p)} \frac{\partial (q_s B_d)}{\partial x} = 0 \tag{4.19}$$

with:

$$B_h = b + \frac{h}{\tan \gamma} \qquad B_d = b + \frac{d}{\tan \gamma} \tag{4.20}$$

in which Z_b is the channel bed level above a datum (see Fig. 4.2a), q_s is the instantaneous sediment transport rate through a unit width of the channel at the considered section, p is bed porosity, B_h and B_d are the depth-averaged widths over the channel depth (h) and water depth (d), respectively, b is the bottom width, γ is the side slope (see Fig. 4.2b).

It is worth mentioning that B_h, B_d, and b are the local channel widths at an arbitrary distance x. These widths are not constant and vary correspondingly to the variations of the bottom and the water depth along the channel. Hence, Eq. 4.19 is just a pointwise (local) equation and does not show the morphological development of the channel as a whole, particularly the increase in the channel width. However, in order to allow for a comparison with measurements we need to express the lateral growth through a nominal width, which is representative for the whole channel.

For this purpose, Eq. 4.19 is rewritten in the following form:

$$-\frac{\partial}{\partial t}(B_h h) + \frac{1}{(1-p)} \frac{\partial (q_s B_d)}{\partial x} = 0 \tag{4.21}$$

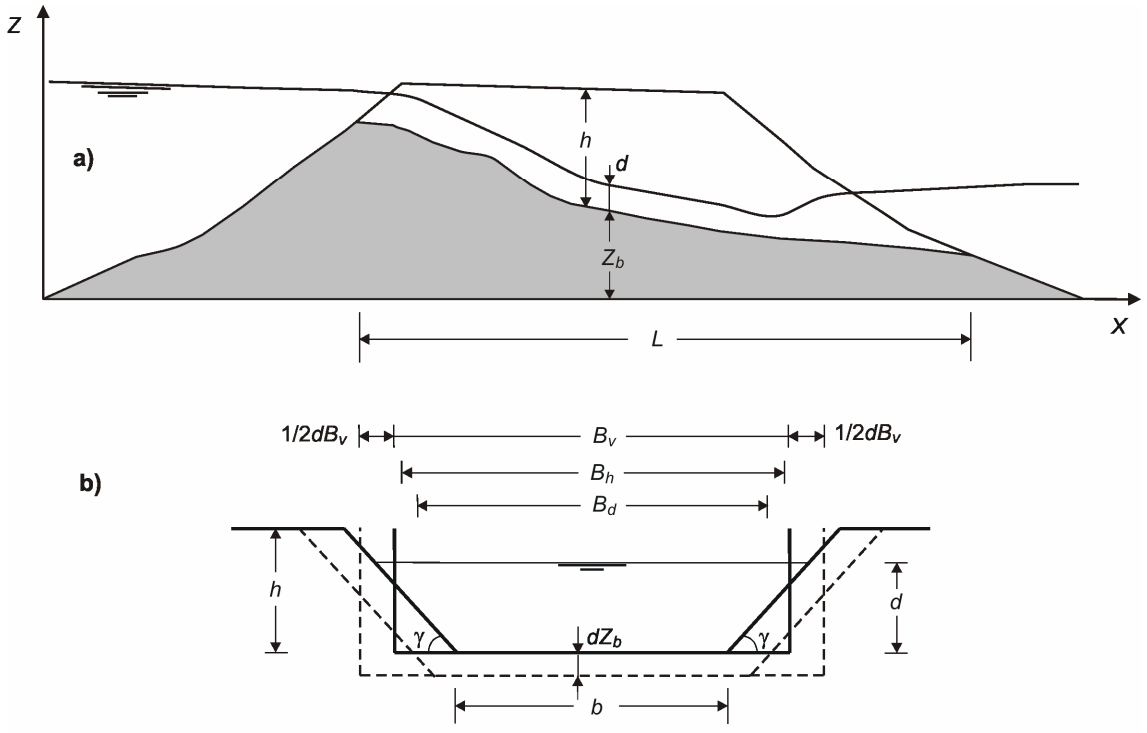

Figure 4.2 Definition sketch for an erosional channel in an overflow situation
a) channel longitudinal section b) arbitrary trapezoidal cross-section

where $\frac{\partial B_h}{\partial t} h dx = \frac{\partial (B_h h)}{\partial t} - \frac{\partial h}{\partial t} B_h$ and $\frac{\partial Z_b}{\partial t} B_h = -\frac{\partial h}{\partial t} B_h$ have been substituted.

Integration of Eq. 4.21 with respect to x over the channel length L reads:

$$-\frac{\partial}{\partial t} \int_L B_h h dx + \int_L \frac{1}{(1-p)} \frac{\partial (q_s B_d)}{\partial x} dx = 0 \tag{4.22}$$

where $\int_L \frac{\partial}{\partial t} (B_h h) dx = \frac{\partial}{\partial t} \int_L B_h h dx$ has been substituted, assuming that within a computational time step the increase of the channel length L is negligibly small compared to the increase of the channel cross-sectional area ($B_h h$).

We define a channel width:

$$B_v = \frac{\int_L B_h h dx}{\int_L h dx} = \frac{V_c}{\int_L h dx} \tag{4.23}$$

where V_c is the channel volume, B_v is a volume-averaged (or volumetric) width, which is used from now on as a representative width in describing the rate of lateral channel growth. B_v generally approximates B_h and equals B_h in case of uniform prismatic channels.

Insertion of Eq. 4.23 into Eq. 4.22 and dividing the equation with the channel length L yields the following general equation of channel growth:

$$\frac{\partial B_v}{\partial t} \frac{\int_L h dx}{L} - \frac{\int_L \frac{\partial Z_b}{\partial t} dx}{L} B_v = \frac{\frac{1}{(1-p)} \int_L \frac{\partial (q_s B_d)}{\partial x} dx}{L} \tag{4.24}$$

Equation 4.24 can be transformed to a more compact form by defining other new channel quantities as follows:

$$\frac{\partial B_v}{\partial t} h_L - \left(\frac{\partial Z_b}{\partial t} \right)_L B_v = \left(\frac{\partial A}{\partial t} \right)_L \tag{4.25}$$

where h_L, $\left(\frac{\partial Z_b}{\partial t} \right)_L$, and $\left(\frac{\partial A}{\partial t} \right)_L$ are the averaged quantities of the channel depth, the vertical growth rate, and the rate of change in cross-sectional area caused by erosion, respectively. They are defined as follows:

$$h_L = \frac{1}{L} \int_L h dx \tag{4.26}$$

$$\left(\frac{\partial Z_b}{\partial t} \right)_L = \frac{1}{L} \int_L \frac{\partial Z_b}{\partial t} dx \tag{4.27}$$

$$\left(\frac{\partial A}{\partial t}\right)_L = \frac{1}{L}\frac{1}{(1-p)}\int_L \frac{\partial(q_s B_d)}{\partial x}dx \tag{4.28}$$

It is noted that Eq. 4.24 or 4.25 is of the same form as Eq. 4.19 but now integrated over the whole channel.

4.3.3 Relationship between the vertical and lateral growth rates

Definition of the channel cross-sectional growth index

Providing that the instantaneous unit transport rate q_s is known at any computational section along the channel, Eq. 4.25 or 4.19 each still contain two unknown variables i.e. the channel growth rates in vertical and lateral directions. An additional equation is required to be resolved, which is available if we assume a relation between these two growth rates. Therefore, we introduce the channel growth index, which is defined as the ratio of the vertical to lateral growth rate as follows:

$$K_{vl} = \frac{-\left(\frac{\partial Z_b}{\partial t}\right)_L}{\frac{\partial B_v}{\partial t}} \tag{4.29}$$

where K_{vl} is the channel cross-sectional growth index.

Eq. 4.29 is valid for erosional channels only, i.e. as a whole $\left(\frac{\partial Z_b}{\partial t}\right)_L$ is always negative and $\frac{\partial B_v}{\partial t}$ is always positive.

Visser (1998) implicitly assumes a constant value of K_{vl} throughout the breach erosion process as can be deduced from Eq. 4.16:

$$K_{vl} = \frac{-\frac{\partial Z_b}{\partial t}}{\frac{\partial B_h}{\partial t}} = \tan\gamma_1 \tag{4.30}$$

The analytical model by Kraus (2003) suggests a dependency of K_{vl} on both the instantaneous and equilibrium channel geometries (width and depth), and on the constant maximum transport rates through the breach (see Eqs. 4.17 and 4.18).

$$K_{vl} = \frac{h}{B}\frac{Q_{b,\,\max}}{Q_{s,\,\max}}(1-\frac{h}{h_e})/(1-\frac{B}{B_e}) \tag{4.31}$$

Formulation of the cross-sectional growth index

Table B.1 shows the result of the measured cross-sectional growth index from the mobile-bed overwash experiment (see details in Chapter 5). It is noted that signifi-

cant variations of K_{vl} amongst tests and also within runs of one test are observed. Therefore, a constant growth index as determined by Eq. 4.30 seems doubtful since the channel cross-section changes its form noticeably during different stages of the breaching process. Although Eq. 4.31 can account for such variation, it is also inappropriate because additional unknown quantities need to be estimated empirically. However, Eq. 4.31 hints that K_{vl} could be a function of the instantaneous channel geometry and characteristics of the sediment transport through the channel. Hence, we adopt this suggestion and assume K_{vl} is a function of time.

If one assumes that the vertical and lateral growth rates originate from the net transport rates along the bottom and the sides of the channel, respectively, then Eq. 4.24 can be split up into two separate equations:

$$-\left(\frac{\partial Z_b}{\partial t}\right)_L B_v = \frac{\dfrac{1}{(1-p)}\displaystyle\int_L \frac{\partial Q_{s,b}}{\partial x}\,dx}{L} \tag{4.32a}$$

$$\frac{\partial B_v}{\partial t} h_L = \frac{\dfrac{1}{(1-p)}\displaystyle\int_L \frac{\partial Q_{s,s}}{\partial x}\,dx}{L} \tag{4.32b}$$

in which $Q_{s,b}$ and $Q_{s,s}$ are instantaneous space-varying total transport rates along the bottom and the sides of the channel, respectively.

To avoid confusion, it should be noted that the lower-case q denotes the transport rate per a unit width while the upper-case Q is that already multiplied by a width through which sediment is transported.

The separation resulting in Eq. 4.32 is only meaningful in elaborating the growth index. To predict the channel development Eq. 4.24 is still required since the transport rate through the channel is always determined as cross-sectional integrated transport (including the transports both on the bottom and the sides).

The cross-sectional growth index can now be deduced from Eqs. 4.32:

$$K_{vl} = \frac{h_L}{B_v} \frac{\displaystyle\int_L \frac{\partial Q_{s,b}}{\partial x}\,dx}{\displaystyle\int_L \frac{\partial Q_{s,s}}{\partial x}\,dx} = \frac{h_L}{B_v} \frac{Q_{s,bL} - Q_{s,b0}}{Q_{s,sL} - Q_{s,s0}} \tag{4.33}$$

where notations with subscripts $(_0)$ and $(_L)$ denote values at the beginning and end of the channel, respectively.

It is assumed that the pre-entrained sediment content (before entering the channel) is negligibly small compared to the transport in the channel. Also, it is shown in Visser (1998) that the largest transport rate is likely to occur at the end of erosional channels (if the sediment adaptation length is larger than the channel length, which is always the case for Dutch dikes). Therefore, Eq. 4.33 can be redefined as below:

$$K_{vl} \cong \frac{h_L}{B_v}\frac{Q_{s,bL}}{Q_{s,sL}} = \frac{h_L}{B_v}\frac{Q_{s,b\max}}{Q_{s,s\max}} \tag{4.34}$$

in which $Q_{s,b\max}$ and $Q_{s,s\max}$ are instantaneous maximum total transport rates along the bottom and sides of the channel, respectively.

The term $\dfrac{Q_{s,b\max}}{Q_{s,s\max}}$ in Eq. 4.34, and so K_{vl}, generally expresses the ratio of sediment transport potential between that on the bottom and on the sides concurrently induced by a flow. Therefore, the determination of the growth index K_{vl} comes down to investigating this ratio in terms of transport capacity.

Considering the total transport load the bed shear stress and the initiation of motion are the major factors that determine the transport capacities along the bottom and along the sides. To develop an expression for the growth index, the total transport rate q_s is determined following a general power-law form (see Nielsen, 1992, Sections 2.3, 2.4):

$$q_s = M(\tau_b - \tau_{b,cr})^n \tag{4.35}$$

where n is a dimensionless transport exponent of the order of 1.5, M is a dimensional transport coefficient, τ_b and $\tau_{b,cr}$ are bed shear stress and critical bed shear stress, respectively.

$$\tau_b = \rho g h I \approx \rho g h \tan\beta \tag{4.36}$$

$$\tau_{b,cr} = \theta_{cr}\rho g(s-1)d_{50} \tag{4.37}$$

in which h is a water depth, θ_{cr} is a critical Shields parameter, I is the surface gradient which approaches the bed slope $\tan\beta$ at the end of the channel, d_{50} is the median diameter of sediment, s is specific density.

Assuming conservation of the net sediment transport volume between the trapezoidal cross-section (bottom width b, side slope $\tan\gamma$, and depth h) and the equivalent rectangular cross-section (representative width B_v, and depth h), the sum of the transport rates along the bottom and sides of the channel reads:

$$Q_B = Q_s + Q_b \tag{4.38}$$

where Q_s, Q_b, and Q_B are the transport rates along the sides, the bottom channel width b, and the representative width B_v, respectively.

From Eq. 4.36 and assuming a linear distribution of the bed shear stress from the water surface ($z = h_L$) to the bottom ($z = 0$), the shear stress at an arbitrary level z above the bed reads:

$$\tau_b = \rho g(h_L - z)\tan\beta \tag{4.39}$$

To facilitate the elaboration we use intermediary variables so that the critical bed shear stresses (in Eq. 4.35) at the sides of the channel can be expressed also through Eq. 4.39. Equalizing between Eq. 4.39 and Eq. 4.37 we derive the following nominal parameters:

$$Z_{cr,b} = h_L - k_\beta \theta_{cr,0}(s-1)d_{50} / \tan\beta \tag{4.40a}$$

$$Z_{cr,s} = h_L - k_\beta k_\gamma \theta_{cr,0}(s-1)d_{50} / \tan\beta \tag{4.40b}$$

in which $Z_{cr,b}$ and $Z_{cr,s}$ are nominal critical heights determined according to the critical bed shear stresses at the bottom and at the sides, respectively, k_β and k_γ are factors accounting for effects of the longitudinal (β) and transverse (γ) slopes on the critical Shields parameter, respectively, and $\theta_{cr,0}$ is the critical Shields parameter on a horizontal bed (see Van Rijn, 1993).

$$k_\beta = \frac{\sin(\phi-\beta)}{\sin\phi} \tag{4.41a}$$

$$k_\gamma = \cos\gamma\left(1-\frac{\tan^2\gamma}{\tan^2\phi}\right)^{0.5} \tag{4.41b}$$

with γ is the slope angle of the sides, ϕ is sediment angle of repose.

Using Eqs. 4.35 and 4.40, the total transport rate Q_B through the channel with the representative width B_v and the depth h_L is:

$$\begin{aligned} Q_B &= M\left(\rho g h_L \tan\beta - \rho g(h_L - Z_{cr,b})\tan\beta\right)^n B_v \\ &= M(\rho g \tan\beta Z_{cr,b})^n B_v \end{aligned} \tag{4.42}$$

Similarly, the transport rate along the two sides of the channel Q_s is as follows:

$$\begin{aligned} Q_s &= 2M\int_0^{h_L}\left(\rho g(h_L - z)\tan\beta - \rho g(h_L - Z_{cr,s})\tan\beta\right)^n \frac{dz}{\sin\gamma} \\ &= 2M(\rho g\tan\beta)^n \frac{1}{\sin\gamma}\int_0^{Z_{cr,s}}(Z_{cr,s}-z)^n dz \end{aligned}$$

$$Q_s = \frac{2M}{n+1}(\rho g\tan\beta)^n \frac{1}{\sin\gamma} Z_{cr,s}^{n+1} \tag{4.43}$$

The ratio of the transport potential of the bottom to the sides $Q_{s,b} / Q_{s,s}$ reads:

$$\frac{Q_{s,b}}{Q_{s,s}} = \frac{(Q_b / b)B_v}{\dfrac{Q_s}{(2h_L / \sin\gamma)}2h_L} = \frac{B_v}{b}\frac{(Q_B - Q_s)}{Q_s \sin\gamma} \tag{4.44}$$

in which the relation $Q_b = Q_B - Q_s$ according to Eq. 4.38 has been substituted.

Insertion of Eqs. 4.42 and 4.43 into Eq. 4.44 and taking $b \approx B_v - h_L / \tan\gamma$ yields:

$$\frac{Q_{s,b}}{\mathrm{Q_{s,s}}} = \frac{1}{2}[(n+1)\frac{B_v}{Z_{cr,s}}\left(\frac{Z_{cr,b}}{Z_{cr,s}}\right)^n - \frac{2}{\sin\gamma}]\frac{B_v}{B_v - h_L / \tan\gamma} \tag{4.45}$$

It follows from substitution of Eq. 4.45 into Eq. 4.34 that:

$$K_{vl} \cong \frac{h_L}{B_v}\frac{Q_{s,b}}{\mathrm{Q_{s,s}}} = [(n+1)\frac{B_v}{Z_{cr,s}}\left(\frac{Z_{cr,b}}{Z_{cr,s}}\right)^n - \frac{2}{\sin\gamma}]\frac{h_L}{B_v - h_L / \tan\gamma} \tag{4.46}$$

Alternatively, we can express K_{vl} by the following equation:

$$K_{vl} = a_1[(n+1)\frac{B_v}{Z_{cr,s}}\left(\frac{Z_{cr,b}}{Z_{cr,s}}\right)^n - \frac{2}{\sin\gamma}]\frac{h_L}{B_v - h_L / \tan\gamma} + a_2 \tag{4.47}$$

where a_1 and a_2 are dimensionless coefficients to be calibrated.

By definition, the coefficient a_1 should be in the order of unity ($a_1 = 1$). Mathematically, a_2 can be determined based on a known state. In the present study, channel growth induced by a flow (breach or overwash) starts with an initial (pilot) channel. Hence, the coefficient a_2 can somehow be connected to this initial state of channel growth. In an overflow situation at the very beginning the flow width is always much wider then the flow depth, viz. the initial channel is very flat, so $B_{v0} >> h_{L0}$, $\sin\gamma \approx 1$, and $Z_{cr,s} = Z_{cr,b} = h_{L0}$. Moreover, by the nature of the flow the growth index has a monotonous increase in the early periods (see Table B.1). Therefore, it is plausible to assume that $K_{vl} \approx 0$ (no cross-sectional growth) at the start of the process.

From the above argument, it can be deduced from Eq. 4.47 that $a_2 \cong -(n+1)$.

Calibration of the growth index

In the following we use laboratory data of the channel morphological development to calibrate the two coefficients in Eq. 4.47. Selection of a suitable value of the transport exponent n for the two specific cases of erosional channel in the present study, i.e. overwash and breach channels, is also discussed.

The high resolution 3D topographic data of the channel development during overwash tests (Figs. B.1 through B.5 of Appendix B) allow for an accurate measurement of the growth index according to Eqs. 4.23, 4.27, and 4.29 (see also Table B.1 and Section 5.3). Regression analysis for Eq. 4.47 using the measurement of the growth index with some common values of the transport exponent n = 1.50, 1.65, 1.73, and 2.0 (1.73 corresponds to the best fit) indicates $a_1 = 1.0$ and $a_2 = -(n+1)$ are indeed theoretically correct. The comparison of the calculated growth index with that measured in the overwash experiment is shown in Fig. 4.3.

Hence, Eq. 4.47 becomes:

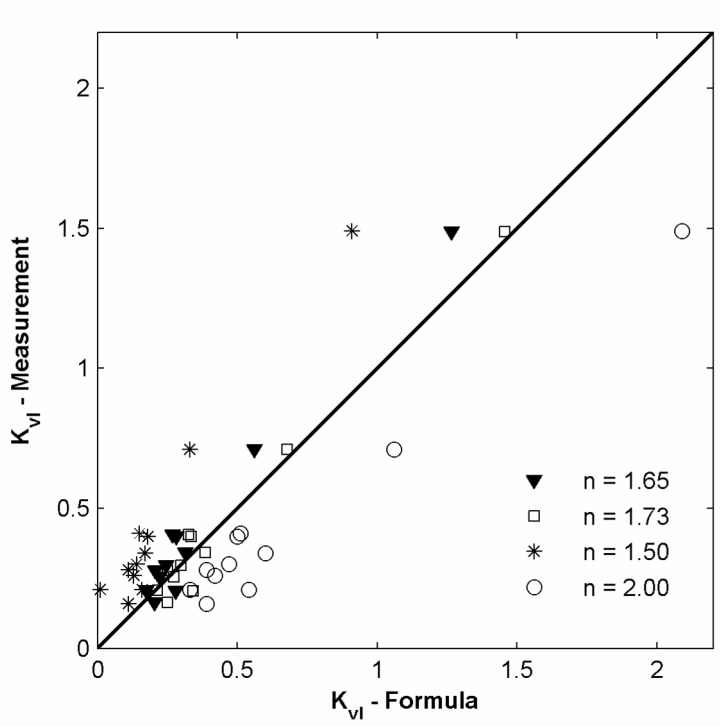

Figure 4.3 Growth index for overwash channels: measured versus calculated

$$K_{vl} = [(n+1)\frac{B_v}{Z_{cr,s}}\left(\frac{Z_{cr,b}}{Z_{cr,s}}\right)^n - \frac{2}{\sin\gamma}]\frac{h_L}{B_v - h_L/\tan\gamma} - (n+1) \tag{4.48}$$

In steep bed channels when $Z_{cr,b} \approx Z_{cr,s} \approx h_L$ (see Eqs. 4.40), Eq. 4.48 reduces to:

$$\begin{aligned} K_{vl} &= [(n+1)\frac{B_v}{h_L} - \frac{2}{\sin\gamma}]\frac{h_L}{B_v - h_L/\tan\gamma} - (n+1) \\ &= \frac{1}{\frac{B_v}{h_L}\tan\gamma - 1}\left((n+1) - \frac{2}{\cos\gamma}\right) \end{aligned} \tag{4.49}$$

It is worth mentioning that the transport exponent n in Eq. 4.48 or 4.49 is an empirical constant, whose value has been used variously amongst transport formulae (see e.g. Meyer-Peter and Muller, 1948; Nielsen, 1992; Ribberink, 1998). Therefore, it is logical to consider also this exponent in the calibration of the channel growth index.

To investigate the validity of the above finding for overwash channels to the case of breach channels, the small-scale dike breach data of Caan (1996) are used. Figure 4.4 plots the breach profile development during the last two stages of the breaching process (breaching stages according to Visser, 1998). The corresponding breach top widths are given in Table 4.1. The breach data of the first three stages (up to the breach time t = 135 s) are disregarded since the measurement of the lateral breach growth was not considered in the experiment for this period (see Chapter 6 for more details on this issue). Bearing in mind that the breach widths given in Table 4.1 were measured at a single section and are not the representative channel width we need. Also,

there was no 3D topographic measurement of the breach development in detail. To resolve this, a reasonable approximation of the representative width is given below:

$$B_v = B_t - \frac{h_L}{\tan\gamma} \tag{4.50}$$

where B_t is the top width of the breach channel with a trapezoidal cross-section, the side slope angle $\gamma = 32^o$ (according to Visser, 1998).

Following the same procedure as is done previously for the overwash channels, the determination of the growth index (measured and calculated) for the breaching case is summarized in Table 4.1. It follows that the calculated values show a monotonous decay over time of the growth index whilst this tendency is not clear from the measurements. This can be explained by the uncertainty in determining breach parameters during the experiment as mentioned earlier. However, good agreement between the prediction and the experimental data is found for the averaged values over the considered breach period (relative short period of 200 s) of the growth index, particularly for n = 1.65. Figure 4.5 describes the effect of the transport exponent on the accuracy of the prediction for the growth index, which also shows that a reasonable agreement can be achieved with $n = 1.65$.

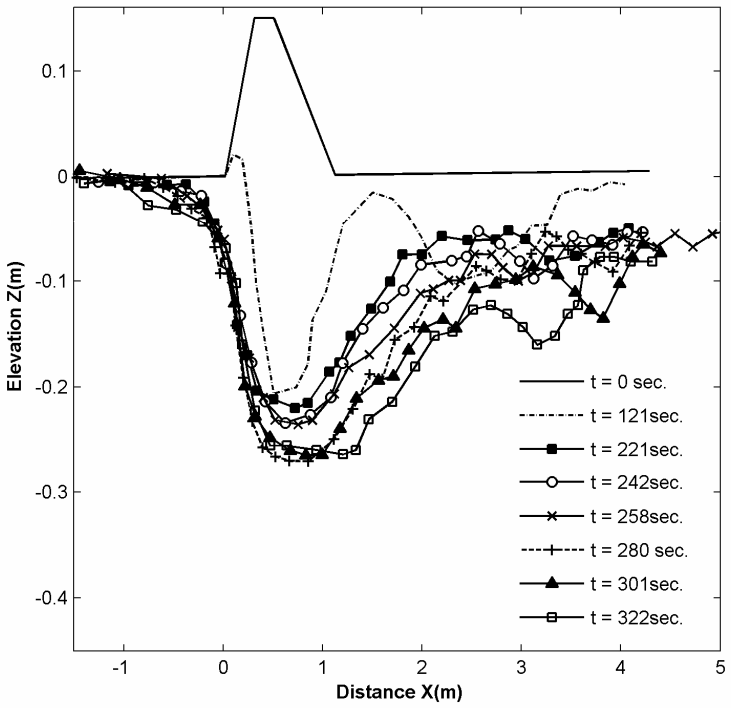

Figure 4.4 Vertical breach growth of the Caan's (1996) laboratory dike breach experiment

Table 4.1 The growth index determined according to the breach data of Caan (1996)

Breach time (sec.)	B_t (m)	h_L (m)	B_v (m)	Calculated K_{vl} with exponents n				K_{vl} Measured
				1.5	**1.65**	**1.73**	**2.0**	
0	0.200	0.030	0.200					
121	0.260	0.073	0.260					
221	0.700	0.109	0.525	0.084	0.172	0.220	0.379	0.1386
242	0.960	0.117	0.773	0.055	0.113	0.144	0.248	0.0295
258	1.090	0.124	0.891	0.043	0.088	0.112	0.194	0.0658
280	1.200	0.141	0.974	0.042	0.086	0.110	0.189	0.2032
301	1.400	0.151	1.158	0.040	0.082	0.104	0.180	0.0538
322	1.580	0.162	1.320	0.036	0.074	0.094	0.163	0.0694
Averaged				**0.050**	**0.103**	**0.131**	**0.226**	**0.093**

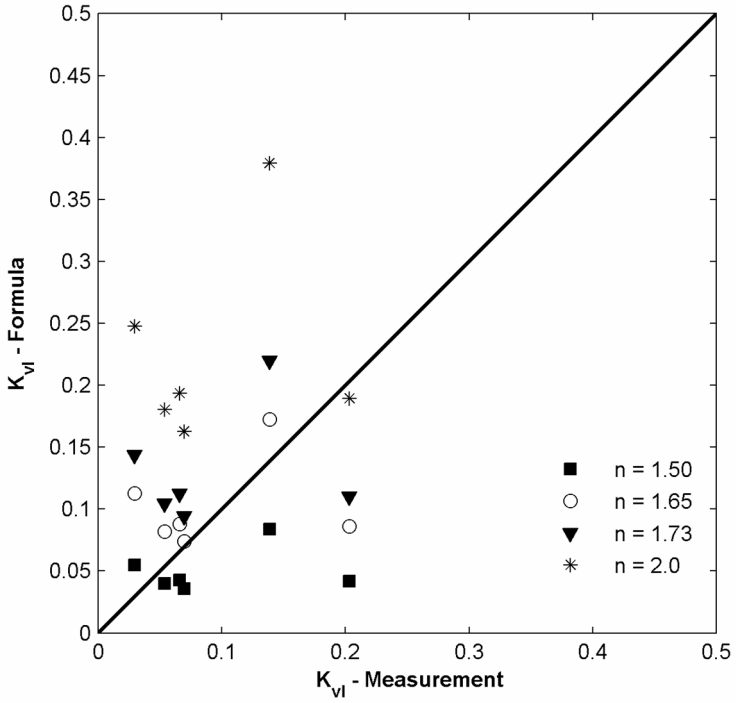

Figure 4.5 Growth index for breach channels: measured versus calculated

Discussion

By definition, $K_{vl} \geq 0$ does not mean a channel is eroding everywhere, instead it can be sedimentating locally but is eroded as a whole. Because of this non-negativity property of the growth index in erosional channels, one can deduce from Eq. 4.49 that:

or

$$\cos\gamma \geq \frac{2}{n+1}$$
$$\tan\gamma \leq \frac{1}{2}\sqrt{(n-1)(n+3)} \tag{4.51}$$

The above condition also means Eq. 4.49 is valid only if $\tan\gamma \leq 0.89$ or $\gamma \leq 41^{o}$ with $n = 1.65$. Therefore, the formulation of the growth index, viz. Eq. 4.48 or 4.49, is generally valid for sand channels since their side slopes are about the natural repose angle of sediment ($\gamma < 35^{o}$).

Some understanding of the channel morphological development can be drawn from the magnitude as well as the variation of the growth index. Regarding breach growth, Table 4.1 indicates that the growth index is relatively small and gradually decreasing during the last stages of breaching due to overflow, which corresponds to a low rate of the vertical growth and in contrast, a high rate of the lateral growth in this period. In a qualitative sense, this interpretation of the growth index for the considered breaching case is in agreement with the description of the five-stage breach erosion process by Visser (1998). A somewhat different evolution for overwash channels can be understood from the growth index in this case (see Table B.1). During the last period of an overwash event, as the barrier crest gets lower and lower, the overwash flow tends to be more and more intensive. This contradicts with the breaching case, in which the breach flow tends to neutralize near the end. As a result, overwash channels continue to grow vigorously in both lateral and vertical directions even during the last period of the overwash process (until water starts to overflow the crest).

Interesting implications for the channel growth in general can also be deduced from Eq. 4.49 in that, apart from the power of transporting sediment (exponent n), geometric factors considerably affect how the channel grows, e.g. a flatter cross-section (large B_v/h_L) tends to have a stronger lateral growth and vice versa. Equally, a cross-section of steeper side slopes (a larger $\tan\gamma$ makes smaller $\cos\gamma$) also slows down the vertical growth as can be explained physically by bank avalanching feeding extra sediment into the flow.

4.3.4 Numerical discretization and procedure

The channel growth equations (Eqs. 4.19 and 4.25) together with the expressions for the growth index derived so far (Eqs. 4.29 and 4.48 or 4.49) enclose a system of equations which can be solved to describe the time-dependent channel morphological development.

Substitution of Eq. 4.29 into Eq. 4.25 yields the following equation describing the increase of channel width B_v:

$$\left(h_L + K_{vl}B_v\right)\frac{\partial B_v}{\partial t} = \left(\frac{\partial A}{\partial t}\right)_L \tag{4.52}$$

Because it is assumed that the net transport volume of sediment is conserved between two cross-sections (see Eq. 4.38), the time-dependent increase in the cross-sectional

area of the channel, i.e. the right hand side of Eq. 4.52, can be calculated as follows (instead of its original expression by Eq. 4.28):

$$\Delta A_L = \frac{\frac{1}{(1-p)} B_v \int_L \frac{\partial q_s}{\partial x} dx}{L} = \frac{1}{(1-p)} \frac{B_v}{L} (q_{s,L} - q_{s,0}) = \frac{1}{(1-p)} \frac{B_v}{L} q_s^* \tag{4.53}$$

where $q_{s,0}$ and $q_{s,L}$ are the sediment transport rates per unit width at the beginning and the end of the channel, respectively, $q_s^* = (q_{s,L} - q_{s,0})$ is the net transport rate over the channel.

Eq. 4.52 now can be rewritten as:

$$\left(h_L + K_{vl} B_v\right) \frac{\partial B_v}{\partial t} - \frac{1}{(1-p)} \frac{q_s^*}{L} B_v = 0 \tag{4.54}$$

Since the growth index K_{vl} is fully determined using Eq. 4.46 or 4.47, the above equation is a genuine partial differential equation with respect to the variable B_v, which can be solved numerically using an explicit scheme:

$$B_v(t_j + \Delta t) = B_v(t_j) + \frac{\Delta t}{(1-p)} \frac{B_v(t_j)}{h_L(t_j) + K_{vl}(t_j) B_v(t_j)} \frac{q_s^*(t_j)}{L(t_j)} \tag{4.55}$$

where t_j is a previous time level, Δt is a computational time step.

To start the computation with Eq. 4.55, one needs to know the initial dimensions of the channel (B_v and h_L at t = 0).

Updating of the bed level (at $t_j + \Delta t$) at a computed node is done using Eq. 4.21:

$$-\frac{\partial}{\partial t}(B_h h) + \frac{1}{(1-p)} \frac{\partial (q_s B_d)}{\partial x} = 0 \tag{4.21}$$

where B_h and B_d can be calculated via the use of the representative width B_v:

$$\begin{aligned} B_h &= B_v - \frac{1}{\tan \gamma}(h_L - h) \\ B_d &= B_v - \frac{1}{\tan \gamma}(h_L - d) \end{aligned} \tag{4.56}$$

A discretized form of Eq. 4.21 is as follows:

$$\begin{aligned} \langle B_h h \rangle (x_i, t_j + \Delta t) = \langle B_h h \rangle (x_i, t_j) \\ + \frac{1}{2(1-p)} \frac{\Delta t}{\Delta x} \left(\langle q_s B_d \rangle (x_{i+1}, t_j) - \langle q_s B_d \rangle (x_{i-1}, t_j) \right) \end{aligned} \tag{4.57}$$

Consequently, the new bed level at a computed node i is:

$$Z_b(x_i, t + \Delta t) = Z_b(x_i, t) + h(x_i, t) - h(x_i, t + \Delta t) \tag{4.58}$$

It is noted that in case that the channel is sufficiently wide $B_d \approx B_h \approx B_v$, then Eq. 4.21 and so Eq. 4.57 reduce to the conventional equation of mass conservation for the bed level only (the Exner equation):

$$Z_b(x_i, t_j + \Delta t) = Z_b(x_i, t_j) - \frac{1}{2(1-p)} \frac{\Delta t}{\Delta x} \big(q_s(x_{i+1}, t_j) - q_s(x_{i-1}, t_j) \big) \tag{4.59}$$

Equation 4.59 can be used in cases when only the bed profile is considered. For instance, in the computation of wave overwash if the initial dimensions of a potential channel are not known in advance and the response of the barrier profile needs to be known to assess the barrier breaching potential. The geometric condition for which an overwash channel is considered wide is discussed in Chapter 5.

To avoid abrupt transitions of the bed profile, a numerical smoothing procedure is applied to the newly updated nodes in Eqs. 4.57 and 4.58 (see e.g. Horikawa, 1988 and Steetzel, 1993):

$$Z_b(x_i, t + \Delta t) = Z_b(x_i, t + \Delta t) + \frac{1}{2} \psi \big[Z_b(x_{i+1}, t) - 2Z_b(x_i, t) + Z_b(x_{i-1}, t) \big] \tag{4.60}$$

where ψ is a numerical smoothing factor that depends implicitly on the rate of bed level changes. This factor is in the range of 0.01 ~ 0.05 and should be determined from trial computations.

Prior to the above bed smoothing procedure, additional smoothing techniques might be required in some cases to handle sudden changes of the sediment transport rate at transitional areas such as at the boundary of a hydraulic jump in the breach channel (see Chapter 6).

4.4 SUMMARY AND CONCLUSIONS

As hinted at in Chapter 2 the modelling of the morphological development of erosional channels induced by overflow such as the breach growth in sand barriers needs to be done according to a hydrodynamic approach, in which both the lateral and vertical channel growth are simulated. However, three-dimensional morphodynamic modelling of this phenomenal process requires lots of efforts and is computationally expensive. This is why, in this chapter, a new process-based approach for modelling the growth of erosional channels induced by overflow is introduced. The developed approach is used later on for modelling both the overwash development across a coastal sand barrier (see Chapter 5) and then the breach growth in that barrier (see Chapter 6). The goal is to model this morphological process in a more efficient way, i.e. computationally inexpensive but sufficiently reliable.

The flow modeling is based on the shallow water equations, which can be solved using any robust upwind numerical scheme such as the first-order Riemann approximation by Roe (1981) to resolve numerical difficulties arising from complex flow conditions. For the computation of the channel growth in both vertical and lateral directions, a set of closed equations has been derived in connection with several new morphologic

parameters such as the representative channel width and the channel cross-sectional growth index. To this end, it is assumed that the channel expansions in vertical and lateral directions originate from the net sediment transport rates along the bottom and the sides of the channel respectively. The growth index is defined as the ratio of the vertical growth rate to the lateral one and is found to depend mainly on the instantaneous channel geometry and the sediment transport exponent. The parameter has been calibrated with existing experimental data of breach growth and of overwash channel development.

In conclusion, the new approach allows for an efficient process-based computation of the channel growth in both vertical and lateral directions. The approach is reliable and suitable for incorporating in 1D/2DV morphodynamic models of channel growth. Implications on the general tendency of channel growth induced by overflow have also been drawn out.

Chapter 5

RESPONSE OF LOW-CRESTED SAND BARRIERS DURING STORM SURGES: MOBILE-BED EXPERIMENTS AND NUMERICAL MODELLING*

5.1 INTRODUCTION

A relatively large number of post-storm field surveys on wave overwash has been reported in literature. These field observations provide a comprehensive qualitative description of overwash processes and washover morphologies. In some studies, the pre- and post cross-shore profiles in overwashed areas are also available. However, none of these field data contains a quantitative description of the hydraulic conditions of the associated events. Hence, they can not be used for quantitative investigation of the transport processes and corresponding morphological changes of barriers during overwash events. This is also the case for preceding laboratory studies on overwash, which have been rare so far and were mainly aiming at empirical descriptions of wave overwash (see also Donnelly et al., 2006).

Because of the above reasons and as a follow-up to the fixed-bed experiment in Chapter 3 the mobile-bed experiment presented in this chapter aims to increase understanding of the morphological development during overwash. Also, quantitative data of detailed morphology changes are used for the purpose of model calibration on the barrier response during storm surges.

This chapter is composed of two major parts in terms of content. The first part deals with the mobile overwash experiment. The development of the numerical morphological model for the barrier response is discussed in the second part.

* Excerpts from this chapter were published as: Tuan, T.Q. *et al.*, 2007a. Numerical modelling of wave overwash on low-crested sand barriers, in: *Proc. 30th Coastal Engineering Conference*, San Diego, USA, World Scientific.

The experimental set-up is described in Section 5.2. In Section 5.3 the experimental results are analyzed that lead to a quantitative description of the barrier response during overwash tests. A qualitative description of the processes of the barrier response during storm surges in general together with major overwash morphological features is given in Section 5.4. In Section 5.5, the findings of the two previous chapters are used to elaborate the numerical model for the response of low-crested sand barriers during storms. The model calibration and sensitivity analysis are carried out in Section 5.6 and Section 5.7 respectively. Finally, the chapter ends with a summary and conclusions drawn in Section 5.8.

5.2 EXPERIMENTAL SET-UP

5.2.1 Model scales

In order to model the barrier geometry and to translate the experimental findings to prototype conditions, we need to determine the model length and time scales. As usual, the Froude number and the sediment fall speed parameter similitude criteria are selected to satisfy as they are the major underlying physics behind the gravity-induced sediment transport processes (see e.g. Hughes, 1993). Also, it is customary to use the same sediment as is in nature and the model is geometrically undistorted. These lead to the following scale relations:

$$N_t = \sqrt{N_L} \tag{5.1}$$

$$N_\omega = \sqrt{N_L} \tag{5.2}$$

in which N_L, N_t, and N_ω are the length-scale, the morphological time-scale, and the sediment fall-speed-scale factors (prototype to model), respectively.

It is noted that the relations in Eqs. 5.1 and 5.2 are identical to those derived by Vellinga (1986) for the case of geometrically-undistorted models.

It follows from Eq. 5.2 that the model length scale should be selected in accordance with the sediment fall speed scale, which turns out to be dependent on the sand size used for the model and the given sand size in prototype.

The fall speed of sediment in the intermediate range can be calculated using the following formula (Van Rijn, 1993):

$$w_s = \frac{10\nu}{d_{50}}\left[\left(1 + 0.01\Delta g (d_{50})^3 \nu^{-2}\right)^{0.5} - 1\right] \qquad \text{for } 0.1\,\text{mm} < d_{50} < 1.0\,\text{mm} \tag{5.3}$$

where w_s is the sediment fall speed, ν is the molecular fluid viscosity, and Δ is the specific density of sediment ($\Delta = 1.65$).

As a guess on the model length scale, we take the prototype median diameter from sand samples collected at the Hue barrier site (Vietnam) $(d_{50})_p$ = 350 μm and the

model sand diameter $(d_{50})_{\mathrm{m}} = 125$ μm (see Fig. 5.1). Eq. 5.3 gives the sediment fall speeds $w_s = 5.2$ and 1.2 cm/s in prototype and in model, respectively. We yield from Eqs. 5.1 and 5.2 that $N_L \approx 20$ and $N_t = N_\omega \approx 4.45$.

5.2.2 Physical set-up

Four overwash tests of model sand barrier of various widths and crest levels were constructed in the long wave-sediment flume at Delft University of Technology. Fig. 5.2 depicts the layout of the experiment and the basic dimensions of the barrier. The barrier was built of fine quartz and narrow graded sand with a median diameter $d_{50} = 125$ μm and $d_{90} = 165$ μm (see also Fig.5.1). The barrier slopes were 1/10 on the seaside and from 1/6 to 1/5 on the bay (lagoon) side. A water-tight wall was installed in the barrier core, avoiding possible geotechnical failures due to seepage through the barrier. Also, a 12m long and 10 cm thick sand bed was placed in front of the barrier to mimic a more natural transition between the barrier and the flume bottom as if the barrier is resting on a foreshore in the field. A view of the barrier in place is presented in Fig. 5.3.

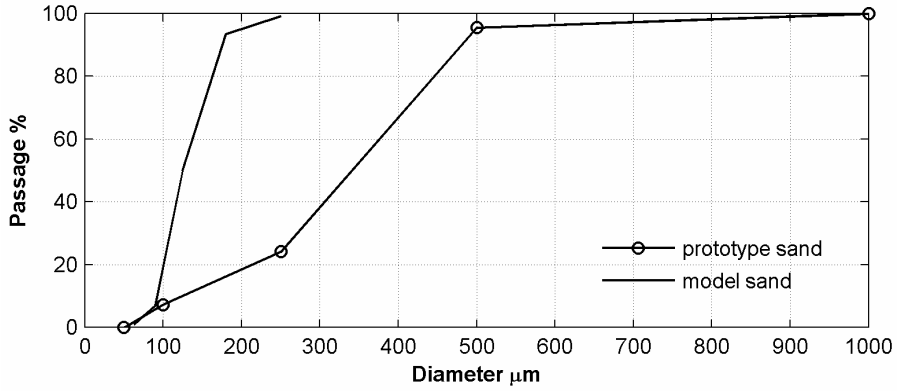

Figure 5.1 Grain size distributions of model and prototype sands

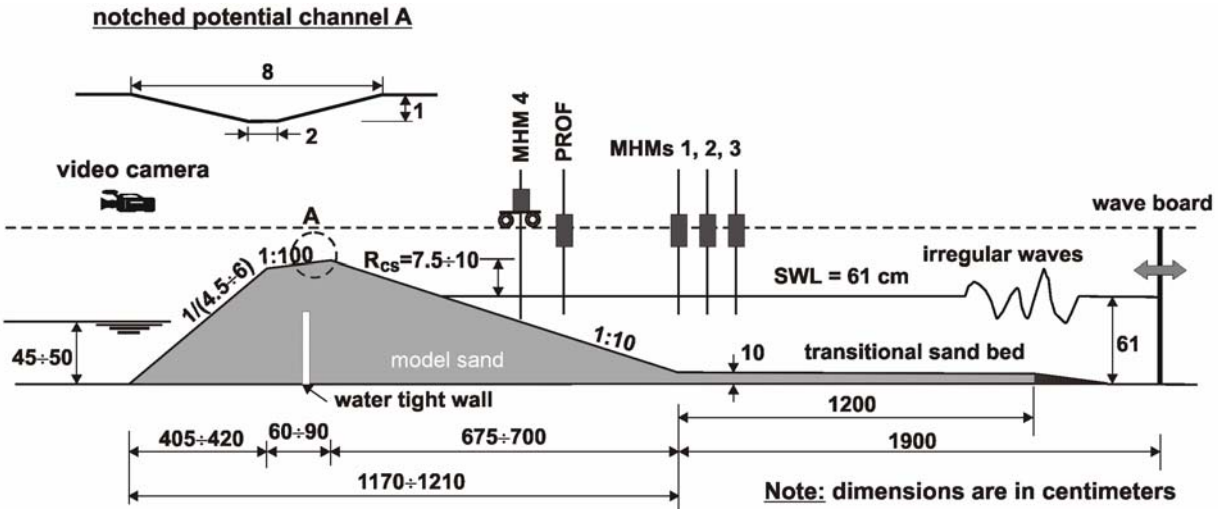

Figure 5.2 Experimental set-up of sand barriers under attack of irregular waves

Table 5.1 Overwash test program

Parameters			**OW1**	**OW2**	**OW3**	**OW4**
Barrier crest level		(cm)	70	75	72	71
Seaside slope		(-)	1/10	1/10	1/10	1/10
Bay side slope		(-)	1/6	1/6	1/6	1/4.5
Barrier crest width		(cm)	90	70	90	100
Sea water level		(cm)	61	61	61	61
Bay water level		(cm)	47	48	47	47
Incident wave H_{mo}		(cm)	13.5	14.0	14.0	12.0
Peak spectral period T_P		(sec.)	2.0	2.0	2.0	2.2
Number of morphology recordings		(-)	2	3	3	3
Morphology recording at	1	(min.)	10	20	15	16
	2	(min.)	20	30	25	30
	3	(min.)	-	45	37	39.5

Figure 5.3 The barrier in the wave flume looking towards the sea

Irregular waves of the standard JONSWAP spectra were employed in all the tests. Four concurrent wave gauges (WHM) were used to measure the incident wave at the sea-most boundary of the barrier and at the breaker line (the first three gauges were used to separate the incident wave from the imposed signal). The test wave parameters in association with the barrier geometry are specified in Table 5.1. The initial

barriers were low-crested relative to the wave heights at the toe (generally $R_{cs}/H_{mo,toe} \leq$ 1.0) to create conditions of moderate to severe overwash.

5.2.3 The preferred overwash channel and experiment assumptions

During pilot tests of planar back barrier surfaces it was observed that a system of several small channels appears in the early phase of overwash. However, the existence of this channel system is transient and there is always a tendency towards forming a main (preferred) channel, starting at the back slope of the barrier. The main channel is quickly formed and attracts most of the overtopping discharge. On hydrological grounds, the occurrence of this phenomenon is obvious as the overwash flow in the very early stage occurs as thin water sheets. The flow at this stage has the nature of an overland sheet flow, e.g. as occurs under surface runoff, forming rill and gully flows (see e.g. Hydrology handbook-ASCE, 1996 and Marshall *et al.*, 1996). In field conditions, a preferred channel can pre-exist as a result of previous overwash or simply a relatively depressed portion in a barrier. Hence, the initial process of overland flow forming a preferred channel is ephemeral and is irrelevant to the overwash process as a whole.

From the above arguments, it was decided to notch a preferred channel of 1 cm deep at the middle of the barrier from the beginning so as to have more controllable overwash (see Figs. 5.2 and 5.3, the dashed line indicates the channel position on the back slope). As discussed later, the present process-based approach of overwash modelling allows the width and depth of this initial channel to be arbitrary as these are amongst the input variables that affect the development of overwash afterwards. In the present experiment the initial channel dimensions were based on the visual observations from the pilot tests.

In summary, in order to experimentally investigate overwash in a wave flume the following assumptions should hold:

- The prior process forming the preferred channel is negligible. Hence, without loss of generality wave overwash is modelled starting with a pre-determined preferred channel.
- The morphology change due to overwash is symmetric with respect to the central line of the channel.

Furthermore, the test results are valid only if the channel lateral enlargement is not hampered by the flume, i.e. the channel final width must be smaller than the flume width. This means a test must stop as soon as the top edges of the channel banks get close enough to the flume walls. A safety margin of 10 cm on each side of the flume was therefore applied. Overwash is a relatively short-lasting process (due to runup only in the present context, see Subsection 2.2.2) and the channel width in the end can be small. So, this constraint on the flume width can be easily satisfied if a good combination of test parameters is chosen, i.e. of the barrier geometry, the model scales, and the hydraulic conditions.

5.2.4 Experimental procedure

Initially, the seaward part of the flume was filled up to a level of 61 cm above the flume bottom. The water level on the bay side was about 15 cm lower than that on the upstream side and was kept as constant as possible during the tests. Each test consists of several runs of 10 ~ 20 minutes that were determined at moments of noticeable morphological changes. Also, wave tests performed in the flume showed that a run duration of at least 10 minutes is required to assure adequate reproduction of the major frequency window. The flume on the sea side was refilled to the original water level after each run. A test is ended as soon as the barrier crest has lowered to and reached a safety margin (a few centimetres above the mean water level) so as to prevent an unintended breakthrough due to overflow.

After each run the morphological changes were measured using an electronic profile follower (PROF) mounted on a moving carriage. The PROF position across the flume width is adjustable. Calibration of the PROF was done before the measurement of each run. The seaward part of the barrier was profiled and averaged over three parallel lines: two near the side walls and one at the middle of the flume. As the morphology change on the crest and the back side of the barrier is more complex, detailed 3D topographic measurement was performed with a resolution of 0.2 cm/point along the flume and (2 ~ 5 cm)/point in the transverse direction.

After each test, the barrier was rebuilt and then saturated to promote self consolidation in combination with manual compaction. Samples were taken from various parts of the barrier to monitor the sand compaction. The sand porosity was kept consistent around 40 % in all the tests.

5.3 Experimental results

5.3.1 Morphological features

There are some typical morphological features observed from the experiment, which characterize the response of low-crested barriers during storm surges. Figure 5.4 depicts the response of a barrier with these features both in profile and in plan. These features are essential to the understanding of morphological processes of wave overwash as well as to the morphological modelling presented later.

1. The inland deposition delta (washover fan): the delta is formed around the inland water level by sediment deposition brought in from the upstream side. The sediment is diffusing, forming a fan-shaped delta. If dynamic loads on the bay side of the barrier are inconsiderable then the deposition of this delta is largely governed by the downstream water level.
2. The overwash channel: the channel is formed as a result of the erosion process induced by the overtopping flow. Erosion taking place along this channel largely contributes to the formation of the washover fan. The overwash channel plays a major role in the morphological processes of overwash. Starting from the back-

barrier slope, the channel gradually expands seawards and in the end takes over the barrier crest.

3. The transitional zone: this is a transitional location on the barrier crest where the overwash flow is critical and almost has no capacity of carrying sediment. The rate of bed changes is therefore rather low and the crest level remains nearly constant or sometimes even elevates until the collapse of this zone. This is also the most elevated area of the barrier. The sea-most edge of the crest, named the crest front hereinafter, acts as a sill that controls the input amount of wave overtopping. The transitional zone gradually shrinks down to a sharp crest front when the overwash channel expands seawards and meets the upstream crest boundary.
4. The seaward evolution: this part of the barrier morphology change is caused by the process of dune and beach erosion. However, due to frequent overwash, there is no dune scarp but a rather gentle beach face above the water line.

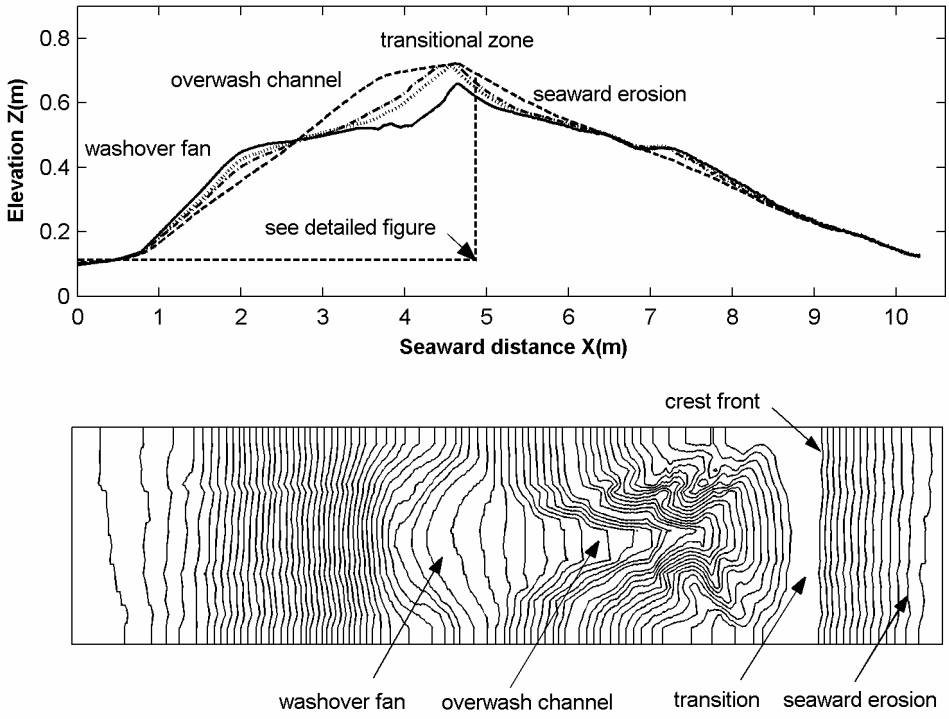

Figure 5.4 Major overwash morphological features

The crest front in the transitional zone plays an important role in the present model approach, providing a unique connection between the two across-shore transport processes, i.e. between dune and beach erosion and wave overwash.

5.3.2 Response of the barrier profile and growth of the overwash channel

In terms of breach initiation during a storm event, the response of a low-crested barrier can be sufficiently characterized through the response of the barrier profile and through the lateral enlargement of the overwash channel.

Figures B.1 through B.5 show the experimental results of the barrier response, shown both in plan and in profile, for all the tests from OW1 to OW4. It follows that the final channel width in all cases was within the safety margin and the lateral growth of the channels was rather symmetric. This confirms the validity of the experimental conditions chosen to satisfy the experiment assumptions mentioned above.

According to the approach described in Chapter 4, the overall channel lateral growth can be expressed via a representative channel width B_v. The detailed 3D topographic measurement allows the determination of this parameter according to Eq. 4.23 as follows.

$$B_v = \frac{V_c}{Lh_L} = \frac{V_{s0} - V_{sj}}{Lh_L} \tag{5.1}$$

where V_{s0} and V_{sj} are the initial volume and the volume at a measured time level j of the barrier back constrained by a fixed datum and the channel bed, respectively.

The channel average width h_L is calculated from Eq. 4.26 as:

$$h_L = \frac{1}{L}\sum_L h_i \Delta x_i \tag{5.2}$$

where h_i and Δx_i are discretized channel depth and space grid length at a calculated cell i, respectively.

For the purpose of modelling channel growth the cross-sectional growth index K_{vl} also needs to be measured, which follows from Eqs. 4.27 and 4.29:

$$K_{vl} = -\frac{(\Delta Z_b)_L}{\Delta B_v} = -\frac{\frac{1}{L}\sum_L \Delta Z_{bi}\Delta x_i}{B_v(j+1) - B_v(j)} = -\frac{1}{L}\frac{\sum_L [Z_b(i,j+1) - Z_b(i,j)]\Delta x_i}{B_v(j+1) - B_v(j)} \tag{5.3}$$

where *X(i, j)* stands for the value of X at a calculated cell i at a time level j.

The measured values of the channel geometry (width, depth), the growth index K_{vl}, and the average barrier crest level for different runs of all the test cases are given in Table B.1. The experimental results of all the tests are summarized in the following Table 5.2.

5.3.3 Sediment transport in wave overwash

Transport mode

In the present experiment, no intra-flow measurements such as of the bed boundary shear stress and the sediment concentration could be made allowing a deeper insight into the sediment transport processes in overwash (in fact it was technically too complicated to measure those parameters in such a very shallow flow, see also discussions in Chapter 3). However, it was observed during the fixed-bed (Chapter 3) and mobile-bed experiments that the overwash flow resembles a simple boundary layer flow

with virtually no turbulence-generating mechanism (sediment stirring). This is also supported by a PIV experimental study on wave overtopping of a trapezoidal structure by Stansby and Tong Feng (2004). Visual observation from the mobile experiment indicates sediment was transported in a dense layer above the bottom. Also, the channel bed was planar, which implies high-regime transport conditions (see Fig B.5).

From the above, it is rational to argue that sediment transport in wave overwash occurs under sheet flow conditions, in which bed load is the principal mode. It is also logical from the characteristics of the overwash flow that its shallowness and intermittence would hamper the processes of bringing sediment into suspension.

Table 5.2 Summary of the experimental results

Test	Run	V_c (m^3)	V_f (m^3)	B_v (m)	Q_{sw} ($10^{-6}\times m^3/s$)	h_L (m)	L (m)	$\overline{Z}_{crest}$ (m)	K_{vl} measured
OW1	t = 0’			0.050		0.010		0.700	
	t = 10’	0.0279	0.0543	0.242	44.0 (±6)	0.066	1.75	0.703	0.34
	t = 20’	0.0737	0.1199	0.319	33.0 (±6)	0.112	2.07	0.643	0.71
OW2	t = 0’			0.050		0.010		0.744	
	t = 20’	0.0051		0.188		0.038	0.71	0.748	0.28
	t = 30’	0.0131	0.0156	0.198	1.4 (±2)	0.040	1.65	0.745	0.16
	t = 45’	0.0296	0.0350	0.277	3.2 (±4.5)	0.064	1.67	0.725	0.30
OW3	t = 0’			0.050		0.010		0.721	
	t = 15’	0.0293	0.0361	0.298	7.6 (±4.5)	0.051	1.93	0.720	0.21
	t = 25’	0.0419	0.0580	0.334	15.5 (±6)	0.066	1.90	0.716	0.40
	t = 37’	0.0743	0.0904	0.362	7.0 (±5.5)	0.108	1.90	0.676	1.49
OW4	t = 0’			0.050		0.010		0.708	
	t = 16’	0.0261	0.0494	0.265	24.3 (±4)	0.055	1.790	0.718	0.26
	t = 30’	0.0496	0.0927	0.334	23.6 (±5)	0.083	1.790	0.704	0.41
	t = 39.5’	0.0758	0.1332	0.407	25.1 (±6)	0.098	1.900	0.656	0.21

Note: $\overline{Z}_{crest}$ is the average level of the crest front, (±•) indicates an estimate of the measurement errors.

Swash transport

In the response of low-crested barriers to wave attack, the swash-zone can be considered as the interface between two regions in which a different process dominates, viz. the process of dune and beach erosion and the overwash process. This area is therefore a transitional boundary in terms of the sediment transport for modelling overwash. Obviously, there is a difference in the swash transport between beaches without overwash and those with overwash, which is discussed in the following.

It is observed from the tests that a considerable amount of sediment is entrained in the up-rushing water before reaching the barrier crest. The landward intrusion of this sediment entrainment was observed via an elevated part of the bed in the transitional zone during the early period of overwash (sediment was brought in and was deposited due to weak transport capacity at this location). Examples are the first runs of the tests OW2 and OW4, as shown in Fig. B.5 or in Table 5.2 by the increase of the level of the crest front.

The still water basin on the bay side acts as a sand trap. Hence, the swash transport discharge through the barrier crest for each run of a test can be estimated based on the net of the accumulative volume between the washover fan and the channel as shown in Eq. 5.4. The results are given in Table 5.2.

$$Q_{sw} = \frac{V_f - V_c}{t_r} \tag{5.4}$$

where Q_{sw} is the average sediment discharge brought in by swash, V_c is the channel volume, V_f is the accumulative volume of the washover fan, t_r is the duration of a run.

A cross-comparison with the volume balance of the seaward part (the volume conservation across the whole barrier) was not possible because there is no detailed 3D-topographic measurement on this side and the volume estimate using the measured averaged cross-shore profiles is insufficiently accurate.

It should be noted that the determination of Q_{sw} based on the bathymetric measurement is not always quantitatively accurate. In the present experiment, the bed profile follower PROF, due to turbidity of the water, had a measurement error of ± 2mm according to calibration results. Consequently, the maximum errors in volume for V_f and V_c are 0.002×0.5×0.8 and 0.002×2.0×0.8 or ± 0.0008 and ± 0.0032 m^3, respectively (the maximum length for V_f is 0.5m and for V_c is 2.0 m). This also means that the maximum volume error for (V_f – V_c) is 0.004 m^3. In all, with a minimum run of 10 minutes, the swash sediment discharge measured according to Eq. 5.4 would have a maximum error of 6×10^{-6} m^3/s. Hence, of all the tests, Table 5.2 indicates that the measurement of Q_{sw} for test OW2 is quantitatively inaccurate.

Based on the visual observations and the measurements, it can be concluded that the sediment transport in the upper part of the swash zone is significant and landward-directed in the case of occurrence of wave overwash. This can be explained as follows. The swash transport over a wave cycle is the net result between the transport during up-rush and that during backwash. On high beaches without overwash, due to the domination of the backwash transport, the transport in the swash zone is usually seaward-directed, typically during storm conditions. In contrast, on overwash beaches, due to the crest shortage, a considerable amount of sediment brought over the crest during wave up-rush never returns during backwash. Moreover, in this case the beach crest is low, the backwash flow becomes weaker and thus the swash asymmetry is enhanced. As a result, in the near crest area of the swash zone the net transport rate is landward-directed.

5.4 RESPONSE OF LOW-CRESTED BARRIERS DURING STORM SURGES

Through analyzing the experimental results, the response of low-crested barriers during storm surges can clearly be distinguished in three successive morphological stages, namely the barrier narrowing, the transitional stage, and the crest lowering. In practice, depending on the hydraulic conditions and the barrier geometry, overwash processes can terminate at any of these stages. Descriptions of these stages are given in the following. The seaward profile response is not discussed in detail, but emphasis is placed on the back-barrier part.

It should be restated that wave overwash, in the present study, is considered to have ended as soon as the water level on either side of the barrier (sea or bay side) has exceeded the barrier crest. After this moment, the following process, with or without wave attack, is regarded as breaching principally driven by overflow.

At the first stage of the barrier response, the barrier profile is narrowed on both sides as a result of the two across-shore transport processes, i.e. dune and beach erosion on the seaward side and overwash on the bay side. Figure 5.5a depicts the evolution of this stage, in which the development of the overwash channel and the reduction of the barrier crest width are the major features. The channel grows both laterally and vertically. The channel cross-section is generally trapezoidal. As the side slopes become unstable, bank avalanching also occurs and is quickly washed away by the flow. Besides the increase in the cross-sectional area, the seaward expansion of the channel is also noticeable. Together with the landward retreat, this results in marked narrowing of the barrier profile along the channel axis. As aforementioned, the crest front in the transitional zone acts as a sill that controls the input amount of wave overtopping. At this stage, it migrates landwards as a result of the beach face erosion. Because of low transport capacity of the overwash flow in this area, the barrier crest shows little change in elevation. At the end of the stage, the transitional zone and so the barrier crest reduces to a sharp crest front as the seaward expansion of the channel meets the upstream boundary. The position of this sharp crest front on the profile depends upon the retreat rates on both sides of the barrier. However, it is generally situated more seawards because of a relatively fast seaward expansion of the overwash channel.

The crest front remains nearly unchanged both in position and level throughout the next, i.e. the transitional, stage (see Fig. 5.5b). Therefore, there is no significant change in the overtopping rate compared to the previous stage. Meanwhile the back-barrier slope becomes milder as the channel reaches the upstream boundary. Consequently, the channel growth appears to slow down. This transitional stage is relatively short-lasting and ends as the existing sharp crest front from the previous stage starts to displace.

At the last stage, i.e. the crest lowering (see Fig. 5.5c), the continuation of the vertical channel growth causes the crest front to progress seawards and in the meantime to decline markedly. Overtopping therefore becomes increasingly intensive and less intermittent. As a result, the overwash channel continues to grow sharply in both vertical and lateral directions. A considerable amount of suspended sediment entrained from the seaside enters the channel. This landward transport reduces the slope of the

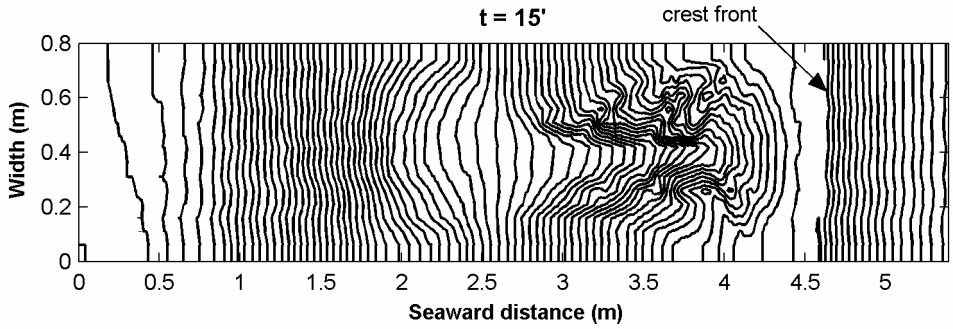

a) Stage 1 – Barrier narrowing: channel growth and reduction of crest width

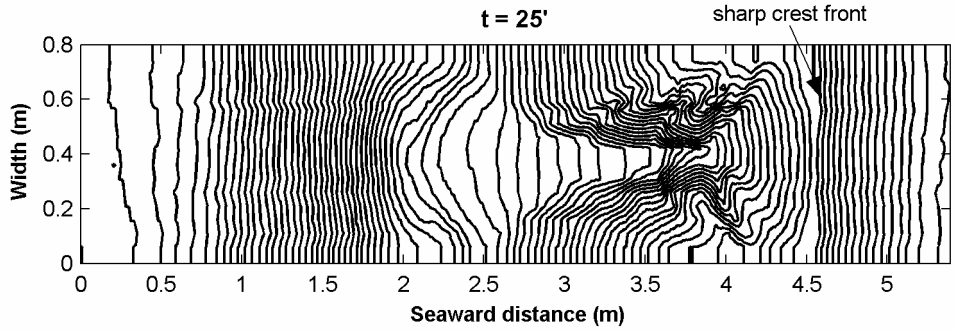

b) Stage 2 – Transitional: sharp crest front, slowdown of channel growth

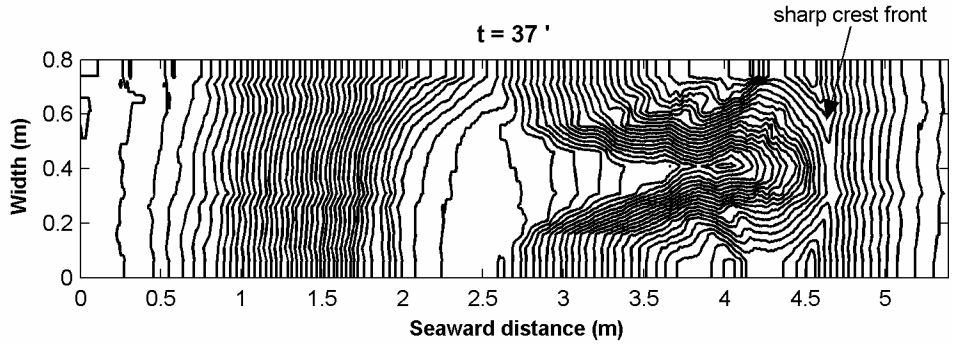

c) Stage 3 – Crest lowering: crest level reduction, continuation of channel growth

Figure 5.5 Stages of the response of low-crested barriers during storm surges (figures from the results of the test OW3)

beach face on the seaward barrier profile significantly. On the bay side, the channel bed slope also gets gentler, especially near the washover fan area. It is noted that the continuation of enlargement of the overwash channel even at the end of the stage is in contrast to the case of breaching due to overflow, in which the breach channel tends to evolve towards an equilibrium state due to gradual neutralization of the driving water head difference.

If the storm continues, the final stage still ends as the remaining crest front has receded to mean sea level. In other words, overwash eventually cuts through the barrier at mean sea level, creating a pilot (initial) breach channel. Right after this moment, overwash is immediately followed by the breaching process due to overflow through

the overwash-created channel. Wave attack, if continued, only plays a secondary role in this breach erosion process.

5.5 NUMERICAL MODELLING OF BARRIER RESPONSE DURING STORM SURGES

5.5.1 Modelling approach

On overwash beaches, the overall response of low-crested barriers during storm surges can be discriminated by two across-shore transport processes, i.e. dune and beach erosion on the seaward side and wave overwash on the landward side. Modelling of overwash relies heavily on the specification of wave overtopping as the hydraulic input from the seaside (see the problem schematization in Fig. 3.1). This overtopping input is determined according to the approach presented in Chapter 3, in which the hydraulic conditions and the seaward barrier geometry as output from the modelling of the process of dune and beach erosion are needed. In return, overwash imposes a significant landward sediment transport and thus alters the seaward barrier profile, specifically on the beach face area. This defers substantially from the case of high beach profiles where there is no or negligible transport in the landward direction. These two processes are therefore interrelated and must be convoluted in one single model.

Modelling of the seaward profile changes has been pursued intensely by many researchers (see Schoonees et al., 1995 for a review and cross-comparison). Since it is not the objective of the present research, as stated in Chapter 2, to further this work, the UNIBEST-TC model formulations (Bosboom et al., 2000) are selected for the incorporation of overwash. This selection is based on the criteria of validity and consistency with the modelling approach of overwash as well as the resource availability. Also, the UNIBEST-TC is considered the most complete in terms of the major cross-shore transport principles. Apart from the review of the model formulations presented in Chapter 2, additional detail relevant to the overwash modelling is given in the following.

5.5.2 UNIBEST-TC model for the seaward profile changes

The UNIBEST-TC model consists of five modules as shown below. Fig. 5.6 depicts an overview of their relations in the model.

- Wave propagation module
- Mean current profile module (undertow)
- Wave orbital velocity module
- Bed load and suspended load transport module
- Bed level change module

Detail of these modules can be found in Bosboom et al. (2000). In connection with the modelling of overwash, the wave propagation module and some aspects regarding the mass flux balance and the transport in the swash zone are briefly discussed as follows.

Across-shore wave decay

The wave conditions across a shore profile at a computed time step are solved primarily according to the equations of time-averaged wave energy balance proposed by Battjes and Janssen (1978). To improve the prediction of wave set-up, the surface roller model of Nairn (1990) is also incorporated. The basic equations are as follows.

$$\frac{\partial}{\partial x}(EC_g \cos\theta) = -D_w - D_f \tag{5.5}$$

$$E = \frac{1}{8}\rho g H_{rms}^2 \tag{5.6}$$

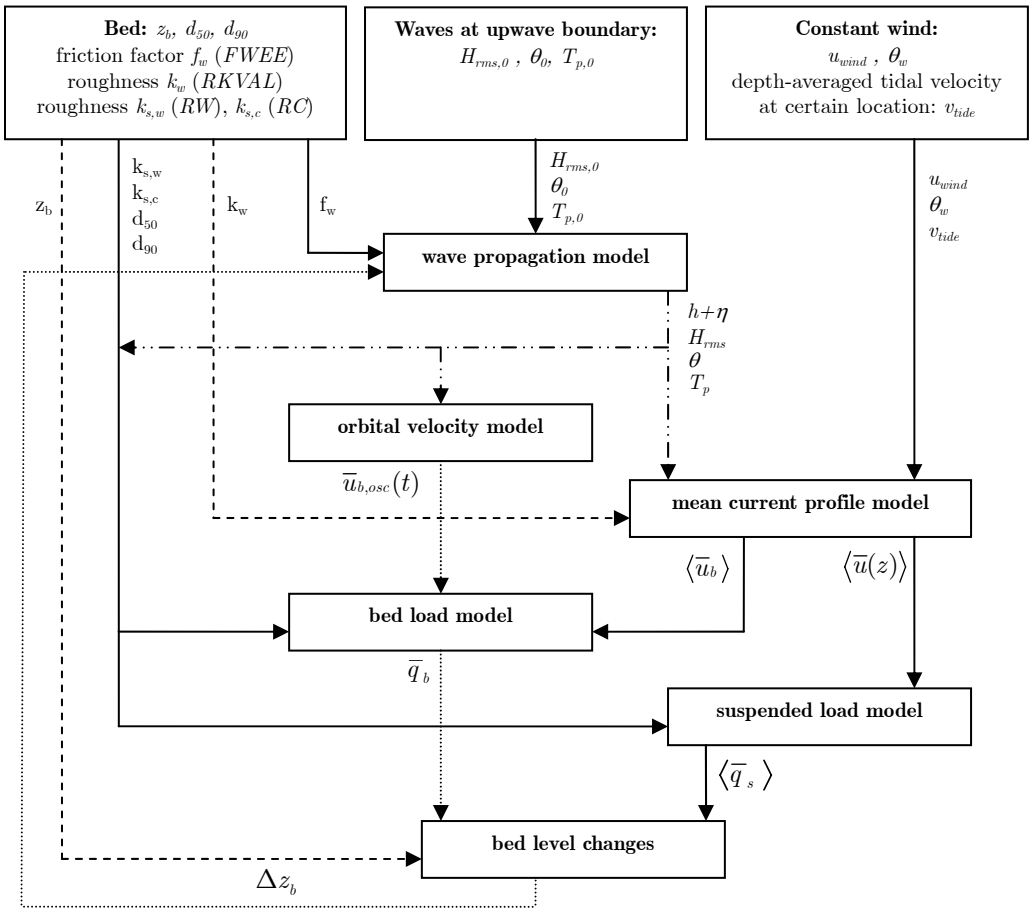

Figure 5.6 Overview of the UNIBEST-TC sub-models (after Bosboom, et al., 2000)

$$D_w = \frac{1}{4}\rho g \alpha f_p H_{\max}^2 Q_b \tag{5.7}$$

$$D_f = \frac{f_w \rho}{\sqrt{\pi}} u_{orb}^3 \tag{5.8}$$

in which C_g is the wave group velocity, θ is the wave incident angle, D_w is the dissipation of wave energy due to breaking, D_f is the dissipation due to bottom friction, E is the wave energy defined according to linear wave theory, H_{rms} is the root-mean-square wave height, Q_b is the fraction of wave breaking, α is a coefficient of the order of 1, $f_p = 1/T_p$, f_w is a friction factor, and u_{obr} is the amplitude of the wave orbital velocity based on the linear wave theory and H_{rms}.

The roller energy balance equation:

$$\frac{\partial}{\partial x}(2E_r c \cos\theta) = D_w - D_S \tag{5.9}$$

where E_r is the roller kinetic energy, c is the wave propagation speed, D_S is the dissipation of the roller energy modelled through the power of the shear stress between the roller and the water surface.

$$D_S = 2\beta g \frac{E_r}{c} \tag{5.10}$$

with β is the surface slope of the wave.

Mass flux and cross-shore mean velocity without overwash

The mass flux balance is the principle constraint for the computation of the mean current profile in layer below the wave trough. The mass flux in the surface layer (above the wave trough) consists of two parts, i.e. one due to the progressive wave character and the other due to the surface roller in breaking waves.

$$q_{drift} = q_{non-breaking} + q_{roller} = \frac{E}{c} + \rho \frac{Ac}{T} = \frac{E + 2E_r}{c} \tag{5.11}$$

where A is the roller area, q_{drift} is the total mass flux, $q_{non-breaking}$ and q_{roller} are the mass flux by non-breaking waves and by the roller, respectively .

In a "closed-tank" situation (without overtopping), the above mass flux is locally balanced by a return flow (undertow) with the mean velocity $\overline{u}_x$ determined below:

$$\overline{u}_x = -\frac{q_{drift,x}}{\rho d} = -\frac{q_{drift}\cos\theta}{\rho d} \tag{5.12}$$

where $q_{drift,x}$ is the mass flux in x-direction (shore normal), d is the local water depth, the negative sign indicates an offshore-directed flow.

Transport in the swash zone

In the swash zone, the above formulation of the undertow is not applicable. At present, the process of swash motion on the beach face and the associated sediment transport mechanism are not so well understood. For this reason, most cross-shore transport models including the UNIBEST-TC model adopt an "engineering" approach, extrapolating the net transport rate from a seaward boundary of the swash zone up to the run-up limit or up to the crest level (see e.g. Walstra and Steetzel, 2003). It should be noted that the transport rate at the crest level is set to zero, i.e. no transport in the landward direction (see also Fig. 5.8). This assumption seems to work rather well in the case of high beach and dune face profiles without overwash.

In the UNIBEST-TC model (Walstra and Steetzel, 2003), the transport rate at a point in the swash zone reads:

$$q_{st}(x) = q_{st}^{*} F(z_b) \tag{5.13}$$

where *F(z)* is a runup-related reduction function based on the relative volume of water that passes the level z_b above the water line, q_{st}^{*} is the transport rate at a prescribed seaward swash boundary.

The swash transport boundary q_{st}^{*} is determined either at a distance of one quarter of the local wave length from the water line or at the location where the water depth is prescribed as function of the peak wave period T_p.

5.5.3 Overwash modelling

Modelling of wave overwash follows closely the general approach as presented in Chapter 4 for modelling the growth of an erosional channel. In this case, the induced flow is the overwash flow.

Figure 5.7 depicts the aggregate computational flow-chart for modelling the overall barrier response, showing the inter-connections between the aforementioned across-shore processes. The computation ceases as the barrier crest has lowered to a certain level compared to the mean surge level, which is specified later on. In the following, we discuss some major modelling issues.

Hydraulic input at the upstream boundary and the back-barrier overwash flow

As aforementioned, the hydraulic conditions at the upstream crest boundary, specifically at the crest front, are a prerequisite for the overwash flow computation using the numerical approach presented in 4.2. These include, in principle, only two of the three basic flow parameters, i.e. discharge, water depth, and velocity, which are also the overtopping parameters at this boundary.

Earlier studies on wave overtopping at coastal dikes and dunes (see e.g. Tega and Kobayashi, 1996; Schuttrumpf, 2003) widely presume that the regime of the overtopping flow at the entrance section on the dike crest is critical, which is in accordance with the hydraulic principles of steady flows in transitional areas with changes in the bed slope. Recently, a PIV (Particle Image Velocimetry) study on wave overtopping

on a trapezoidal structure by Stansby and Tong Feng (2004) has shown quantitatively that this assumption is generally valid. Utilizing this finding for the case of wave overwash on barriers, the instantaneous average overwash depth at the crest front in the transitional zone of the barrier can be deduced from the instantaneous average overwash discharge as follows.

$$d_{ovw,c} = \sqrt[3]{q_{cd}^2 / g} \tag{5.14}$$

where $h_{ovw,\,c}$ is the overwash depth at the crest front.

The instantaneous average overwash discharge q_{cd} is determined using Eqs. 3.10, 3.11, and 3.12 (see also Fig. 3.4). It is noted that the incident wave height $H_{rms,toe}$ for overtopping calculation is determined at location where the water depth equals to three quarter of the incident deep water significant wave height (viz. at $d = 0.75\,H_{s,0}$, see also Tuan, 2003). This is the lower boundary of the submerged barrier profile defined according to Vellinga (1986).

With the input discharge and depth imposed at the upstream boundary, the overwash flow on the barrier crest and on the back-barrier slope can now be solved using the numerical approach discussed in Section 4.2. It is noted that in the present "wet" bed flow model, the dry bed (due to the intermittence of wave overtopping) is wetted with an extremely small layer of water $d = 10^{-6}$ m.

Mass flux balance with overwash and its effects on the cross-shore transport

Loss of the mass flux due to severe overwash in the landward direction can be considerable. The reduction of the return flow velocity and so of the associated transport is proportional to this loss and can be significant. The situation of an "open tank" (zero return flow) occurs as the barrier crest is overflowed by the surge.

To account for this effect, the overtopping volume must be subtracted from the landward-drifting mass flux by waves as follows.

$$\int_0^{t_{ovt}} \frac{1}{\rho} q_{drift}^{ovw} dt = \int_0^{t_{ovt}} \frac{1}{\rho} q_{drift} dt - \int_0^{t_{ovt}} q_{cd} dt = \int_0^{t_{ovt}} \frac{1}{\rho} q_{drift} dt - \frac{1}{2} q_{cd,\max} t_{ovt} \tag{5.15}$$

where the integral $\int_0^{t_{ovt}} (\bullet) dt$ gives the total volume transported (by waves or by overtopping) through a unit-width vertical section during the overtopping time t_{ovt}, q_{drift}^{ovw} and q_{drift} are the mass fluxes for cases with and without overwash, respectively.

For an arbitrary moment Eq. 5.15 can be written as:

$$\frac{1}{\rho} q_{drift}^{ovw} = \frac{1}{\rho} q_{drift} - q_{cd} \tag{5.16}$$

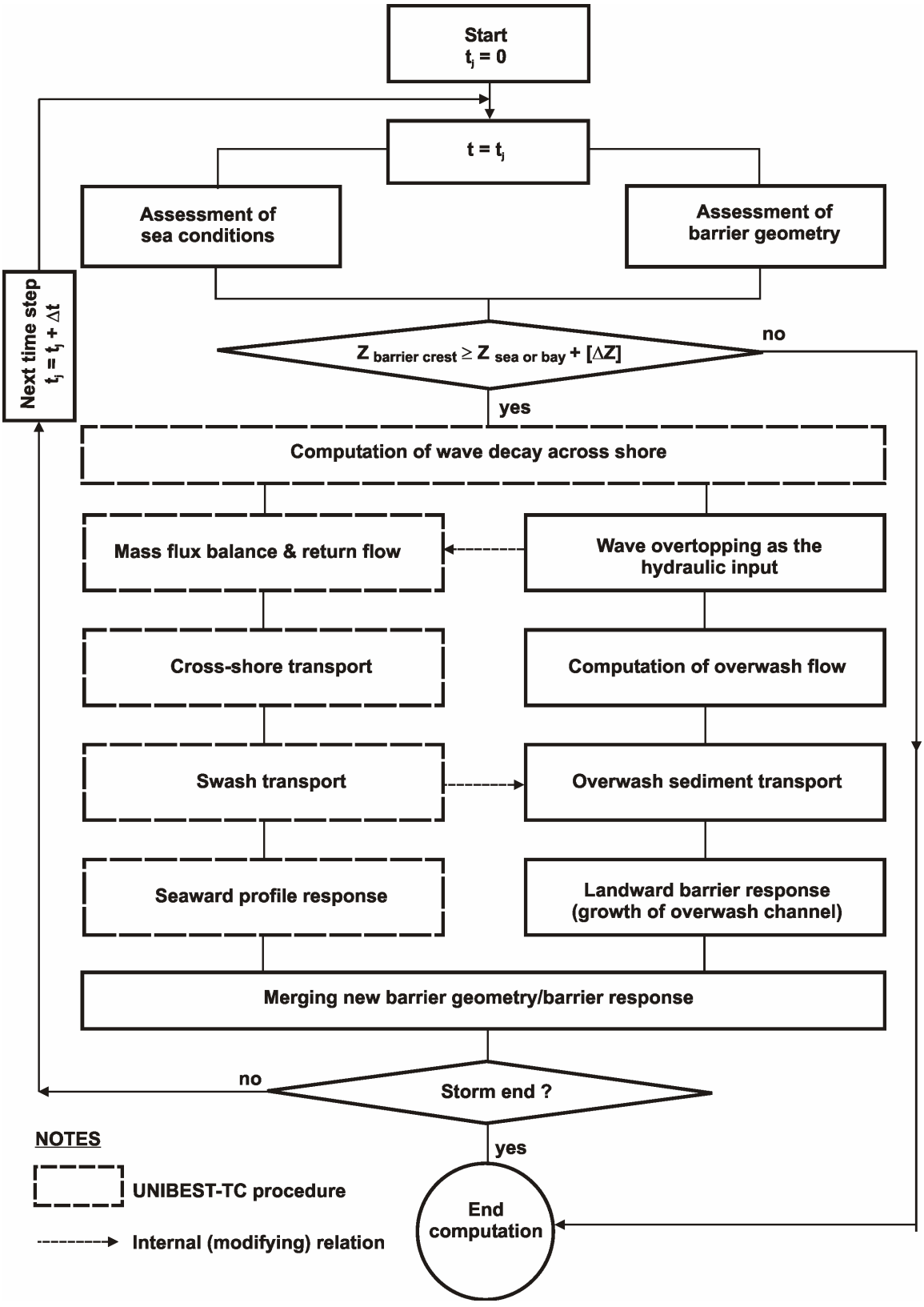

Figure 5.7 The aggregate computational flow-chart for modelling the barrier response

For use in the morphological modelling of the seaward profile changes, Eq. 5.16 is averaged over two periods during and not during overwash respectively, yielding:

$$\begin{aligned} \frac{1}{\rho} q_{drift}^{ovw} &= \frac{1}{\rho} q_{drift} - \frac{q}{F_{cd}} && 0 \le t \le t_{ovt} \quad \text{(overwash period)} \\ \frac{1}{\rho} q_{drift}^{ovw} &= \frac{1}{\rho} q_{drift} && t_{ovt} < t \le T_m \quad \text{(dry period)} \end{aligned} \tag{5.17}$$

in which $\frac{1}{2} q_{cd,\max} = \frac{q}{F_{cd}}$ has been substituted (see Section 3.3).

It is noted that q_{drift}^{ovw} is nonnegative ($q_{drift}^{ovw} \ge 0$), hence $\frac{q}{F_{cd}} \le \frac{1}{\rho} q_{drift}$, and $q_{drift}^{ovw} = 0$ in overflow situations when $F_{cd} \to 1$.

The mean cross-shore velocity can now be determined just similarly to Eq. 5.12.

$$\overline{u}_x^{ovw} = -\frac{q_{drift}^{ovw} \cos\theta}{\rho d} \tag{5.18}$$

with $\overline{u}_x^{ovw}$ is the mean cross-shore velocity for the case with overwash.

However, to facilitate the incorporation of the new mass flux balance in the cross-shore flow module, we introduce a velocity reduction factor due to effects of overwash. This factor is found by comparing Eq. 5.12 with Eq. 5.18 together with substitution of q_{drift}^{ovw} from Eq. 5.17.

$$\begin{aligned} f_u &= \frac{\overline{u}_x^{ovw}}{\overline{u}_x} = 1 - \frac{\rho}{q_{drift}} \frac{q}{F_{cd}} = f_u^{ovw} \le 1 && \text{for } 0 \le t \le t_{ovt} \\ f_u &= \frac{\overline{u}_x^{ovw}}{\overline{u}_x} = 1 && \text{for } t_{ovt} \le t \le T_m \end{aligned} \tag{5.19}$$

where f_u is the overwash-induced velocity reduction factor.

Following the energetics transport approach, which is widely applied to transport in coastal areas (see e.g. Bailard, 1981, 1982; Nairn, 1990), the sediment transport rate is related to some power of the velocity, i.e. $q_{st} \sim u|\overline{u}|^m$. Hence, the effect of overwash on the cross-shore transport rate can be expressed explicitly via f_u^{ovw} as follows.

$$q_{st,ovw} = F_{st} q_{st} \tag{5.20}$$

with:

$$F_{st} = (f_u^{ovw})^{m+1} F_{cd} + 1 - F_{cd} \le 1 \tag{5.21}$$

in which q_{st} and $q_{st,ovw}$ are the cross-shore transport rates averaged over the wave cycle for cases without and with overwash, respectively, F_{st} is the overwash-induced transport reduction factor, m is the energetics transport power ($m \approx 2.0$).

Regarding the validity of F_{st}, it is noted that in overflow situations as $F_{cd} \to 1$ and $f_u^{ovw} = 0$ then $F_{st} = 0$ (no offshore transport), in the case of minor or no overwash $F_{cd} \cong 0$ then $F_{st} \cong 1$ (minor or no effects of overwash).

Using Eqs. 5.20 and 5.21, the effect of overwash on the cross-shore transport can now be explicitly accounted for.

Computation of sediment transport

From the assumption that overwash occurs under sheet flow conditions, the overwash transport is probably best related to some power of the bed shear stress or to the Shields parameter (see Ribberink, 1998 for a review). However, there exists in the literature some ambiguity with respect to the principal mode of transport under such conditions (see Masselink and Hughes, 1998). Therefore, it is useful to investigate the applicability of both approaches, i.e. transport as bed load and as total load, to the modelling of overwash. The formulations of Van Rijn (1984a, b) and Ribberink (1998) are chosen for this purpose.

Retaining distinction between bed load and suspended load, Van Rijn (1984a, b) developed an approach for the total load transport as the summation of these two transport modes. The formulation was calibrated with a large number of experimental data from the field and laboratory. Reference is made to Van Rijn (1984a, b) for detail of the formulations and to Visser (1998) for discussions.

Considering transport as bed-load alone, Ribberink (1998) proposed a general bed-load formula, which is valid for a wide range of the Shields parameter (between 0.07 and 7.0). The formulation is based on a large amount of laboratory data of sediment transport under both steady and oscillatory unsteady currents. For the sake of consistency with the concept of the growth index, this transport approach is briefly introduced as follows:

$$\Phi_s(t) = \frac{q_s(t)}{\sqrt{(s-1)gd_{50}^3}} = \begin{cases} 11.0\left(\theta'(t) - \theta_{cr}\right)^n & \text{for } \theta' \geq \theta_{cr} \\ 0 & \text{for } \theta' < \theta_{cr} \end{cases} \tag{5.22}$$

where $\theta'(t)$ is the instantaneous effective Shields parameter (skin friction), $\Phi_s(t)$ is the dimensionless transport rate, $q_s(t)$ is the time-dependent transport rate, $n = 1.65$ is the transport exponent.

The determination of $\theta'(t)$ is according to:

$$\theta'(t) = \frac{\tau(t)}{\rho(s-1)gd_{50}} \tag{5.23}$$

$$\tau(t) = \frac{1}{2}\rho f_c u^2(t) \tag{5.24}$$

with $\tau(t)$ is the instantaneous bed-shear stress, f_c is the friction factor, $u(t)$ is the instantaneous stream velocity.

It is noted that Eq. 5.22 is in fact a specified form of Eq. 4.35, which is used for the elaboration of the growth index K_{vl} presented in Chapter 4.

The determination of the friction factor in Eq. 5.24 is a difficult task. In an overwash situation, the flow is treated as quasi-steady and hence it is probably appropriate to estimate this factor using the concept of the boundary layer flow (see e.g. Hughes, 1995):

$$f_c = 2\left(\frac{\kappa}{\ln 12d / k_s}\right)^2 \tag{5.25}$$

Where κ (= 0.40) is the von Karman constant, k_s is the Nikuradse roughness, and d is the boundary layer thickness that is assumed to cover the entire overwash depth.

The friction factor according to Eq. 5.25 is time-and-space-varying as a function of the local water depth. However, at locations where the overwash depth is too shallow while the flow velocity is relatively high, Eqs. 5.23 through 5.25 produce unrealistically large values for the mobility parameter. To avoid instability in such cases, the friction factor is restricted to a constant maximum value ($f_{c,\max} = 0.005 \sim 0.010$).

Transport in the swash zone with overwash

As stated previously in Subsection 5.3.3, the transport in the upper part of the swash zone in the case of overwash is landward-directed. In the present model, a simple linear transport distribution in the swash zone is used (viz. $F(z_b)$ in Eq. 5.13 is a linear function with respect to the level difference from the boundary), which is shown in Fig. 5.8. The seaward swash boundary is kept the same as in the UNIBEST-TC model. The transport rate on the top of the barrier (the overwash rate) is stipulated by the capacity of the overwash flow. In the case of weak or no overwash transport, the biased trapezoidal distribution automatically reduces to that in the ordinary situation. The expression for the transport in the swash zone up to the barrier crest level is given below.

$$q_{st}(x) = q_{st}^{*} + \frac{(z_b - z_b^{*})}{(z_b^{cr} - z_b^{*})}(q_{st}^{ovw} - q_{st}^{*}) \tag{5.26}$$

in which q_{st}^{*} and q_{st}^{ovw} are the net transport rates at the swash boundary and at the barrier crest, respectively, the bed level z_b with superscript $(^{*})$ is at the swash boundary and that with $(^{\mathrm{cr}})$ is at the crest (see also Fig. 5.9).

Growth of the overwash channel

Modelling the growth of the overwash channel, i.e. the back-barrier profile evolution and the increase of the channel width, just follows the general approach proposed in Chapter 4.

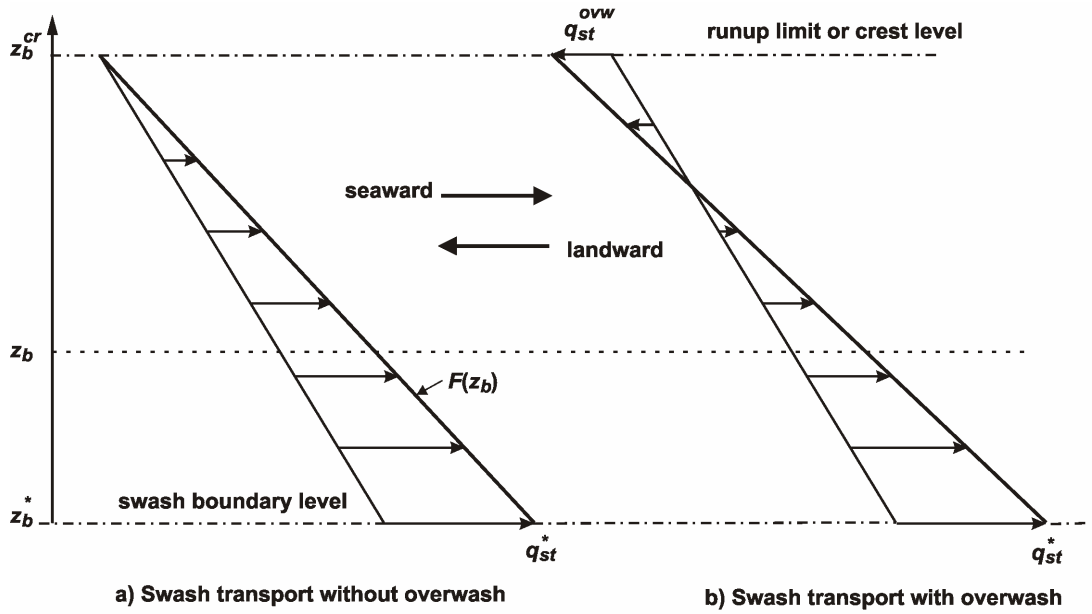

Figure 5.8 Transport distribution in the swash zone without and with overwash

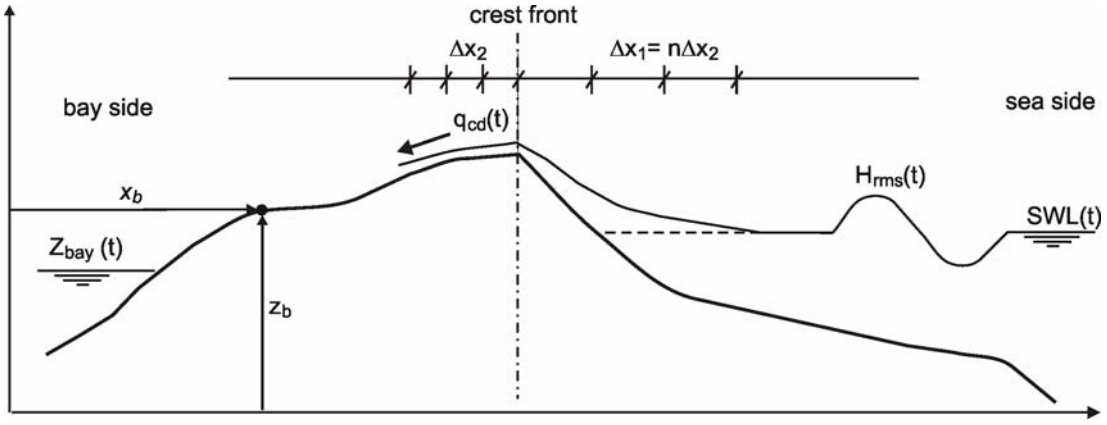

Figure 5.9 Model setup and coordinate system

5.5.4 Set-up of computational model and morphological time step

The spatial computational model domain together with the coordinate system is shown in Fig. 5.9. At a computation time step, the model employs two distinct uniform spatial grids, one for the seaward part of the profile up to the crest point and the other for the remaining landward part. The latter grid is refined relative to the former one.

For every wave cycle, the seaward profile change is computed once. Meanwhile, on the bay side, the morphological development of the overwash channel (lateral and vertical growth) is updated twice, once over the wet period and once over the draining period of the overwash discharge histogram. The draining period, which is a fraction of the dry period, is counted starting from the end of the wet period till the moment when

the flow on the back-barrier slope dries out completely. It is observed that sediment transport is negligible when the flow depth is too shallow (in the order of one centimetre). Therefore, to avoid unrealistic transports, a depth threshold is also imposed, below which sediment transport is assumed not to occur.

The time step for the computation of the overwash flow is automated according to the Courant stability condition for an explicit numerical scheme (see also Section 4.2).

$$\Delta t = \frac{\Delta x \times \mathrm{CFL}}{\lambda_{\max}} \tag{5.27}$$

where the Courant value CFL < 1.0 is an user's input so as to ensure model stability.

5.6 MODEL CALIBRATION

As constructed, the model is composed out of two interrelated process components, viz. a beach and dune erosion process and an overwash process. Since performance of the latter component is largely dependent on that of the former one, preliminary calibration effort is first made with focus on the seaward part of the barrier profile. The overall model calibration with respect to the barrier response as a whole is then carried out to determine also parameters of the landward processes that influence the overwash morphology and the beach face area.

Regarding the seaward profile response, numerous calibration efforts have been carried out to improve the performance of the cross-shore transport model of UNIBEST-TC. Calibrated standard values for the basic parameters can be found in Bosboom et al. (2000) and Walstra and Steetzel (2003). In Steetzel (1993) detailed calibration on wave energy decay and swash transport effect is also discussed. Also, some specific aspects regarding effects of the wave period on the prediction of dune erosion using UNIBEST-TC is discussed in Den Heijer (2005). Without any further calibration effort as expected, numerical simulations of the laboratory tests were successfully made with the basic experimental conditions specified in Table 5.1. Values of some user's input parameters are shown in Table 5.3.

Table 5.3 Model user's input and calibrated parameters

Parameter	Unit	Process component	Value
Model length scale N_L	-	Both	5.00
Morphological time scale N_t	-	Both	2.24
Bed porosity p	-	Both	0.40
Sediment fall speed w_s	m/s	Both	0.025
Grain-related roughness k_s	m	Both	0.0006
Sediment angle of friction $\tan\phi$	-	Both	0.60
Wave-related roughness RW	m	Beach and dune erosion	0.005
Current-related roughness RC	m	Beach and dune erosion	0.005
Energetics transport power m	-	Overwash (-induced effects)	2.00
Composite-slope parameter η	-	Overwash	0.30
Courant number CFC	-	Overwash	0.03
$T_P/T_{m\text{-}1.0}$	-	Overwash	1.10
Transport exponent n (growth index)	-	Overwash	1.65
Maximum friction factor $f_{c,\,max}$ (Ribberink)	-	Overwash	0.006
Overall bed roughness	m	Overwash	0.001
Depth threshold for transport	m	Overwash	0.010

Much calibration work was necessary and carried out for the morphological modelling of overwash. To this end, factors that affect the model performance were investigated as shown hereinafter. These include the swash transport distribution, the composite-slope parameter η, the side-discharge contribution, the transport exponent n of the growth index, the overwash-induced transport reduction factor, and the characteristic wave period $T_{m\text{-}1.0}$. Values of calibrated parameters which give the best model performance are shown in Table 5.3.

It should be noted that the intra-calibration for the internal processes, e.g. the instantaneous overtopping input and the channel lateral growth, was actually done in the preceding chapters. The present phase of the model calibration is essentially related to specific process outputs, i.e. the barrier profile response and the overwash channel development.

5.6.1 Transport distribution in the swash zone

An essential element affecting the beach-face geometry above the water line and so wave overwash is the transport distribution in the swash zone (see Fig. 5.8). To judge whether the new adjustment (Fig. 5.8b) is indeed appropriate to the case of overwash, the barrier profile changes were computed using each of those two distributions. It is noted that, in both cases, the computation was carried out with occurrence of overwash. Figure 5.10 shows the comparison between the observed geometry of the beach face and that predicted by the model for all the tests OW1 through OW4.

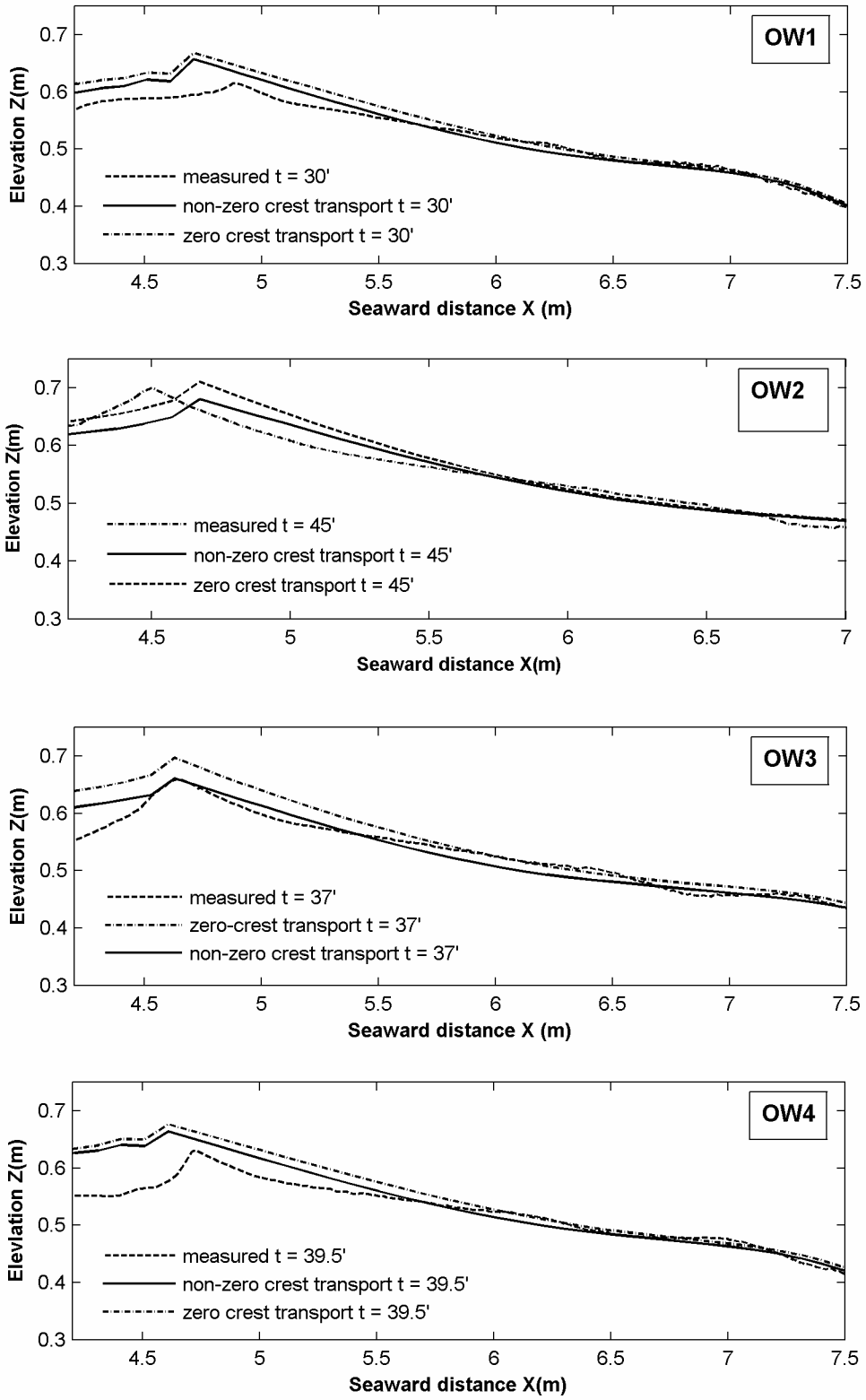

Figure 5.10 Beach face comparison for cases with and without crest transport

It follows that the biased trapezoidal distribution apparently gives better predictions for the beach face geometry. Because of non-zero transport at the crest, the conventional distribution generally underestimates the rate of the crest lowering more than the new distribution. Also, it predicts a steeper beach face or a dune scarp (if no overwash occurs), which is not observed for the case of low-crested barriers with frequent occurrence of overwash.

5.6.2 Effects of the composite-slope parameter η

The composite-slope parameter is a variable in the formulation of the instantaneous overtopping discharge. As concluded in Section 3.5, this parameter has a favourable range between 0.10 and 0.50, over which the overtopping discharge and the overtopping time are both promising for yielding a satisfactory level of regression. The value $\eta = 0.20$ is recommended for the pure purpose of overtopping estimates. However, it is questionable whether this would also be the best choice in terms of its effects on the overwash morphology. To investigate this, model computations were carried out with various values of this parameter for all the tests. Figures 5.11 and 5.12 respectively show the effects of the parameter on the final width of the overwash channel and the final barrier crest level. It is noted that the observed crest levels were averaged over the channel breadths, which are higher than those of the middle profiles.

It appears from the figures that the channel width is most sensitive to the composite-slope parameter. Generally speaking, a smaller value of η introduces a larger extent of the crest lowering as well as a larger lateral channel enlargement and vice versa. However, large values of η between 0.40 and 0.5 give the best agreement with respect to the final channel width, whereas the crest level is (slightly) better predicted with smaller values such as $\eta = 0.10 \sim 0.20$. As a consequence, when the overall agreement is considered, the median value $\eta = 0.30$ (between 0.1 and 0.5) seems to be the most appropriate choice. As expected, in terms of the overwash morphology, this value does not coincide perfectly with that previously recommended for pure overtopping estimates. However, the results show quite a good consistency and the parameter appears to be well determined.

5.6.3 Side-discharge contribution

In the present one dimensional approach, a relatively depressed portion in a sand barrier, where overtopping takes place, is schematized as a channel of trapezoidal or rectangular cross-section. However, in reality, waves may also overtop at higher parts, which are adjacent and steep to the channel. This can contribute a significant amount of overtopping to the main flow as it does in the nature of overland flows. An increase of the crest level would lead to an exponential reduction of the overtopping volume. Hence, taking an averaged crest level over the entire considered length seems to underestimate the overtopping strength. In the present model, this side contribution is accounted for in a simple but appropriate way by adding it to the main flow as follows. A considered overwash segment of a barrier is divided into a number of subordinate parts of various (average) elevations beside the main channel. During overwash

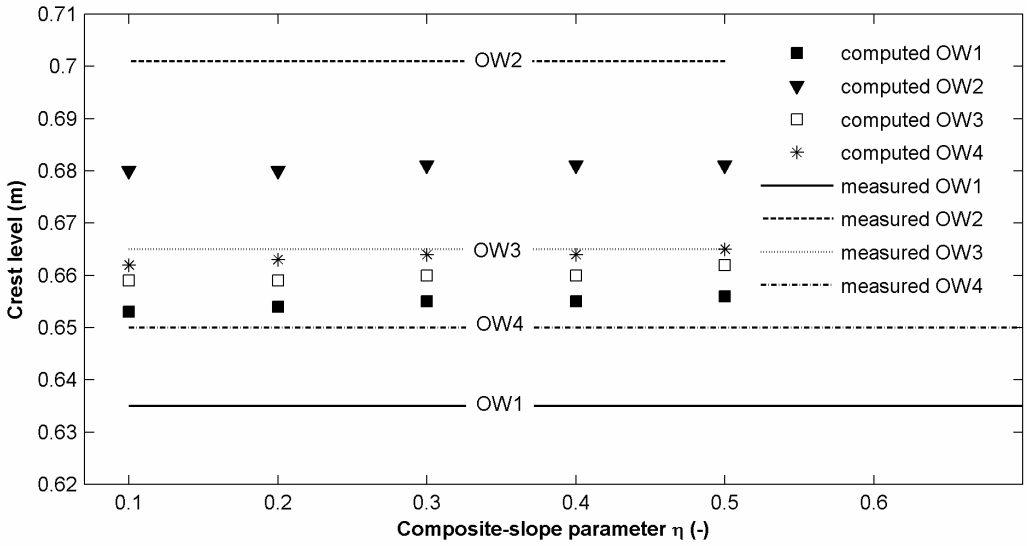

Figure 5.11 Effects of the composite-slope parameter η on the prediction of the barrier crest level

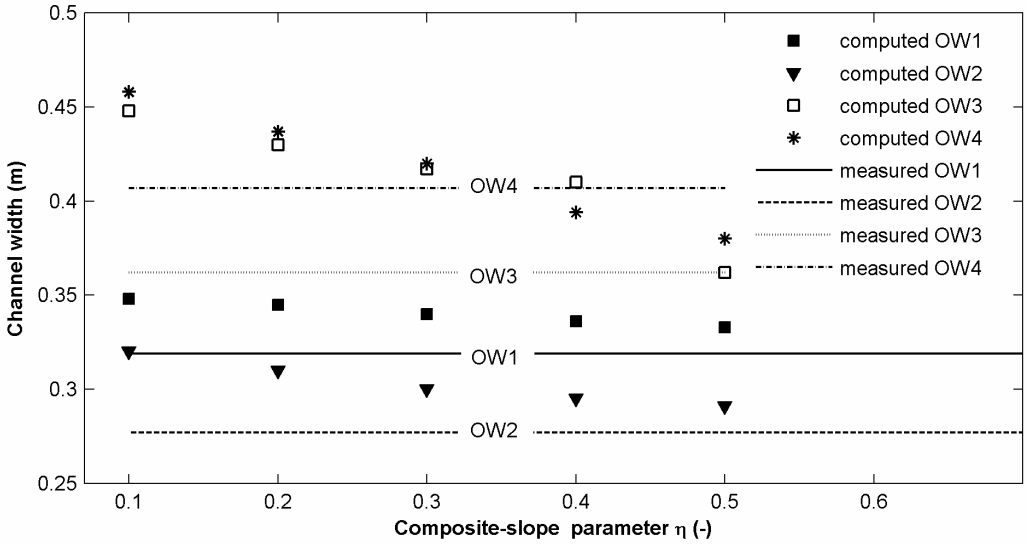

Figure 5.12 Effects of the composite-slope parameter η on the prediction of the channel width

widths of these subordinate parts reduce sequentially as the channel grows laterally while it is assumed that their elevations are not affected. Overwash discharges through the channel and over the subordinate parts are determined separately and then summed to give the total discharge through the channel:

$$q_{cd,total} = \frac{q_{cd}(R_{cs})B_v + \sum_j^{Np} q_{cd}^j(R_{cs} + \Delta R_{cs}^j)L_{sub}^j}{B_v} = q_{cd}(R_{cs}) + \frac{1}{B_v}\sum_j^{Np} q_{cd}^j(R_{cs} + \Delta R_{cs}^j)L_{sub}^j \quad (5.28)$$

in which $q_{cd,total}$ is the total instantaneous overwash discharge per unit channel width including the side contribution, $q_{cd}(R)$is the instantaneous (unit) discharge as a func-

tion of a crest freeboard R, R_{cs} and $R_{cs}+\Delta R_{cs}^{j}$ are the momentary crest freeboard at the channel and at a subordinate part j, respectively, ΔR_{cs}^{j} is the bed level difference of a subordinate part j relative to the channel, L_{sub}^{j} is the width of a subordinate part j, N_p is the total number of defined subordinate parts.

In the case of the laboratory tests, applying Eq. 5.28 to the flume conditions with one subordinate part outside the channel of the length $L_{sub} = B_{flume} - B_v$, we yield:

$$q_{cd,total} = q_{cd}(R_{cs}) + \frac{B_{flume} - B_v}{B_v} q_{cd}(R_{cs,0}) \tag{5.29}$$

where $R_{cs,0}$ is the crest freeboard of the subordinate part outside the channel, unchanged and equal to the initial crest freeboard. $B_{flume} = 0.80$ m is the flume width used for all tests OW1 to OW4.

The second term on the right hand side of Eqs. 5.28 and 5.29 is the contribution from the side discharge. It follows from Eq. 5.29 that at the very early moment of the flume tests when B_v is still rather small, the side-discharge contribution is considerable. Computer simulations of the laboratory tests also indicate that overwash is largely underestimated in the early stages if this term is neglected. In the field, the terrain is usually complex, so it is recommended to take into account this side-discharge contribution using the above approach (Eq. 5.28). The total considered width, including the subordinate parts and the channel, should be larger than the estimated final width of the overwash channel.

5.6.4 The transport exponent *n*

In the present model, the transport exponent n plays a role in quantifying growth of the overwash channel. Its effects on the channel development vary with the applied sediment transport approaches.

When the transport rate is not dependent from the transport exponent, influences of n on the channel growth are straightforward as they stem only from the growth index K_{vl}. The exponent is proportional to the magnitude of the growth index and so inversely proportional to the increase of the channel width (see Eqs. 4.48 and 4.49). As a result, a larger n tends to give a larger vertical growth rate but a smaller lateral growth rate and vice versa. This is the case for the Van Rijn's (1984a, b) transport formulations, in which the exponent is absent. Figure 5.13 clearly indicates the effects of n on the channel growth of an example case, test OW1, with n = 1.65, 1.73, and 2.0.

The influences are not straightforward when the sediment transport rate is also influenced by the exponent. This is the case when the general bed-load formula of Ribberink (1998) is used (Eq. 5.22). As indicated above, an increase of n and so K_{vl} would reduce the increase of B_v, however now the transport rate also increases correspondingly, which tends to raise B_v. This happens reversely when one decreases n. Consequently, in a qualitative way, with a given value of n, the model predictions of the

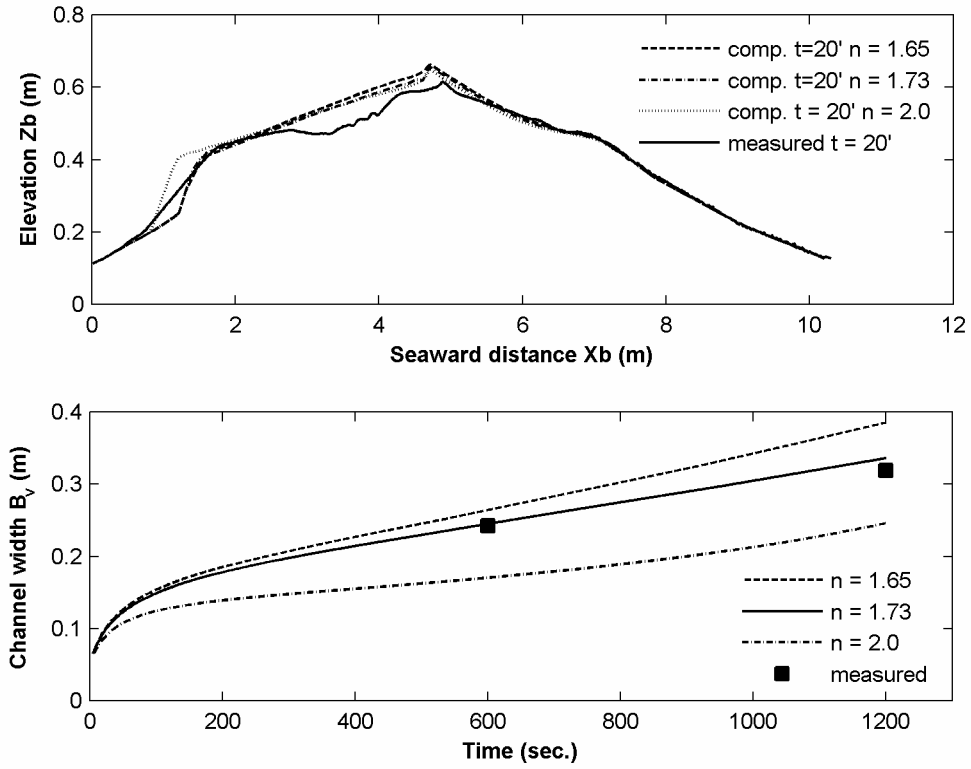

Figure 5.13 Effects of n on growth of the overwash channel, Van Rijn's transport approach; upper graph: profile response, lower graph: channel width increase

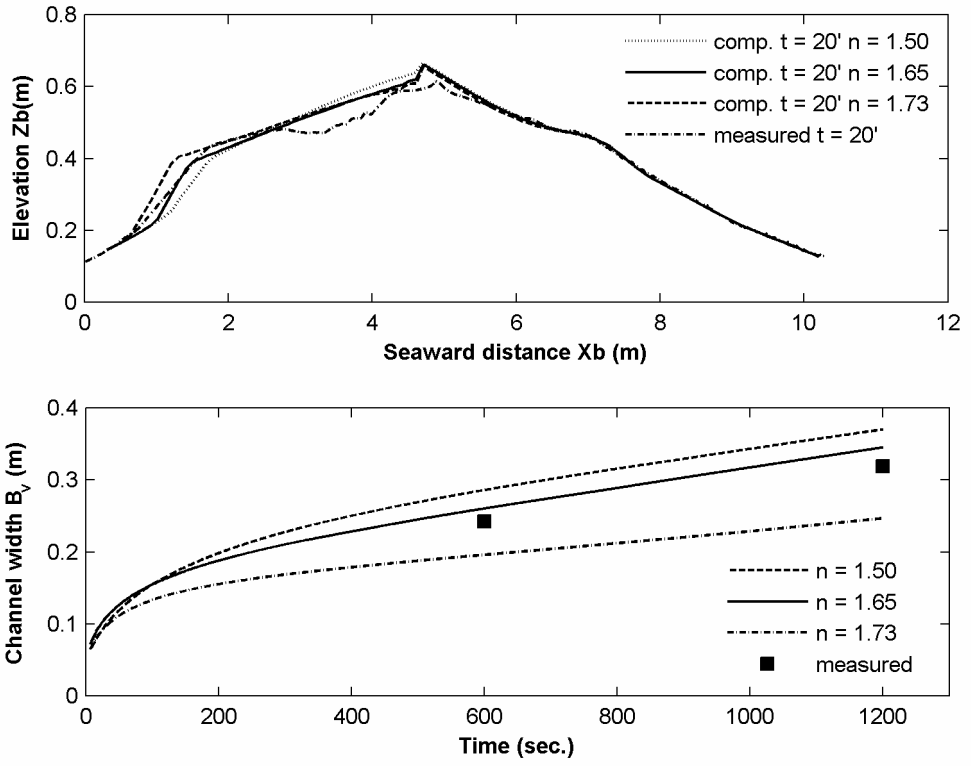

Figure 5.14 Effects of n on growth of the overwash channel, Ribberink's transport approach; upper graph: profile response, lower graph: channel width increase

rate of width increase using Van Rijn's approach are larger than those using Ribberink's approach. In other words, a smaller value of n is to be expected in the latter transport approach. Figure 5.14 shows the comparison of the barrier response between the laboratory data of test OW1 with that of the model prediction with various values of the transport exponent $n = 1.5$, 1.65, and 1.73 respectively.

It follows from the above figures that the effect of n given via the index K_{vl} on the channel growth is the most influential. In general, a larger value of n results in a milder increase rate of the channel width but, in contrast, a larger vertical growth rate and vice versa. The transport exponent $n = 1.73$, which is also the calibrated value for use in the growth index formulation, is found to give the best agreement with the laboratory data in the case of Van Rijn's approach. Using Ribberink's approach, $n = 1.65$, smaller as expected, gives the best model performance. This is also the original value of n used in the general of bed-load formula of Ribberink (1998).

Apart from the effects on growth of the overwash channel, the transport exponent also influences the beach face slope via the overwash transport rate. A larger n seems to slightly increase erosion on the beach face and thus to result in a milder beach-face slope.

5.6.5 Overwash-induced reduction of the cross-shore transport

It can be observed clearly from the laboratory tests (see Figs B.5 and also Fig. 5.15) that during the last periods of overwash, in spite of on-going wave attack, the build-up of the seaward sand bar is significantly slowed down and is nearly negligible in some cases. This is, in part, because the undertow becomes very weak due to a significant loss of mass flux caused by severe overwash near the end of the overwash processes.

Figure 5.15 plots the computed results of the sand bar evolution versus the measurement for test OW2. The overwash-induced transport reduction effect was included in the computation with the energetics transport power $m = 2.0$ (in Eq. 5.21). Good agreement in terms of the bar dimensions and of the time-varying evolution is found. It is learnt from the computation that the transport reduction factor F_{st} is less sensitive to the magnitude of m as it is indeed largely affected by the relative total overtopping time F_{cd} (see also Eq. 5.12). In general, a transport reduction by 10% to 20% due to overwash was observed during the computation. The overwash-induced mass-flux reduction appears to be responsible for the observed slowing down of the bar build-up in the case of severe overwash.

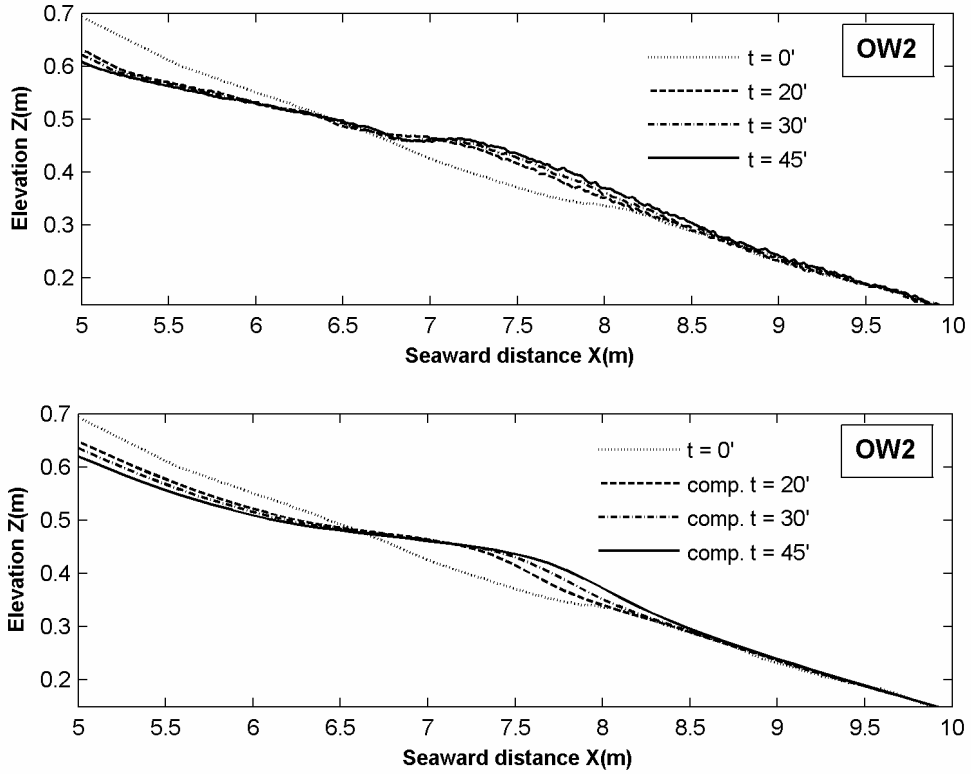

Figure 5.15 Slowing down of bar build-up rate, test OW2
upper graph: measurement, lower graph: computed.

5.6.6 Overall comparison and discussion

Figures 5.16 through 5.19 show the comparison between the model predictions of the barrier response (profile response and channel width increase) using the above two transport approaches for all the tests from OW1 to OW4 with those of the laboratory measurements.

Overall, a good resemblance of the barrier profile evolution with the measurement is found. The time-dependent barrier profile response and the channel width increase are fairly predicted. Overwash morphologic features such as the crest front, and the overwash channel agree reasonably well with the measurements. The height of the washover fan is always overestimated by the model. This is due to the horizontal spreading of sediment downstream of the channel, which leads to a flatter and more extended washover fan. This phenomenon has not been covered yet in the present model.

Both the sediment transport approaches of Van Rijn (1984a, b) and Ribberink (1998) appear to be suitable for use in the overwash computation with more or less the same level of performance. None of the two formulations shows absolute prevalence over the other in terms of prediction capability.

In comparison with the qualitative description of the barrier response mentioned in Section 5.4, the model successfully describes the general course of the barrier morpho-

logical development during wave attack with frequent occurrence of overwash. The existence of the crest front as well as the transitional zone and the channel development are very well simulated. These results indicate that the modelling approach for wave overwash presented so far is appropriate.

However, the crest level is slightly underestimated for the final runs with near-inundated crest freeboards (see Figs. 5.16 and 5.19). Such underestimations are attributed to the fact that the barrier crest near the end got so close to the sea level and the bore crest level itself was even higher than the barrier. As a consequence, overtopping at this moment is no longer a simple boundary layer flow as originally defined. Instead, it is rather a sort of breach flow by wave transmission over the crest with strong turbulence-generating mechanisms, which induce more erosion in the overwash channel (irregular bottom and scour was observed in the measured profiles in tests OW1 and OW4, see Figs. 5.16 and 5.19). This phenomenon, however, goes beyond the current model capability, which only deals with wave overwash without inundation. A constraint should therefore be applied to the lower end of the relative freeboard in order to cease the computation at the right moment. This can be done by making use of the relative overtopping time F_{cd}, which represents the intermittent character of wave overtopping. A reduction of the relative freeboard leads to an increase of F_{cd} and thus overtopping is less discontinuous.

It follows from Eq. 3.22 that F_{cd} approaches its maximum value $F_{cd} \rightarrow F_{cd,\max}$ when $R_{cs} / H_{m0} \rightarrow 0$ and $a_1 \rightarrow a_{1,\max} = 0.25$ (see Table 3.2).

$$F_{cd,\max} = a_{1,\max} \sqrt{\tan\alpha / s_m} = 0.25 \sqrt{m_s / s_m} \tag{5.30}$$

where $\tan\alpha = m_s$ for the case of zero crest freeboard has been substituted.

The computation must stop before F_{cd} reaches the above maximum value. A freeboard margin should therefore be applied to F_{cd} based on trial computations. The model validity condition with respect to the lower end of the relative crest freeboard reads:

$$F_{cd} \leq [F_{cd}] = 0.22 \sqrt{\frac{m_s}{s_m}} \tag{5.31}$$

where $[F_{cd}]$ is the allowable relative overtopping time.

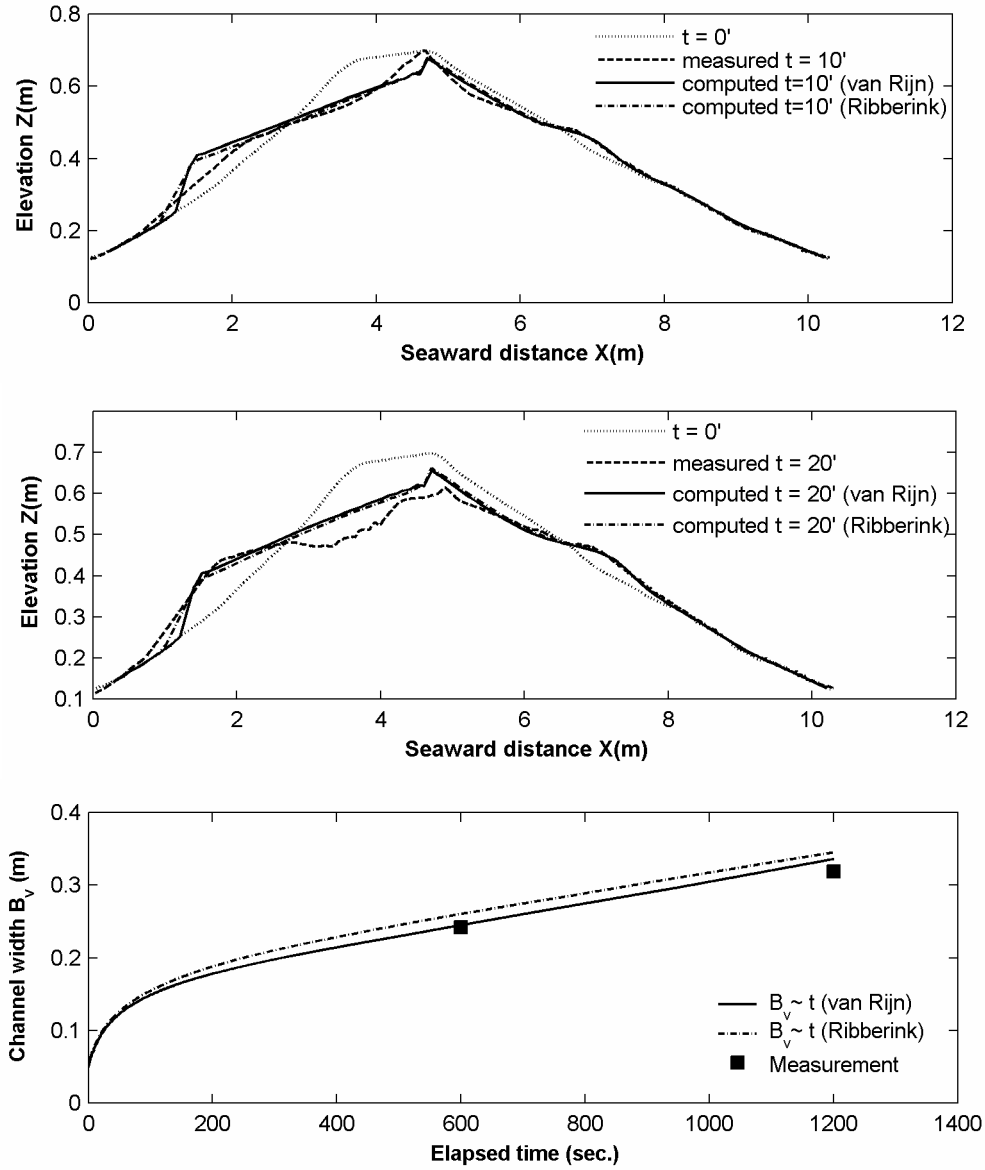

Figure 5.16 Barrier response test OW1: computed versus measured

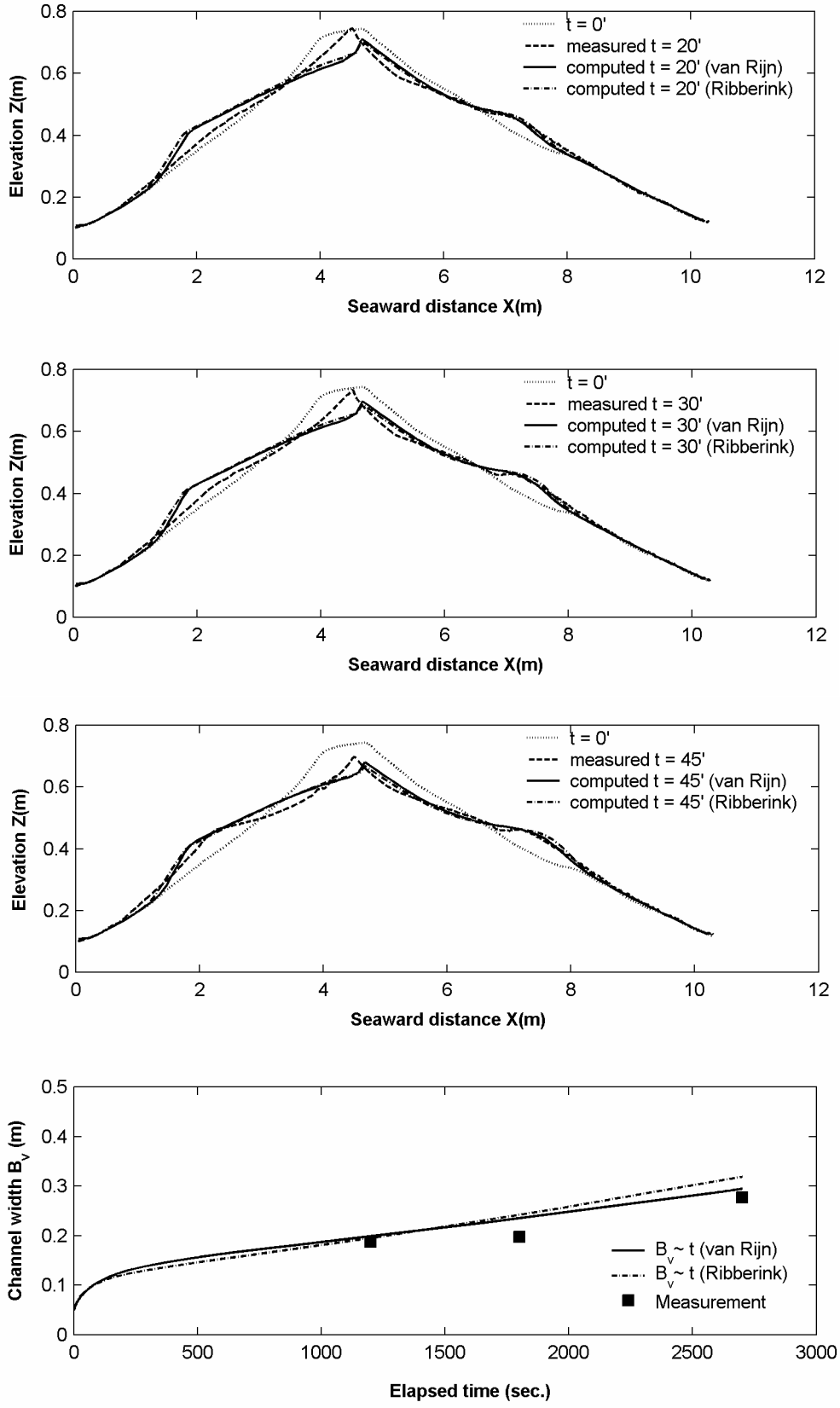

Figure 5.17 Barrier response test OW2: computed versus measured

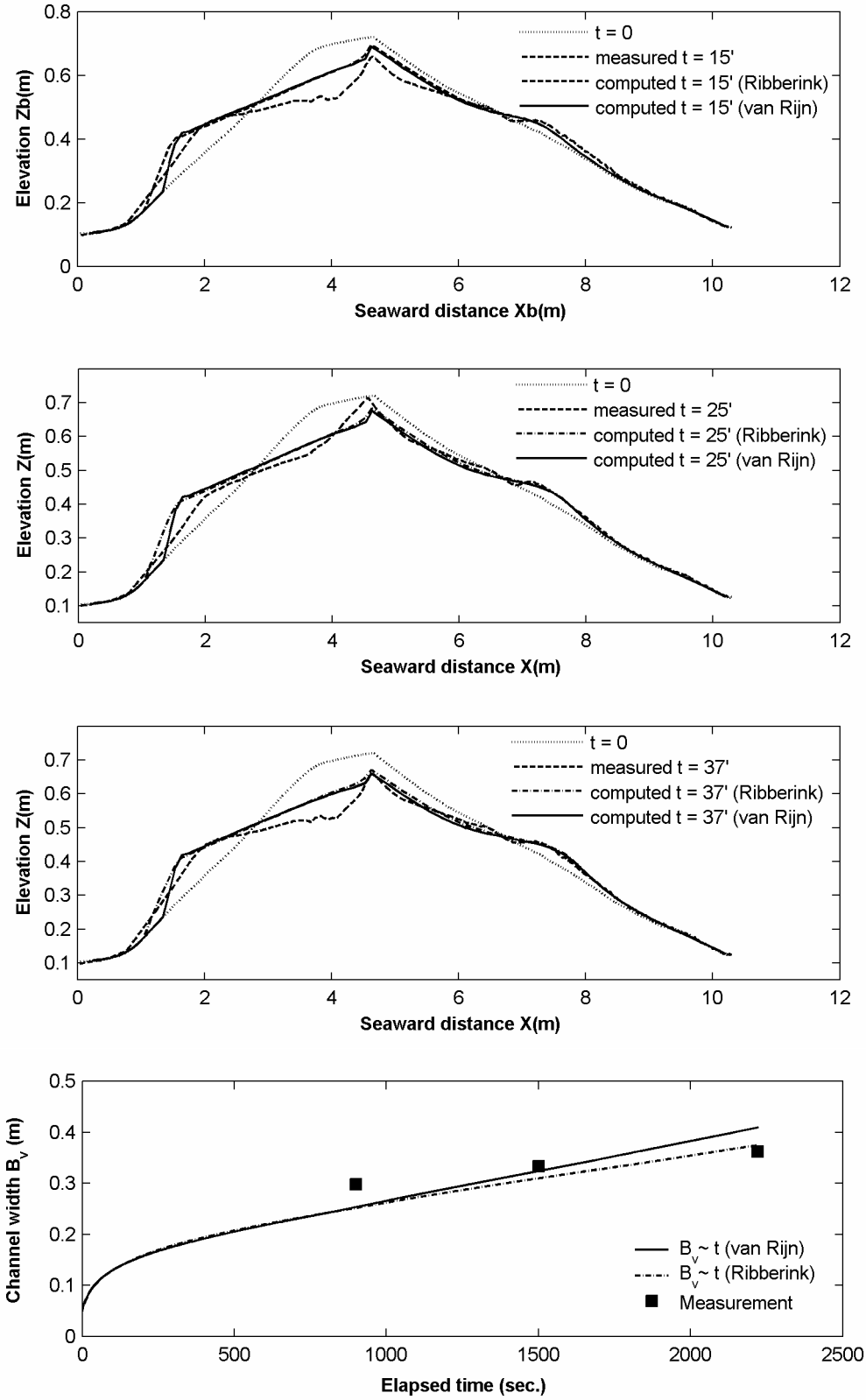

Figure 5.18 Barrier response test OW3: computed versus measured

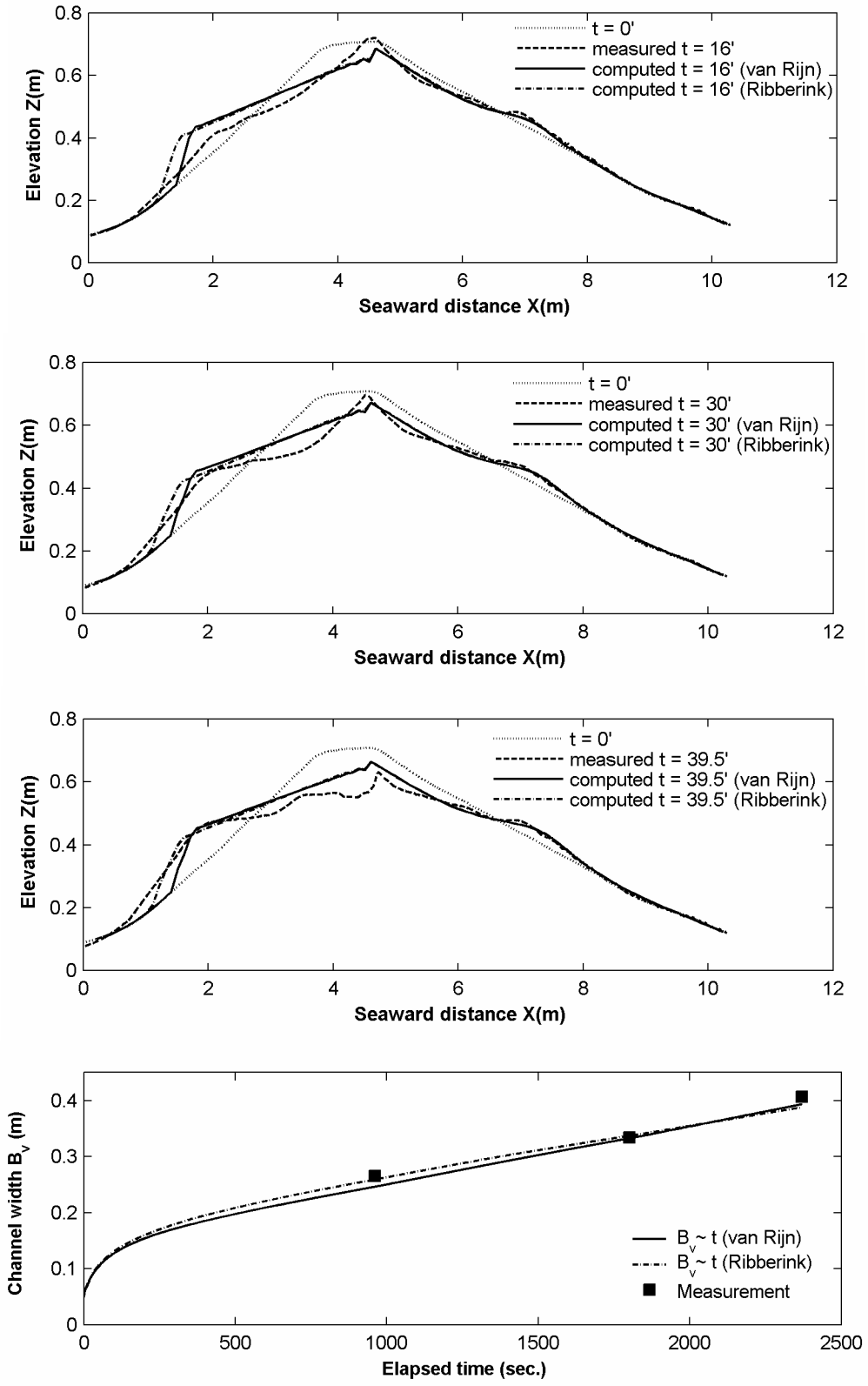

Figure 5.19 Barrier response test OW4: computed versus measured

5.7 MODEL SENSITIVITY ANALYSIS

In this section, some secondary aspects that may affect the model performance are discussed. These include the determination of the spectral period $T_{m-1.0}$ and the dimensions (depth and width) of the initial channel.

5.7.1 Characteristic wave period $T_{m-1.0}$

In Chapter 3, we have concluded that the spectral period $T_{m-1.0}$ is considered most appropriate for the empirical determination of overwash discharge since it can account for the effects of wave energy spectra transformation in shallow water. However, accurate prediction of $T_{m-1.0}$ using a frequency-evolutional model would be too complex and impractical to incorporate in the present model. On not too shallow foreshores, where wave spectra are not flattened out, $T_{m-1.0}$ can be adequately related to T_p through a fixed empirical conversion factor. In Van der Meer (2002), $T_p = 1.10 T_{m-1.0}$ is recommended for clear peak spectra with known T_p. Although it is uncertain whether this conversion is accurate, one still can investigate its sensitivity on the model output.

Without loss of generality, the computation was carried out for a chosen test case, test OW4, using three distinct conversion values $T_p/T_{m-1.0} = 1.07, 1.10, \text{and } 1.25$. The results are plotted in Fig. 5.20. It is obvious that longer wave periods (viz. smaller conversion values) cause more erosion and vice versa. In general, the channel development and especially the deposition delta are the most sensitive. It follows that $T_p = 1.10 T_{m-1.0}$ is reasonably appropriate and can be generally used for modelling of overwash on barriers on shallow foreshores.

5.7.2 Dimensions of the initial overwash channel

A model sensitivity analysis is carried out with respect to the initial width and depth of the channel to further investigate these geometric effects on the overwash development. It also helps determine to what extent a channel is considered wide so as to neglect the lateral growth effects on the profile evolution. This can be useful in cases that these channel dimensions are not well-determined beforehand but the barrier profile response is still of interest.

To investigate this, model simulations were made on an imaginary barrier in prototype scale, whose geometric and hydraulic conditions are scaled up from the model barrier of test OW1. Figures 5.21 and 5.22 show the computation results after a short duration t = 2000 s (or 0.56 hrs) for various combinations of the initial channel width and depth. The computed profile for the case of a wide channel (channel of a unit width while the channel lateral growth is not considered) is also shown for the purpose of comparison.

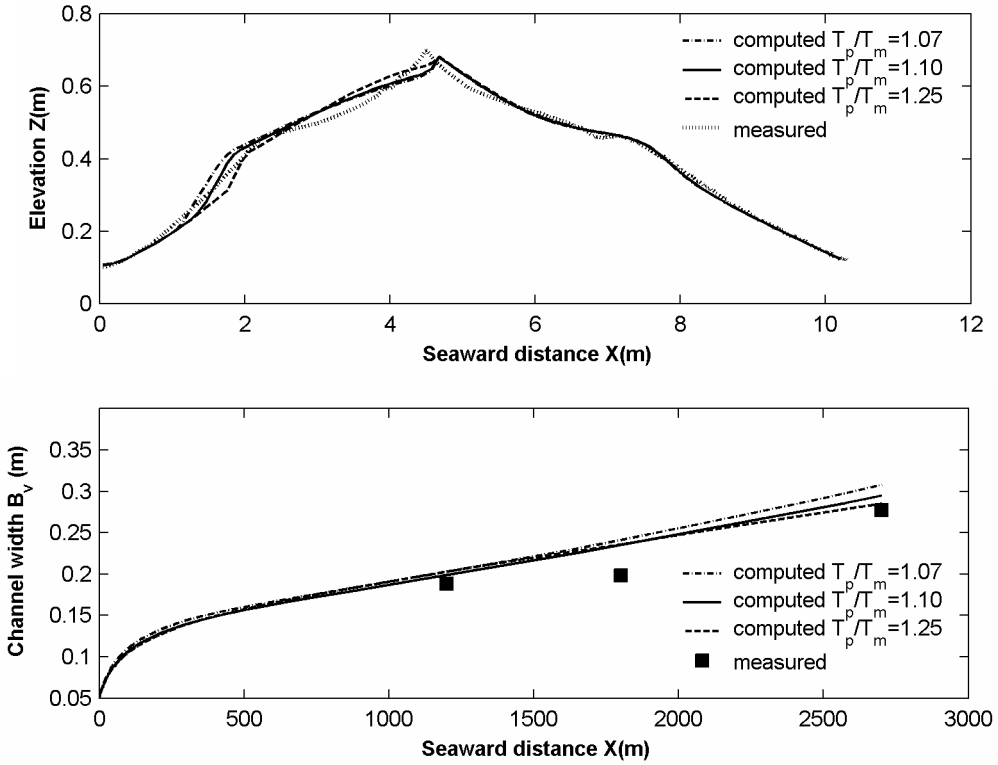

Figure 5.20 Effects of $T_{m\text{-}1.0}$ on the prediction of the barrier response

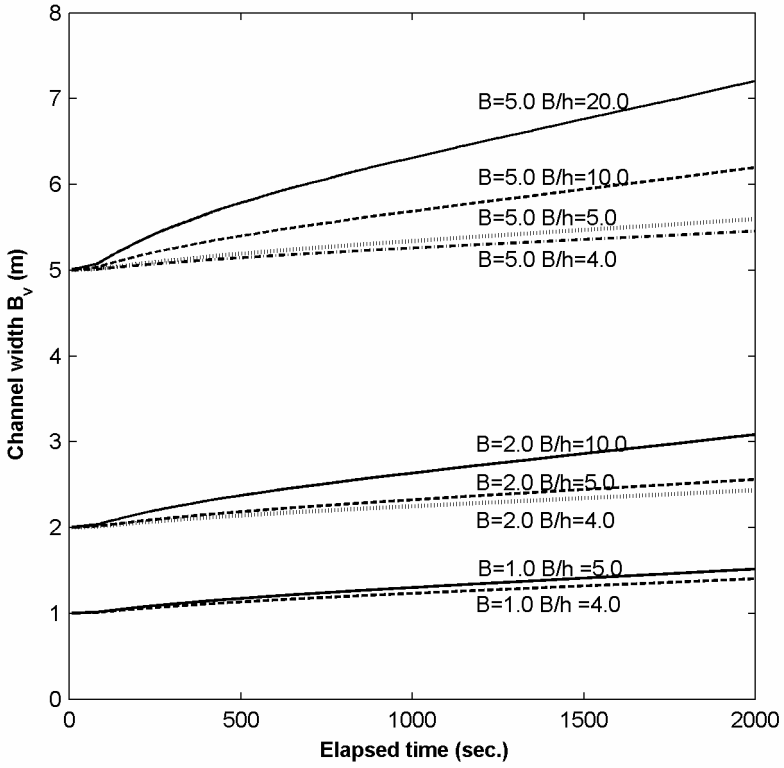

Figure 5.21 Effects of the initial channel dimensions on the channel lateral growth

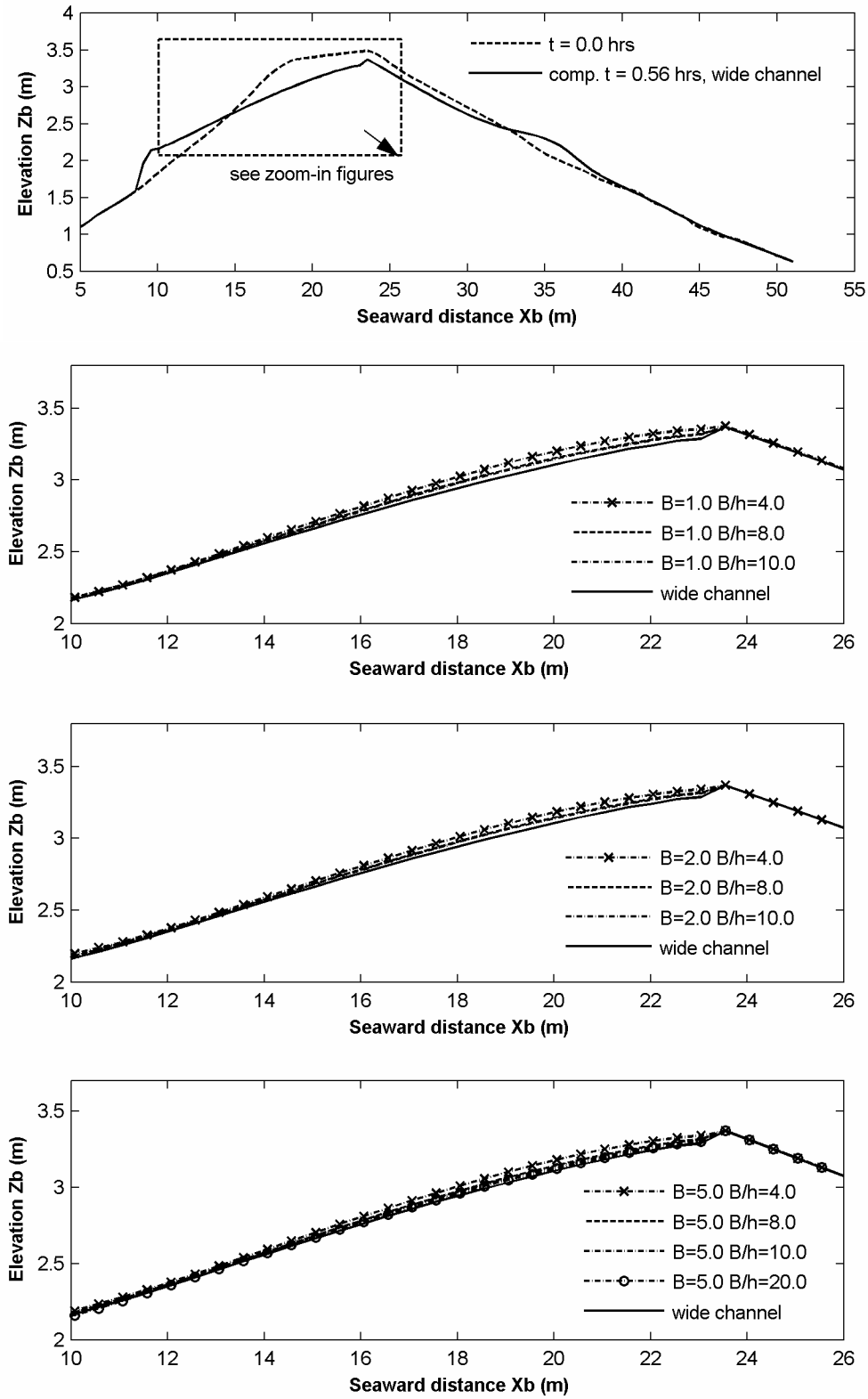

Figure 5.22 Effects of the initial channel dimensions on the channel vertical growth. From top to bottom: computed channel profile with wide channel option; channel profiles computed with various combinations of initial width and width-depth ratio, B = 1.0, B = 2.0, and B = 5.0 m and B/h = 4~20.

The channel initial dimensions appear to be variables that play a role in the development of the overwash processes. Their effects, as shown quantitatively in the figures, obey the general rule deduced earlier from the equation of cross-sectional growth index (see Section 4.3), i.e. a flatter initial channel would result in a faster increase rate of the channel width and depth and vice versa. Also, those computed profiles with a wider and flatter initial channel are closer to the wide-channel profile. Consequently, the vertical channel growth (bed level changes) can be virtually independent from the initial channel geometry as long as the initial channel is wide enough. The computation suggests a channel is considered sufficiently wide when its width $B \geq 5.0$ m and its width-to-depth ratio $B/h \geq 10$.

When overwash starts with a wide initial channel, the lateral enlargement has negligible effects on the vertical growth. This option therefore can be used in case the barrier crest level is uniform and only the barrier profile response is of interest.

5.8 SUMMARY AND CONCLUSIONS

Laboratory experiments were carried out to increase the understanding of the processes of mobile-bed (sand) barrier response during storm surges and also to generate data for calibration of the new numerical overwash model. Observations during the experiment and the measured topographic data have led to a qualitative description of the process of low-crested barrier response during storm surges together with some major overwash features, which were later used for judgement of the model performance. Also, overwash-related phenomena such as the overwash-induced reduction of the cross-shore transport and the landward-directed transport in the upper part of the swash-zone were clearly observed.

A numerical model of barrier response, which integrates the processes of beach and dune erosion and of wave overwash, has been developed. The approach of the UNIBEST-TC model was adopted for modelling the processes of beach and dune erosion. Overwash modelling is principally based on the findings of the preceding Chapters 3 and 4. Overwash-induced effects are also effectively incorporated. The model has been calibrated with the laboratory data on the barrier response (the barrier profile response and overwash channel development). Satisfactory agreement between the model prediction and the measurement was found. A model sensitivity analysis was also carried out with respect to the estimation of the spectral period $T_{m\text{-}1.0}$ and the dimensions of the initial channel.

In conclusion, the present model is capable of simulating the time-dependent barrier response during storm surges under the occurrence of moderate to severe overwash. The integration of the processes of beach and dune erosion and wave overwash was successful. Overall, the process of the barrier response together with its major morphological features was fairly well predicted. The new wave overtopping parameters elaborated in Chapter 3 have proven to be eligible for the overwash modelling. Also, the model capability of predicting the overwash channel growth indicates that the new process-based approach of modelling the channel growth presented in Chapter 4 is efficient and reliable for the morphodynamic modelling of wave overwash.

Chapter 6

COASTAL BARRIER BREACH MODELLING*

6.1 INTRODUCTION

In Chapter 5 we discussed the breach initiation phase due to wave and surge action during storms, which results in a potential initial breach channel in sand barriers. This phase is immediately followed by the breach erosion process in the case of landward breaching (surge overflow). Otherwise, seaward breaching (bay water overflow) is initiated whenever water starts to flow over a depressed portion in a barrier, which is either natural or created by previous overwash processes.

The present chapter is concerned with the development of a new numerical model of coastal sand barrier breaching due to overflow. As indicated in Chapter 2 the new model needs to be hydrodynamic-based so as to cope with the complex breach flow conditions. Breaching is regarded as a gradual erosion process starting with an initial (or pilot) channel. The breach modelling in fact comes down to a description of the enlargement in time of this channel both vertically and laterally. To this end, the modelling of breach growth can primarily rely on the process-based approach presented in Chapter 4. However, during the first stages of the breaching process a turbulent hydraulic jump is present and induces the scour formation and development in the breach. Therefore, effects of the jump need to be accounted for by a locally refined module.

We first discuss in Section 6.2 the flow modelling that considers the hydraulic jump as part of the breach flow conditions. To this end, a jump-turbulence source term is added to the horizontal momentum balance of the shallow water equations. The jump modelling is then calibrated with existing well-documented experimental data on the jump surface profile. In Section 6.3 the current profile under the effects of the jump turbulence and the associated breach sediment transport are discussed. The procedure for the computation of breach growth in both vertical and lateral direction is given in Section 6.4. Calibration and verification of the breach growth model using existing breach experimental data are addressed in Section 6.5. Discussion and

* Excerpts from this chapter were published as: Tuan, T.Q., Verhagen, H.J and Visser, P.J., 2006b. Advances in one-dimensional breach modelling of coastal sand barriers. *Proc. 3rd Int. Scour Erosion Conf.*, CURNET, pp. 649-658.

evaluation of the model performance are given in Section 6.6. We finalize the chapter with a summary and some conclusions in Section 6.7.

6.2 MODELLING THE BREACH FLOW WITH A TURBULENT HYDRAULIC JUMP

6.2.1 Hydraulic jump and scour in the breach channel

The hydraulic jump takes place at the downstream side of the breach, where there is a transitional state between the upstream supercritical and downstream subcritical flow. The jump properties, i.e. position, height, length, and turbulence are governed by the hydraulic conditions as well as by the breach geometry and bed roughness. During the breaching process, the jump can progress upstream as the downstream water level increases. Once a turbulent jump exists, the current profile as well as the surface profile are substantially modified. Extraordinarily, the maximum velocity is found very close to the bed (see e.g. Hager, 1992) which is in contrast with the logarithmic profile of open channel flows without a jump, where the maximum velocity is at the surface. Much more sediment is therefore agitated and brought into transport by the highly turbulent flow in the jump. As a consequence, a scour hole, which is a noticeable morphologic feature in the development of the breach, develops around the jump (see Fig. 6.1). The scour in the breach channel is highly dynamic illustrated by the observation that the jump moves back and forth during breaching.

It is argued by Visser (1998) that the vertical breach growth during the first three stages of breaching is controlled by the rate of erosion (or by the sediment transport rate) at the toe of the inner slope. In Visser's BRES model, this erosion rate is related to the uniform depth-averaged velocity at the toe of the inner slope using a prescribed sediment transport formula. With the presence of the jump covering the toe of the inner slope, the transport rate and so the erosion rate at this location is no longer sufficiently described by a depth-averaged velocity. Instead the flow structure of the jump should be considered (see Fig. 6.2). As a result, the jump turbulence strongly accelerates the vertical breach growth during this period. Hence, to model breach growth properly in general, it is essential to include the hydraulic jump as part of the breach flow conditions and to account for its effects on the breach sediment transport.

In order to model the scour formation and development, the flow structure in the jump is first required, which can be best resolved using 2DV Reynolds averaged Navier-Stokes (RAN) flow equations coupled with a turbulence closure model. This approach has been widely used to study stationary hydraulic jumps in hydraulic structures with a fixed bottom (see Section 6.3). However, it would be very complex and not efficient when it is applied to the non-stationary breaching of sand barriers, involving rapid bed level changes. To the author's knowledge no attempt has been made in using such a complex flow modelling approach in breach modelling. Alternatively, in a more efficient and sufficiently reliable approach one can utilize many (semi-) empirical jump formulations from the hydraulic engineering literature,

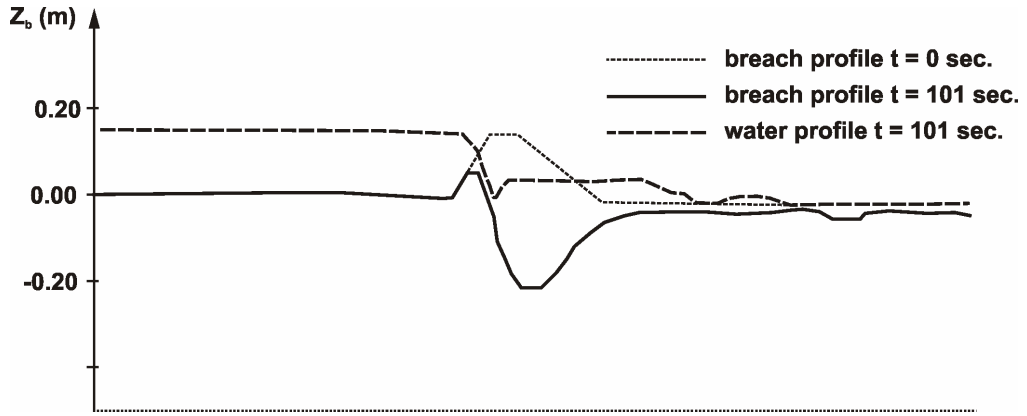

Figure 6.1 Laboratory dike breach experiment (Caan, 1996) showing the hydraulic jump and scour in the breach channel

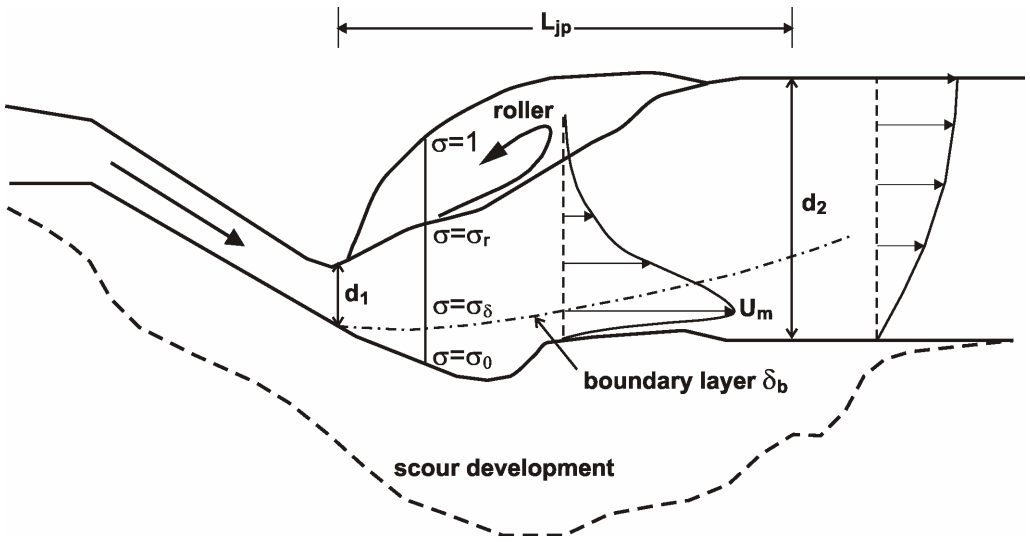

Figure 6.2 Definition sketch of the hydraulic jump and scour in the breach channel

whereby the flow structure of a turbulent jump is related to jump parameters such as the jump position, length, and depth. In the present study this latter approach is selected.

6.2.2 Jump-related source term in the horizontal momentum balance

As argued above, for modelling the breach growth it is of importance to predict the location, depth and the length of the jump reliably as a part of the breach flow conditions. Figure 6.2 illustrates a definition sketch of a turbulent hydraulic jump and associated scour development in the breach channel.

Most models of shallow flows (e.g. St. Venant equations) with shock-capturing techniques are able to predict the jump position well (Toro, 1997). The jump length, however, is dependent on the spatial discretization; typically it is of the order of several grid intervals (see e.g. Gharangik and Chaudhry, 1991; Khan and Steffler, 1996). This drawback is mainly attributed to the effect of depth integration, because of which information on the vertical velocity profile is lost. As a consequence, turbulent stresses and dissipation of turbulent energy across the jump cannot be fully accounted for in the horizontal momentum balance. Based on this implication a relatively simple approach to improve the jump modelling is derived as follows.

We start with the two dimensional RAN equations, which for an incompressible fluid are the equation of continuity:

$$\frac{\partial u}{\partial x} + \frac{\partial w}{\partial z} = 0 \tag{6.1}$$

and the equation of horizontal momentum:

$$\frac{\partial u}{\partial t} + u\frac{\partial u}{\partial x} + w\frac{\partial u}{\partial z} = -\frac{1}{\rho}\frac{\partial p}{\partial x} + \frac{1}{\rho}\frac{\partial \tau_{xx}}{\partial x} + \frac{1}{\rho}\frac{\partial \tau_{xz}}{\partial z} + \nu\left(\frac{\partial^2 u}{\partial^2 x} + \frac{\partial^2 u}{\partial^2 z}\right) \tag{6.2}$$

Neglecting vertical acceleration terms, the pressure distribution across the jump may be assumed hydrostatic (see e.g. Madsen and Svendsen, 1983):

$$p = \rho g(d - z) \tag{6.3}$$

Multiplying the equation of continuity by u and adding it to the horizontal momentum equation yields:

$$\frac{\partial u}{\partial t} + \frac{\partial u^2}{\partial x} + \frac{\partial uw}{\partial z} = -\frac{1}{\rho}\frac{\partial p}{\partial x} + \frac{1}{\rho}\frac{\partial \tau_{xx}}{\partial x} + \frac{1}{\rho}\frac{\partial \tau_{xz}}{\partial z} + \nu\left(\frac{\partial^2 u}{\partial^2 x} + \frac{\partial^2 u}{\partial^2 z}\right) \tag{6.4}$$

After rearranging we get:

$$\frac{\partial u}{\partial t} + \frac{\partial}{\partial x}\left(u^2 + \frac{p}{\rho} - \frac{1}{\rho}\tau_{xx} - \nu\frac{\partial u}{\partial x}\right) = \frac{\partial}{\partial z}\left(-uw + \frac{1}{\rho}\tau_{zx} + \nu\frac{\partial u}{\partial z}\right) \tag{6.5}$$

where, ν and ν_t are molecular and eddy viscosities, respectively; τ_{xx} and τ_{zx} are turbulent (Reynolds) stresses. These stresses can be determined based on the Boussinesq relations and the eddy-viscosity concept as follows.

$$\begin{aligned} \tau_{xx} &= -\rho\overline{u'u'} = \rho\nu_t\frac{\partial u}{\partial x} \\ \tau_{zx} &= -\rho\overline{u'w'} = \rho\nu_t\frac{\partial u}{\partial z} \end{aligned} \tag{6.6}$$

Integrating 6.2 over the flow cross-section A and neglecting the effect of molecular viscous stresses, the momentum equation is transformed into:

$$\frac{\partial U}{\partial t}+\frac{\partial}{\partial x}\left((1+\beta)U^2+\frac{1}{\rho}\int_A p\mathrm{d}A-\frac{A}{\rho}T_{xx}\right)=\frac{1}{\rho}\int_A\frac{\partial}{\partial z}\tau_{zx}\mathrm{d}A \tag{6.7}$$

in which β is the energy correction factor:

$$\beta=\int_A\left(\frac{u}{U}\right)^2\mathrm{d}A-1\ \ \beta=0 \text{ means a uniform flow,}$$

U is the depth-averaged velocity:

$$U=\frac{1}{A}\int_A u\mathrm{d}A$$

and T_{xx} is the depth-averaged normal stress:

$$T_{xx}=\frac{1}{A}\int_A\tau_{xx}\mathrm{d}A=\rho\overline{\nu}_t\frac{\partial U}{\partial x}$$

with $\overline{\nu}_t$ being the depth-averaged eddy viscosity.

Equation 6.7 can be rewritten as:

$$\frac{\partial Q}{\partial t}+\frac{\partial}{\partial x}\left(\frac{Q^2}{A}+gI_{1\mathrm{P}}\right)=\frac{\partial}{\partial x}\left(\frac{A}{\rho}T_{xx}\right)+\frac{1}{\rho}\int_A\frac{\partial}{\partial z}\tau_{zx}\mathrm{d}A \tag{6.8}$$

where we have substituted $\frac{\partial}{\partial x}(\beta)\approx 0$ and $I_{1\mathrm{P}}$ is the hydrostatic pressure force term

$$I_{1\mathrm{P}}=\int_A(d-z)\mathrm{d}A$$

The second term on the right hand side of Eq. 6.8 accounts for the effects of the turbulent shear stress (hereinafter designated R^*). Without the presence of a discontinuity (e.g. a jump) in the flow, this term can be quantified as follows.

$$R^*=\frac{1}{\rho}\tau_{zx}\Big|_{z=0}^{z=Z_s}=\frac{1}{\rho}\overline{B}(\tau_{zx}\big|_{z=Z_s}-\tau_{zx}\big|_{z=Z_b}) \tag{6.9}$$

where, Z_s and Z_b stand for the elevations at the surface and the bottom, respectively.

If the shear stress is assumed zero at the surface, R^* retains only the bed shear stress, i.e. the second term on the right hand side of Eq. 6.9. Further simplification by neglecting the contribution from the normal stress T_{xx} reduces Eq. 6.8 to the ordinary shallow water equation (or St. Venant). It is worth noticing, on mathematical grounds, that the integration in Eq. 6.9 is only viable as long as τ_{zx} is differentiable at any arbitrary elevation z over the flow depth domain. In other words, τ_{zx} must be first continuous and then $\partial\tau_{zx}/\partial z$ must exist or be bounded at any z.

However this may not be the case over a vertical section in a turbulent hydraulic jump, where a part of the roller slides against the incident flow (see e.g. Svendsen et

al., 2000). In a mechanical sense, along the lower limit of the roller there exists sliding stresses against the flow underneath. These sliding forces make τ_{zx} discontinuous along this boundary and thus indifferentiable. Further, as the flow structure in the roller is violently turbulent with entrained air bubbles and vortices, it is uncertain whether τ_{zx} is continuous over the roller.

From the above, R^* resulting from the integration over the entire water depth including the roller may result in errors in the horizontal momentum balance. Therefore, the roller should be treated separately as a turbulence source regardless of its internal turbulence structure. Following this approach, R^* is integrated until the lower limit of the roller and then supplemented with the shear stress imposed by the roller:

$$R^* = R_{jp} - \frac{1}{\rho}\frac{A}{d}\tau_b = \frac{1}{\rho}\frac{A}{d}(\tau_r - \tau_b) \tag{6.10}$$

where the subscript $(_r)$ denotes the lower limit of the roller, τ_r is the shear stress imposing by the roller. R_{jp} is the stress term arising from the roller:

$$R_{jp} = \frac{1}{\rho}\overline{B}\,\tau_{zx}\big|_{z=Z_s} = \frac{1}{\rho}\frac{A}{d}\tau_r \tag{6.11}$$

We regard the roller as an independent source of turbulent energy that is transmitted into the flow underneath. Mechanically, τ_r can therefore be estimated through the work done by the roller.

$$\tau_r = \rho\frac{D_t}{u_r} = \rho\frac{D^*}{\varepsilon_j u_r} \tag{6.12}$$

In which D_t is the production of the turbulent energy by the roller or loss of the mean flow energy to turbulence, D^* is the dissipation of the turbulent energy, which is not necessarily equal to D_t, u_r is a nominal relative velocity between the roller and the incident flow, ε_j is an energy efficiency factor, ε_j =1 implies local equilibrium.

In a turbulent flow, loss of the mean flow energy is first converted into the turbulent kinetic energy (via production) and then gradually dissipated into heat (via dissipation). It is therefore rational, in a jump, to relate the dissipation D^* to the head loss (energy loss expressed in terms of water head) across the jump:

$$D*(x) = \beta_h\frac{gq\delta h}{L_{jp}} \tag{6.13}$$

in which $D^*(x)$ is the space-varying energy dissipation, δh is a local head loss, L_{jp} is the length of the jump, q is the unit discharge, and β_h is an energy correction factor.

With Eq. 6.13 substituted, Eq. 6.12 can be rewritten as:

$$\tau_r = \left(\frac{\beta_h}{\varepsilon_j}\frac{U}{u_r}\right)\frac{\rho g d\delta h}{L_{jp}} = \beta_j\beta_u\frac{\rho g d\delta h}{L_{jp}} \tag{6.14}$$

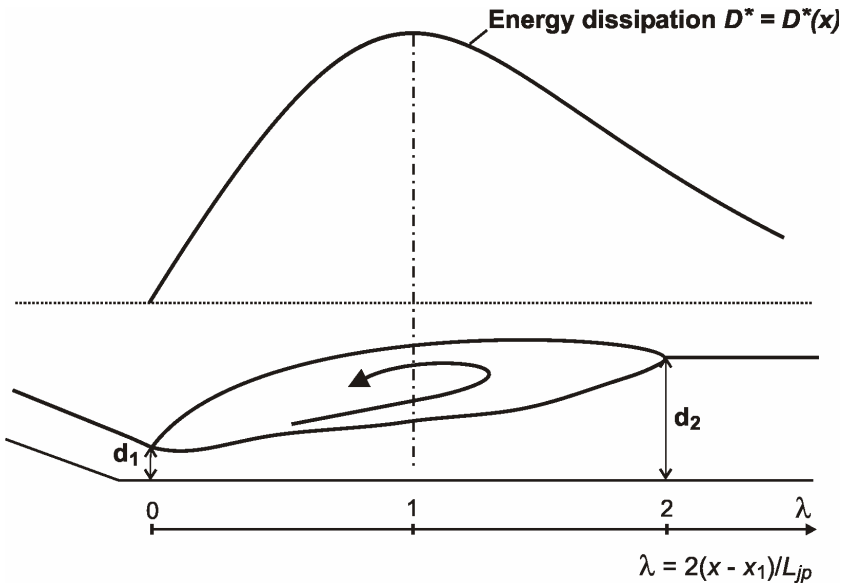

Figure 6.3 Spatial distribution of the energy dissipation

where we have substituted $q=U^*d$, U and d are the depth-averaged flow velocity and the mean flow depth, respectively, $\beta_j = \beta_h / \varepsilon_j$ and $\beta_u = U / u_r$ are empirical coefficients to be specified later.

Physically, β_j stipulates the spatial distribution of the dissipation D^* in relation with the production D_t, and β_u is a nominal relative velocity factor.

Now the jump source term in Eq. 6.11 becomes:

$$R_{jp} = \beta_u g A \frac{\delta h(x)}{L_{jp}} = \beta_u g A S_{jp} \tag{6.15}$$

where $\delta h(x) = \beta_j^* \delta h$ and the term $S_{jp} = \delta h(x) / L_{jp}$ represents the slope of the head loss across the jump.

The inclusion of the above jump source term in the momentum equation requires a spatial distribution of $D^*=D^*(x)$ or $\delta h = \delta h(x)$. Preceding studies on turbulent jumps (see e.g. Madsen and Svendsen, 1983) indicate that empirical distributions of the dissipation D^* can be adopted, generating the character of the jump turbulence. Hence, the spatial distribution of δh can be expressed as follows.

$$\delta h(\lambda) = \Delta h . f(\lambda) \tag{6.16}$$

Where Δh is the total head loss across a classical hydraulic jump, $f(\lambda)$ is a shape function of the energy loss.

To specify $f(\lambda)$, some relevant features of a turbulent jump must be realized. These are the turbulence production mostly generated within the roller length, but the dissipation spreads over a distance of several times the jump length (a four-jump length distance is usually considered). Also, the largest dissipation occurs at the central region of the roller (see e.g. Madsen and Svendsen, 1983; Svendsen et al., 2000).

Mathematically, the following properties of $f(\lambda)$ are realized from the above arguments (see also Fig. 6.3):

$$f = 0 \qquad \text{for} \begin{cases} \lambda = 0 \quad \text{or } x = x_1 \\ \lambda \to \infty \text{ or } x \to \infty \end{cases} \tag{6.17a}$$

$$\begin{aligned} f &= f_{\max} && \text{for } \lambda = 1 \text{ or } x = x_1 + 1/2L_{jp} \\ \partial f / \partial \lambda &> 0 && \text{for } \lambda < 1 \\ \partial f / \partial \lambda &< 0 && \text{for } \lambda > 1 \end{aligned} \tag{6.17b}$$

$$\int_0^\infty f(\lambda) d\lambda = 1. \tag{6.17c}$$

where λ is a dimensionless length parameter $\lambda = 2(x - x_1)/L_{jp}$.

The following function is introduced that fully satisfies the above criteria Eq. 6.17a through Eq. 6.17c:

$$f(\lambda) = \lambda e^{-\lambda} \tag{6.18}$$

Neglecting the source term by the depth-averaged normal stress $\frac{\partial}{\partial x}(A T_{xx}/\rho)$, the horizontal momentum balance Eq. 6.8 can be written as follows:

$$\frac{\partial Q}{\partial t} + \frac{\partial}{\partial x}\left(\frac{Q^2}{A} + g I_{1P}\right) = gA(S_{bx} - S_f + \beta_u S_{jp}) \tag{6.19}$$

where S_{bx}, S_f, and S_{jp} are the bottom, friction, and jump head loss slopes respectively.

Equation 6.19 compared to its original form in Eq. 4.2 contains one extra jump-related source term on the right hand side. As already presented in Section 4.2, this term needs to be upwinded using the approach of Garcia-Navarro and Varquez-Cendon (2000). Consequently, for the case of breach flow with a hydraulic jump, the source term coefficient $\hat{\beta}$ in Eq. 4.13 reads (see also Eq. 4.14):

$$\hat{\beta} = \frac{g\Delta x}{2\hat{c}} \overline{A}(\overline{S}_{bx} - \overline{S}_f + \beta_u S_{jp}) \tag{6.20}$$

It is noted that, by definition, the jump source term S_{jp} in Eq. 6.20 is negligible outside the jump affected region ($f(\lambda)$=0.003 at λ = 8.0 or four times the jump length) so that it does not influence the momentum balance of the flow in that area.

The total head loss in a classical hydraulic jump can be estimated analytically as (see Hager, 1992):

$$\Delta h = \frac{(d_2 - d_1)^3}{4 d_1 d_2} \tag{6.21}$$

where d_1 and d_2 are the water depths at the toe and at the end of the jump, respectively. These depths d_1 and d_2 are not known in advance so iterations are needed.

The laboratory experimental data of jump surface profiles of Gharangik and Chaudhry (1991) and of Hermann and Hager (1998) are selected to calibrate the empirical coefficient in the jump source term, viz. the nominal relative velocity factor β_u. The former experiments were carried out in a rectangular and horizontal flume with Froude numbers between 2.30 and 7.0. In the latter experiments hydraulic jumps were formed downstream of an embankment.

Figures 6.4 and 6.5 show the computed jump profiles in comparison with the laboratory measurements. In the computation the Manning coefficient for the flume was determined by trial and error to achieve the best agreement with the measurements. This coefficient varies in the ranges between 0.008 and 0.010 for the first case (in agreement with Gharangik and Chaudhry, 1991) and between 0.028 and 0.037 for the second case. In both cases, fairly good agreement of the surface profiles is found for a constant value of the nominal relative velocity factor $\beta_u = 2.0$.

It is worth mentioning that the present study disregards undular jumps (waves), i.e. Froude number less than 2.0 and jumps formed outside the breach channel, because of their irrelevance to the breach sediment transport. Moreover, the shallow water equations are capable to model this specific type of short waves.

6.2.3 Discussion

In general, agreement of the computed jump profiles with those from measurements is reasonably good for various jump strengths and bed slope conditions. In the case of jumps formed at the toe of the inner slope of the embankment, agreement is less satisfactory when the downstream water level is high (near submerged situation). However, all necessary jump parameters for the present objective such as the position, depths, and length are well predicted. The present approach appears to be reliable and easy for incorporating in the breach flow modelling.

6.3 FLOW STRUCTURE IN A JUMP AND BREACH SEDIMENT TRANSPORT

6.3.1 Flow structure in turbulent hydraulic jumps

The flow structure in hydraulic jumps has been studied extensively given its importance to the design of hydraulic works. Models of the flow structure in hydraulic jumps can be categorized into full hydrodynamic and semi-hydrodynamic. In the first group the RAN equations (or similar type) coupled with the standard turbulent closure k-ε model are used to resolve the flow structure. Examples of models of this type are described by Long et al. (1991), Liu Qinchao and Uwe Drewes (1994), and Busnelli (2001). In the second group, which is much simpler and less fundamental, the shape of the velocity profile is empirically specified in several zones over the vertical

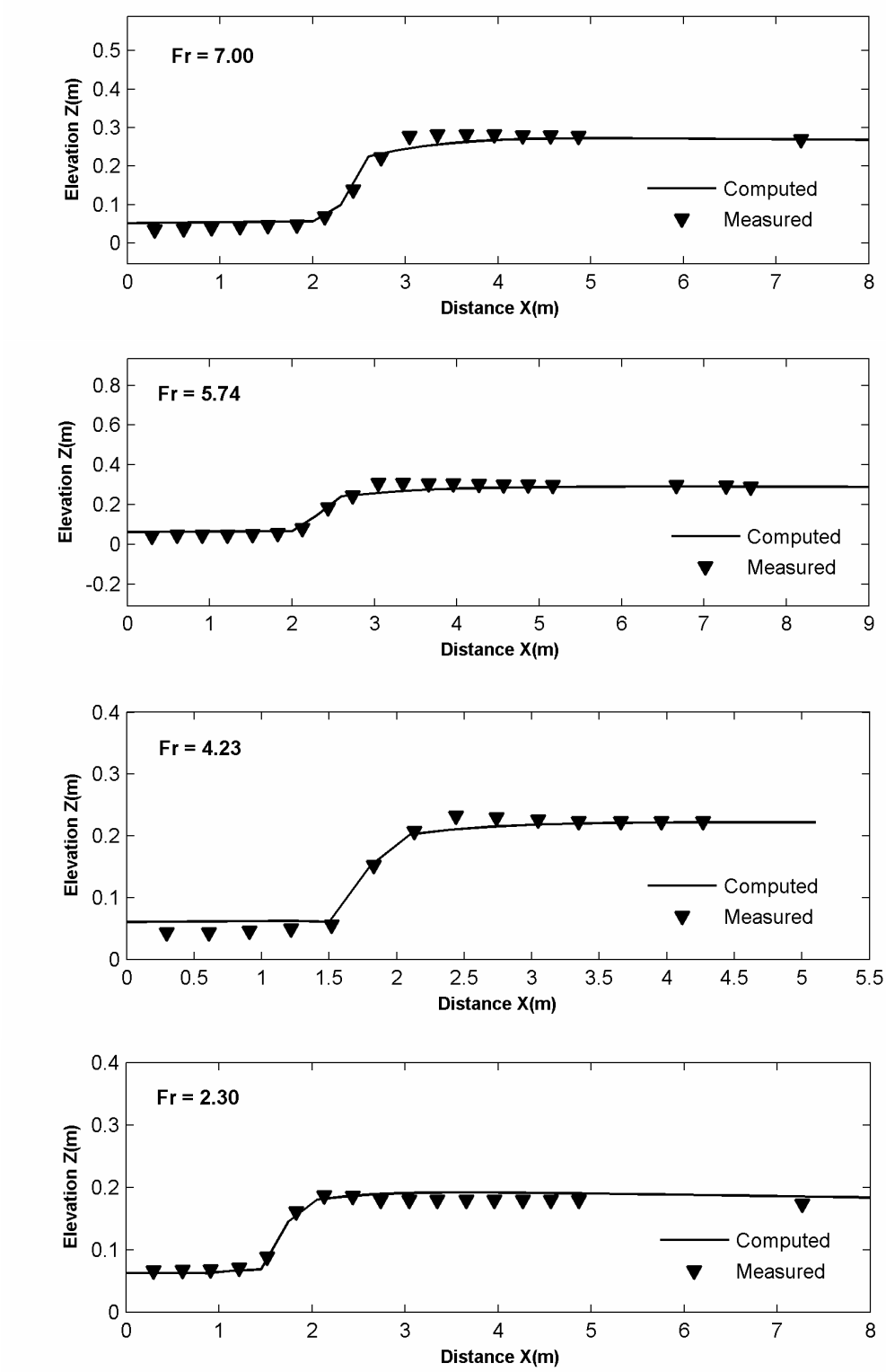

Figure 6.4 Computed jump profiles on a horizontal bed (measured data by Gharangik and Chaudhry , 1991)

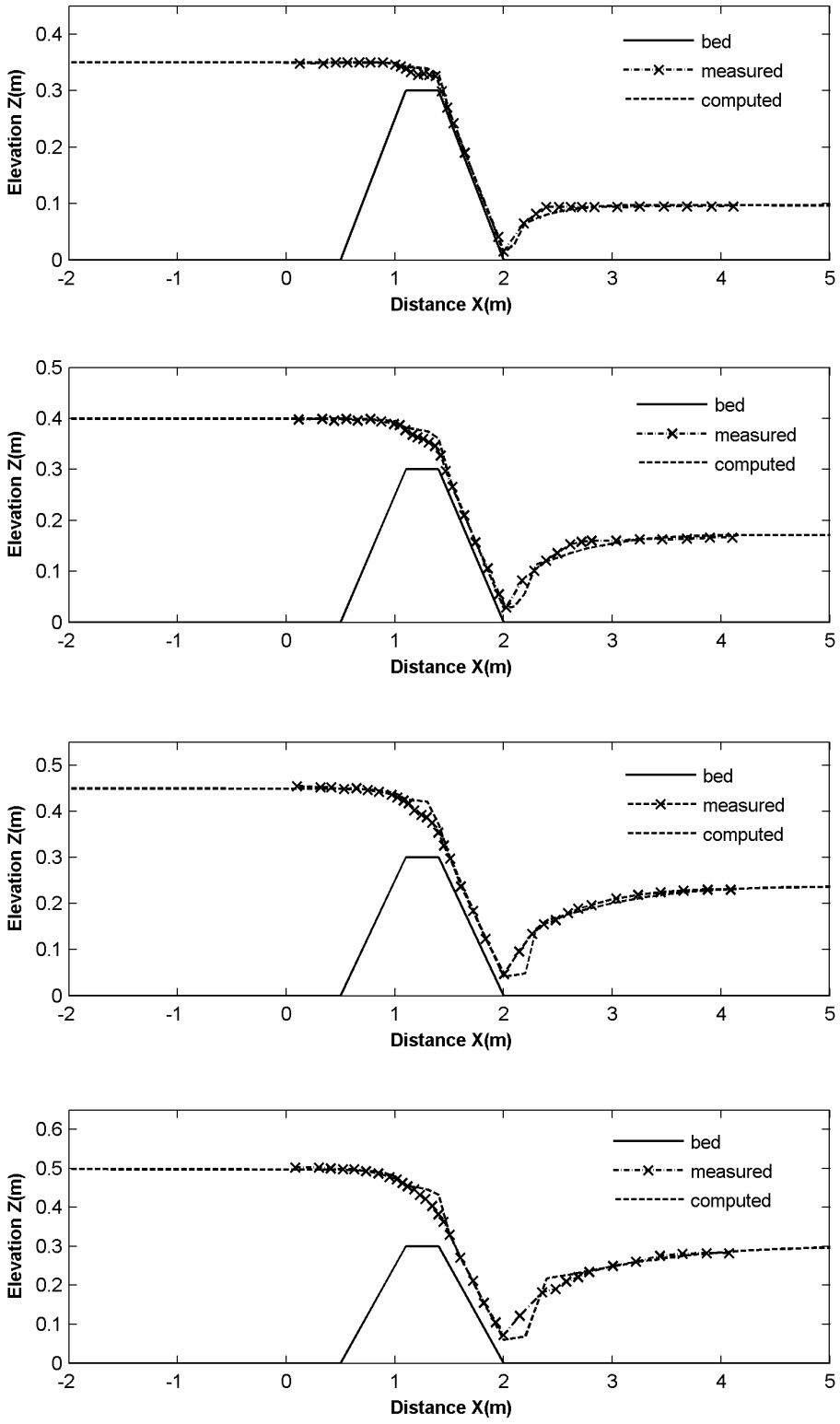

Figure 6.5 Computed jump profiles behind an embankment (measured data by Hermann and Hager, 1998)

or is based on a simplified turbulence closure model (e.g. one or zero equation). Some typical models are described by Madsen and Svendsen (1983), and Svendsen et al. (2000). The flow structure in turbulent hydraulic jumps is highly complex. A more complicated model that requires more computational time does not always give more reliable results. Therefore, a choice of a modelling approach amongst those model groups should depend also on the particular situation so that a problem of interest can be solved efficiently with a sufficient level of reliability.

To be efficient and consistent with the jump modelling discussed earlier, a three-layer approach is used in the present model to compute the flow structure of the hydraulic jump in the breach channel. The depth domain of the flow within the jump-affected region is divided into three layers as shown in the following (see also Fig. 6.2). The velocity profile over the layers is specified according to the approach of Ohtsu reported by Chanson and Brattberg (2000) and Hager (1992), which is commonly used for jump modelling.

The boundary (or near wall) layer ($Z_0 \leq z \leq \delta_b$):

The boundary layer extends from the bottom to the elevation of the maximum horizontal velocity U_m. The velocity in this layer obeys the law of the wall for a jet, increasing away from the bed in a power manner:

$$\frac{u}{U_m} = \left(\frac{\sigma}{\sigma_b}\right)^{\alpha} \quad \text{with} \quad \alpha = 1/7 \tag{6.22}$$

The mixing (middle) layer ($\delta_b \leq z \leq Z_r$):

The mixing layer lies between the boundary layer and the surface roller. The velocity distribution in this zone is quadratic exponential as follows:

$$\frac{u}{U_m} = \exp\{-[\eta(\frac{\sigma}{\sigma_b} - 1)]^2\} \tag{6.23}$$

The roller layer ($Z_r \leq z \leq d$):

The roller above the mixing layer is treated as a "dead" layer, only yielding a shear stress boundary on the incident flow. The flow structure in this zone is disregarded since it is irrelevant to the sediment transport in the breach.

The boundary layer gradually grows in the streamwise direction, starting from the toe of the jump. The thickness of the boundary layer δ_b can be deduced from Hager (1992), using the dimensionless length λ and $L_{jp} = mL_r$:

$$\frac{\delta_b}{d_2 - d_1} = 0.06\left[1 + 5\left(\frac{m\lambda}{2} - \frac{1}{4}\right)^2\right] \quad \text{for } \frac{0.1}{m} \leq \lambda \leq \frac{2.8}{m} \tag{6.24}$$

In the above formulations, σ is the dimensionless vertical coordinate (see also Fig. 6.2) $\sigma = z/d$, $u = u(\sigma)$ is the velocity at an arbitrary level σ, $\sigma_0 = Z_0/d$, $\sigma_b = \delta_b/d$, σ_r

$= Z_r/d$, $U_m = u(\sigma = \sigma_b)$, L_r is the length of the surface roller, Z_0 is the zero velocity level, coefficient $\eta = 0.44$ deduced from the formulation of Ohtsu (see Chanson and Brattberg, 2000), and m ≈ 1.25 (Hager, 1992).

It follows from Eqs. 6.22 and 6.23 that the entire velocity profile can be determined if the maximum velocity at the top of the boundary layer U_m is known. This can be resolved by averaging $u(\sigma)$ over the vertical domain $[\sigma_0, \sigma_r]$:

$$\frac{1}{\sigma_r}U = \frac{1}{\sigma_r}\left(\int_{\sigma_o}^{\sigma_b} u d\sigma + \int_{\sigma_b}^{\sigma_r} u d\sigma\right) \tag{6.25}$$

It is noted that $1/\sigma_r$ on the right hand side of Eq. 6.25 is the correction to the depth-averaged velocity as in the flow model the mean velocity U is averaged over the entire water depth including the roller. Substitution of Eqs. 6.22 and 6.23 into Eq. 6.25 and after some algebraic manipulation yields:

$$U_m = \frac{U}{\sigma_b\left(\frac{\sqrt{\pi}}{2\eta}\,\mathrm{erf}(\eta(\frac{\sigma_r}{\sigma_b} - 1)) + \frac{1}{1+\alpha}\right)} \tag{6.26}$$

where erf(•) is the error function.

The error function erf(•) is quickly asymptotic to unity as (•) → 2.9. Consequently, erf(•) ≈ 1 when $\sigma_r/\sigma_b \geq 4.40$, which is valid within the roller area ($\lambda \leq 1.60$) as can be deduced from Eq. 6.24 ($\sigma_b = 0.228$ with $\lambda = 1.60$). Hence, Eq. 6.26 can be further simplified to:

$$U_m = \frac{U}{\sigma_b\left(\frac{\sqrt{\pi}}{2\eta} + \frac{1}{1+\alpha}\right)} \qquad \text{for } \lambda \leq 1.60 \tag{6.27}$$

For the determination of U_m the effect of the unknown roller height in the roller area is therefore eliminated. Outside the roller area (λ >1.60) Eq. 6.26 is used with $\sigma_r = 1$.

With the depth-averaged velocity U and the jump profile (d_1, d_2, L_{jp}) determined from the flow model presented earlier, the velocity profile in the jump-affected region is fully determined using Eqs. 6.22 and 6.23 together with Eqs. 6.24, 6.26 and 6.27.

6.3.2 Breach Sediment Transport

In terms of sediment transport the breach channel is split into two regions, one under the jump and the other outside the jump.

Outside the jump a suitable depth-averaged transport approach can be used. An investigation of various formulae for this purpose has been presented by Visser (1998). In the present model the formulations of Van Rijn (1984a, b) are used. These formulations are widely used in practice, especially applicable for purposes of numerical morphological modelling.

To the author's knowledge there has been no study on the sediment transport under turbulent hydraulic jumps, for which more physical insight into the sediment bursting processes is needed. In the present model we propose the following computational approach for this manner, which utilizes the flow structure in the hydraulic jump.

We consider the total transport load as the sum of suspended load and bed load. The suspended load is calculated as the integration of the product between the velocity $u(z)$ and the sediment concentration $c(z)$ over the water depth:

$$q_s = \int_a^{Z_r} u(z)c(z)dz \tag{6.28}$$

with a is a reference level above the bed where the reference concentration is specified.

The concentration profile is determined numerically using the diffusion equation:

$$c(z)w_s + \varepsilon_s(z)\frac{dc}{dz} = 0 \tag{6.29}$$

where w_s is the sediment fall velocity, ε_s is the sediment mixing coefficient at height z above the bed, $\varepsilon_s(z)$ is adopted here as a parabolic-constant distribution (see Van Rijn, 1984b), the reference concentration required at the level a above the bed is also determined according to Van Rijn (1984b).

In the jump the maximum horizontal velocity is located near the bottom. Therefore, the shear stress exerting on the bed is high and transport near the bed is expected to occur as sheet flow conditions. Bed-load formulae, in which the bed shear stress is based on the depth-averaged velocity such as in Van Rijn (1984a), appear to underestimate the transport rate. For this reason, the general bed load formulation of Ribberink (1998) is selected (see also Eq. 5.22):

$$\frac{q_b}{\sqrt{g\Delta d_{50}^3}} = M_b(\theta' - \theta_{cr})^n \qquad \text{for}\,\theta' > \theta_{cr} \tag{6.30}$$

where $M_b \approx 11.0$ is a dimensionless empirical constant.

The transport rate q_b depends largely on the determination of the effective Shield number θ' or of the bed shear stress:

$$\theta' = \frac{\tau_b}{\rho g \Delta d_{50}} = \frac{u_*^2}{\Delta g d_{50}} \tag{6.31}$$

where u_* is the bed friction velocity.

In steady flows the bed shear stress τ_b can be related to the depth-averaged velocity U, assuming a logarithmic profile over the entire water depth:

$$\tau = \frac{1}{2}\rho\frac{U^2}{C^2} \qquad \text{with}\, C = 18\log\left(\frac{12h}{k_s}\right) \tag{6.32}$$

$$\begin{aligned} k_s &= 3\theta' d_{90} \qquad \text{for } \theta' > 1 \\ k_s &= 3 d_{90} \qquad \text{for } \theta' < 1 \end{aligned} \tag{6.33}$$

where C is the Chezy coefficient, k_s is the effective roughness according to Van Rijn (Van Rijn, 1984a).

Alternatively, according to the law-of-the-wall, τ_b can be determined using the velocity at a prescribed level above the bed in the logarithmic layer (Ribberink, 1998):

$$\tau_b = \frac{1}{2}\rho f_c u_b^2 \tag{6.34}$$

$$f_c = 2\left(\frac{0.4}{\ln Z_\delta / Z_0}\right)^2 \tag{6.35}$$

in which f_c is the friction coefficient, Z_δ is an arbitrary level, $Z_0 = k_s/30$ is the zero velocity level, u_b is the velocity at Z_δ.

In general, the determination of the bed shear stress according to the latter approach is more valid than the former one because a logarithmic velocity profile is assumed over a small layer near the bed only instead of over the whole water column.

To avoid numerical iterations in the determination of the effective Shields number due to k_s being also a function of θ' for areas inside the jump ($\theta' > 1$), we estimate the bed shear stress at height $Z_\delta = k_s$. From Eq. 6.35 a constant friction coefficient f_c (~ 0.02) is found. Using Eq. 6.22 for u_b, Eq. 6.33 for k_s and then substituting into Eq. 6.34 we yield:

$$\frac{\tau_b}{\rho} = u_*^2 = \frac{1}{2} f_c' U_m^2 \tag{6.36}$$

with f_c' being an another friction coefficient as follows:

$$f_c' = f_c \left(\frac{3\theta' d_{90}}{\delta_b}\right)^{2\alpha} \tag{6.37}$$

Eventually, the effective Shields number reads:

$$\theta' = \left(\frac{1}{2} f_c U_m^2 \left(\frac{3 d_{90}}{\delta_b}\right)^{2\alpha}\right)^{1/(1-2\alpha)} \tag{6.38}$$

It is noted that although we have estimated the friction coefficient at Z_δ, i.e. $u_b = u(z = Z_\delta)$, relations Eq. 6.36 through Eq. 6.38 allow the explicit determination of the bed shear stress through the maximum velocity U_m at the top of the boundary layer.

The present model assumes only one major jump in the breach channel and thus disregards any other jumps and associated scours further downstream of the breach.

6.4 COMPUTATION OF THE VERTICAL AND LATERAL BREACH GROWTH

The computation of breach growth again follows the process-based approach presented in Section 4.3 (Chapter 4) with the transport rates presented in the previous section.

To avoid spurious discontinuity of the bed due to an abrupt increase of the transport rate at the toe of the jump, the calculated transport field is smoothed using a response function before it is used in Eq. 4.57 to update the bed level change:

$$\frac{dq_{st}}{dx} = \frac{q_{st,c} - q_{st}}{L_a} \tag{6.39}$$

where $q_{st,c}$ is the total sediment transport rate obtained directly from the transport module, q_{st} is the transport after smoothing and is used for updating the bed change, L_a is an adaptation length for the sediment entrainment.

It is noted that such a smoothing procedure is commonly used in numerical morphological modelling since the flow needs some transitional distance before it can fully adapt to the local conditions (see e.g. Jorgen Fredsoe and Rolf Deigaard, 1992). It is shown by Visser (1998) that the adaptation length for sediment entrainment plays a role in the breach transport modelling, necessary to compute the breach erosion rate more properly.

Visser (1998) adopted the approach of Galappatti (1983) for L_a to the breaching case:

$$L_a = \xi \frac{Ud}{w_s \cos\beta} \tag{6.40}$$

where ξ is an empirical constant, β is a local bed slope (here we use $\cos\beta = \cos\gamma \approx 1$).

In principle, a larger ξ and so L_a would result in a milder erosion rate and vice versa. An appropriate value of ξ should be chosen for each particular situation. Visser (1998) uses $\xi = 1.0$ for his first three stages (L_a includes then also the adaptation length of the supercritical flow on the downstream slope) and $\xi = 0.40$ for the last two stages (subcritical regime) of the breach erosion process. In the present model, a mixed-regime flow (both subcritical and supercritical) is allowed to occur during breaching. Hence, different values of this parameter for different flow regions can be used. Especially, within the jump region high turbulence stirs up sediment violently and thus tends to shorten the adaptation length for sediment entrainment, i.e. $\xi < 0.40$ is expected for the jump-affected region.

Behind the downstream end of the breach channel, the flow is complex having a three dimensional structure with horizontal circulations. Here the sediment transport spreads out widely. Therefore, the mass balance equations for the channel growth (Eqs. 4.21 and 4.52) are no longer valid at this location. To overcome this problem, a non-depositing bed boundary is applied. This assumption seems to work well as seen later in a comparison of the computational results with the laboratory breach data of Caan (1996).

6.5 MODEL CALIBRATION AND VERIFICATION

6.5.1 Existing breach experiments

The breach model formulated so far needs empirical calibration and verification. For this purpose, we utilize the data from the existing breach experiments, which were used to calibrate and validate the BRES model (Visser, 1998). These include the Zwin'94 field experiment and the laboratory experiment of Caan (1996). The laboratory experiment is selected for the model calibration since this experiment is most complete, including observation of the scour development. The model is then verified against the data from the field experiment. In both experiments, the breach was initiated by a small pilot channel made in the crest of the dike. The flow of water through this pilot channel started the breach development process. Details of the experimental procedures and the measurements can be found in Visser (1998) and Caan (1996, see also Visser, 1998). In the following only a brief description is given.

The Zwin'94 field experiment was carried out in 1994 in the Zwin channel, a tidal inlet at the Dutch-Belgian border. A sand-dike closing the Zwin channel was built with a height of 2.6 m above the channel bottom and a width at the crest level of 8 m. The pilot channel was 0.8m in depth and width was 1 m at the bottom and 3.6 m at the dike crest. The test was carefully prepared to measure the complete breach erosion process. Unfortunately, due to a technical failure during the experiment only a limited number of data points of the breach level were logged and only those of the channel lateral development were completely measured. Because of the incident, the experiment left behind some ambiguity about the scour development and the reliability of the breach bottom level observation. It was then decided to conduct an additional laboratory experiment, viz. the Caan's experiment. This experiment consisted of two tests of small-scale dikes constructed in a wave basin. Video and photo cameras were used to capture the vertical and lateral breach development. The breach profile was video-taped through a glass-wall which acted as the central axis of the breach. Initially, water flowed through a pilot channel of 3cm deep and 20 cm wide notched in the dike crest. The flow spilled downstream into a dry sand polder. The first test was less successful because the sand bed was so thin that the basin bottom was exposed shortly after the start of the breaching. From this experience the dike geometry and the sand bed were adjusted yielding a successful breach development in the second test. However, due to exaggerated scale effects only a part of the experimental data of the breach scour development can be used. This is from the beginning up to the moment when the dike was completely washed out with a scoured base (say until t = 300 s). After this moment, irregular bumps and scour holes continued to develop vigorously but mainly on the downstream side (outside) of the breach channel. This noticeable secondary downstream scour, which was caused by a relatively dry and soft sand bed polder behind the dike, had a substantial influence on the vertical breach growth (see Fig. 6.6). Moreover, video observations and the measurements indicate that the breach flow in the later period was significantly disturbed by the supply discharge pumped into the upstream section of the breach (two pipes with maximum capacity of $0.66 m^3/s$). Figure 6.6 partly explains the situation, in which water was virtually pumped directly into the breach.

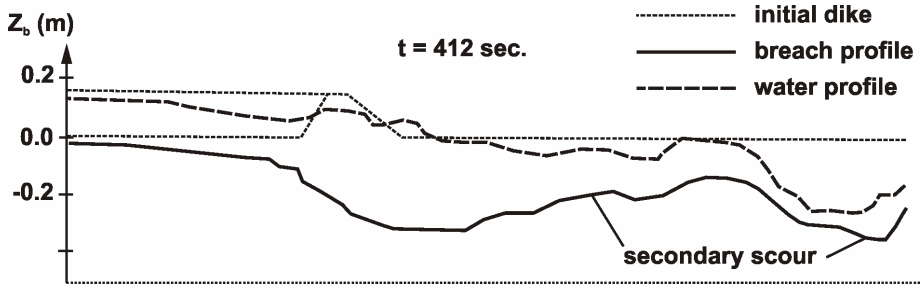

Figure 6.6 Noticeable secondary scour (scale effects) downstream of the breach, Caan's laboratory experiment

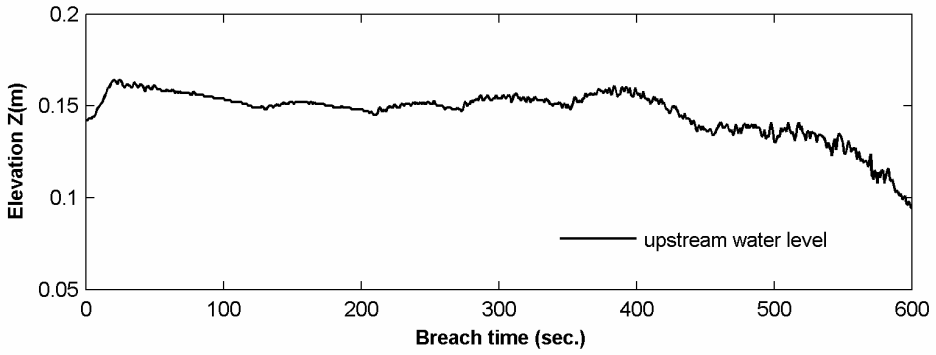

Figure 6.7 Measured upstream water level variation, Caan's laboratory breach experiment

6.5.2 Model calibration

Based on the experimental results of Caan (1996), the simulation period was chosen up to the moment when the scour within the breach channel has largely reached its maximum dimension (at the breach time t = 300 s). As mentioned earlier, only the measured data within this period are considered relevant for the present calibration purpose.

The following parameters were used as input for the simulation of the laboratory dike breach (see also Caan, 1996 and Visser, 1998).

- Hydraulic boundary: upstream water level: variation in time as shown in Fig. 6.7, downstream water level: dry (no measurement available);
- Pilot channel: $B_{t0} = 0.20$ m, $h_{L0} = 0.03$ m;
- Sand properties: $d_{50} = 0.088$ mm, $d_{90} = 0.12$ mm, $w_s = 0.007$ m/s, angle of internal friction $\gamma = 32^{o}$, porosity $p = 0.35$;
- Transport and breach growth: transport exponent $n = 1.65$, friction coefficient $f_c = 0.015$, bed roughness $k_{s,c} = 0.01$ m (for suspended load transport according to Van Rijn, 1984b), Manning coefficient $M_n = 0.02$, $\xi = 0.10$ and 0.40 for inside and outside jump-affected regions, respectively;
- Numerical scheme: $\Delta x = 0.02$ m, CFC = 0.30.

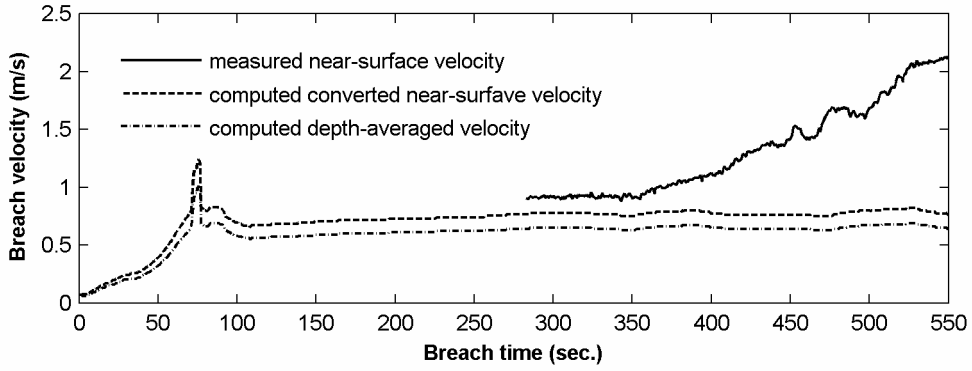

Figure 6.8 Velocity of a point in the breach ($x = 1.3$ m): computed versus measured, Caan's laboratory experiment

Unfortunately, there are almost no reliable data available for the calibration purpose of the hydrodynamic part of the model since this was not aimed at in the experiment. The breach velocity was measured near the water surface at only one location in the breach and this was only possible during the last period of breaching.

Figure 6.8 shows the comparison of the measured velocity histogram at the upstream edge of the dike crest with that computed by the model (at $x = 1.30$m, see also Fig. 6.9; measured velocity is available from t = 280 s). In the figure the near-surface velocity is given by the measurement whilst the model computes the averaged velocity. Hence, for the sake of comparison a conversion factor is assumed as follows, based on a logarithmic velocity profile over the entire water depth at the considered point (see also Van Rijn, 1993):

$$\frac{U(z=d)}{U} = \frac{\ln(33d/k_{s,c})}{\ln(33d/k_{s,c})-1} \tag{6.41}$$

where $k_{s,c}$ is the current-related bed roughness.

Fair agreement is found for the first part of the measured hydrograph. Clearly, at around t = 400 s the upstream water level started to decline (see Fig. 6.7), which, in case of a self developing breach, should not lead to an increase of the breach velocity but to a decrease, as also predicted by the model. However, the measured data of Fig. 6.8 show the opposite. This is most probably due to the disturbance effects of the water supply addressed earlier (at this moment the dike in the breach section has been completely washed out).

Figures 6.9 and 6.10 show the comparison of the computed and measured breach profiles at various time steps. The comparison for the lateral breach growth is shown in Fig. 6.11. It is noted that the model computes the representative breach width while the breach top width is given from the measurements. Therefore, a conversion between these two width quantities according to Eq. 4.50 (see Section 4.3) is necessary for the sake of comparison. Agreement of the breach profile evolutions is fairly good for the early period of the breaching process (until the dike is completely washed-

out). However, the model under-predicts the scour depth systematically in the last breaching period. The lateral breach growth is generally well predicted.

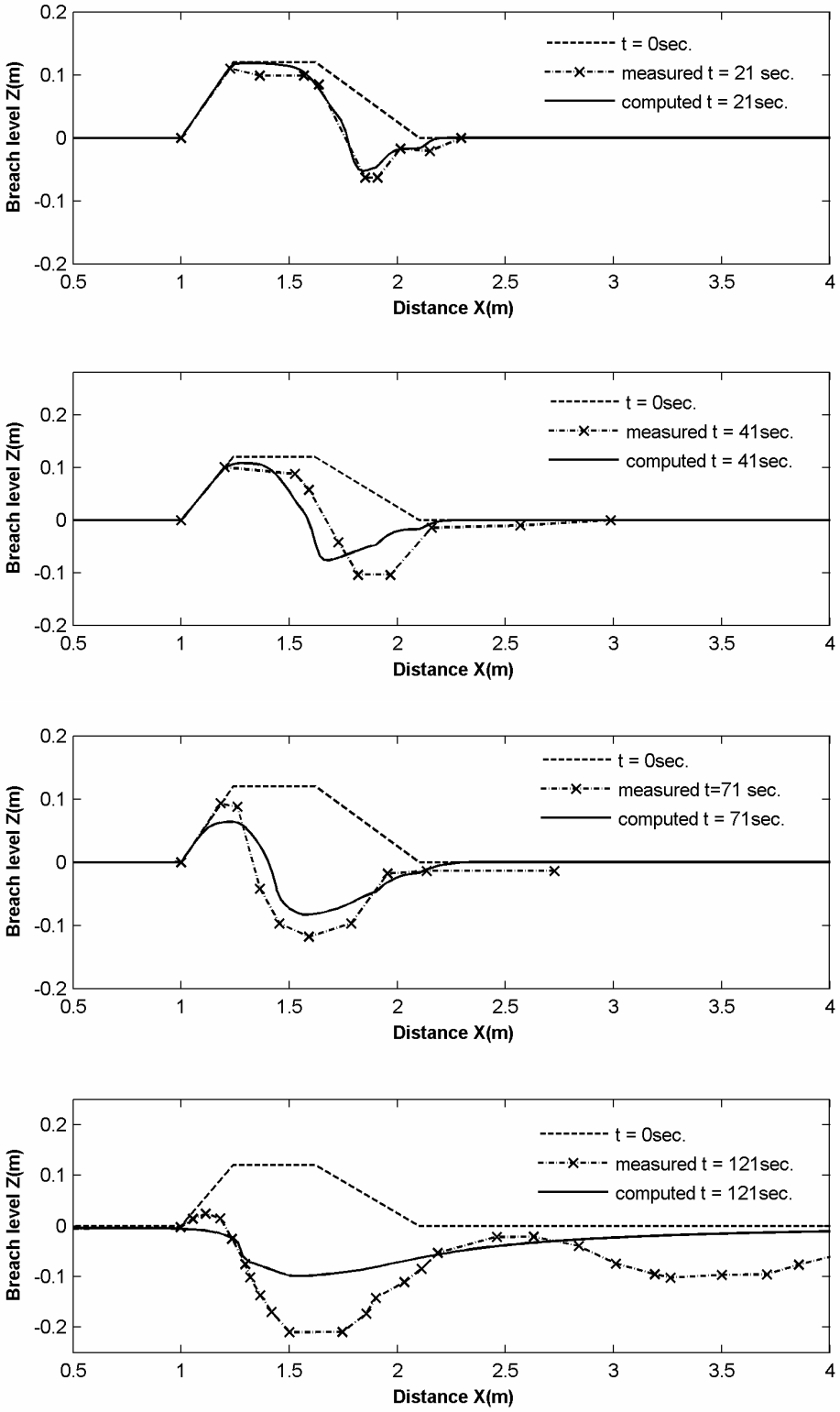

Figure 6.9 Vertical breach growth: computed versus measured, up to t = 121 s, Caan's experiment

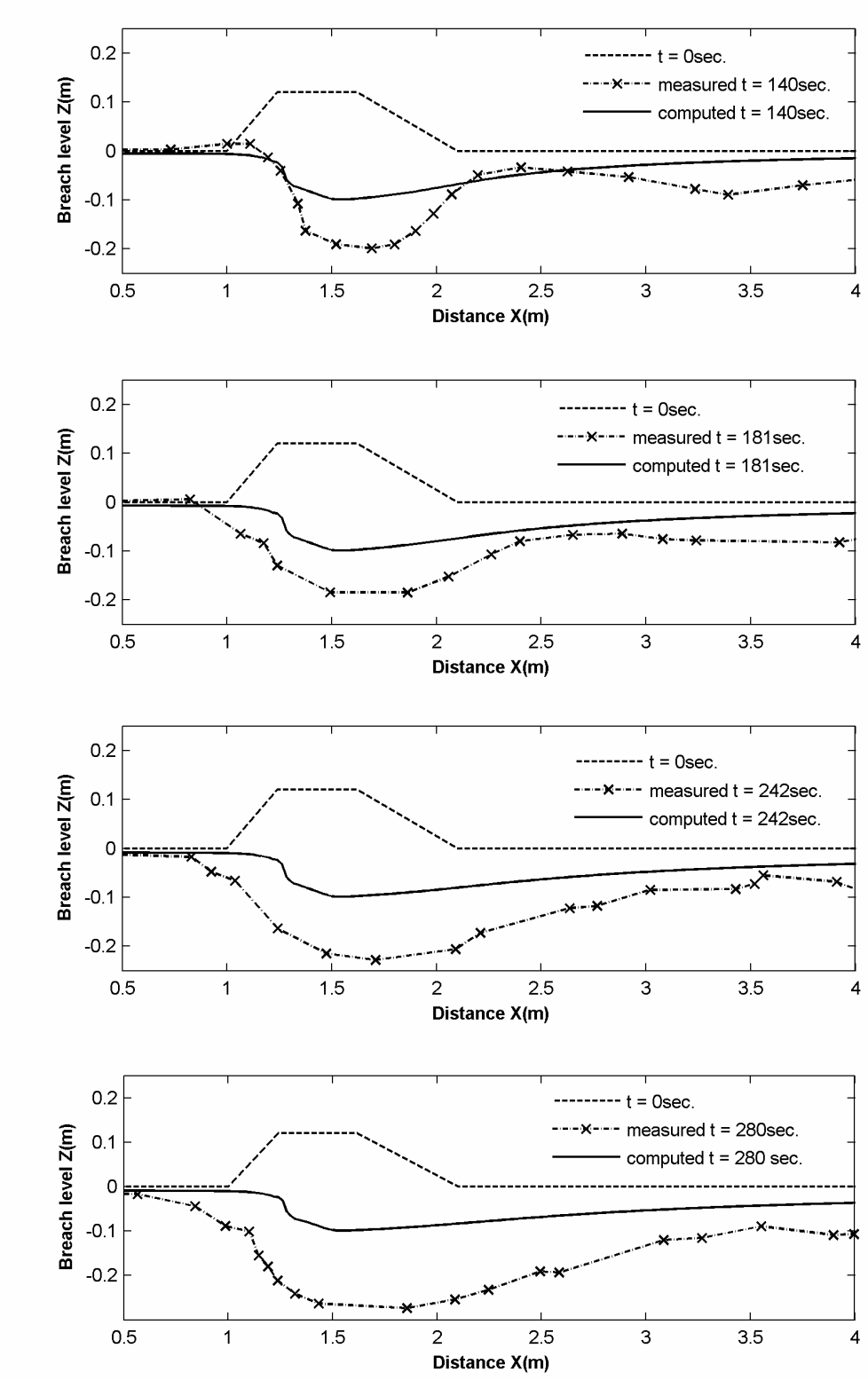

Figure 6.10 Vertical breach growth: computed versus measured, up to t=280 s, Caan's experiment

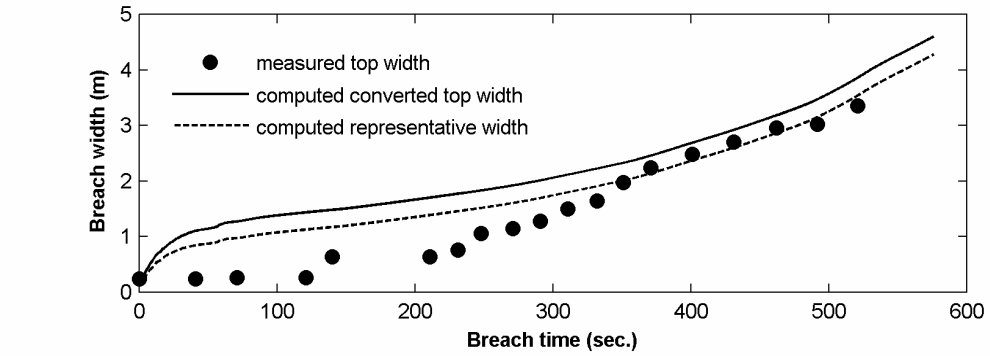

Figure 6.11 Lateral breach growth: computed versus measured, Caan's experiment

6.5.3 Model verification

We verify the present model with the data from the Zwin'94 field breach experiment. The following inputs were used for the computation (see also Visser, 1998).

- Hydraulic boundary: upstream and downstream hydrographs are shown in Fig. 6.12;
- Pilot channel: $B_{t0} = 2.30$ m, $h_{L0} = 0.8$ m;
- Bed properties: $d_{50} = 0.22$ mm, $d_{90} = 0.35$ mm, $w_s = 0.028$ m/s, angle of internal friction $\gamma = 32^{\circ}$, porosity $p = 0.40$, bed roughness $k_{s,c} = 0.15$m;

Again, there are very limited relevant data available on the breach hydrodynamics since all the velocity measuring stations were located too far away from the main stream of the breach (see Visser, 1998). For the present verification purpose we can use the observation data on the surface velocity in the breach. This velocity was measured during breaching by video-capturing floats over a streamwise measuring distance of 5m long. However, the number of data points is limited because the camera failed to capture some of the floats. The floats were put into the flow around the upstream edge of the dike. Hence, we can assume that this observation represents the velocity at that location. Figure 6.13 plots the computed breach velocity at the upstream edge of the dike crest (at $x = 40.8$ m, see also Fig. 6.14) in comparison with that observed from the experiment. The computed surface velocity was determined also using Eq. 6.41. Fair agreement is found in terms of magnitude and phase of the breach velocity considering that the observed values are not instantaneous.

The model predictions for the breach profile evolutions are shown in Fig. 6.14 through Fig. 6.16. Some observed scour depths at t = 1200 s and 1440 s are also given for comparison in Fig. 6.15. The comparison of the computed breach width increase with the measurement is shown in Fig. 6.17. Again, fair agreement between the measurement and the model prediction is found for the lateral breach growth. The scour depth in the breach channel is slightly underestimated at some locations.

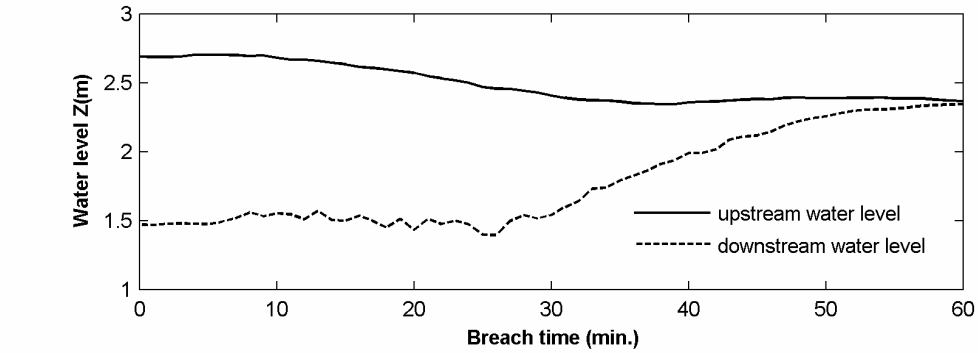

Figure 6.12 Water level variations upstream and downstream of the breach, Zwin'94 experiment

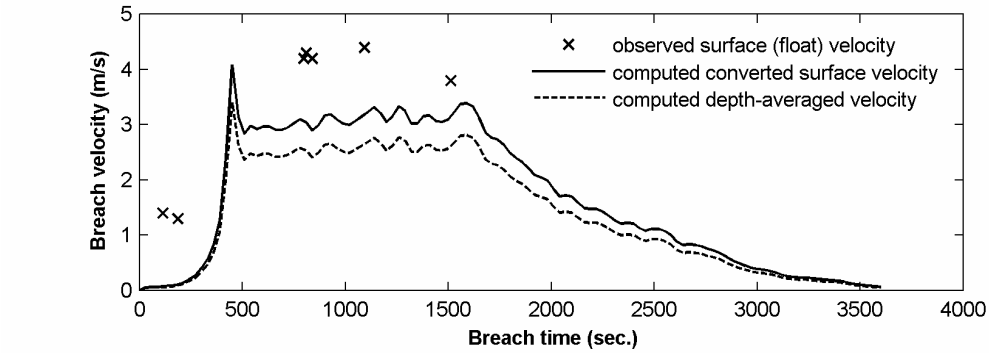

Figure 6.13 Velocity of a point in the breach ($x = 40.8$m): computed versus measured, Zwin'94 experiment

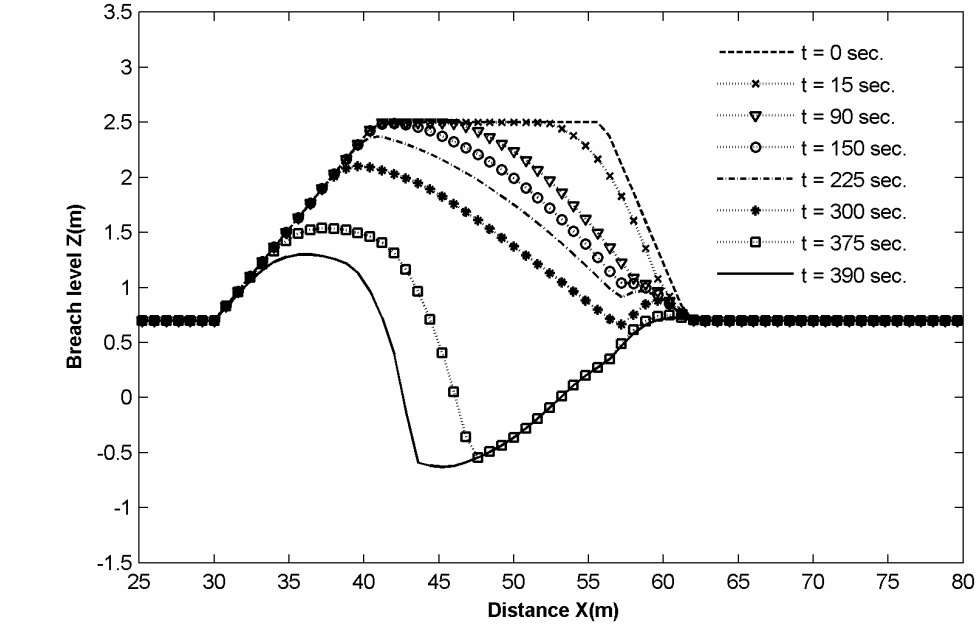

Figure 6.14 Computed vertical breach growth up to t = 390 s, Zwin'94 experiment

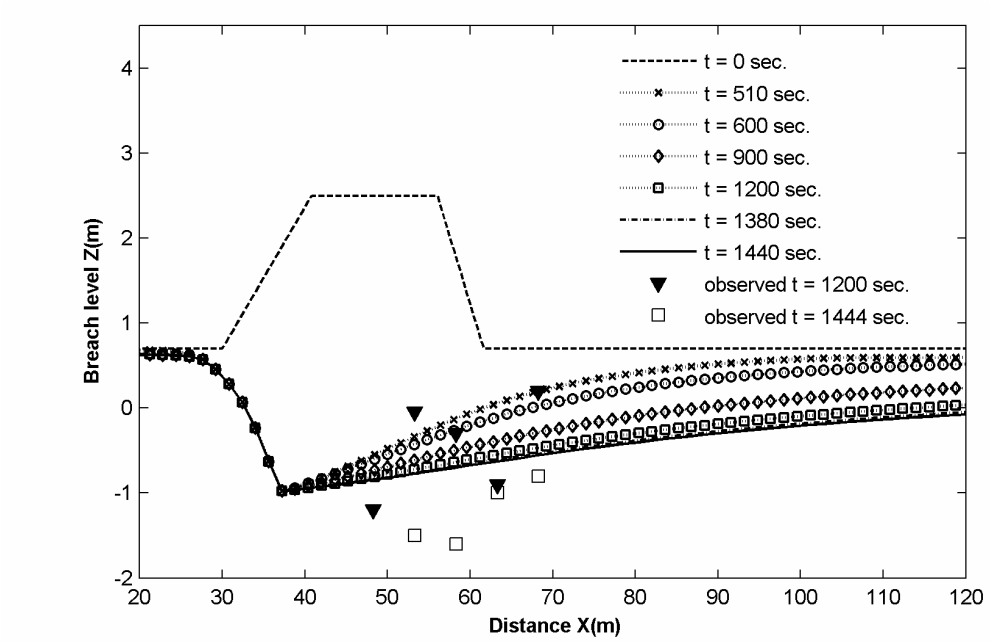

Figure 6.15 Computed vertical breach growth up to t = 1440 s, Zwin'94 experiment

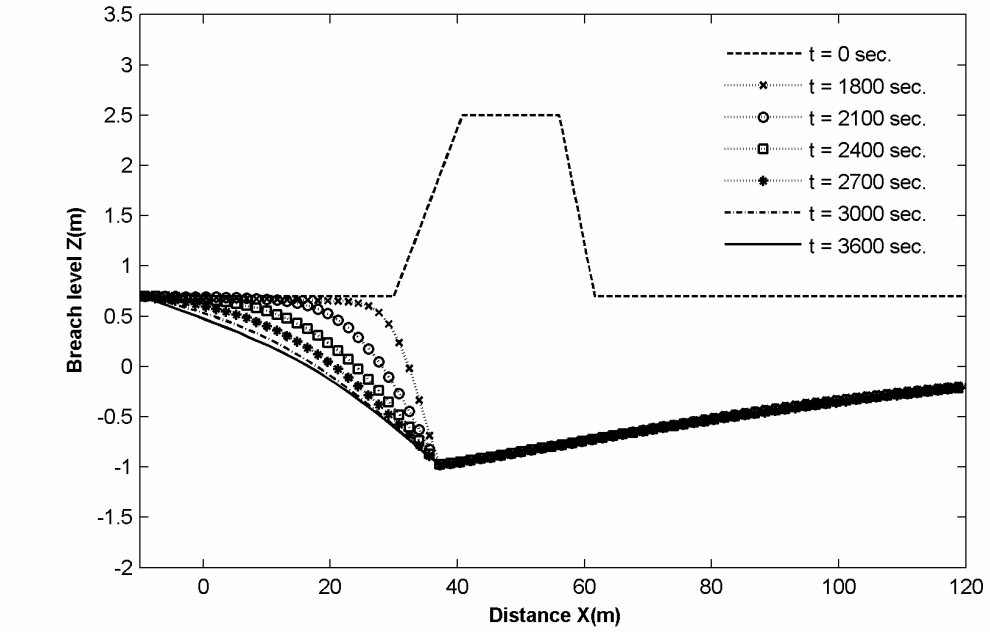

Figure 6.16 Computed vertical breach growth up to t = 3600 s, Zwin'94 experiment

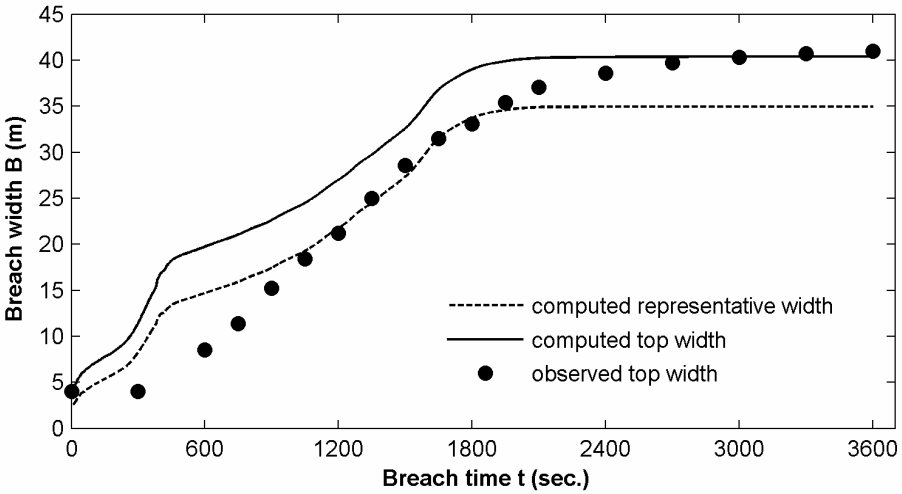

Figure 6.17 Lateral breach growth: computed versus measured, Zwin94's experiment

6.6 Discussion

6.6.1 Scour development and the role of the hydraulic jump in the vertical breach growth

In general, the time-dependent vertical breach growth including the scour development in the breach channel during the early stages of the breaching process (before complete wash-out of the dike) is in good agreement with the experimental data. This is because the formation and development of the scour during this period is strongly related to the hydraulic jump, which is well described by the present model. After this period the jump tends to weaken and quickly disappears in the breach channel as the driving water head difference gradually neutralizes in the last stages. Therefore, from the moment of the jump disappearance the development in depth of the scour is weakly accounted for in the model (only transport computed by depth-averaged quantities). It is observed that the scour indeed continues to develop with a slower rate even after the jump has disappeared. As a result, the final scour depth is consistently under-predicted by the model, especially for the laboratory case. It can be explained physically that the underestimation is due to the mechanism for the scour development during the last (subcritical regime) breaching stages is not related to the jump turbulence and therefore is not yet covered by the model. Possible improvement can be achieved for this by including a so-called "local scour hole" mechanism as described by Hoffmans (1992) in the modelling of the scour development during that subcritical period of breaching. Hereto, the flow structure within a local scour hole must be known, which requires a 2DV detailed flow modelling and this cannot be incorporated in the present model.

It is worth mentioning that questions still remain about the reliability and representation of the quantitative data of morphological breach development in the experi-

ments, especially regarding the vertical breach development. The breach profiles were captured along the glass wall (in the laboratory case) or along the central breach axis (in the field experiment), where the maximum gully depths are expected. Furthermore, there are uncertainties, e.g. inhomogeneous porosity due to uneven compaction, which cannot be accounted for in the breach model. Appreciable differences in the breach profile evolutions between two control tests with the same hydraulic testing conditions are observed during the laboratory experiment of Caan (1996). This can only be explained by the fact that the sand compaction was different between those tests. Uneven compaction within the dike and its base is also assumed to explain sudden increases of the scour depth in loosely-packed areas as observed in the experiment. The scour depth was sometimes even larger than the mean flow depth and the breach flow resembled a flow pouring into a deep hole. For this reason, the scour depth in the laboratory experiment was in fact dominated by small-scale effects (geotechnical-related) phenomena.

Nevertheless, it appears from the laboratory data that the scour in the breach channel attains a large part of its final depth during the first stages of breaching before the complete washout of the remaining sand plug (qualitatively the first three stages according to Visser, 1998). After that moment the scour slows down its development in depth considerably, while expanding in both upstream and downstream directions. This somewhat disagrees with the breach profile development described by Visser (1998), which does not assume the scour to develop during the first three stages.

The laboratory data and the results from the model computations help increase the understanding of the morphodynamics of the scour in particular and the vertical breach growth in general during the early stages of the breach erosion process. As stated earlier in Section 6.2, this breach morphodynamics is strongly related to the hydraulic jump.

Regarding the scour development, the scour starts to form in the breach channel at the location of the jump, where the sediment transport capacity under the effects of jump turbulence prevails over the sediment supply brought in by the upstream breach flow. The scour is highly dynamic because it is associated with the jump location and the jump turbulence, which are governed by the instantaneous relative strengths between the upstream flow, the downstream water level and the bed roughness. In the above case of the laboratory experiment (Fig. 6.9), i.e. a polder-dike breach, the jump progresses upstream as the retrograde erosion process takes place simultaneously with the increase of the downstream water level. As a result, the scour expands gradually upstream before the complete washout of the dike. In general, it is expected that breaching with low (or dry) downstream water level certainly leads to a more severe breach scour depth.

Apart from initiating the scour, the hydraulic jump also accelerates the retrograde erosion process. We carried out some numerical simulations to investigate this. Figure 6.18 shows the breach profile evolutions in the first three breaching stages of the laboratory dike of Caan (1996) computed with various jump strengths. The jump strength was adjusted by changing the downstream water level. Two cases of the downstream water level are considered, one with tail-water effects of the level of 0.05 m and the other with dry-bed downstream (represented in the model by an extremely

small water layer). The case of 'no-jump' is fictitious by turning off the jump modelling component and without tail-water effects.

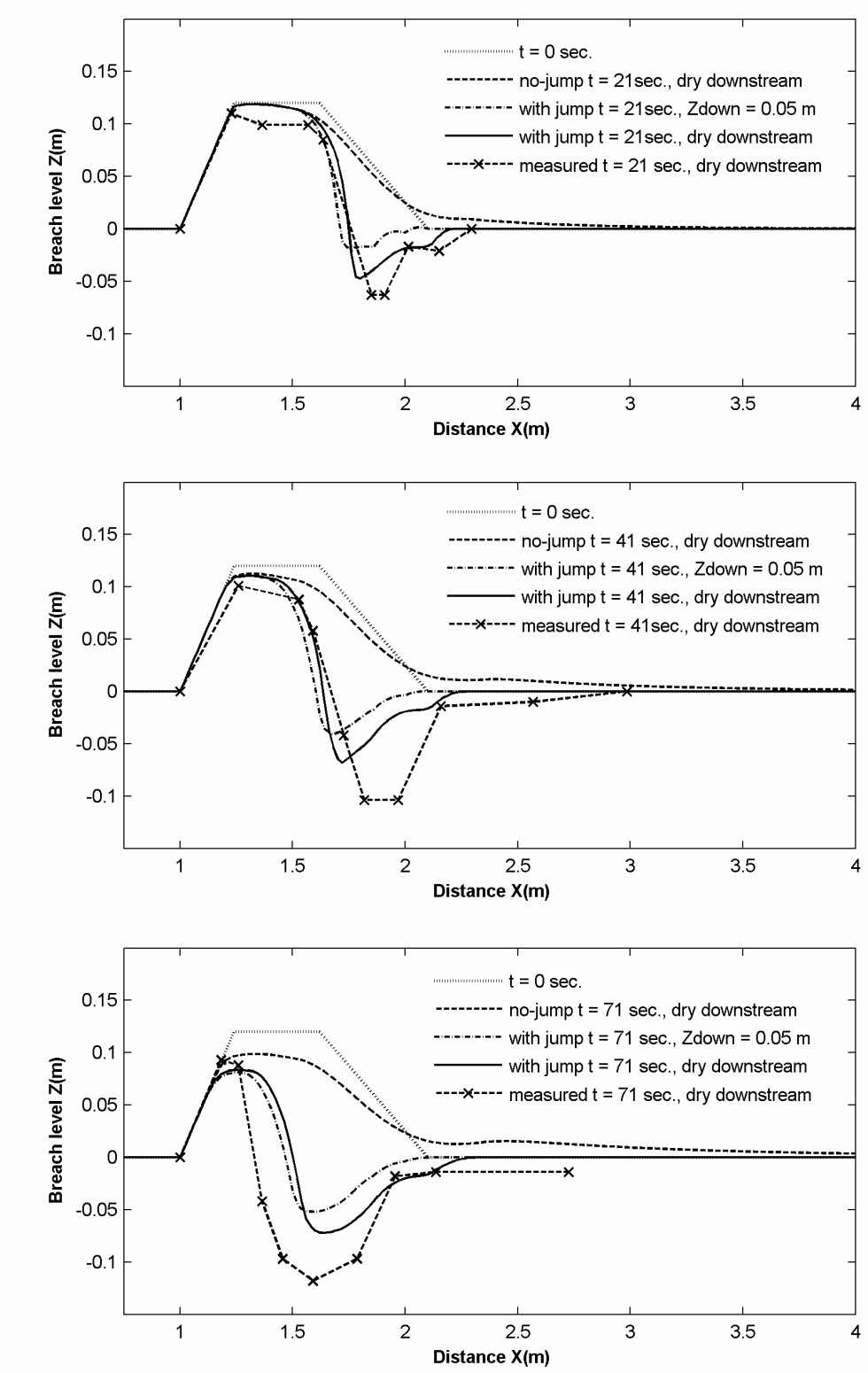

Figure 6.18 Breach profile evolutions with various jump strengths

Clearly, the jump-induced transport at the toe of the inner slope of the dike accelerates the vertical breach growth considerably. A much steeper breach profile is found compared to the case without the jump effects, which is in agreement with observations from the laboratory experiment. In general, the jump strength affects the vertical breach growth significantly, in which the water level on the downstream side of the breach plays a role. A higher water head difference leads to a higher jump strength and hence to a more severe breach scour depth and vice versa.

6.6.2 Breach lateral growth

In general, the time-dependent width increase of the breach in both considered experiments is fairly well predicted by the model. The present model predicts a continuous increase of the (representative) breach width throughout the breaching process including the first two stages defined by Visser (1998). In the above two experiments and also in the BRES model, the breach width was claimed (or assumed in the case of model) to be constant and equal to the initial value until the end of the second stage (until t = 80 s and 390 s for the laboratory and field experiments respectively). It should be noted that this width was measured at a fixed single section on the dike crest in both of the experiments and hence could not present the breach channel as a whole in quantifying the lateral breach growth (see also Section 4.3). To illustrate this, it is questionable from Fig. 6.9 that the laboratory dike breach was claimed not to widen even when about two third of the dike had been completely washed out at t = 71 s (not yet at the end of the second stage).

The pilot channel plays a role in the present breach model as part of the initial input conditions. The significance of the initial channel geometry can be studied from the cross-sectional growth index as addressed earlier in Chapter 4 and Chapter 5 of this thesis. In short, with fixed given hydraulic conditions on both sides of a barrier, a bigger pilot channel would result in a faster breaching process and larger final breach dimensions and vice versa. Generally speaking, the natural hydraulic boundary conditions are dynamically variable during breaching, hence the effects of the initial breach dimensions on the breaching process and therefore on the final breach dimensions are complex.

6.7 Summary and conclusions

The laboratory experiment of Caan (1996) indicates that the scour development in the breach channel phases out the breach erosion process in sand barriers noticeably in comparison with the five-stages defined by Visser (1998). This is due to effects of turbulence of the hydraulic jump at the toe of the downstream slope. Therefore, modelling of the scour formation and development during the first stages of breaching in connection with the jump turbulence is essential to have a proper prediction of the breach growth. To incorporate this, the flow structure in the jump is required, which can be efficiently modelled using one of the many semi-empirical formulations from the hydraulic jump modelling literature. In this way, the computation of the flow

structure reduces to capturing the jump parameters reliably as part of the breach flow conditions. This can be resolved by adding an additional jump-turbulence source term to the horizontal momentum balance of the shallow water equations. For modelling the bed level changes under the jump-affected region a local refined morphological module is used, in which the depth domain is divided into three layers in association with the determined flow structure.

The above jump-induced scour mechanism is integrated into the modelling approach presented in Chapter 4 to form a new process-based numerical model of barrier breaching. The jump modelling has been calibrated with the existing experimental data on the jump profiles with various jump strengths and bed slope conditions. The laboratory dike breach experiment of Caan (1996) and the Zwin'94 field experiment (Visser, 1998) were used for calibration and verification of the model. Agreement between the model predictions and the measurements is acceptable given the uncertainties in the experiments.

The present breach model is capable of simulating the breach erosion process of sand barriers under arbitrary hydraulic conditions. The time-dependent breach growth including the scour development is successfully modelled without defining any evolutional stages. The modelling of the scour formation and development induced by the turbulent hydraulic jump during the early stages of breaching is a step forward in improving the model prediction for the vertical breach growth. The process-based approach for modelling the growth of an erosional channel presented in Chapter 4 has proven to be also suitable for the breaching case.

The computational results help to increase understanding of the dynamics of the scour in the breach channel. Under the effects of the jump turbulence the scour is found to develop vigorously and reaches a major part of its final depth during the early stages of the breach erosion process before completely washing out the remaining sand plug. During the last breaching stages with subcritical flow, the continuation of the scour development is not related to the jump, which explains the systematic underestimation of the final scour depth by the model. This can be improved by including additional appropriate scouring mechanism for that period such as that of "local-scour holes" by Hoffmans (1992). It is also learnt that more insight into the sediment transport under the turbulence induced by hydraulic jumps is necessary to further improve the modelling of the breach growth.

Chapter 7

CYCLONE-INDUCED BREACHING OF THE COASTAL LAGOON BARRIER OF HUE*

7.1 INTRODUCTION

As addressed in Chapter 1, due to the high activity of tropical cyclones the narrow coastal strip in the central coast of Vietnam, specifically the coastal lagoon area of Hue, is subject to frequent attack both by surges and waves on the sea side and by floods on the bay side. These attacks pose a serious annual breaching threat to the lagoon barrier. Better understanding of this breaching threat is of interest for a proper safety management of the lagoon, in which the following two issues are concerned:

- Breach initiation as a result of the processes of dune beach erosion and the wave overwash on the barrier during storm surges.
- Time-dependent barrier breach growth due to overflow (river flood or storm surge).

The above two issues can be addressed through analyses of the computational results from the two model components, viz. the barrier response and the barrier breach, respectively. For the safety management of the lagoon in general, the first aspect helps to identify weak spots in the barrier so as to avoid unintended breaching using appropriate protective measures. Prediction of the time-dependent breach growth is of importance to disaster mitigation strategies such as for devising a proper evacuation plan, flood risk analysis, and coastal design. Also, in case of intended breaching, knowledge of breach growth can be utilized to alleviate the inland flood level where and when necessary. In the case of Hue lagoon, this potential solution is worth considering since the existing lagoon outlets have insufficient capacity to discharge extreme river floods.

---

* Excerpts from this chapter were published as: Tuan, T.Q. *et al.*, 2006c. Breaching vulnerability of coastal barriers under effects of tropical cyclones: a model study of Hue lagoon-Vietnam, in: *Proc. 2nd Int. Estuary and Coast Conf.*, Guangzhou, China.

To resolve part of the above issues, in this chapter the present model is applied to study the historical breaching incident induced by cyclone EVE in November 1999. It is also used to investigate the model capability of simulating such a prototype breach event. In spite of uncertainty in the available data, an attempt is made to reconstruct the breach initiation and the time-dependent breach growth of the barrier under such extreme conditions.

The unfavourable natural conditions and the phenomena facing the Hue coastal lagoon area are introduced in Section 7.2. The situation and the breach incident during the historical event in 1999 are also briefly introduced. The model application is presented in Section 7.3, preceded with an assessment of the morphological situation before breaching and a review of the available data. The chapter ends with a summary and some conclusions drawn in Section 7.4.

7.2 CYCLONE-INDUCED BREACHING OF THE HUE LAGOON BARRIER

7.2.1 Phenomena

Hue shares common topographic features with the central coast as discussed in Section 1.2. This coastal area is subject to frequent attack by tropical cyclones, on average five cyclones a year from June to November. Tropical cyclones are the major cause of flooding hazards in the area. Statistical data indicate that tropical cyclones have been responsible for over 80% of the flooding events that occurred in the region. The annual precipitation observed in the region is exceptionally high, which is a result of high activity of tropical cyclones, sometimes in combination with one of the local climatologic features such as a cold front or monsoon. Because of a steeply sloped catchment towards the sea, heavy rainfall quickly results in a high flood level at the coast. The response time with regard to river flooding of the area is about 6 to 7 hours (see Le and Bui, 2000). Flooding, from either the sea side or the river side, is inherent to the geographical situation and is an annual threat to the coastal lagoon area during the storm season.

The coastal lagoon of Hue stretches over 68 km along the central coast of Vietnam (see Fig. 1.1). Its water surface of 22,000 ha, protected from the sea by a long natural sand barrier, is a vast aquacultural sanctuary providing major income for over 300,000 local inhabitants. The lagoon habitats are rich and unique in terms of biodiversity. The barrier island is also a dwelling place for thousands of local households. Unfortunately, this beautiful coastal area is highly vulnerable to flooding and breaching hazards due to its complex geographical conditions.

In terms of hydrodynamics, Hue lagoon is highly complex with input discharges from six rivers and with two main outlets to the South China Sea. The barrier, providing protection for the lagoon, is exposed to frequent attack both by floods from rivers and by surges and waves from the sea. These forces pose a serious threat of breaching to the barrier during the storm season.

Attack on the barrier during a cyclone event is immediate by high waves and surges on the sea side and is then possibly followed by a severe flood on the lagoon side. During the storm surge severe overwash on the barrier can narrow and lower the barrier cross-section considerably, creating vulnerable spots for breaching by overflow to occur afterwards. From historical incidents it is observed that overflow can be either from the seaside or from the riverside. We designate these possibilities as two corresponding breaching scenarios and address these as follows. In the first scenario surge overflow is an immediate follow-up to the processes of dune and beach erosion and wave overwash. Hence, in this case the barrier breaching is both initiated and induced by the effects during the storm surge alone. In the second and most recently occurred scenario breaching is induced by river flood overflow. Due to the quick-flood-response character river flooding can reach the lagoon in a matter of one day. The discharge capacity of the main outlets is usually insufficient because of earlier sedimentation processes. The discharge of river flooding to the sea is hampered by the alongshore barrier and sometimes also by a simultaneous high water level at sea (surge). As a consequence, the lagoon water level is quickly elevated and water overflows the barrier crest through depressed portions, inducing breaches. In this scenario earlier attack by surges and waves can exaggerate the probability of barrier breaching significantly, i.e. breaching can be initiated during the storm surge.

7.2.2 Historical event in 1999

During the past two decades, breaching of the Hue lagoon barrier due to effects of tropical cyclones occurred several times, causing catastrophic consequences. The most recent serious incident was induced by tropical cyclone EVE in November 1999. Cyclone EVE made landfall at the central coast region in late October 1999. It was in fact a rather moderate storm in terms of Beaufort scale but its secondary impacts were fatal. The cyclone induced weeks of torrential rainfall in a large, affected inland area. The region experienced the worst flooding ever in 50 years. The precipitation measured in Hue was 2288 mm, a new historical record. During the first days of November 1999 most of the rivers in the central coast were above their highest alarm levels. The water level on the Perfume River (main river discharging in the lagoon) measured in 01/11/1999 in Hue was 5.6 m above the mean sea level. Because of the high inundation level, the lagoon barrier was broken at six different locations. Among those the breach at Hoa Duan community was the largest with a final width of around 600 ~ 900 m and a depth of around 5 ~ 9 m (see also Figs. 7.1 and 7.2). During this serious flooding event, 352 people drowned and 25,000 houses were washed away.

7.3 MODEL APPLICATION

7.3.1 Situation before breaching and available data

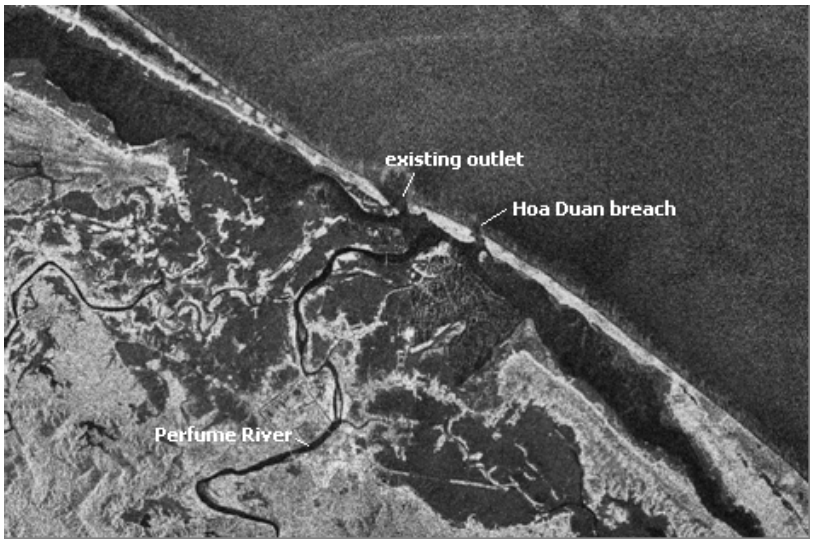

Figure 7.1 Satellite image of Hue lagoon in 3/11/1999.

Figure 7.2 Hoa Duan breach 03/11/1999

A problem of concern in breach modelling in general is the availability and reliability of breach data since data acquisition is not a priority during a disaster event. In the present considered breach, there was almost no observation on hydraulic as well as on morphological conditions, particularly on the sea side before, during, and even after the incident. The most available data are the flood water levels obtained from dozens of upstream inland hydrological stations along the river courses. In order to have input to the model, we make as much as possible use of all available data and information from various sources such as hindcast models, eye-witness reports, and photos. Also, appropriate assumptions are introduced if necessary.

Figure 7.3 Situations at the Hoa Duan breach section.
Upper picture: 3 months before breaching; Lower picture: on 31/10/1999, 3 days before breaching and 12 days after storm landfall; G (×) the landward end of the groin; the dash-dot line indicates the most vulnerable spot where the breach occurred.

First, we need to understand the morphological situation at the Hoa Duan beach before the event. The breach site was in fact a natural weak section of the barrier island, which used to be the location of an ephemeral river-mouth. Earlier field surveys reveal that the beach was suffering from severe erosion due to negative effects from a system of groins constructed in 1997 in the vicinity (see NCKH-NN, 2001). Figure 7.3 shows the comparison of the Hoa Duan beach situation three months and just three days before breaching (pictures obtained from RNE mission report, 1999 and Goichot and Pluijm, 2000). Clearly, the seaward part of the barrier profile and the gentle foreshore were disappearing rapidly. Sediment in the surfzone brought offshore by cross-shore transport was lost in the alongshore littoral drift. More seriously, the deepened foreshore had a negative influence on the barrier by accommodating more severe wave conditions at this specific beach location. As a consequence, the beach suffered from severe landward erosion and overwash during rough seas, which had caused the barrier to retreat and lower its crest from the original level of 3.6 m before the groin construction to 2.5 m at the moment just before the breach occurrence (Goichot and Pluijm, 2000). From the investigation by Goichot and Pluijm (2000), it is believed that one day before breaching the barrier crest width at the breach section was about 50 m, which is also in agreement with claims by local eye-witnesses. The narrow and

low-crested beach barrier at this location was the most vulnerable spot for the breach to occur later on.

In summary, the Hoa Duan breach is believed to have occurred as a result of the following sequential causes:

- Negative effects from the groin field had narrowed a part of the barrier and especially its gentle foreshore was swept away.
- Due to a deepened foreshore, beach and dune erosion and overwash had been promoted during winter time especially during cyclone EVE event, remarkably narrowing and lowering the barrier cross-section. A highly vulnerable spot was created as a result.
- Breaching due to overflowing of the barrier through the vulnerable section by the sudden release of extreme river floods (following the cyclone) to the sea.

To study the effects of overwash, we first need a representative pre-storm beach profile at this location. This can be extrapolated from a detailed bathymetric survey of the lagoon carried out in late April 1999, viz. six months before breaching. At that moment, the barrier at the breach section was 220 m wide above the mean tide and the averaged crest level was 3.0 m (see Fig. 7.4 and also NCKH-NN, 2001). It is assumed that the shape of the foreshore at the start of the storm was the same as it had been six months earlier. Hence, the position of the seaward barrier profile can be shifted landwards to fit the remaining width of 210 m to account for the six-month period of erosion (estimated erosion rate of about 20 m per year according to visual observation by the local authority). The barrier slope on the lagoon side is assumed to be 1/25, the average slope of measured barrier profiles.

Regarding the sea conditions we utilize the results from a hindcast model study that estimated the wave parameters and the maximum surge level using the wind conditions during cyclone EVE. This hindcast study is part of a national research program on the rehabilitation of Hue lagoon (NCKH-NN, 2001). The astronomical tide at Hue location is perfectly semi-diurnal with an average amplitude of 0.5 m. The sea conditions estimated for the coast of Hoa Duan during the landfall of cyclone EVE are described in Table 7.1.

The sea water level, composed of a surge and the astronomical tide, is assumed to vary in a cosine manner as described in Eq. 7.1 (see also Steetzel, 1993). The storm surge hydrograph is shown in Fig. 7.5.

$$Z_{sea}(t) = MSL + A_t \cos\frac{2\pi(t - t_m)}{T_a} + A_s \cos^2\frac{\pi(t - t_m)}{T_s} \tag{7.1}$$

where $MSL = 0.20$ m is the mean sea level at Hoa Duan (relative to VN-2000 datum, the Vietnamese datum level designated in 2000), $T_a = 12.42$ hours is the standard period of the semi-diurnal tide. The second and third terms on the right hand side describe the contributions of the astronomical tide with amplitude $A_t = 0.50$ m and the surge effect with magnitude $A_s = 1.50$ m, respectively. The effective storm duration equals four tidal cycles (about 2 days) $T_s = 4T_a \approx 50$ hours. It is assumed that the maximum surge coincides with the maximum tide at $t = t_m = 1/4\,T_a = 3.105$ hours.

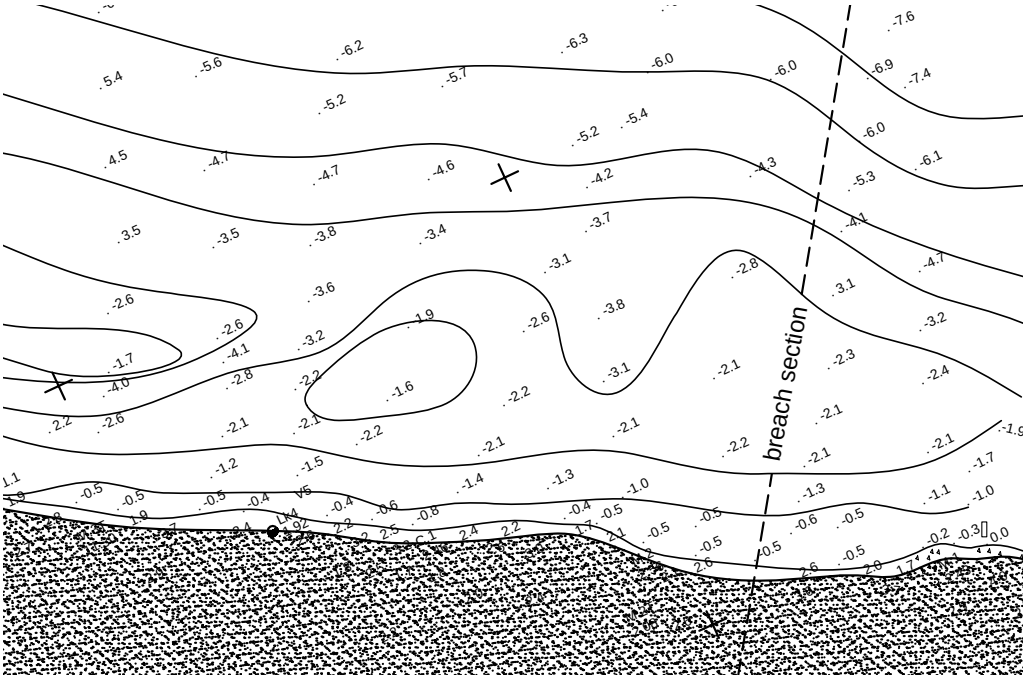

Figure 7.4 Bathymetric condition of the Hoa Duan beach in April 1999 (elevations in meter, relative to VN-2000 datum)

Table 7.1 Sea conditions during the attack by cyclone EVE at the Hoa Duan beach

Parameters		
Tidal amplitude (semi-diurnal)	m	0.50
Maximum surge height	m	1.50
Deep water incident wave height H_{so}	m	5.0
Peak period T_p	sec.	10.0
Effective storm duration	tidal cycle	4.0 (2.0 days)

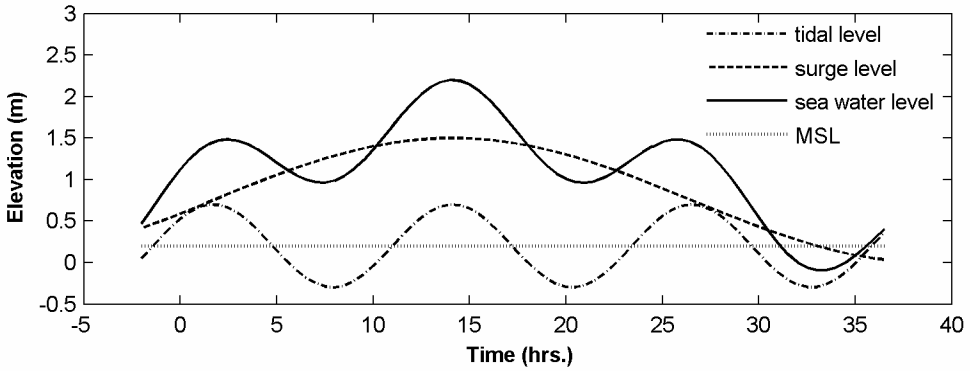

Figure 7.5 Hindcast storm surge hydrograph during EVE cyclone 1999 at the Hoa Duan beach (*MSL* is at 0.20 m)

Under such sea conditions and given the pre-storm barrier geometry, it is likely that the barrier was under attack by severe wave overwash.

The post-storm barrier profile is then used for the computation of the barrier breach erosion process. At the moment when the breach initiated, the lagoon water level was reported to be at around 2.60 m. The breach development was not observed during or even right after the event. It is not clear when the breaching ended but it is claimed that the breach dimensions were around 600 ~ 900 m in width and around 5 ~ 9 m in depth (NCKH-NN, 2001). Several months later, this gap measured 1,000 m wide in a bathymetric survey in support of a design for gap closure.

7.3.2 Model hindcast results of the breach

Breach initiation by wave overwash

It is unclear when the storm actually started. However, with regard to the breach initiation it is most likely that the barrier was suffering moderate to severe overwash. Hence, a computation of the barrier response is carried out for the most intensive day of the storm surge hydrograph (a 28-hour period starting from t = 0 hrs. with the sea water level around and above 1.0 m). It is assumed that the deep water wave parameters as described in Table 1 were invariable during this period. The water level on the lagoon side is kept constant at 0.5 m. The sand diameters were according to samples taken from the breach site, with diameter sizes d_{50} = 250 μm and d_{90} = 300 μm. Since the dimensions of the initial overwash channel (initial depressed portion) are not known, it is assumed that this channel is sufficiently wide so that only the development of the barrier profile is considered (see Section 5.7).

Figure 7.6 shows the computational results of the time-dependent response of the barrier profile during the storm. It appears that during the first 12 hours of storm overwash occurred moderately and the major barrier response consisted of the profile narrowing on the seaward side caused by the process of dune and beach erosion. Overwash on the barrier was most intensive during the period of high water between t = 12 hours and t = 18 hours when the barrier flattened out appreciably. The barrier crest level after the storm is about 2.50 m, which is in agreement with the water level at which the breach was reported to start.

Overall, we can conclude that wave overwash had increased the breaching potential of the barrier by digging through it a pilot channel of about 0.5m deep. In fact, severe overwash during the landfall of cyclone EVE was largely responsible for the initiation of the Hoa Duan breach.

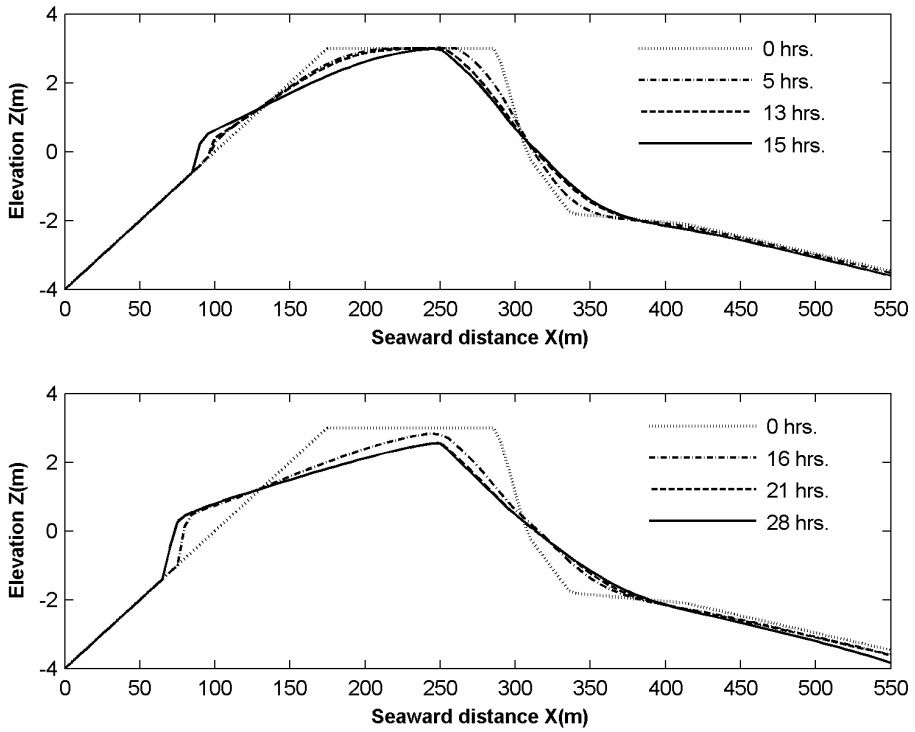

Figure 7.6 Time-dependent response of the Hoa Duan barrier profile during the most intensive 28-hour attack by cyclone EVE, showing significant flattening of the barrier

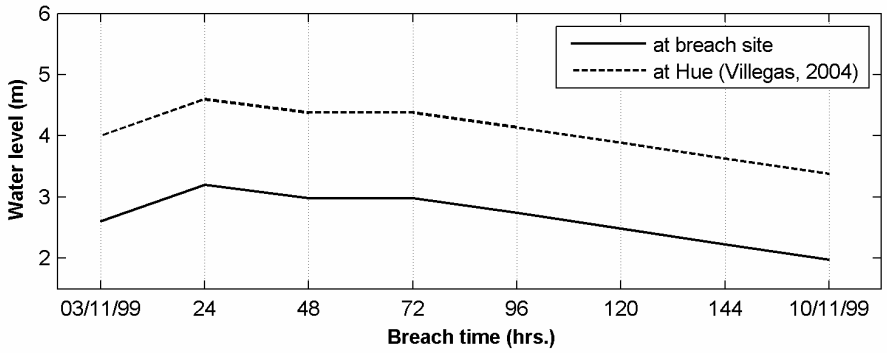

Figure 7.7 Water level hydrograph upstream of the Hoa Duan breach during the first week of flooding (03/11 – 10/11/1999), extrapolated from the flood level data of Villegas (2004)

Barrier breaching

When the breaching is driven by a river flood, the breach erosion process will last until the end of the flood, which is usually days or even weeks. In the case of the Hoa Duan breach, the flood and so the breaching process lasted for about one week. Unfortunately, the hydraulic conditions at the breach site during the flood are very uncertain. Nevertheless, it is believed that the major breach dimensions (depth and width) had developed within the first day of breaching (the first 24 hours). After that the breach grew mainly laterally. Hence, it is probably most relevant to consider the breach development during the first 24-hour most important period of breaching.

In the computation, the upstream (lagoon) water level during the flood is assumed to vary in a piece-wise linear manner as shown in Fig. 7.7. This water level variation at the breach site is extrapolated from the hindcast flood level at the city of Hue by Villegas (2004), assuming a constant water surface slope. The downstream water level variation (sea water level) follows the tidal hydrograph component as presented by Fig. 7.5. For the computation of the breach lateral growth the dimensions of the initial breach (depth and width) are required. For this, a channel of 0.5m deep (the channel highest bottom level is 2.50 m as the output from the overwash computation) and of 25 m wide is assumed.

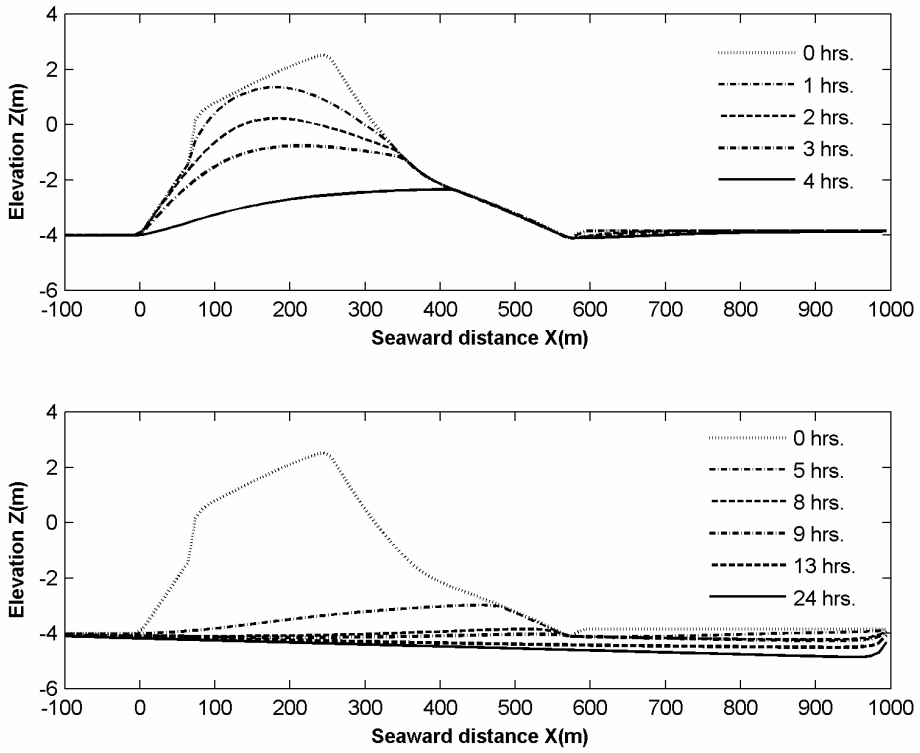

Figure 7.8 Breach profile development during a 24-hour period

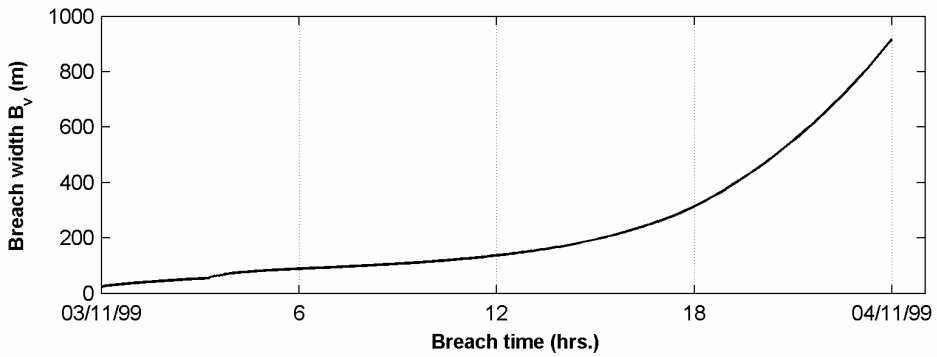

Figure 7.9 Breach width development during a 24-hour period

Figure 7.8 shows the model hindcast of the breach profile development for different time levels. The increase of the breach width in time is shown in Fig. 7.9. The results indicate that the barrier was completely washed out after about 8 hours of breaching. The breach reached a maximum depth of about 7.50m after 24 hours, which is almost the final breach depth. At this time the breach is predicted to widen to 900m. After this moment the breach continued to grow vigorously mainly in lateral direction as the current through the breach was still rather strong.

Overall, the hindcast results are rather realistic and in agreement with the available reported data on the breach dimensions.

7.4 SUMMARY AND CONCLUSIONS

An application of the present model to study the breaching vulnerability of the Hue coastal lagoon due to tropical cyclones was carried out with the particular conditions of the historical cyclone EVE in 1999. The topographic condition before and after the storm was reconstructed. In spite of the uncertainty in the available data, attempts were successfully made to simulate the barrier response and the barrier breaching process under such extreme conditions. The hindcast results seem realistic and are in agreement with reported data.

With regard to the breaching phenomenon of the lagoon barrier of Hue the following conclusions are drawn:

- The phenomena of dune and beach erosion and wave overwash on the seaside and flooding on the river side are the dual effect of a tropical cyclone on the barrier.
- Due to unfavourable geographical conditions the breaching threat to the barrier, posed by the dual effect of tropical cyclones, is inherent and serious.
- During the attack by a tropical cyclone, severe wave overwash on the barrier can considerably narrow and lower the barrier profile. As a result, a vulnerable spot in the barrier can be created, strengthening the barrier breaching potential.
- Then, in a worst case scenario, a breach in the barrier occurs due to water overflow through a vulnerable spot, which is usually a result of an earlier overwash event.
- Apart from river flooding, it is evidenced from the historical incidents that breaching of the barrier can also be induced by surge overflow during a severe storm. Recently, activity of tropical cyclones in the region has become more serious both in terms of frequency and magnitude. Hence, with the natural low-crested condition at many locations of the barrier, there is an increasingly high probability that the barrier is breached due to storm surge effects alone.
- Breaching of the barrier due to surge overflow during a storm is immediate and more difficult to anticipate in comparison with that induced by river flooding. Consequently, as indicated by historical incidents, this landward barrier breaching causes more catastrophic consequences.

With regard to the lagoon safety management, the following conclusions and implications are drawn:

- The landward breaching of the barrier due to storm surge overflow is unavoidable at least in the present situation. However, sea-defence works and proper spatial planning can be applied to mitigate consequences.
- A soft protective measure such as beach nourishment in combination with vegetation planting on the barrier is a potential solution to control the breach initiation and to prevent the landward breaching of the barrier during storm surges.
- Care should be taken when applying a hard protective measure to the barrier. Negative effects from a sea-defence work can induce local favourable conditions for a breach to occur (the negative effect from the groin system in the Hoa Duan beach is a typical lesson).
- Artificial or intended breaching in combination with a proper and active spatial planning is a technically and economically feasible solution that should be considered to alleviate the inland river flood level and thus minimize flooding hazards.
- Constant monitoring of the barrier beach morphological changes and observations of the sea hydraulic conditions are essential to the assessment of the barrier safety against the impact of tropical cyclones.

Chapter 8

CONCLUSIONS AND RECOMMENDATIONS

8.1 CONCLUSIONS

The phenomenon of coastal sand barrier breaching due to tropical cyclones was investigated in the present study. The objective was to develop a reliable process-based numerical model for coastal barrier breaching in which the following two groups of processes were described and formulated:

- The breach initiation as a result of the barrier response induced by the processes of dune and beach erosion and wave overwash during storm surges.
- The breach erosion process due to overflow from either side of the barrier.

A new numerical model has been successfully developed that is capable of predicting the time-dependent development of those coastal barrier breaching processes. More insights into the physics of the processes have been gained. The processes involved and the modelling approaches for each of the two model components are summarized respectively.

8.1.1 Breach initiation by wave overwash

In the first model component the overall response of low-crested sand barriers to wave attack during storm surges is distinguished into two across-shore transport processes, i.e. dune and beach erosion on the seaward side and wave overwash on the landward side. The overwash modelling relies heavily on the specification of wave overtopping as the hydraulic input from the seaside. It is found that a closer-to-nature description of wave overtopping instead of the conventional average discharge is needed in order to model wave overwash on barriers properly. A fixed-bed experiment was carried out to formulate wave overtopping discharge according to an event-based approach. New overtopping parameters such as the relative overtopping time, the overtopping asymmetry, and the average instantaneous discharge have been derived and formulated, which better represent the overtopping nature such as its intermittent character and associated strength. For the empirical determination of wave overtopping, a single-valued equivalent slope is commonly used. This slope is found to affect the reliability

of the overtopping determination significantly, especially in the case of overtopping on sandy beaches. A new slope definition for sandy beaches has been derived that also takes effects of the wave period into account. It has been experimentally proven to be advantageous over the conventional approach.

The present study is largely concerned with morphological processes induced by "flash" overflow, viz. overwash or breach flow. The modelling of this type of flow, based on the shallow water equations, requires a robust numerical scheme to cope with discontinuities (hydraulic jump and intermittent flow) and abrupt changes of the bed level. For this, the Roe upwind numerical approach discretized using the Finite Volume Method was adopted. Regarding the channel morphological development, a process-based approach has been developed that allows the morphodynamic computation of the time-dependent channel growth in both lateral and vertical directions. In this approach, several new morphologic factors such as the channel cross-sectional growth index and the channel representative width have been derived and formulated. The cross-sectional growth index generally expresses the ratio of sediment transport potential on the bottom to that on the sides concurrently induced by a flow. The index was formulated and calibrated with experimental data on the channel growth. From the formulation of the index it follows that apart from the flow power the channel geometry affects strongly how the channel grows in general.

As a follow up to the fixed-bed model experiment a mobile bed (sand) experiment was carried out to increase understanding of the processes of sand barrier response during storm surges. A qualitative description of the process of the response of low-crested barriers during storm surges was given. Quantitatively, the time-dependent growth of the overwash channel was measured in detail to construct a complete data set for calibration of the model. From laboratory observations it was presumed that the sediment transport in wave overwash occurs under sheet flow conditions, in which bed load is the principal mode.

Two principal overwash-induced effects on the dune and beach erosion process have been identified and accounted for in the present model. First, it was observed in the mobile-bed experiment that under occurrence of severe wave overwash, the sediment transport in the upper near-crest part of the swash zone is significant and landward-directed. This landward transport flattens the beach face slope substantially compared to the situation on high beaches without overwash. Therefore, a biased-trapezoidal transport distribution in the swash zone for the case of overwash was used. Second, loss of mass flux in the landward direction due to heavy overwash reduces the mean cross-shore velocity (undertow) and so the cross-shore transport rate. This effect was accounted for by introducing an overwash-induced transport reduction factor, which is found to depend primarily on the relative overtopping time addressed earlier.

Fairly good agreement of the computational results with the measurements indicates that the new elaboration of wave overtopping and the new process-based approach for describing the channel growth are eligible for the numerical modelling of wave overwash.

8.1.2 Barrier breach erosion process

Modelling of the barrier breaching process is treated in the second model component. A breach in the barrier occurs as water starts to overflow the barrier crest through a pilot (initial) channel. Breaching is regarded as a gradual erosional process whereby the breach modelling in fact comes down to describe the enlargement in time of this pilot channel both vertically and laterally. To this end, the modelling of breach growth can primarily rely on the common process-based approach mentioned earlier for the overwash channel. However, it has been observed that a noticeable scour forms and develops in the breach channel particularly during the first supercritical stages of breaching when the barrier has not been completely washed out. The mechanism behind this phenomenon has been first addressed in the present study and attributed to the effects of turbulence induced by the hydraulic jump at the toe of the inner slope of the barrier. The vertical flow structure within the jump is noticeably modified by the jump turbulence, specifically the maximum velocity is found close to the bottom. As a result, more sediment is brought into suspension, which induces scour within the jump-affected region. Hence, to improve the model prediction of breach growth the jump-related turbulence must be accounted for by a locally refined morphological module in the breach model.

To model the scour the flow structure within the jump is needed. This can be efficiently computed as a function of the jump properties (position, length, and depth) using a suitable (semi-) empirical approach derived from literature on hydraulic jump modelling. However, it is well known that most models of shallow flows (e.g. St. Venant equations) with shock-capturing techniques are able to predict the jump position well but not the jump length and the jump surface profile. It was found out in the present study that this is due to the effect of depth-integration, which cancels out the important role of turbulent stresses particularly in the horizontal momentum balance within the jump-affected area. This problem was effectively resolved by adding a jump turbulence-related source term to the horizontal momentum balance of the shallow water equations.

The sediment transport under the jump was distinguished into bed load and suspended load. For the determination of the bed load, the effective bed shear stress was related to the maximum velocity at the top of the jump bottom boundary layer. The suspended load was determined by integrating the product between the sediment concentration and the current profile over the water column.

The existing dike breach data of the laboratory experiment of Caan (1996) and of the Zwin'94 field experiment (Visser, 1998) were used for calibration and verification of the present breach model. The final scour depth was consistently under-predicted by the model, which can be explained by lack of another scour inducing mechanism for the subcritical stages of breaching. Overall, fairly good agreement was found. The computational results indicate that inclusion of the jump turbulence effects in breach modelling is the key to model the scour formation and development in the breach channel, improving the prediction of breach growth. The new process-based approach for describing the channel growth has also proven to be suitable for modelling breach growth. The present model is capable of simulating the breach erosion process in sand barriers under arbitrary hydraulic conditions on both sides of the breach. The time-

dependent breach growth including the scour formation and development is successfully modelled without defining any evolutional stages.

The developed model of coastal barrier breaching was applied to reconstruct the development of a historical breach incident of the coastal lagoon of Hue in the central coast of Vietnam induced by cyclone EVE in 1999. Despite the fact that the documented data on the breach were rather poor, a satisfactory agreement was found. From these results, implications for the lagoon safety management and precaution on the breaching threat of the lagoon in general were derived.

8.2 RECOMMENDATIONS

The following recommendations are given for further development and verification of a coastal barrier breaching model.

With regard to the modelling approach of the response of low-crested barriers during storm surges:

- The modelling of overwash relies heavily on wave overtopping parameters at the landward boundary as the hydraulic input. In the present model these parameters are quantified empirically. For a complete process-based hydrodynamic approach a process-based hydrodynamic computation of overtopping should be developed.
- It is recommended to carry out additional laboratory mobile overwash experiments, in which intra-flow measurements of the sediment transport are made to increase more insight into the sediment transport processes in wave overwash.
- Bed infiltration and vegetation factors have been neglected in the modelling of wave overwash. To describe overwash under field conditions more closely, effects of these factors should be taken into account.

With regard to the modelling approach of the barrier breach erosion due to overflow:

- The present model neglects the effect of wave transmission over the barrier crest at the start of the breaching process induced by surge overflow. It is recommended to take into account this effect for a proper description of the breach growth during this early stage.
- For a proper description of the vertical breach growth in general and the formation and development of the scour in particular during the first supercritical stages of breaching, better understanding of the flow structure and the sediment transport within the hydraulic jump-affected region is needed. It is recommended to further investigate in detail the processes and mechanisms of sediment transport under a turbulent hydraulic jump.
- The present model consistently under-predicts the final scour depth. This is because the continuation of development of the scour during the last subcritical stages of breaching is not related to the jump turbulence. To improve

the model performance on this aspect, an additional scour-inducing mechanism such as the "local scour hole" described in Hoffmans (1992) should be incorporated.

- The new process-based approach for modelling the growth of an erosional channel can be used in a 2DV morphodynamic breach model to compute the lateral breach growth more efficiently.
- The mechanism of bank avalanching is implicitly modelled via the channel cross-sectional growth. To approximate the nature of the phenomenon closer, it is recommended to model this discrete erosion process in a process-based approach in which geotechnical aspects involved are described.

With regard to the model calibration and verification:

- For the modelling of the time-dependent development of morphological processes in general, viz. breach growth and barrier response in the present study, knowing the final situation is usually insufficient to understand the temporal behaviour. It is recommended to design laboratory experiments in such a way that more detailed data on the time-dependent morphological development of these processes can be obtained. This issue is further addressed in the following recommendations.
- Quantitative field data of the response of barrier response during storm surges are needed for model calibration and verification. However, this type of data is scarce and far from complete. In most cases only the post-storm profiles are available but not the associated driving hydraulic conditions. Hence, it is highly recommended to carry out large-scale model experiments to construct a complete set of the time-dependent response of the barrier response during storm surges.
- As discussed in Section 6.5 there are uncertainties in the existing breach data. Hence, also for the breach modelling a large scale breach experiment is recommended in which the 3D time-dependent breach morphological development can be reliably measured.

With regard to the extension of the present model application:

The present model (barrier breach component) has been developed for breaching of sand barriers. The model is morphodynamic and incorporates the effect of the hydraulic jump turbulence in describing the scour formation and development. Therefore, the present model is conceptually adaptable to breach modelling of cohesive bodies such as clay dikes, where details of the flow structure modified by the jump turbulence are very essential. It is recommended to investigate this possibility of adaptation for modelling of breach growth in clay-dikes.

BIBLIOGRAPHY

Bailard, J.A., 1981. An energetics total load sediment transport model for a plane sloping beach. *J. Geophysical Res., AGU*, 86, C11, pp. 10938-10954.

Bailard, J.A., 1982. Modelling on-offshore sediment transport in the surfzone, *Proc. 18th Coast. Engrg. Conf., ASCE*, pp. 1419-1438.

Basco, D.R. and C.S. Shin, 1999. A one-dimensional numerical model for storm breaching of barrier islands. *J. Coast. Res., CERF*, 15, 1, pp. 241-260.

Battjes, J.A., 1974. Surf similarity. *Proc. 14th Coast. Engrg. Conf., ASCE*, pp. 466-480.

Battjes, J.A. and Janssen, J.P.F.M., 1978. Energy loss and set-up due to wave breaking of random waves. *Proc. 16th Coast. Engrg. Conf., ASCE*, pp. 569-589.

Bosboom, J., Aarninkhof, S.G.J., Reniers, A.J.H.M., Roelvink, J.A. and Walstra, D.J.R., 2000. UNIBEST-TC 2.0 - Overview of model formulations. *WL | Delft Hydraulics*, Rep. H2305.42, Delft, the Netherlands.

Broich, K., 1998. Mathematical modelling of dam-break erosion caused by overtopping. *Proc. CADAM - Concerted action on dam-break modelling*, paper No.3, Munich, Germany, 27 pp.

Bruun, P., 1954. Coast erosion and development of beach profiles. *Technical memo No.44*, Beach erosion board, U.S. Army Corps of Civil Engineers.

Burguete, J. and Garcia-Navarro, P., 2001. Efficient construction of high-resolution TVD conservative schemes for equations with source terms: application to shallow water flows. *Int. J. Numer. Meth. Fluids*, 37, pp. 209-248.

Busnelli, M.M., 2001. Numerical simulation of free surface flows with steep gradients. *Communications on Hydraulic and Geotechnical Engineering*, Rep. No. 01-3, Delft Univ. Techn., Delft, the Netherlands, 180 pp.

Caan, C.P., 1996. Bresgroei: een experimental onderzoek naar de ontwikkeling van de ontgrodingskuil (Breach growth: an experimental investigation of the development of the scour hole), *Master thesis*, Hydraulic and Geotechnical Eng. Div., Dept. Civ. Eng., Delft Univ. Techn., Delft, the Netherlands, 100 pp.

Chanson, H. and Brattberg, T., 2000. Experimental study of the air-water shear flow in a hydraulic Jump, *Int. J. Multiphase Flow*, *Elsevier*, 26, pp. 583-607.

Coleman, S.E., Andrews, D.P. and Webby, M.G., 2002. Overtopping breaching of noncohesive homogenous embankments. *J. Hydr. Eng., ASCE,* 128, 9, pp. 829-838.

Cunge J.A., Holly, F.M. and Verwey A., 1980. Practical aspects of computational river hydraulics, *Massachusetts Pitman*, London, U.K.

Dally, W.R. and Dean, R.G., 1984. Suspended sediment transport and beach profile evolution. *J. Waterw. Port Coastal Ocean Eng., Div. ASCE*, 110, 1, pp. 15-33.

Dean, R.G., 1977. Equilibrium beach profiles. *U.S. Atlantic and Gulf coasts, Ocean engineering*, Rep. No. 12, Dep. Eng., Univ. Delaware, Newark, 45 pp.

Dean, R.G., 1987. Coastal sediment processes: Towards engineering solutions. *Proc. Coastal Sediments' 87*, *ASCE*, pp. 1-24.

Dean, R.G., 1991. Equilibrium beach profiles: Characteristics and applications. *J. Coast. Res.*, *CERF*, 7, 1, pp. 53-84.

Den Heijer, C., 2005. Effect of wave period on dune erosion. *Master thesis*, Fac. Civ. Eng. Geo. Sciences, Delft Univ. Techn., Delft, the Netherlands.

De Vriend, H.J. and Stive, M.J.F., 1987. Quasi-3D modelling of nearshore currents. *Coastal Engineering*, *Elsevier*, 11, pp. 565-601.

Donnelly C., Kraus, N.C. and Larson, M., 2006. State of knowledge on measurement and modelling of coastal overwash. *J. Coast. Res.*, *CERF*, 22, 4, pp. 965-991.

Engelund, F. and Hansen, E., 1967. A monograph on sediment transport. *Technisk Forlag*, Copenhagen, Denmark.

Fread, D.L., 1984. A breach erosion model for earthen dams. *National Weather Service (NWS) Rep.*, NOAAA, Silver Spring, MA, USA.

Fritz, H.M. and Hager, W.H., 1998. Hydraulics of embankment weirs. *J. Hydr. Engrg.*, *ASCE*, 124, 9, pp. 963-971.

Fujita, Y. and Tamura, T., 1987. Enlargement of breaches in flood levees on alluvial plains. *Natural Disaster Science*, 9, 1, pp. 37-60.

Galappatti, R., 1983. A depth-integrated model for suspended transport. *Communications on Hydraulics*, Rep. No. 83-7, Delft Univ. Techn., Delft, the Netherlands.

Garcia-Navarro, P. and Vazquez-Cendon, M. E., 2000. On numerical treatment of the source terms in the shallow water equations. *Computer & Fluids*, *Elsevier*, 29, pp. 951-979.

Gharangik, A. M. and Chaudhry, M. H., 1991. Numerical simulation of hydraulic jump, *J. Hydr. Engrg., ASCE,* 117, 9, pp. 1195-1211.

Goichot, M. and Pluijm, M., 2000. Hue lagoon closure gap: emergency plan of action - expert opinion, *NDM - partnership reports*, Natural disaster mitigation partnership project, Hanoi, Vietnam.

Gordon, A.D., 1992. Coastal lagoon entrance dynamics. *Proc. 23rd Coast. Engrg. Conf., ASCE*, 2, pp. 2881-2893.

Hager, W. H., 1992. Energy dissipators and hydraulic jumps, *Kluwer Academic, Water Science and Technology Library*, Dordrecht, the Netherlands, 288 pp.

Hancock, M.W. and Kobayashi, N., 1994. Wave overtopping and sediment transport over dunes. *Proc. 24th Coast. Engrg. Conf., ASCE*, 2, pp. 2029-2042.

Hermann, M.F. and Hager, W.H., 1998. Hydraulics of embankment weirs, *J. Hydr. Eng.*, *ASCE*, 124, pp. 963-971.

Hydrology handbook, 1996. Task Committee on Hydrology Handbook, *ASCE,* 784 pp.

Hoffmans, G.J., 1992. Two dimensional mathematical modelling of local-scour holes, *Communications on Hydraulic and Geotechnical Engineering*, Rep. No. 94-7, Delft Univ. Techn., Delft, the Netherlands, 198 pp.

Horikawa, K. (ed.), 1988. Nearshore dynamics and coastal processes: theory, measurement, predictive models. *Univ. Tokyo Press*, 522 pp.

Hughes, A.S. (ed.), 1993. Physical models and laboratory techniques in coastal engineering. *World Scientific,* Singapore, 568 pp.

Hughes, M.G., 1995. Friction factors for wave uprush. *J. Coast. Res.*, *CERF*, 11, 4, pp. 1089-1098.

Hughes, M.G., Masselink, G. and Brander, R.W., 1997. Flow velocity and sediment transport in the swash zone of a steep beach. *Marine Geology*, *Elsevier*, 138, pp. 191-103.

Jorgen Fredsoe and Rolf Deigaard, 1992. Mechanics of coastal sediment transport, *Advanced Series in Ocean Engineering*, *World Scientific*, Singapore, Vol. 3, 369 pp.

Khan, A.A. and Steffler, P.M., 1996. Physically based hydraulic jump mode for depth-averaged computations. *J. Hydr. Engrg.*, *ASCE*, 112, 10, pp. 540-548.

Kobayashi, N., 1987. Analytical solution for dune erosion by storms. *J. Waterw. Port Coastal Ocean Eng. Div.*, *ASCE*, 113, 4, pp. 401-418.

Kobayashi, N. and Poff, M.T., 1994. Numerical model RBREAK2 for random waves on impermeable coastal structures and beaches. Research Rep. No. CACR-94-12, Centre for Applied Coastal Research, Univ. Delaware, Delaware, USA.

Kobayashi, N., Tega, Y. and Hancock, M.W., 1996. Wave reflection and overwash of dunes. *J. Waterw. Port Coastal Ocean Eng. Div.*, *ASCE*, 122, 3, pp. 150-153.

Kraus, N.C., 2003. Analytical model of incipient breaching of coastal barriers. *Coastal Engineering Journal, World Scientific and JSCE*, 45, 4, pp. 511-531.

Kriebel, D.L., 1990. Advances in numerical modelling of dune erosion. *Proc. 22nd Coast. Engrg. Conf., ASCE*, 2, pp. 2304-2317.

Larson, M., Kraus, N.C. and Byrnes, M.R., 1990. SBEACH: numerical model for simulating storm-induced beach change, Report 2: Numerical formulation and model tests. *Techn. Rep. CERC-89-9*, US Army Engineer Experiment Station, Vicksburg, MS, USA.

Larson, M., Kubota, S. and Erikson, L., 2004. Swash-zone sediment transport and foreshore evolution: field experiments and mathematical modelling. *Marine Geology*, *Elsevier,* 212, 1-4, pp. 61-79.

Larson, M., Wise, R.A. and Kraus, N.C., 2005. Modelling dune response due to overwash transport. *Proc. 29th Coast. Engrg. Conf.*, *World Scientific Press*, pp. 2133–2145.

Leatherman, S.P. (ed.), 1981. Overwash processes. *Benchmark paper in geology, Hutchinson Ross Pub. Co.*, Stroudsburg, PA, 58, 376 pp.

Le, V.T. and Bui, T.B., 2000. Characteristics of tropical cyclones in the East sea and a review on cyclone disaster mitigation activities (in Vietnamese), *UNDP VIE/97/002-DMU Official Rep.*, Hanoi, Vietnam.

Liu Qinchao and Uwe Drewes, 1994. Turbulence Characteristics in Free and Forced Hydraulic Jumps, *J. Hydr. Research, ASCE*, 32, 6, pp. 877-898.

Long, D., Steffler, P. M. and Rajaratnam, N., 1991. A numerical study of submerged hydraulic jumps, *J. Hydr. Research, IAHR,* 29, 3, pp. 293-308.

Madsen, P.A. and Svendsen, I.A., 1983. Turbulent bores and hydraulic jumps, *J. Fluid Mech.*, 129, pp. 1-25.

Marshall, T.J., Holmes, J.W. and Rose, C.W., 1996. Soil Physics. *Cambridge Univ. Press*, London, 469 pp.

Masselink, G. and Hughes, M.G., 1998. Field investigation of sediment transport in the swash zone, *Cont. Shelf Res.*, 18, pp. 1179-1199.

Mayer, R.H. and Kriebel, D.L., 1994. Wave runup on composite slope and concave beaches. *Proc. 24th Coast. Engrg. Conf., ASCE,* pp. 2325-2339.

Mayer-Peter, E. and Muller, R., 1948. Formulas for bed-load transport. *Proc. 2nd Congress IAHR*, Appendix 2, pp. 39-64.

Mojib, R.M., 1990. Development of a computer program for gradual failure of earthen dams due to overtopping. *Doctoral thesis*, Univ. Tennessee, Knoxville, TN, USA.

NCKH-NN, 2001. Rehabilitation and adaptation of the Hue lagoon and its inlets (in Vietnamese). *Special issues Rep.*, *National research program*, MOET, Hanoi, Vietnam.

Nairn, R.B., 1990. Prediction of cross-shore sediment transport and beach profile evolution. *Doctoral thesis*, Dept. Civil Eng., Imperial College, London.

Nielsen, P., 1992. Coastal bottom boundary layers and sediment transport. *Advanced Series in Ocean Engineering*, *World Scientific*, Singapore, Vol. 4, 324 pp.

Odd, N.V.M, Roberts, W. and Maddocks, J., 1995. Simulation of lagoon breakout. *Proc. 26th Congress IAHR*, 3, pp. 92-97.

Peviani, M.A., 1999. Simulation of earth-dams breaking processes by means of a morphological numerical model. *Proc. CADAM - Concerted action on dam-break modelling*, Paper 23, Zaragoza, Spain, pp. 381-397.

Ponce, V.M. and Tsivoglou, A.J., 1981. Modelling gradual dam breaches. *J. Hydr. Div., ASCE*, 107, HY7, pp. 829-838.

RNE mission report, 1999. *Pre-project workshop "Coastal Engineering in Vietnam"*, Water Resources Univ., Hanoi, Vietnam, 33 pp.

Ribberink, J. S., 1998. Bed-load transport for steady flows and unsteady oscillatory flows. *Coastal Engineering*, *Elsevier*, 34, pp. 59-82.

Roe, P.L., 1981. Approximate Riemann solvers: parameters and difference schemes. *J. Computational Physics*, *Elsevier*, 43, pp. 357-372.

Roelvink, J.A. and Stive, M.J.F., 1989. Bar-generating cross-shore flow mechanisms on a beach. *J. Geophys. Res.*, *AGU*, 94, C4, pp. 4785-4800.

Rozov, A.L., 2003. Modelling of washout of dams. *J. Hydr. Research, IAHR*, 41, 6, pp. 565-577.

Schoonees, J.S. and Theron, A.K., 1995. Evaluation of ten cross-shore sediment transport/morphological models. *Coastal Engineering, Elsevier*, 25, pp. 1-41.

Schuttrumpf, H., 2003. Wave overtopping flow on seadikes - experimental and theoretical investigations. *PIANC-Bullettin*, 114, pp. 7-23.

Singh, V.P., 1996. Dam breach modelling technology. *Kluwer,* Dordrecht, the Netherlands.

Srinivas, R. and Dean, R.G., 1996. Cross-shore hydrodynamics and profile response modelling. *Coastal Engineering, Elsevier,* 27, pp. 195-221.

Stansby, P.K. and Tong Feng, 2004. Surf zone wave overtopping a trapezoidal structure: 1-D modeling and PIV comparison. *Coastal Engineering*, *Elsevier*, 51, pp. 483-500.

Svendsen, I. A., Veeramony, J., Bakunin, J. and Kirby, J. T., 2000. The flow in weak turbulent hydraulic jumps*, J. Fluid Mech.*, 418, pp. 25-57.

Steetzel, H.J., 1993. Cross-shore transport during storm surges. *Delft Hydraulics Communication*, Rep. No. 476, Delft, the Netherlands, 291 pp.

Stive, M.J.F. and Wind, H.G., 1986. Cross-shore mean flow in the surfzone. *Coastal Engineering*, *Elsevier*, 10, pp. 325-340.

Tega, Y. and Kobayashi, N., 1996. Wave overwash of sub-aerial dunes. *Proc. 25th Coast. Engrg. Conf., ASCE*, 3, pp. 4148 - 4161.

Tega, Y. and Kobayashi, N., 1999. Numerical modelling of over-washed dune profiles. *Proc. Coastal Sediment'99*, *ASCE*, pp. 1355-1369.

Tinney, E.R. and Hsu, H.Y., 1961. Mechanics of washout of erodible fuse plug. *J. Hydr. Div.*, *ASCE*, 87, HY3, pp. 1-29.

Toro, E.F., 1997. Riemann solvers and numerical methods for fluid dynamics: a practical introduction. *Springer-Verlag*, Berlin, 624 pp.

Tuan, T.Q., 2003. Time-varying beach slope for overwash models in simulation of lagoon initial breaching (on CD). In: *Proc. 6th COPEDEC*, Paper 89, 7 pp.

Tuan, T.Q., Verhagen, H.J, Visser, P.J. and Stive, M.J.F., 2006a. Wave overwash at low-crested beach barriers, *Coastal Engineering Journal*, *World Scientific and JSCE*, 48, 4, pp. 371-393.

Tuan, T.Q., Verhagen, H.J and Visser, P.J., 2006b. Advances in one-dimensional breach modelling of coastal sand barriers. *Proc. 3rd Int. Scour Erosion Conf.*, *CURNET,* pp 649-658.

Tuan, T.Q., Stive, M.J.F. and Visser, P.J., 2006c. Breaching vulnerability of coastal barriers under effects of tropical cyclones: a model study of the Hue lagoon-Vietnam, in: *Proc. 2nd Int. Estuary Coast Conf.*, Guangzhou, China.

Tuan, T.Q., Verhagen, H.J., Visser, P.J. and Stive, M.J.F., 2007a. Numerical modelling of wave overwash on low-crested sand barriers, in: *Proc. 30th Coast. Engrg. Conf., World Scientific Press.*

Tuan, T.Q., Stive, M.J.F., Verhagen, H.J. and Visser P.J., 2007b. Process-based modelling of the overflow-induced growth of erosional channels, *Coastal Engineering, Elsevier, in review.*

UNDP-Vietnam, 2002. Disaster events. *Annual official reports of Disaster Management Unit*, Hanoi, Vietnam.

Van der Meer, J.W. and Janssen, J.P.F.M., 1995. Wave run-up and wave overtopping at dikes. *Wave forces on inclined and vertical structures*, *ASCE*, pp. 1-26.

Van der Meer, J.W., 1998. Wave run-up and overtopping. In: *Dikes and revetments: design, maintenance and safety assessment*, Pilarczyk, K.W. (ed.), *A.A.Balkema*, Rotterdam, the Netherlands, pp. 145-159.

Van Gent, M.R.A., 2001. Wave runup on dikes with shallow foreshores. *J. Waterw. Port Coastal Ocean Eng.*, *ASCE*, 127, 5, pp. 254-262.

Van Rijn, L.C., 1984a. Sediment transport, part I : bed load transport. *J. Hydr. Eng.*, *ASCE*, 110, pp. 1431-1456.

Van Rijn, L.C., 1984b. Sediment transport, part II : suspended load transport. *J. Hydr. Eng.*, *ASCE*, 110, pp. 1631-1641.

Van Rijn, L.C., 1993. Principles of sediment transport in rivers, estuaries and coastal seas. *Aqua Publications*, Amsterdam, the Netherlands.

Varquez-Cendon, M.E., 1999. Improved treatment of source terms in upwind schemes for the shallow water equations in channels with irregular geometry. *J. Comp. Phys.*, *Academic Press,* 148, pp. 497-526.

Vellinga, P., 1986. Beach and dune erosion during storm surges. *Delft Hydraulics Communication*, Rep. No. 372, Delft, the Netherlands, 169 pp.

Verhagen, H.J., Steenaard, J. and Tuan, T.Q., 2005. Infiltration of overtopping water in a breakwater crest. *Proc. 29th Coast. Engrg. Conf., World Scientific Press*, 1, pp. 4253-4262.

Villegas, P., 2004. Flood modelling in Perfume river basin, Hue province, Vietnam. *Master thesis*, Int. Institute Geo-information Science Earth Observation, Enscede, the Netherlands, 86 pp.

Visser, P.J., 1998. Breach growth in sand-dikes. *Communication on Hydraulic and Geotechnical Engineering*, Rep. No. 98.1, Delft Univ. Techn., Delft, the Netherlands.

Walstra, D.J.R., and Steetzel, H.J., 2003. Description of improvements in the UNIBEST-TC model: Upgrade of UNIBEST-TC Version 2.04 to 2.10. *WL | Delft Hydraulics*, Rep. Z3412.

Appendix A

RESULTS FROM FIXED-BED OVERWASH EXPERIMENTS

Table A.1 Overtopping data for crest freeboard = 10.0 cm

Test name	**T** (min.)	**Volume** (litre)	$\mathbf{H_{m0,\ inc.}}$ (m)	$\mathbf{T_{m,\ inc.}}$ (sec.)				$\mathbf{H_{toe}}$ (m)	$\mathbf{T_{m,\ toe}}$ (sec.)			$\mathbf{q_{ovt}}$ (l/s/m)	$\mathbf{T_{ovt}}$ (sec.)	$\mathbf{t_{rise}/t_{ovt}}$ **(-)**	$\mathbf{1/F_{cd}}$ **(-)**
				$\mathbf{T_{0.1}}$	$\mathbf{T_{0.2}}$	$\mathbf{T_P}$	$\mathbf{T_{-1.0}}$		$\mathbf{T_{0.1}}$	$\mathbf{T_{0.2}}$	$\mathbf{T_{-1.0}}$				
I11T25	45	172.5	0.110	2.13	2.02	2.50	1.54	0.101	1.42	1.14	1.66	0.0796	180.74	0.227	14.01
I13T25	46	291.7	0.129	2.12	2.01	2.50	1.54	0.106	1.49	1.19	1.77	0.1304	229.42	0.245	11.43
I16T25	45	452.0	0.158	2.10	1.98	2.50	1.54	0.110	1.60	1.25	1.96	0.2085	263.10	0.244	9.55
I12T20	40	114.2	0.118	1.70	1.62	2.00	1.35	0.105	1.31	1.09	1.54	0.0592	122.56	0.236	18.11
I13T23	40	225.5	0.128	1.93	1.84	2.30	1.44	0.108	1.41	1.14	1.69	0.1170	186.16	0.248	12.01
I15T20	40	232.0	0.146	1.69	1.62	2.00	1.35	0.109	1.37	1.13	1.65	0.1203	175.76	0.235	12.72
I17T20	40	306.2	0.164	1.69	1.61	2.00	1.35	0.109	1.41	1.14	1.74	0.1588	198.16	0.236	11.35
I15T23	40	318.0	0.148	1.93	1.84	2.3	1.44	0.111	1.47	1.17	1.79	0.1649	217.92	0.235	10.36
I17T23	40	406.0	0.168	1.92	1.82	2.3	1.44	0.112	1.51	1.18	1.89	0.2106	229.26	0.248	9.84
I15T15	30	57.0	0.142	1.31	1.26	1.5	1.18	0.104	1.15	0.99	1.39	0.0394	80.64	0.236	20.21
I17T15	30	89.7	0.158	1.32	1.27	1.5	1.18	0.106	1.18	1.00	1.44	0.0619	97.58	0.238	16.53
I13T17	35	64.5	0.127	1.45	1.39	1.7	1.24	0.104	1.22	1.04	1.43	0.0382	86.60	0.227	22.32
I15T17	35	102.0	0.145	1.45	1.39	1.7	1.24	0.107	1.23	1.04	1.48	0.0604	111.92	0.241	17.25
I17T17	35	137.5	0.163	1.46	1.40	1.7	1.25	0.108	1.26	1.05	1.54	0.0815	133.42	0.238	14.48
I14T25	45	340.0	0.140	2.11	1.99	2.5	1.54	0.110	1.52	1.20	1.83	0.1568	228.36	0.244	11.09
I14T27	50	439.0	0.139	2.27	2.14	2.7	1.60	0.112	1.64	1.30	1.92	0.1823	252.66	0.240	10.93
I16T27	50	574.5	0.160	2.25	2.12	2.7	1.60	0.113	1.71	1.33	2.07	0.2386	285.42	0.246	9.85

Table A.2 Overtopping data for crest freeboard = 7.5 cm

Test name	T (min.)	Volume (l)	$H_{m0,\,inc.}$ (m)	$T_{m,\,inc.}$ (sec.)				H_{toe} (m)	$T_{m,\,toe}$ (sec.)			q_{ovt} (l/s/m)	T_{ovt} (sec.)	t_{rise}/t_{ovt}	$1/F_{cd}$
				$T_{0.1}$	$T_{0.2}$	T_P	$T_{-1.0}$		$T_{0.1}$	$T_{0.2}$	$T_{-1.0}$				
I13T15	30	108.0	0.123	1.29	1.24	1.50	1.17	0.098	1.14	0.98	1.36	0.0746	131.96	0.306	12.32
I15T15	30	167.0	0.139	1.31	1.26	1.50	1.18	0.101	1.15	0.98	1.40	0.1153	162.24	0.305	10.15
I11T17	36	132.0	0.106	1.45	1.39	1.70	1.24	0.097	1.20	1.02	1.41	0.0760	171.58	0.290	11.71
I13T17	36	202.0	0.125	1.45	1.39	1.70	1.24	0.102	1.20	1.02	1.44	0.1164	186.16	0.293	10.78
I15T17	36	271.0	0.142	1.45	1.39	1.70	1.25	0.104	1.22	1.03	1.49	0.1561	205.00	0.308	9.75
I11T20	40	214.0	0.107	1.70	1.62	2.00	1.35	0.100	1.32	1.11	1.51	0.1110	217.44	0.270	10.36
I13T20	40	312.0	0.126	1.69	1.61	2.00	1.35	0.104	1.30	1.07	1.57	0.1618	246.44	0.292	9.21
I15T20	40	470.0	0.144	1.69	1.62	2.00	1.35	0.106	1.36	1.11	1.67	0.2438	279.20	0.285	8.01
I17T20	40	545.0	0.163	1.69	1.61	2.00	1.35	0.107	1.40	1.13	1.77	0.2827	287.74	0.289	7.78
I11T23	42	363.0	0.107	1.97	1.87	2.30	1.48	0.101	1.38	1.13	1.62	0.1793	294.12	0.264	7.99
I13T23	42	490.0	0.127	1.97	1.87	2.30	1.51	0.106	1.41	1.14	1.71	0.2421	299.86	0.271	7.81
I15T23	42	610.0	0.146	1.93	1.84	2.30	1.44	0.107	1.47	1.17	1.84	0.3014	318.80	0.276	7.41
I17T23	42	707.0	0.165	1.95	1.84	2.30	1.52	0.109	1.53	1.20	1.96	0.3493	313.98	0.280	7.61
I11T25	45	418.0	0.108	2.13	2.02	2.50	1.54	0.102	1.43	1.15	1.68	0.1928	328.02	0.284	7.80
I13T25	48	580.0	0.127	2.12	2.01	2.50	1.54	0.106	1.50	1.20	1.80	0.2509	354.42	0.283	7.69
I15T25	45	692.0	0.147	2.10	1.98	2.50	1.54	0.108	1.57	1.23	1.94	0.3192	347.34	0.280	7.32
I11T27	50	518.0	0.108	2.29	2.17	2.70	1.59	0.102	1.52	1.22	1.75	0.2151	345.82	0.273	8.19
I13T27	50	677.0	0.127	2.27	2.15	2.70	1.60	0.106	1.59	1.26	1.89	0.2811	369.74	0.276	7.69

Appendix B

RESULTS FROM MOBILE-BED OVERWASH EXPERIMENTS

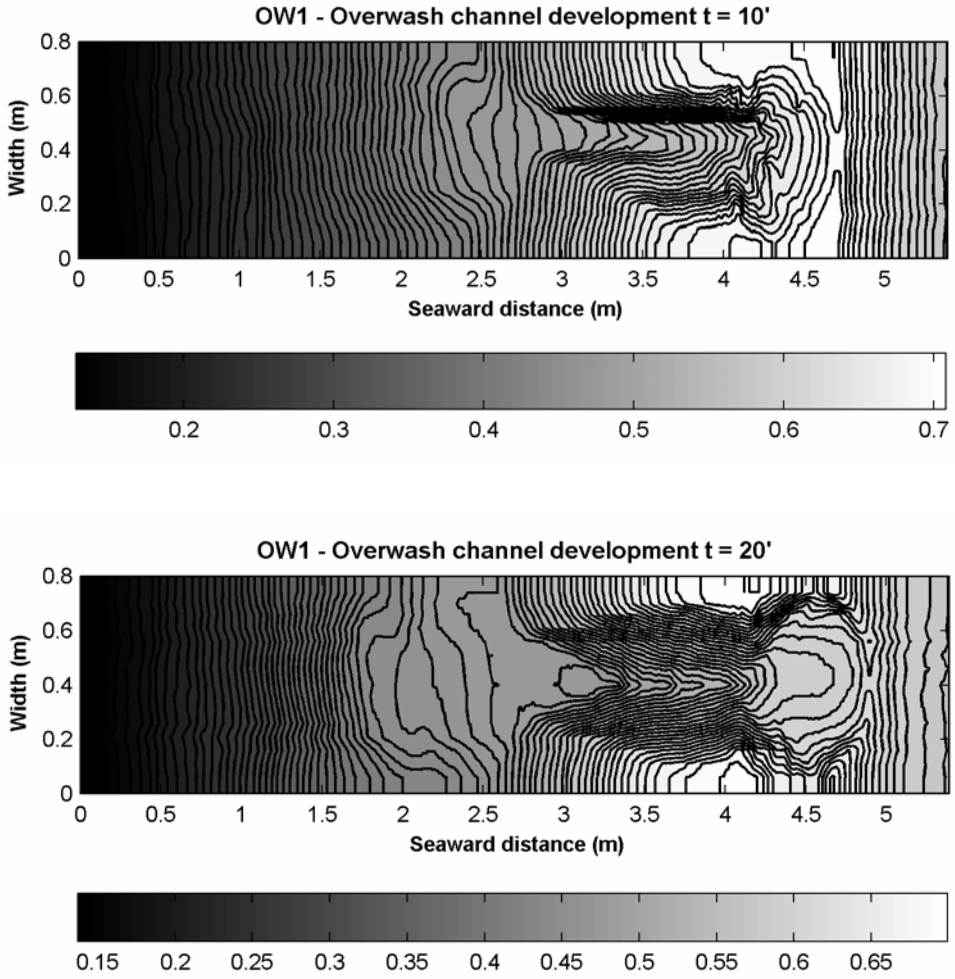

Figure B.1 Test OW1 - Overwash channel development at t = 10' and 20'

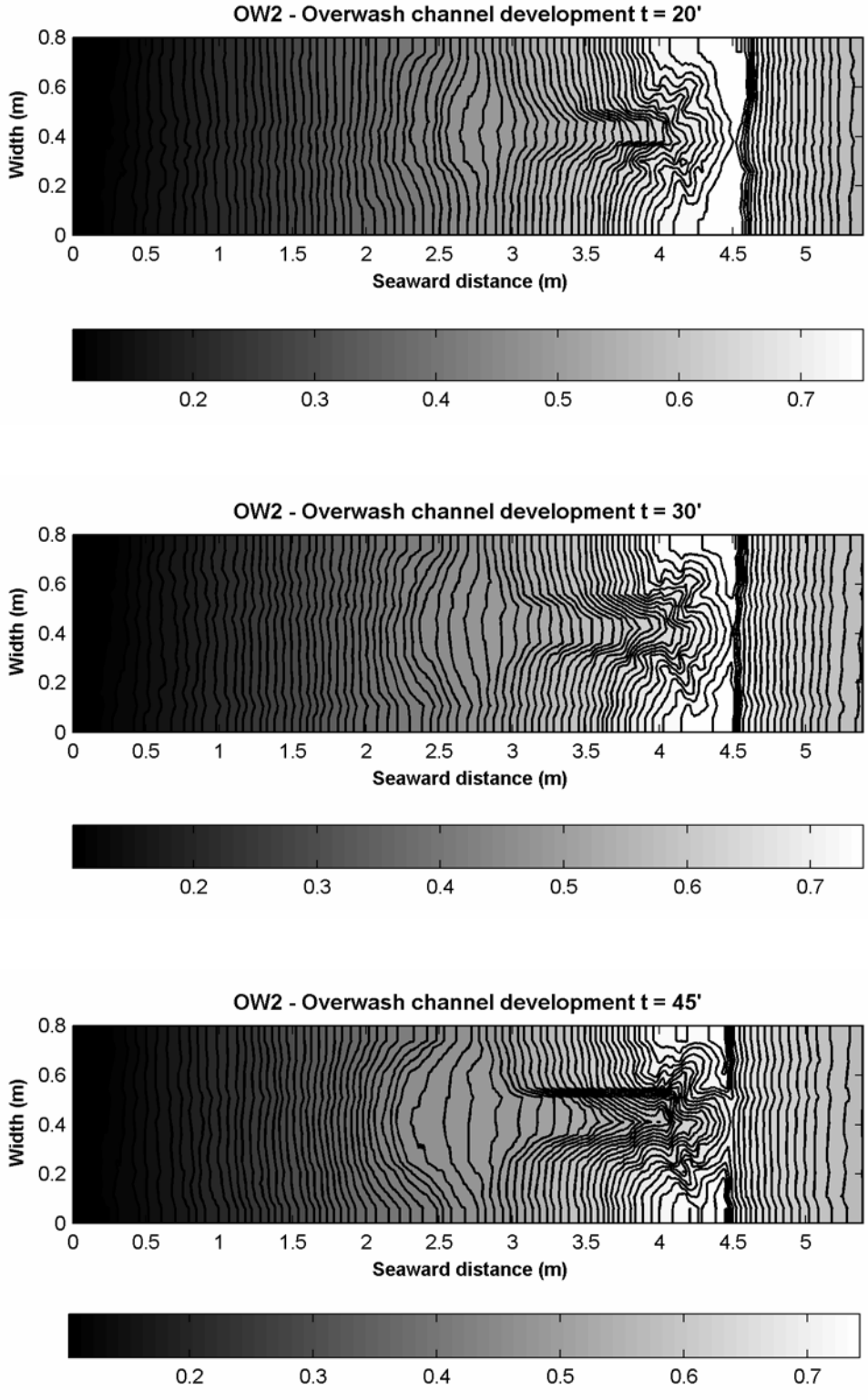

Figure B.2 Test OW2 - Overwash channel development at t = 20', 30', and 45'

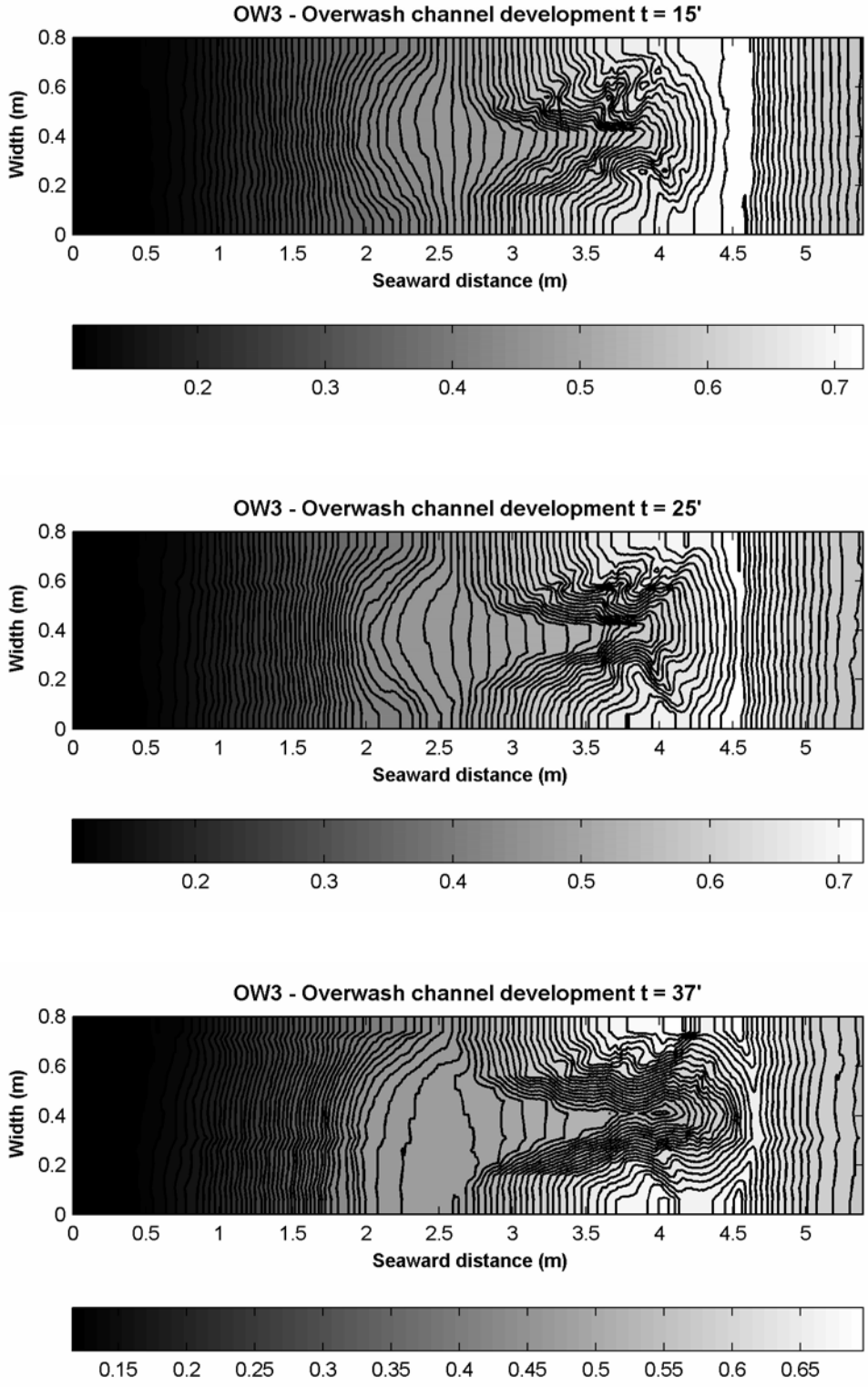

Figure B.3 Test OW3 - Overwash channel development at t = 15', 25', and 37'

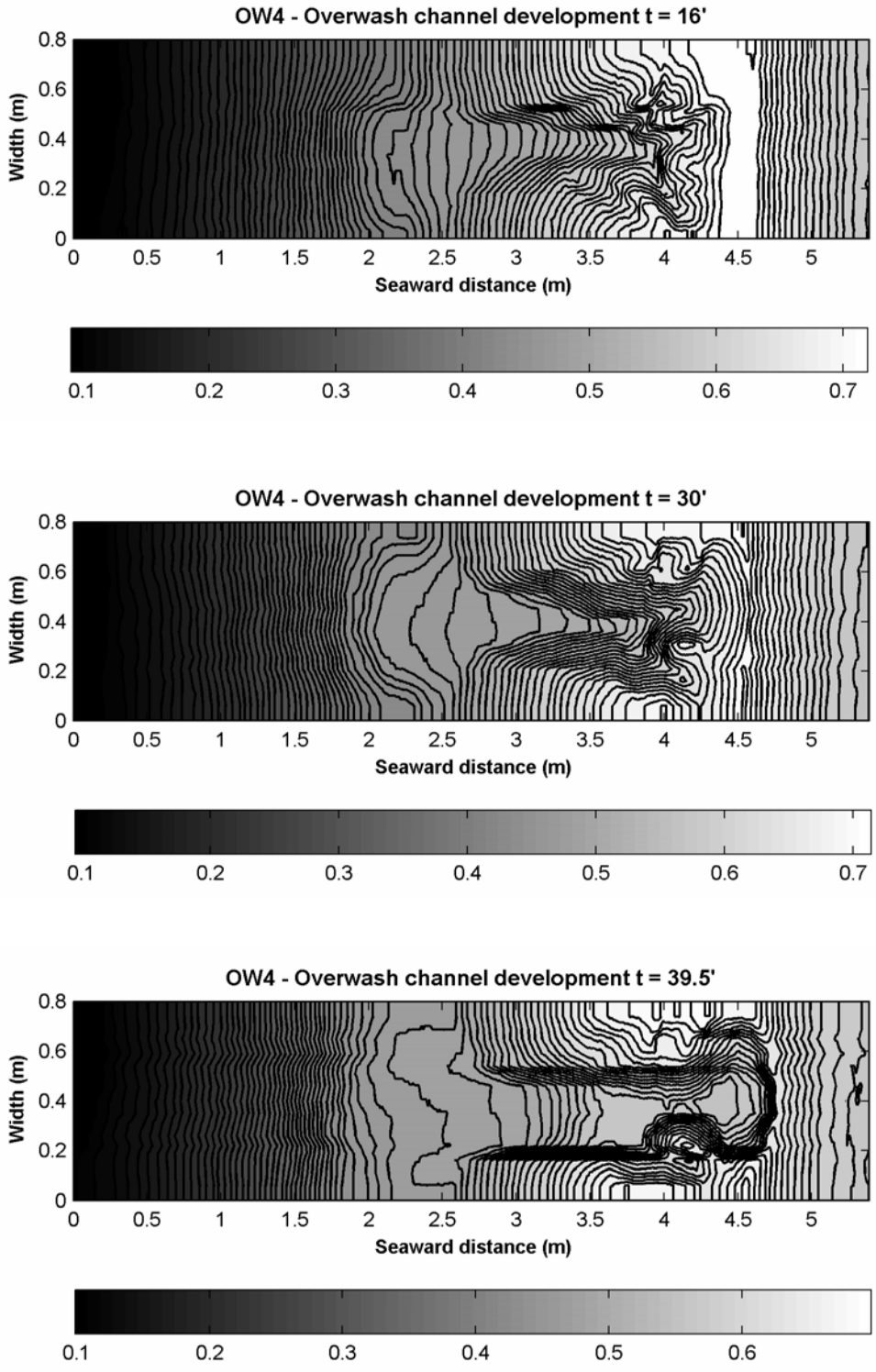

Figure B.4 Test OW4 - Overwash channel development at t = 16', 30', and 39.5'

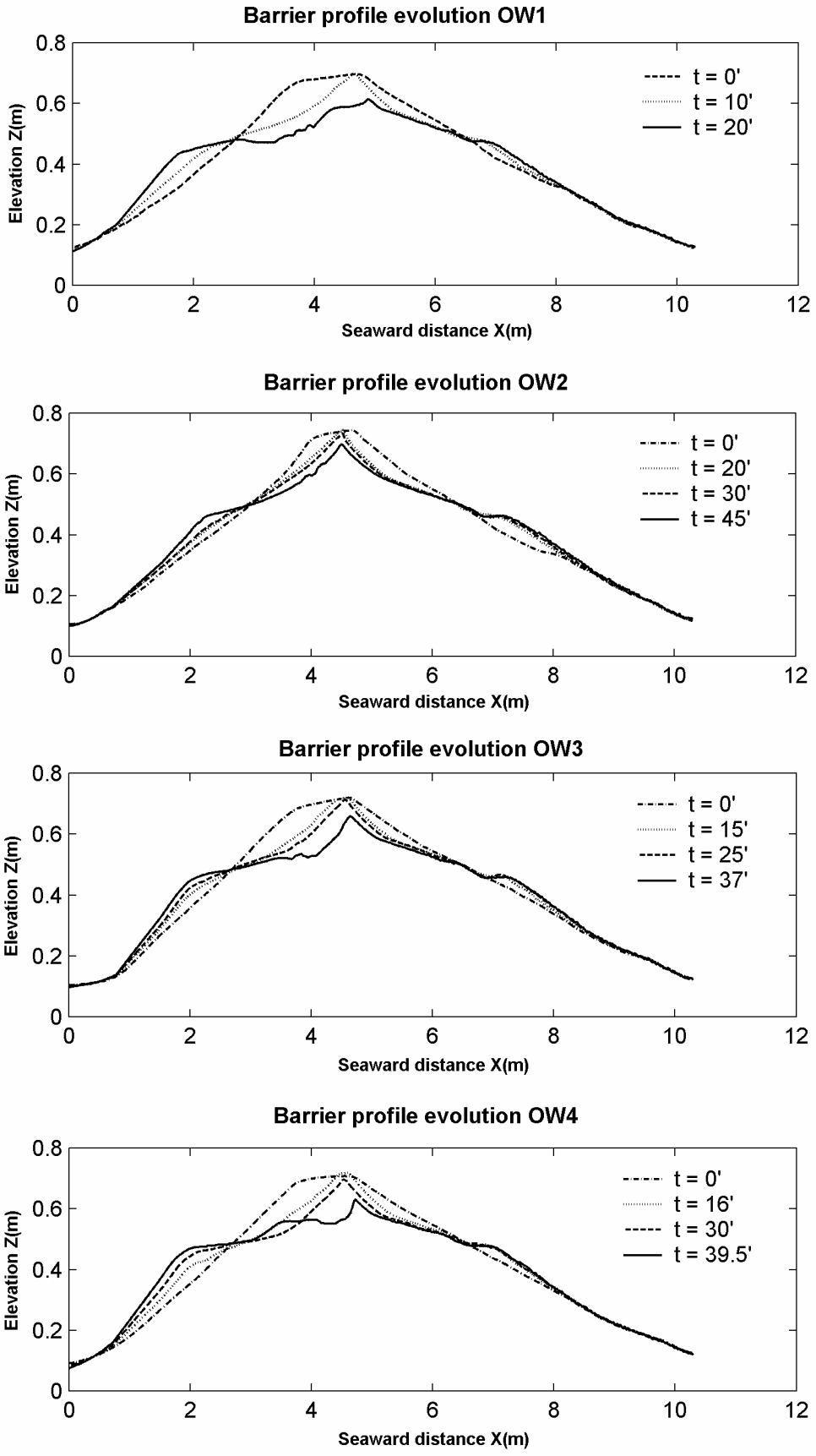

Figure B.5 Response of the barrier profile to wave attacks: overwash tests OW1 to OW4

Table B.1 The measured geometry of overwash channels and the determination of the growth index

Test	**Run**	$\tan\beta$	$\overline{\tan\beta}$	$\tan\gamma$	$\overline{\tan\gamma}$	K_β	K_γ	B_v	$\bar{B}_v$	h_L	$\bar{h}_L$	$\bar{h}_L / \bar{B}_v$	$(\Delta Z_b)_L$	$Z_{cr,b}$	$Z_{cr,s}$	K_{vl} **calculated (Eq. 4.48) with n =**				K_{vl} **measured**
		(-)	(-)	(-)	(-)	(-)	(-)	(m)	(m)	(m)	(m)	(-)	(m)	(m)	(m)					
(1)	(2)	(3)	(4)	(5)	(6)	(7)	(8)	(9)	(10)	(11)	(12)	(13)	(14)	(15)	(16)	**1.50**	**1.65**	**1.73**	**2.00**	(21)
OW1	t = 0’	0.17		0.55				0.050		0.010						(17)	(18)	(19)	(20)	
	t = 10’	0.11	0.14	0.57	0.56	0.78	0.39	0.242	0.146	0.066	0.038	0.260	0.066	0.038	0.038	0.17	0.30	0.37	0.60	0.34
	t = 20’	0.08	0.09	0.5	0.54	0.85	0.46	0.319	0.281	0.112	0.089	0.317	0.055	0.089	0.089	0.33	0.55	0.67	1.06	0.71
OW2	t = 0’	0.18		0.55				0.050		0.010										
	t = 20’	0.16	0.17	0.57	0.56	0.72	0.39	0.188	0.119	0.038	0.024	0.202	0.038	0.024	0.024	0.11	0.19	0.24	0.39	0.28
	t = 30’	0.15	0.15	0.55	0.56	0.74	0.39	0.198	0.193	0.040	0.039	0.202	0.002	0.039	0.039	0.11	0.20	0.24	0.39	0.16
	t = 45’	0.13	0.14	0.55	0.55	0.76	0.42	0.277	0.238	0.064	0.052	0.219	0.024	0.052	0.052	0.14	0.24	0.29	0.47	0.30
OW3	t = 0’	0.19		0.55				0.050		0.010										
	t = 15’	0.14	0.16	0.55	0.55	0.73	0.42	0.298	0.174	0.051	0.031	0.175	0.051	0.030	0.030	0.01	0.17	0.20	0.33	0.21
	t = 25’	0.12	0.13	0.40	0.48	0.79	0.59	0.334	0.316	0.066	0.059	0.185	0.014	0.058	0.058	0.18	0.28	0.33	0.50	0.40
	t = 37’	0.12	0.12	0.31	0.36	0.80	0.78	0.362	0.348	0.108	0.087	0.250	0.042	0.087	0.087	0.91	1.26	1.45	2.09	1.49
OW4	t = 0’	0.19		0.55				0.050		0.010										
	t = 16’	0.13	0.16	0.55	0.55	0.73	0.42	0.265	0.158	0.055	0.033	0.206	0.055	0.032	0.032	0.13	0.22	0.26	0.42	0.26
	t = 30’	0.11	0.12	0.55	0.55	0.80	0.42	0.334	0.300	0.083	0.069	0.230	0.028	0.069	0.069	0.15	0.26	0.32	0.51	0.41
	t = 39.5’	0.07	0.09	0.57	0.56	0.85	0.39	0.407	0.371	0.098	0.091	0.244	0.015	0.090	0.090	0.16	0.27	0.33	0.54	0.21

Note: the measured values of K_{vl} are determined according to Eq. 4.29 or Eq. 5.3, viz. $K_{vl} = -(\Delta Z_b)_L / \Delta B_v$.

LIST OF MAIN SYMBOLS

Roman symbols

a	reference level above bed in suspended load formula of Van Rijn (1984b)	m
A	wetted cross-sectional area of breach or overwash flow	m^2
$\overline{A}$	average wetted cross-sectional area	m^2
$a_1,\ a_2$	regression coefficients in overtopping formulations	--
b	bottom channel width at an arbitrary channel section	m
$c(z)$	volumetric sediment concentration at level z above the bed	m^3/m^3
B_d	depth-averaged (over depth d) channel width at an arbitrary section	m
B_h	depth-averaged (over depth h) channel width at an arbitrary section	m
B_t	top channel width at an arbitrary section	m
B_v	representative (volumetric) channel width	m
$\hat{c}^{1,2}_{i+1/2}$	Roe average celerity	m/s
C	Chezy coefficient	$m^{0.5}/s$
C_r	overall wave reflection coefficient	--
CFC	Courant constant	--
d	water depth at an arbitrary channel section; boundary layer thickness	m
$d_1,\ d_2$	water depths at the toe and at the end of a hydraulic jump	m
d_{toe}	water depth at the toe of the barrier	m
d_{50}	sediment median diameter	m
d_{90}	90% passing sediment diameter	m
D_t	production of roller turbulent energy in a hydraulic jump (per unit bed)	W/m^2
$D^*(x)$	space-varying energy dissipation across the jump (per unit bed)	W/m^2
f_c	friction coefficient in formulation of Ribberink (1998)	--
$f(\lambda)$	shape function of spatial energy dissipation across a hydraulic jump	--
$F(x,U)$	numerical flux vector using in FVM	--
F_{cd}	relative overtopping time	--
$[F_{cd}]$	allowable relative overtopping time	--

$F_{i\pm1/2}$	numerical flux at cell boundary i ± ½ using in FVM	--
F_{st}	overwash-induced reduction factor	--
g	gravitational acceleration	m^2/s
h	channel depth at an arbitrary channel section	m
h_{L}	channel-averaged channel depth	m
H_{m0}	zeroth moment wave height	m
$H_{\mathrm{m0,\,toe}}$	zeroth moment wave height at the toe of the barrier	m
H_{s}	significant wave height	m
H_{rms}	root-mean-squared wave height	m
H_{s0}	significant wave height in deep water	m
H_{rms0}	root-mean-squared wave height in deep water	m
$H_{\mathrm{rms0,\,i}}$	incident deep water root-mean-squared wave height	m
I_{P}	hydrostatic pressure force term	$\mathrm{m}^4/\mathrm{s}^2$
k_{s}, $k_{\mathrm{s,c}}$	Nikuradse roughness and current-related bed roughness	m
K_{vl}	channel cross-sectional growth index	--
L	channel length	m
L_{a}	adaptation length for sediment entrainment	m
L_{jp}	hydraulic jump length	m
L_{sub}	width of a defined subordinate part in Eq. 5.28	m
m	equivalent slope in overtopping calculation; energetics transport power	--
m_{s}	submerged (below water) slope	--
m_{b}	beach (dry) slope	--
MSL	mean sea level	m
n	dimensionless transport exponent	--
N_{L}	length scale factor	--
N_{t}	morphological time scale factor	--
N_{ovt}	number of overtopping wave	--
N_p	number of subordinate parts in Eq. 5.28	--
N_{w}	characteristic number of waves	--
p	bed porosity	--
q	average overtopping discharge	$\mathrm{m}^3/\mathrm{s/m}$
q_{cd}	average instantaneous overtopping discharge	$\mathrm{m}^3/\mathrm{s/m}$
$q_{\mathrm{cd,\,max}}$	maximum average instantaneous overtopping discharge	$\mathrm{m}^3/\mathrm{s/m}$
q_{drift}	shore-normal mass-flux induced by wave propagation without overwash	kg/s/m
$q_{\mathrm{drift}}^{\mathrm{ovw}}$	shore-normal mass-flux induced by wave propagation with overwash	kg/s/m

Q	discharge through the breach or overwash channel	m^3/s
q_s	sediment transport rate per unit channel width (landward)	$m^3/m/s$
q_{st}	unit cross-shore sediment transport rate (seaward)	$m^3/m/s$
q_{st}^{ovw}	sediment overwash rate at the barrier crest	$m^3/m/s$
Q_s	total sediment transport rate (along bottom and sides)	m^3/s
$Q_{s,b}$ $Q_{s,s}$	sediment transport rates along bottom and sides	m^3/s
R	hydraulic radius of (overwash or breach) channel	m
R_{cs}	crest free-board above mean water level	m
R_u	runup level above mean water level	m
s_{0p}	wave steepness based on peak spectral period	--
s_m	fictitious wave steepness based on spectral period T_m and H_{m0}	--
$S(x,U)$	source-term vector	--
S_{bx}	bed slope	--
S_f	friction slope	--
S_{jp}	jump head-loss slope	--
SWL	still water level	m
T	a test duration (fixed-bed or mobile bed overwash)	sec.
T_m	a characteristic wave period	sec.
$T_{m\text{-}1.0,\ toe}$	minus one-zero spectral wave period at the toe of the barrier	sec.
$T_{m\text{-}1.0}$	minus one-zero spectral wave period	sec.
t_{rise}	total rising time of overtopping waves	sec.
$t_{rise,\ w}$	rising time of an individual overtopping wave	sec.
T_{ovt}	total overtopping time of a test	sec.
t_{ovt}	wave-averaged overtopping time	sec.
$t_{ovt,\ w}$	overtopping time of an individual wave	sec.
T_p	peak spectral wave period	sec.
$u(z)$	velocity u at level z above the bed	m/s
$\hat{u}_{i+1/2}^{1,2}$	Roe average velocity	m/s
$\overline{u}_x$	cross-shore mean flow velocity (undertow) without overwash	m/s
$\overline{u}_x^{ovw}$	cross-shore mean flow velocity (undertow) with overwash	m/s
U	depth-averaged velocity	m/s
$U(x)$	conserved flow vector using in FVM	--
$U_L,\ U_R$	left and right values of $U(x)$ using in FVM	--
U_m	maximum velocity at the top of jump boundary layer	m/s
U_i^n, U_i^{n+1}	values of U for node i at present (n) and calculated (n+1) time levels	--

v	stand deviation coefficient of overtopping data	--
V_c	channel volume	m^3
x	horizontal coordinate, arbitrary distance in streamwise direction	m
z	vertical coordinate, an arbitrary elevation above channel bed	m
Z_b	channel bottom elevation	m
Z_{crest}	crest level of the barrier	m

Greek symbols

α	($\tan\alpha = m$) single-valued equivalent slope for overtopping calculation	deg.
$\alpha^{1,2}_{i+1/2}$	Roe coefficients at cell interface $i+1/2$	m^2
β	longitudinal bed slope	deg.
$\widehat{\beta}$	coefficient in Eq. 4.14	--
β_u	nominal relative velocity factor	--
δ	overtopping asymmetry	--
δ_b	thickness of the jump boundary layer	m
δh	local head loss at a point in a hydraulic jump	m
Δ	specific density = $(\rho_s - \rho)/\rho$	--
Δh	total head loss across a classical hydraulic jump	m
Δt	computational time step	sec.
Δx	computational horizontal spatial step	m
Δz	computational vertical spatial step	m
ε	scattering coefficient	--
ϕ	sediment angle of repose	deg.
γ	channel side slope angle	deg.
ξ	surf similarity parameter (Irribaren number); coefficient in Eq. 6.40	--
ξ_m	Irribaren number based on s_m	--
ξ_{toe}	Irribaren number at the toe of the barrier	--
η	composite-slope parameter	--
κ	von Karman constant	--
$\hat{\lambda}^{1,2}_{i+1/2}$	eigenvalues of Roe matrix	m/s
λ	dimensionless length parameter	--
ν_t	eddy viscosity	m^2/s
ν	molecular viscosity	m^2/s

θ	wave incident angle	deg.
θ'	effective mobility parameter (Shields number)	--
θ_{cr}	critical Shields parameter	--
$\theta_{cr,0}$	critical Shields parameter on a horizontal bed	--
ρ	density of water	kg/m^3
ρ_s	density of sediment	kg/m^3
σ	a dimensionless vertical ordinate	--
σ_b	dimensionless vertical ordinate of jump boundary layer	--
σ_r	dimensionless vertical ordinate at the level underneath the roller	--
σ_0	dimensionless vertical ordinate at zero velocity level above the bed	--
τ_b	bed shear stress	N/m^2
$\tau_{b,c}$	critical bed shear stress	N/m^2
τ_{xx}, τ_{xz}	turbulent (Reynolds) stresses	N/m^2
w_s	sediment fall speed	m/s
ψ	numerical smoothing factor	--
$\left(\frac{\partial A}{\partial t}\right)_L$	average rate of change in channel cross-sectional area	m^2/s
$\left(\frac{\partial Z_b}{\partial t}\right)_L$	average vertical channel growth rate	m/s